The Dissertation Committee for Katherine Louise Aughenbaugh Certifies that this is the approved version of the following dissertation:

Fly ash-based geopolymers: identifying reactive glassy phases in potential raw materials

Committee:

Maria Juenger, Supervisor

Raissa Ferron

Kevin Folliard

David Fowler

Ken Snyder

Fly ash-based geopolymers: identifying reactive glassy phases in potential raw materials

by

Katherine Louise Aughenbaugh, B.S.; M.S.E.

Dissertation

Presented to the Faculty of the Graduate School of

The University of Texas at Austin

in Partial Fulfillment

of the Requirements

for the Degree of

Doctor of Philosophy

The University of Texas at Austin

August 2013

Dedication

For Mom and Dad, who always thought I could.

Acknowledgements

For funding this research I would like to thank the National Science Foundation, CMMI grant # 0926627. Also, thank you to NIST (Paul Stutzman and Ken Snyder) and the Bureau of Economic Geology (Kitty Milliken, Rob Reed, and Patrick Smith) for use of their microscope facilities for Scanning Electron Microscopy work. Thank you to Donggao Zhao for allowing me to use his carbon coater.

First and foremost I would like to thank Paul Stutzman, without whom this work could not have been completed. I greatly appreciate your patience, technical advice, and encouragement as I pursued this research work. It could not have been done without you! In addition, I would like to thank Dr. Maria Juenger, the other person without whom this work could not have been completed. I have always appreciated your friendly advising style, and I am thankful for the mentoring relationship we have had for the last 6 years of graduate school. Thank you for not only being an advisor but a mentor as well.

Thank you to my committee- Ken Snyder, Raissa Ferron, Kevin Folliard, and David Fowler. Ken, I appreciate your collaborative spirit and support of my coming to work at the NIST facilities several times throughout the project. It truly benefited the research and me to spend the weeks in Gaithersburg that I did. To my UT committee members, thank you for your friendly interactions, wonderful course offerings, and for taking the time to review and comment on my work. I truly appreciate it.

To the lab ladies-- I could not have finished without your support and encouragement. Ramya, Lisa, Zeynep, Sarah, and Saamiya, you have been great friends, and I truly appreciate these years we have spent together. Also, to the other 18Beers including Eric, Anthony, and Chris, who started this journey with me, I have really

enjoyed our years together. Thank you to Irvin Chen for training me on the instruments, methods, and techniques to get me going on this research.

To Mike Rung who has been a huge support throughout this process, both technically and in any other "optimization" problem in my life, as long as it didn't involve an Apple product. Oh yeah, and for finding the best coffee in Austin!

To Sherian Willams for helping keep me straight on all things UT. I also greatly appreciate the always-prompt-and-friendly help of Kathy Rose in the Civil Engineering department.

To the undergraduate researchers who have aided in the experimental work and data analysis, including Andrea Debee-Coffin, Leslie Hollis, Rachel Cano, Christina Phensy, and Aasiyah Baig. Thank you for your excitement about the research and for helping run experiments on this project.

To my brother, who was always encouraging no matter how frustrated I was. I'm so proud of all you have accomplished!

And to my husband Jason. I could not have taken the work to the next level without your expertise in MATLAB. Not to mention the food-cooking, house-cleaning, errand-running, and dog-walking that you took on as I finished everything. Thank you, and I love you.

Fly ash-based geopolymers: identifying reactive glassy phases in potential raw materials

Katherine Louise Aughenbaugh, PhD

The University of Texas at Austin, 2013

Supervisor: Maria Juenger

Geopolymer cements present a unique opportunity to make concrete binders almost entirely out of waste stream materials. Geopolymers made from fly ash, a waste product of coal power generation, as the aluminosilicate source and caustic activating solution were the focus of this study. However, the use of waste stream materials presents many challenges. One major stumbling block is that fly ash is inherently variable in composition and difficult to comprehensively characterize. The purpose of this work was to clarify the relationship between fly ash composition and reactivity in geopolymer cements. Ten fly ashes comprising a wide compositional spectrum were selected for the study and were characterized using quantitative x-ray diffraction and multispectral image analysis (MSIA) of x-ray maps coupled with point compositional analysis. The fly ashes were mixed into geopolymer mortars to determine their reactivity when activated as geopolymers. I hypothesized that the fly ashes that performed well under geopolymer formation conditions would have similarities in the glassy phases identified in them. The fly ashes that resulted in geopolymers with high compressive strengths did have several glassy phases in common. The phases were typically high in calcium, high in silicon, and somewhat low in aluminum. To determine whether the common phases were soluble and therefore likely to be dissolved, a dissolution method

was used in which fly ash was mixed with concentrated caustic solution and continuously agitated; after 7 d and 28 d, the solid residues from the dissolution were studied using MSIA. The results showed that most of the glassy phases hypothesized to react were reactive, although the results were somewhat complex due to the heterogeneity of fly ash. The MSIA method proposed in previous work was further developed through this study, and a new way of selecting the training classes for phase composition assignment in the images was proposed.

Table of Contents

List of Tables

List of Figures

Chapter 1: Introduction

Geopolymer cements are an aluminosilicate-based cementing material that can be used in place of ordinary portland cement in concrete construction (Davidovits 1991). The development of geopolymers came from the need for new construction materials that were strong, durable, and non-flammable (Davidovits 1991). Since then, geopolymers have moved into the forefront of a search for green building materials since they can be made with waste materials such as fly ash from coal burning power plants. The global interest in green building materials has come from an increased scrutiny on the environmental impacts of manufacturing cement; Damtoft *et al*. (2008) reported that cement production accounts for 5 % of the global CO_2 emissions resulting from human activity. However, since waste material raw material sources are not specifically designed for reactivity, in contrast to portland cement, they must be thoroughly characterized in order to optimize the properties of the resulting geopolymer.

The goal of the work presented in this dissertation was to evaluate the crystalline and glassy phases of a variety of fly ashes in order to determine what phases exist in each fly ashes and which of those phases dissolve in caustic conditions to form a strong geopolymer cement. The fly ash characterization data were compared to compressive strengths measured from geopolymer mortar cubes to test the hypothesis that the glassy phases that are the most soluble under caustic conditions, as tested using a dissolution technique, will lead to geopolymers with the highest compressive strength. Ten fly ashes were characterized using x-ray diffraction and scanning electron microscopy coupled with multispectral image analysis before and after being subjected to a dissolution process. The dissolution method used a sodium hydroxide solution as a leachant to dissolve material from the fly ash, and the solid residue was used to assess which phases

dissolved from the ten different fly ashes. These data represent a unique contribution to the literature, since the reactive phases in fly ash are thereby identified. Recognition of these phases in other fly ashes can help to select those that should be expected to react well under caustic conditions.

1.1 MOTIVATION

Geopolymers are a 'green' building material since their composition allows for the reuse of byproduct materials as a raw material source (Duxson et al. 2007). Metakaolin was an early source of aluminosilicate for geopolymer formation (Davidovits 1991; Xu and Van Deventer 2000); however, in large quantities it is expensive, and the material is manufactured rather than recycled. Fly ash from coal burning power plants is a recycled raw material source, which is less expensive than metakaolin, while having compositional similarities to metakaolin. The annual global production of fly ash is approximately 750 million tonnes (Malhotra and Mehta 2008), but approximately 49% of the fly ash produced is currently landfilled (Shi et al. 2006). Geopolymers present an opportunity to use this waste material in a beneficial way and in greater quantities than what is now used in blended mixtures with portland cement It is important to note that geopolymers cannot fully replace portland cement for use in concrete, since the annual production of portland cement is 3.39 billion tonnes, more than four-and-a-half times that of fly ash (Sleight 2013). However, the properties of geopolymer cements may be more suited to some applications than portland cements, so they could be a complementary technology. For example, geopolymers were found to expand less under alkali silica reaction than low-alkali portland cements (Garcia-Lodeiro et al. 2007) and they resist degradation in acidic environments when properly proportioned (Bakharev 2005c). Such

properties affect the sustainability of the material, since they extend the service life of a structure.

1.2 PREVIOUS WORK

There are essentially four factors that affect the properties of a geopolymer: composition and physical characteristics of the aluminosilicate powder, composition of the activating solution, proportioning of the powder to the activator, and curing.

To create geopolymers, an aluminosilicate powder is mixed with a caustic activating solution and allowed to harden. The aluminosilicate powder is typically metakaolin or fly ash; of these two the composition and the physical characteristics of the latter are more variable. Activating solutions for geopolymers are typically alkali hydroxides, which are often blended with alkali silicates so that dissolved silicon is present from the earliest stages of the reaction. The alkali cations in the activating solutions are most commonly sodium and potassium; the choice of cation can result in very different geopolymer properties (Skorina and Tikhomirova 2012) as can the concentration (Criado et al. 2007; Ma, Hu, and Ye 2012; A. Al Bakri et al. 2011).

Geopolymer mixture proportioning can be done in several ways. The simplest method is to use solution-powder ratios or water-powder ratios, similar to proportioning used for portland cement (Bakharev 2005c; Ruiz-Santaquiteria et al. 2012; Oh et al. 2010; Fernández-Jiménez, de La Torre, et al. 2006; A. Al Bakri et al. 2011). Since the compositions of the powders and the solutions are more variable than in portland cement systems, a more appropriate technique is to proportion oxide ratios to optimize the composition of the system. The literature has many recommendations for the oxide ratios, from activated metakaolin geopolymers, that lead to proper polymerization and strength: M_2O/SiO_2 = 0.2-0.48, SiO_2/Al_2O_3 = 3.3-4.5, H_2O/M_2O = 10-25, and M_2O/Al_2O_3

= 0.8-1.6, where M is an alkali metal (Khale and Chaudhary 2007), with many other refinements found in the literature (Fletcher et al. 2005; Duxson et al. 2005; Duxson, Mallicoat, et al. 2007; Duxson and Provis 2008; A. Al Bakri et al. 2011; Criado et al. 2007; Skorina and Tikhomirova 2012).

The proportioning of a geopolymer mixture from fly ash can be complicated since the composition of fly ash is highly variable and fly ashes contain many crystalline and amorphous phases. When using fly ashes for geopolymers, not only are the oxide ratios important, but how the oxides are bound within the fly ash is important. Only the reactive portion of the fly ash should be considered when calculating the proportioning ratios described previously, but determining the reactive constituent of fly ash is difficult. In some work, a hydrofluoric acid dissolution method has been used to determine the amount of reactive silica in fly ash (Fernández-Jiménez et al. 2006). Although this method gives an indication of potential reactivity, it does not necessarily represent the caustic environment of geopolymer formation, and, in addition, the hydrofluoric acid must be handled with extreme care. Analytical methods of fly ash characterization may be used instead, and these include x-ray diffraction (XRD) and scanning electron microscopy (SEM). Previous work has shown that the vitreous alumina content of a fly ash may affect its reactivity as a geopolymer, which is calculated by subtracting the amount of crystalline alumina-bearing minerals obtained using XRD from the bulk oxide composition of fly ash (Fernández-Jiménez, de la Torre, et al. 2006; Fernández-Jiménez, Palomo, et al. 2006). However, it is also recognized that there are multiple glassy phases within a fly ash sample, and these glasses can react differently when exposed to caustic solutions, so not all vitreous alumina is created equal. Several researchers (P. Williams et al. 2005; Chancey et al. 2010; Kruse 2012; Dhole et al. 2013) have used SEM x-ray point counting methods to establish the chemical composition of the various glasses within fly

ash in an attempt to better understand its internal structure and potential for reactivity. This method gives excellent information regarding the composition of various particles throughout the fly ash and, coupled with x-ray mapping, a broader understanding of the fly ash composition is achieved.

Finally, the curing process has a great effect on a hardened geopolymer's properties. Most work reported in the literature used elevated temperature curing regimes, typically between 60° C and 100° C (Davidovits 1991; Bakharev 2005c; Kovalchuk, Fernández-Jiménez, and Palomo 2007; Rowles and O'Connor 2003; Duxson, Mallicoat, et al. 2007). Room temperature curing may be used (Duxson et al. 2005; Somna et al. 2011), but for many raw material compositions, the reaction with activating solution is not rapid enough to gain strength in the short times desired in practice.

Of the four factors affecting the properties of a geopolymer (powder composition, alkaline solution composition, proportioning, and curing), this work focused on the intersection of powder composition and proportioning, with the other two factors held constant. The dissertation organization is described next.

1.3 DISSERTATION ORGANIZATION

The purpose of the work was to determine whether there were phase similarities between fly ashes and whether the phases could be linked to solubility in caustic environments such as geopolymer formation. The materials and methods used to test this hypothesis were chosen based on previous work, modified as needed to this particular task.

This dissertation is organized into several sections. First, background information pertaining to geopolymers, fly ash, and the analytical methods used in this work are presented in chapter 2. Next, the materials and methods particular to this study are

described in chapter 3. In chapter 4, the crystalline and glassy phase characterization results for the ten fly ashes selected for the study are presented. Chapter 5 presents the results for reactivity of the fly ash including geopolymer mortar compressive strengths and compositional changes in the fly ashes after exposure to caustic activating solution in a dissolution technique. In chapter 6, a new method for performing the supervised cluster analysis type of multispectral image analysis is proposed and an example is given. Finally, chapter 7 contains the conclusions made from the work and suggestions for future work.

Chapter 2: Background

The work presented in this dissertation studies the reactivity of fly ash for use in geopolymers activated with sodium hydroxide solution. Raw materials for geopolymer production, geopolymer cements, and characterization methods are described in this chapter.

2.1 RAW MATERIALS FOR PRODUCING GEOPOLYMER

Geopolymers are a class of binder material made from aluminosilicate powders and caustic activating solutions. The work presented in this dissertation used fly ash as the aluminosilicate source for geopolymers. Fly ash and activating solutions are described in this section.

2.1.1 Fly ash

Fly ash is produced as the result of burning coal for electric power generation. The material comes from quenched flue gases that are collected as they exit the combustion chamber. Fly ash particles are typically spherical in shape due to their rapid cooling in the flue. Other morphologies may form through agglomeration or passage of unburned particles such as carbon or quartz through the combustion chamber. There are two main classes of fly ash, which are defined by ASTM as Class C fly ash and Class F fly ash (ASTM C618-12a). The sum of the SiO_2, Al_2O_3, and FeO must be over 50 % to be classified as a Class C fly ash and over 70 % to be classified a Class F fly ash. In practice, Class C fly ashes typically contain more than 20% CaO, while Class F fly ashes typically contain less than 20% CaO. For both classes, the material is mostly glassy, comprised of 50-90% amorphous material as found by x-ray diffraction studies (Ward and French 2006). The remaining portion of the fly ash is made up of crystalline

material, typically quartz, iron-oxides, mullite, lime, and periclase (Hemmings and Berry 1987; Roy, Luke, and Diamond 1984). High calcium fly ashes may also contain portland cement constituents such as tricalcium aluminate and belite (Roy, Luke, and Diamond 1984). The source coal for making fly ash is highly influential over the composition of the fly ash, while the operating conditions of the boiler affect the properties as well (McCarthy et al. 1989).

2.1.2 Glasses in fly ash

Glasses are defined as materials with short-range chemical order but no long-range chemical order (Shelby 2005). This short-range order distinguishes glasses from fully amorphous materials and is a precursor to the formation of fully crystalline structure, which is distinguished in the form of a "hump" in diffraction patterns of glassy materials (Kilgour and Diamond 1987). Hemmings and Berry (1987) discussed the basic glass structure and its many modifications found in fly ash. Fly ash is composed of mainly aluminosilicate glasses, which take the tetrahedral form of the pure silicate (Si + O) glass structure (Hemmings and Berry 1987). Network modification from the ideal glass structure may occur when network substitutions (Fe, B, P, etc.) or network modifiers in the form of cations (Na^+, K^+, Ca^{2+}, Mg^{2+}) are introduced to the structure. Both mechanisms of disorder affect free energy and reactivity, and both occur in fly ash.

While identification and quantification of the crystalline material in fly ash is relatively straightforward using x-ray diffraction, the same is not true of the glassy phases. Investigations on interparticle and intraparticle chemical differences in fly ashes have been completed using Energy Dispersive Spectroscopy (EDS) as part of a scanning electron microscope (SEM) (Joshi et al. 1984; Qian and Glasser 1987; Stevenson and Huber 1986; P. Williams et al. 2005; Chancey et al. 2010; Bumrongjaroen et al. 2011).

Williams et al. (2005) used a point counting method to catalog the variable composition between particles in a Class F (ASTM C618-97) fly ash and found that it contained mainly an aluminosilicate glassy phase, mullite, and quartz. X-ray maps were collected to allow quantification of the amount of each phase present by the segmentation process given in (Bentz et al. 1999). More recently, Chancey et al. (2010) used an x-ray mapping method to identify and quantify the composition of glasses in fly ash; glasses containing calcium, aluminum and silicon made up the largest proportion identified, although aluminosilicate glasses and alkali-modified aluminosilicate glass were identified, too. Iron-containing phases have been identified in crystalline and glassy form within fly ashes (Hemmings et al. 1986, Chancey et al. 2010).

2.1.3 Crystalline phases in fly ash

The major crystalline phases identified in fly ashes are related primarily to the calcium content of the fly ash. In low-calcium fly ashes, four crystalline phases are typically identified: quartz, mullite, hematite, and magnetite (McCarthy 1987). Higher calcium fly ashes typically have more complicated mineralogy (McCarthy et al. 1989). The results from a study of 178 fly ashes separated into low calcium (< 10% by mass), intermediate calcium (10-20% by mass), and high calcium (> 20%, by mass) showed the wide range of mineralogies in fly ashes of varied composition (McCarthy et al. 1989). The results showed that the ten most common phases across all fly ashes in the study were anhydrite, mullite, quartz, melelite, hematite, tricalcium aluminate[1] (C_3A), merwinite, ferrite spinel, lime, and periclase (McCarthy et al. 1989). Low calcium fly ashes commonly contained anhydrite, mullite, quartz, hematite, ferrite spinel, lime, and periclase. Intermediate calcium fly ashes contained anhydrite, mullite, quartz, melelite,

[1] Cement chemistry notation is used here: C = CaO, S = SiO_2, A = Al_2O_3, F = Fe_2O_3, f = FeO, $\overline{S}$ = SO_3, M = MgO, N = Na_2O, K = K_2O, and H = H_2O.

C_3A, merwinite, ferrite spinel, lime, and periclase. High calcium fly ashes commonly contained anhydrite, mullite, quartz, melilite, C_3A, merwinite, ferrite spinel, lime, and periclase. While many of the same phases were identified across the fly ashes in the three categories, differences are observed when noting how many of the fly ashes in the category contained the phase; for example, for the high calcium fly ashes, all of the fly ashes contained all of the phases listed, whereas in the intermediate calcium fly ashes and low calcium fly ashes, only half or more of the fly ashes contained all of the phases listed for that category (McCarthy et al. 1989). The ten phases discussed by McCarthy et al. are considered indicative of most fly ashes produced and are described in more detail in the following paragraphs.

Crystalline silicon dioxide often takes the form of quartz in fly ash. Quartz is a tectosilicate mineral with a chemical formula of SiO_2. The quartz polymorph found at room temperature is low quartz, which is in the hexagonal crystal system (Nesse 2000). The silicon in quartz may be substituted in small amounts by Al and Fe, which requires additional atoms to maintain charge neutrality (Nesse 2000). Quartz does not melt at the temperatures experienced in the boiler, but the edges of the angular particles may be polished by the boiler flame, resulting in more rounded morphology (Hemmings and Berry 1987).

The aluminosilicate crystalline phase identified in fly ash is mullite. Mullite is rare in nature but is common in high temperature materials such as fly ash (Klein and Hurlbut, Jr. 1977). The approximate stoichiometry is $Al_6Si_3O_{15}$, and it is most closely related to the sillimanite mineral. Mullite is hypothesized to crystallize during cooling, and is often identified in larger size fractions of fly ash, since those particles cool more slowly, allowing time for crystallization (Hemmings and Berry 1987).

The iron in fly ash typically takes the form of hematite or maghemite (both of which can be represented by the chemical formula Fe_2O_3) or ferrite spinel, which is a substituted iron oxide with Al, Mg, or Ti for the iron (McCarthy et al. 1989).

Magnesium-containing crystalline phases in fly ash include periclase, melilite, and merwinite. The chemical formula for periclase is MgO, and it is found in trace amounts in fly ash. MgO is often correlated to the CaO content, which means that it is often identified in increasing amount as the CaO content of the fly ash increases (McCarthy et al. 1989). The phase is too small for identification in electron microprobe analysis, which implies it is crystallized in very small particles of under 1-2 μm (Stevenson and Huber 1986). Melilite and merwinite are also Mg-rich phases. Melilite (a solid solution of akermanite and gehlenite containing aluminum, silicon, and magnesium) and merwinite ($Ca_3Mg(SiO_4)_2$) are phases that are typically related to the MgO content of the fly ash (McCarthy et al. 1989). Melilite and merwinite are also found in blast furnace slags, for which it has been shown that they crystallize upon cooling, which is the expected mechanism for their existence in fly ash.

The calcium-containing crystalline phases in fly ash include lime and C_3A. Lime is crystalline CaO, which is found in small amounts in fly ash. Lime is highly reactive with water, and typically crystallizes in very small amounts regardless of the CaO content of the fly ashes (McCarthy et al. 1989). The other high-calcium phase, C_3A, is typical of portland cement. This phase is highly reactive and may cause concern for sulfate resistance if it is present in sufficiently high amount (McCarthy et al. 1989).

2.1.4 Activating solutions

Common activating solutions for geopolymer cements include alkali hydroxide and alkali silicate solutions. The alkali cation in these solutions is typically Na^+ or K^+,

the choice of which can affect the properties of the material as will be discussed later in this chapter. In alkali hydroxide solutions, the alkali and the hydroxide (OH^-) dissociate, and the hydroxide is a catalyst in the dissolution of the glassy phases found in fly ash (Duxson, Fernández-Jiménez, et al. 2007). The alkali becomes incorporated into the resulting geopolymer gel and acts to balance the charge within the geopolymer structure, which is net negative due to the incorporation of aluminum into the tetrahedral silicate glass structure. Typical concentrations for solutions of alkali hydroxide used in geopolymer mixtures range from 8 g/mol to approximately 15 g/mol (Fernández-Jiménez, de la Torre, et al. 2006; Oh et al. 2010). These solutions are very strong bases, thus they require care in handling; however, they are chemically bound in the geopolymer upon curing and do not present a health or safety hazard.

Alkali silicate solution, or waterglass, is often used to increase the amount of silicon in solution when geopolymers are mixed. The silicon in solution is then available more quickly to bond with aluminum as it is dissolved from the fly ash. The use of silicate in activating solutions has an effect on the resulting geopolymer, tending to densify the microstructure compared to hydroxide solutions when used with sodium cation as the activating solution (Ma, Hu, and Ye 2012). In one study, the reaction rate of the fly ash was higher with concentrated sodium hydroxide solution, while the use of a silicate solution retarded the reaction rate but improved the microstructure based on SEM analysis of pastes (Ma, Hu, and Ye 2012). Silicate solutions have been found to slow dissolution of fly ashes in other studies also (Criado et al. 2007).

2.2 GEOPOLYMERS: HISTORY AND DEVELOPMENT

From a historical standpoint, geopolymers were developed as a fire-resistant building material. Several deadly fires that occurred in France during the late 1970's

spurred this interest in a strong and durable material that would also resist the spread of fire. Joseph Davidovits, a chemist who had worked on processes that used zeolites as a catalyst for other reactions, observed that the manufacture of zeolite precursors in largely amorphous form could be very useful to the building industry. An early 1980's patent (Davidovits 1982) described a sialate-based geopolymer material made using metakaolin where sialate refers to a molecule with a composition of Si -- O – Al – O (Davidovits 1991). Alkaline activated cements were not completely novel at this time. Purdon was one of the first to do work in alkali-activated blast furnace slag in the 1930s (Purdon 1940), finding essentially that the development of such materials must be done on a case-by-case basis due to inherent inhomogeneity of the starting material. Many years later, in the 1970's, Glukovoski (also found in the literature as Glukhovsky) researched alkali-activation of aluminosilicate materials (Glukovoski 1979) around the same time as Davidovits began his work in zeolite precursors France. It is important to note that the slag-based and metakaolin-based alkaline-activated systems have very different composition, but neither can be employed as a cement without the use of caustic activating solution, hence their grouping in the same class of materials. Low-calcium aluminosilicate-based alkali-activated cements were initially tested using natural minerals and calcined clay such as metakaolin (Davidovits 1991; Barbosa, MacKenzie, and Thaumaturgo 2000), but the use of fly ash as the aluminosilicate material soon followed (Palomo, Grutzeck, and Blanco 1999).

Using fly ashes as the aluminosilicate source for geopolymers could not have occurred without understanding of fly ash as a cementitious material. Starting in the 1980's and 1990's, characterization of fly ash began in earnest, allowing for its use as a portland cement replacement (Roy, Luke, and Diamond 1984; Hemmings and Berry 1987; Kilgour and Diamond 1987). Once the use of fly ash as a replacement had become

widespread, the interest in environmentally friendly alternatives to portland cements came about. Reports in the early and mid-2000's described the impact on the environment of CO_2 emissions and energy usage from cement production, which were as high as 5 % of anthropogenic CO_2 emissions and 5 % of industrial energy use worldwide (Hendricks et al. 1999; Worrell et al. 2001; Damtoft et al. 2008). These reports were the catalyst for the scientific community to begin investigating alternative cementing materials, bringing alkali-activated cements into the fore once again. Geopolymers made from waste materials were studied beginning in the late 1990's and early 2000's (Palomo, Grutzeck, and Blanco 1999; Xu and Van Deventer 2000; Rowles and O'Connor 2003). Work is ongoing to develop useful, environmentally-friendly building materials from aluminosilicate wastes, and a useful roadmap for such work was presented by Duxson and others in their 2007 "state of the art" report on geopolymer technology. Additional summaries of geopolymer technology and work were published by Khale and Chaudhury (Khale and Chaudhary 2007) and Juenger et al. (Juenger et al. 2011), and the reader is referred to all three papers for further information and references.

2.3 GEOPOLYMERS: DEFINITION AND TERMINOLOGY

Geopolymer cements are made from an aluminosilicate-rich powder mixed with a caustic activating solution. Geopolymer is the name given to this class of materials by Joseph Davidovits (1991), although many other names including "inorganic polymer cement", "alkali-activated cement", and "geocement" describe similar cementitious systems (Duxson, Fernández-Jiménez, et al. 2007). Since geopolymer has been the most commonly used name for alkali-activated binders, it is the name used in this dissertation. In addition, the terms "geopolymer" or "geopolymer cement" are used to refer to the material, and the terms "reaction product" or "gel" are used to refer to the

products that formed through reaction of the aluminosilicate and caustic solution. If the mixture of aluminosilicate and solution after hardening is described, it is called "geopolymer paste".

The aluminosilicate source for geopolymers most commonly consists of clay such as metakaolin, fly ash from coal power generation, or blast furnace slag from iron manufacturing. The activating solution necessary to dissolve the aluminosilicate powder is typically an alkali hydroxide, an alkali silicate, or a blend of the two. Geopolymer cements are often cured at temperatures up to 100° C, but room temperature curing is also possible. In introducing geopolymers as a building material, Davidovits described the conditions under which geopolymers form, which are at atmospheric pressure, under high pH, with concentrated alkalis, and at low temperature (Davidovits 1991). These properties allow for the use of geopolymers in construction applications, and they are an important distinction from the high-temperature and pressure ceramic materials that inspired the development of geopolymer.

2.4 GEOPOLYMER GELS: FORMATION MECHANISMS AND MICROSTRUCTURE

It is widely agreed that geopolymer gel formation is a dissolution-precipitation process (Fernández-Jiménez, Palomo, and Criado 2005; Duxson, Fernández-Jiménez, et al. 2007; Duxson and Provis 2008). The processes of dissolution and precipitation are largely concurrent, as the conditions in the mixture are constantly changing. Several authors have described the dissolution that occurs under caustic conditions, which liberates the ionic network forming silicate and aluminate species from the aluminosilicate powder into the solution (Fernández-Jiménez, de La Torre, et al. 2006; Duxson, Fernández-Jiménez, et al. 2007; Panagiotopoulou et al. 2007; Chen et al. 2011). The dissolution is exothermic (Davidovits 1991) and has been captured with isothermal

calorimetry (Fernández-Jiménez, Palomo, and Criado 2005). Silicon in the form of $HSiO_4^{3-}$ and aluminum in the form of $Al(OH_4)^-$ exist in the solution (Gasteiger, Frederick, and Streisel 1992; Duxson et al. 2005) until a critical concentration is reached, when the species precipitate from solution. It is hypothesized that the formation of the sialate oligimer (Si-O-Si) occurs after a critical amount of ionic species has dissolved into solution, but these have not been found experimentally (Davidovits 1991). The formation of geopolymer reaction product is described as a two-part process, in which an aluminum-rich gel forms early, eventually incorporating additional silicon to become a silicon-rich gel with an ideal Si/Al atomic ratio of around 2 (Fernández-Jiménez, Palomo, and Criado 2005; Fernández-Jiménez, de La Torre, et al. 2006; Duxson, Fernández-Jiménez, et al. 2007). Evidence has shown that even after a rim of reaction product has formed over a particle, diffusion of ionic species occurs through the reaction product to form additional reaction product (Fernández-Jiménez, Palomo, and Criado 2005; Chen et al. 2011). Water, a key part of the dissolution process, is not chemically bound into reaction product and is released throughout the curing process (Duxson et al. 2005; Duxson, Fernández-Jiménez, et al. 2007). This means that similar to portland cements, a high-water geopolymer leads to increased porosity and decreased strength and durability in the hardened product (Barbosa, MacKenzie, and Thaumaturgo 2000; Hardjito et al. 2004; Ruiz-Santaquiteria et al. 2012).

The geopolymer gel is made up of aluminum and silicon tetrahedra, and the arrangement of atoms in the gel can be modeled by the silicate glass system. Perfectly-formed silicate glasses are arranged as silicon-oxygen tetrahedra with oxygens surrounding each silicon ion (Shelby 2005). Aluminum can substitute into this network, but due to its smaller positive charge, the tetrahedral framework has a net negative charge that requires a positively charged ion to charge balance the material, typically Na^+, K^+ or

Ca^{2+} (Davidovits 1991). Therefore, the structure of a geopolymer gel consists of amorphous aluminosilicate tetrahedra, linked by oxygen bridges and charge balanced by cations such as calcium, magnesium, sodium, and potassium (Davidovits 1991; Duxson, Fernández-Jiménez, et al. 2007).

The bonding characteristics of geopolymer gels have been examined using ^{29}Si, ^{27}Al, ^{23}Na, ^{17}O and ^{2}H Magic Angle Spinning- NanoMagnetic Resonance (MAS-NMR) for geopolymer materials made using both metakaolin and fly ash (Davidovits 1991; Palomo et al. 2004; Duxson et al. 2005). Aluminum MAS-NMR shows clear peaks for each coordination of aluminum, with Al(IV) coordination being typical in geopolymers (Davidovits 1991; Duxson, Fernández-Jiménez, et al. 2007). Conversely, silicon MAS-NMR shows very broad resonances that require deconvolution in order to determine the coordination state of silicon (Duxson, Fernández-Jiménez, et al. 2007). Davidovits (1991) hypothesized that the Si resonance could be deconvoluted into contributions from all five possible silicon Q^4 species, which was later confirmed by investigations into aluminosilicate glass structures (Lee and Stebbins 1999). Thus, the aluminosilicate structure has some level of ordering within a gel structure. Oxygen NMR has shown that there are few non-bonded oxygens, which was interpreted to mean that Al-O-Al bonding does occur in geopolymers, particularly in calcium aluminosilicates (Lee and Stebbins 1999), despite prior work suggesting that it does not due to the Lowenstein avoidance principle (Loewenstein 1954; Davidovits 1991). Deuterium MAS-NMR has demonstrated that water is not chemically bound in the geopolymer matrix (Duxson et al. 2005).

Recent advances in analytical techniques have shown that beamline studies of geopolymer paste samples including results from infrared signals, x-ray fluorescence

signals, and nanotomography have the ability to reveal even more detailed information regarding the geopolymer gel structure and bonding (Provis et al. 2013).

2.5 GEOPOLYMERS: HARDENED PROPERTIES, RAW MATERIAL SELECTION, AND PROPORTIONING, AND CURING

Unlike portland cement, which is designed to react when mixed with water, geopolymer raw materials are not specifically made for reactivity, which means that varying the properties of the raw material and the proportions of the mixture can greatly change the hardened material properties. In this section, the hardened material properties to be optimized in geopolymers are first described. Next, the desirable raw material properties that can help optimize the hardened properties are discussed. The effects of impurities introduced into the mixture by using waste aluminosilicate sources are described. Then, activating solutions and their effects on the material are described. The proportioning methods are described, and finally, the effects of curing methods are discussed.

2.5.1 Geopolymers: Criteria for hardened material properties

For use as an engineering material, geopolymers must be strong and durable to meet the performance criteria of the environments in which they are placed. As mentioned in the introduction to the section, geopolymers are designed at the batching level, so the material must be tailored to meet the needs of the environment. The important material properties for a geopolymer include high compressive strength and favorable durability properties. Geopolymer mixtures reported in the literature can be found with high strength, resistance to acid environments, resistance to sulfates, decreased alkali-silica reactivity, and more (Duxson, Provis, et al. 2007).

The expected compressive strengths for geopolymers are similar to those of portland cement concretes since they are designed to be direct replacements for concrete in civil engineering applications. Heat curing accelerates the kinetics of the aluminosilicate-activator reaction, so many of the geopolymers studied in the literature were heat cured, reaching strengths higher than 70 MPa for concrete (van Deventer, Provis, and Duxson 2012). Most of the work on geopolymers has been completed on pastes or mortars, and few studies have been performed on concrete mixtures similar to those that would be applied in the field. When cured at room temperature, geopolymer paste compressive strengths of 20-23 MPa (Somna et al. 2011) and 45 MPa (Temuujin, Williams, and vanRiessen 2009) have been reported. Geopolymer concretes have been shown to reach 60-70 MPa in just a few hours (Duxson, Fernández-Jiménez, et al. 2007). The Young's modulus can match that of portland cement concretes if the proper raw materials and curing conditions are used (Fernández-Jiménez, Palomo, and Lopez-Hombrados 2006; Sofi et al. 2007; Sarker 2009).

The durability of geopolymers under harsh conditions was described favorably in early geopolymer literature (Palomo et al. 1999) with the caveat that testing with longer durations should be conducted. More recent testing revealed that the ability to stand up to harsh environments is very dependent on the microstructure of the geopolymer gel, which must be appropriately proportioned to suit the environment (Bakharev 2005b; Lloyd 2008). The use of alkali-activation sparks many questions regarding degradation due to alkali-silica reaction since the alkali concentration is exceptionally high compared to OPC concretes. Research by García-Lodeiro et al. (García-Lodeiro, Palomo, and Fernández-Jiménez 2007) using a highly reactive opal aggregate and the ASTM C1260-94 method showed that the alkali-activated fly ash geopolymer mortar was less susceptible to alkali-aggregate reaction than the portland cement mortars. Another

durability issue is that of acid resistance for aggressive environments such as sewer piping. Bakharev (Bakharev 2005b) reported that the resistance of geopolymer cements to acidic environments depended greatly on the amount of disorder in the system, a claim upheld by Lloyd (Lloyd 2008), who found that geopolymer cements degraded under exposure to acids. In sulfate environments, Bakharev found that the activator type of the geopolymer and the alkali cation type in the sulfate solution and concentration of the sulfates caused greatly different behavior. For geopolymers made with sodium hydroxide and fly ash and cured at elevated temperature, the compressive strength actually increased after sulfate exposure; whereas, for the geopolymers prepared with sodium hydroxide or blended potassium-sodium hydroxides migration of the ions into the sulfate solutions was observed and cracks formed in the geopolymer (Bakharev 2005a).

Carbonation, another form of degradation, commonly occurs near the surface of concrete materials and can spread further into the material when microcracking is extensive and can occur in geopolymer concretes (van Deventer, Provis, and Duxson 2012). It was reported by Barbosa et al. (2000) that in gels with excess sodium in the pore solution, the sodium migrated to the surface upon drying, where it caused carbonation of the geopolymer. Efflorescence has also been reported in geopolymers cured at ambient temperatures, where it appeared on the surface of the specimen (Temuujin, vanRiessen, and Williams 2009).

2.5.2 Important properties of the fly ash for improving geopolymer properties

An important predictor of whether a fly ash will be successful in forming geopolymer is the proportion of the fly ash that exists in glassy phase (R. Williams and van Riessen 2010). The fraction of glass can be measured in a fly ash using analytical methods such as x-ray diffraction (XRD) to quantify the crystalline phases and, thus, the

glass fraction by subtraction. The glassy phase is typically the most reactive portion of fly ash, and it allows for the dissolved silicon and aluminum to precipitate as network-forming building blocks of the reaction product. Therefore, it is clear that the availability of these network-builders is critical in the raw material. Testing for the availability of these is difficult. Other properties that may indicate the reactivity of fly ashes when mixed with cements or in geopolymer reaction product formation include the location of the fly ash's vitreous halo in x-ray diffraction (Kilgour and Diamond 1987; Hemmings and Berry 1987; Duxson and Provis 2008), the fly ash's vitreous alumina content (Fernández-Jiménez and Palomo 2003), and the morphology and size of the fly ash particles. Studies have indicated that the iron content should be less than 10 % (Fernández-Jiménez and Palomo 2003), the calcium content is important, and the vitreous alumina content must be above some minimum, although a specific value was not recommended for either calcium or aluminum by the study authors (Fernández-Jiménez, de La Torre, et al. 2006).

2.5.3 Effects of impurities on the aluminosilicate framework

Geopolymer gels are based on an aluminosilicate framework, but the use of fly ash as the aluminosilicate source introduces many other elements into the mixture including calcium. The presence of calcium in glassy phases in crystalline form can affect the reactivity of fly ash and the resulting geopolymer significantly (Dombrowski, Buchwald, and Weil 2007; Duxson, Fernández-Jiménez, et al. 2007). In fly ash, calcium contributes to the disordered nature of the glassy phases, which can increase the reactivity of the raw material (Hemmings and Berry 1987). In some fly ashes, particularly Class C ashes with high calcium contents (ASTM C618-12a), calcium may be present as portland cement phases such as alite or belite (McCarthy et al. 1989; Oh et al. 2010), which are

very reactive. However, there is not always a correlation between increased calcium in the fly ash and improved geopolymer compressive strength (assumed to be related to reactivity), which Oh et al. hypothesized to be a result of the calcium's bonding in the fly ash and the inability of some forms of calcium phases to dissolve in the caustic solution (Oh et al. 2010). Thus, while there is disorder introduced to the glassy phases in fly ash by the incorporation of calcium, there must be enough calcium to depolymerize the network and result in improved reactivity, which will be a different amount of calcium for each glassy phase.

Calcium as a supplementary material may be added to the geopolymer mixture to speed up the hardening process (Dombrowski, Buchwald, and Weil 2007; Temuujin, vanRiessen, and Williams 2009). The added calcium has been in the forms of calcium hydroxide and lime. In addition to shortening the hardening time, the addition of calcium also enables the geopolymer to be cured at room temperature without sacrificing strength. For example, for an ambient-cured geopolymer made using Class F fly ash with a 28 d compressive strength of 11.8 MPa, 3 mass % addition of quicklime improved the strength to 22.8 MPa, while 3 mass % addition of calcium hydroxide improved strength to 29.2 MPa (Temuujin, Williams, and vanRiessen 2009). The resultant geopolymer binder included C-S-H and C-A-S-H hydration products in addition to the formation of amorphous geopolymer gel; thus it became a blended system with the addition of the calcium compounds.

Iron is another impurity introduced into geopolymers by using fly ash. It was reported by (Chen et al. 2011) that iron is in early age geopolymer reaction products that were found on the surface of particles. Little characterization has been done to explain how the iron is incorporated into the gel, but its solubility from the fly ash has been documented (Chen et al. 2011). Two other studies showed that the iron does not dissolve

in crystalline form of magnetite (Criado et al. 2007) or in iron-aluminosilicate form (Chen et al. 2011), which would mean that some iron phases remain in unreacted fly ash particles and not in the geopolymer gel.

2.5.4 Effects of activating solutions on geopolymer properties

The concentration and type of alkali cation in the activating solution is another factor that strongly influences the reaction kinetics in geopolymer formation (Lizcano et al. 2012). It has been found that the chemically bound water is increased when the sodium cation is used, as opposed to the potassium cation. Sodium has also been reported to be better at causing the silicon and aluminum ions to dissolve into solution than potassium; this is hypothesized to be due to its smaller size as compared to potassium (Duxson, Fernández-Jiménez, et al. 2007). The hardened properties of geopolymers made using solutions with these two cations are typically very similar to each other, with the exception that sodium systems tend to form more crystalline zeolites in the reaction product than potassium systems (Duxson, Fernández-Jiménez, et al. 2007).

2.5.5 Proportioning

Two main proportioning methods have been used in previous studies: constituent element molar ratios and solution-to-powder / workability methods.

2.5.5.1 Proportioning: Constituent ratios

The ratio of the aluminum and silicon constituents in a geopolymer affects its properties greatly including compressive strength, flexural strength, etc. (Fletcher et al. 2005; Duxson, Mallicoat, et al. 2007; Buchwald, Zellmann, and Kaps 2011; Chindaprasirt et al. 2012). Further, the ratio of the alkalis to the aluminosilicate framework elements is also important to the property development of the material (Duxson et al. 2005; Duxson, Mallicoat, et al. 2007). The literature includes a wide range

of recommended molar ratios for the main constituents of the mixture, which are summarized in Table 2.1. The starting point for many of the initial ratio studies was Davidovits' patent on polysialate polymers (1982), which described the appropriate ratios for the polysialate polymers discussed in his later paper (Davidovits 1991). These ratios resulted from research on metakaolin activated with a blended sodium hydroxide-sodium silicate activating solution. Much work has been done to refine the necessary amounts of the network-forming constituents (Si and Al) (Barbosa, MacKenzie, and Thaumaturgo 2000; Rowles and O'Connor 2003; Fletcher et al. 2005; Duxson et al. 2005; Duxson, Fernández-Jiménez, et al. 2007; Chindaprasirt et al. 2012) and the amount of alkali (K^+, Na^+) (Barbosa, MacKenzie, and Thaumaturgo 2000; Rowles and O'Connor 2003; Fletcher et al. 2005) that must be in a fresh geopolymer paste for it to properly react and form a strong, durable material. The ratios are typically calculated in terms of molar oxide ratios of the reactive portion of the fly ash, which can be calculated as the portion of the fly ash not found in crystalline phases. The non-crystalline portion can also be described as the bulk glassy phase in the material, but it does not does not fully describe the availability of the elements contained in the glassy material to react in solution; thus, the method must be used with this caveat.

Table 2.1: Recommendations made for the ratios of the major constituents in geopolymer cements

Study	Aluminosilicate source	SiO_2/Al_2O_3	Na_2O/SiO_2	H_2O/Na_2O	Na_2O/Al_2O_3	M_2O/Al_2O_3
Davidovits (1982)	metakaolin	4.0	0.25-0.28	16-17.5	-	1.0-1.14
Barbosa, MacKenzie, Thaumaturgo (2000)	metakaolin	3.3	0.25	10	~ 1.0	-
Rowles & Oconnor (2003)	metakaolin	2.83	0.32	-	0.92	-
Duxson et al (2005)	metakaolin	2.15	-	-	-	-
Fletcher et al. (2005)	metakaolin	2	0.3	11	-	-
Duxson et al (2007)	metakaolin	1.87	-	-	-	-
Chindaprasirt et al. (2012)	Class C fly ash	3.20-3.70	-	-	-	-

The silica to alumina ratio affects the microstructure of the geopolymer reaction product. A study was completed by Fletcher et al. (2005) on geopolymers with SiO_2 / Al_2O_3 molar ratios ranging from 0.5 to 300 and constant Na_2O/SiO_2 and H_2O/SiO_2, which showed that the high alumina samples (SiO_2 / Al_2O_3 = 0.5 – 2.0) were of low strength after approximately 24 h of curing, whereas the highest silica (SiO_2 / Al_2O_3 > 24) resulted in a rubbery material that could not be tested. The SiO_2 / Al_2O_3 range of 2.0-24 resulted in characteristic geopolymer properties based on nuclear magnetic resonance (NMR) testing and x-ray diffraction (XRD); the tests also confirmed that the high alumina materials did not appear to be geopolymer cements, whereas all of the high silica, up to SiO_2 / Al_2O_3 = 300 had bonding characteristics of geopolymers. From these results, the SiO_2 / Al_2O_3 range that resulted in geopolymer with the appropriate microstructure and

strength was suggested as 2 – 24, with the ratio of 16 resulting in the highest measured crushing strengths. However, it was reported in a separate study that for a high-calcium fly ash geopolymer the $SiO_2/Al_2O_3 > 4.3$ resulted in decreases in compressive strength (Chindaprasirt et al. 2012). Therefore, the ratios should be in the range of 2.0 – 4.3 and were recommended within this range by several authors resulting from their studies of compressive strength with varying SiO_2/Al_2O_3 including 2.83 by (Rowles and O'Connor 2003), 3.3 by (Barbosa, MacKenzie, and Thaumaturgo 2000), 2.15 by (Duxson et al. 2005), and 1.87 (slightly lower) by (Duxson, Mallicoat, et al. 2007).

The sodium or potassium (or Na + K) to alumina ratio has been recommended to be approximately equal to 1, since the alkali charge balances the aluminosilicate tetrahedra in geopolymer gel, which is negatively charged due to the inclusion of aluminum (Barbosa, MacKenzie, and Thaumaturgo 2000; Khale and Chaudhary 2007; Rees et al. 2007; Oh et al. 2010). It has also been reported that too much sodium (i.e. a high Na_2O / Al_2O_3) can increase carbonation at the surface of the geopolymer and should be minimized to be approximately equal to the amount of alumina for that reason as well (Barbosa, MacKenzie, and Thaumaturgo 2000). Sodium has also been found to remain in pore solution when insufficient aluminum was present in the mixture (when Si/Al was < 1.4 in the study), which was hypothesized to show the correlation of sodium to alumina (Duxson et al. 2005).

The sodium to silica ratio is reported in the literature, however, due to the previous discussion of the relationship of sodium to aluminum, it is often reported rather than recommended. For a given SiO_2/Al_2O_3 ratio, and alkali/Al_2O_3 ratio in a geopolymer, the sodium to silica ratio is not further changeable. However, it is typically low, at approximately 0.25-0.3 as reported in the literature (Davidovits 1982; Barbosa, MacKenzie, and Thaumaturgo 2000; Rowles and O'Connor 2003; Fletcher et al. 2005).

2.5.5.2 Proportioning: Activator-to-ash ratios and workability-based proportioning

The use of solution-to-ash ratios may be used to proportion the geopolymers based on adequate workability, which is similar to the relatively straightforward method used in portland cement concretes (Oh et al. 2010; Ruiz-Santaquiteria et al. 2012; Fernández-Jiménez, de la Torre, et al. 2006; A. Al Bakri et al. 2011). Like in portland cements, excess water present in the geopolymer mixture negatively influences the hardened geopolymer properties such as microstructure porosity and strength development, so it must be minimized (Ruiz-Santaquiteria et al. 2012; Barbosa, MacKenzie, and Thaumaturgo 2000). Conversely, water is necessary to facilitate the reactions between activator and aluminosilicate powder, so the need for water must be balanced by its negative effect on late age properties. Heah et al. reported that a kaolin-based geopolymer cement required a solid-to-liquid ratio of 1.0 to develop the highest strength (Heah et al. 2012), while Al Bakri et al. reported that an activator-to-ash ratio of 0.4 maximized geopolymerization in a fly ash-based geopolymer paste (M. Al Bakri et al. 2012). The choice of solution-to-ash ratio strongly affects the rheology of the mixture since the viscosity of the solution increases with increasing dissolved sodium, potassium and/or silica in the activating solution and increased viscosity leads to increased liquid demand (Chindaprasirt, Chareerat, and Sirivivatnanon 2007). A disadvantage of this method of proportioning includes the trial-and-error necessary to determine how much activator results in suitable rheological properties for the mixture.

2.5.6 Geopolymer curing regimes

Elevated temperature curing is very common for geopolymers. As reported in early literature by Davidovits (1991), amorphous geopolymer reaction products are expected to form at curing temperatures under 100° C. Elevated curing regimes reported in the literature use temperatures falling between 60-90° C (Duxson, Fernández-Jiménez,

et al. 2007). The various curing regimes reported in the literature can be summarized into three general categories: short-term heat curing, long-term heat curing, and room temperature curing. Short-term elevated temperature curing consisted of short durations up to 24 hours at the elevated temperature followed by curing at room temperature until the testing period was completed (Barbosa, MacKenzie, and Thaumaturgo 2000; Rowles and O'Connor 2003; Fletcher et al. 2005; Ruiz-Santaquiteria et al. 2012). Long-term elevated temperature curing typically consisted of holding the elevated temperature for several days or until the testing period was completed (Criado et al. 2007; Fernández-Jiménez, de la Torre, et al. 2006; Fernández-Jiménez, Palomo, et al. 2006). Room temperature curing was completed at temperatures up to 40° C, but typically at around 25° C (Somna et al. 2011; Ma, Hu, and Ye 2012). Of these methods, all resulted in geopolymer formation, and no clear conclusions can be drawn concerning the best method since the raw materials composition was different for the mixtures tested, as well as the curing conditions.

While the majority of studies only reported the curing time and temperature without testing its effects, some did systematically vary curing conditions to test their effects on the resulting geopolymer's properties (Bakharev 2005c; Chindaprasirt, Chareerat, and Sirivivatnanon 2007). Bakharev's (2005) results showed that pre-curing at room temperature for up to 6 h allowed for shorter durations of elevated temperature curing and higher compressive strengths (Bakharev 2005c). Chindaprasirt et al. (2007) found that 1 hour of pre-curing at room temperature was optimal for their materials, followed by 24 h of curing at 60° C.

When room temperature curing is used, the studies reported in the literature have shown that pre-grinding is the best way to increase reactivity and strength. Somna et al. (2011) found that the use of room temperature curing resulted in geopolymers that had

excellent compressive strengths of 20-23MPa, but the fly ash had to be ground from d_{50}=41 μm to d_{50}=10 μm and the concentrations of sodium hydroxide activating solution were very high, between 9.5 and 14 M (Somna et al. 2011). Similarly, Temuujin et al. (2009) reported compressive strength increases from 16 MPa to 45 MPa at 28 days when mechanical grinding was used on the fly ash prior to making geopolymer cured at ambient temperature (Temuujin, Williams, and vanRiessen 2009). Therefore, room temperature curing is best used for geopolymers made using very fine fly ashes, typically resulting from grinding ashes ahead of time. Otherwise, elevated temperatures can result in favorable geopolymer properties without the use of mechanical processing.

2.5.7 Summary of geopolymers

In geopolymer materials, the essential condition is the dissolution of silicon and aluminum into solution, such that it becomes concentrated enough to precipitate out as a geopolymer gel. There are many recommendations as to what amounts of the main constituents of the gel should be, including SiO_2/Al_2O_3, Na_2O/Al_2O_3, and H_2O/alkali ratios. Further, the material is designed at the batching level since its raw materials were not specifically designed for reactivity, so the proportions of the raw materials and the curing methods used are essential to the successful geopolymerization process. These factors have been described in detail in the previous sections. Next, some of the analytical techniques employed for analysis of the raw materials and hardened geopolymer gels are presented and discussed.

2.6 Analytical Methods

The analysis of raw materials for use in geopolymer cements may be completed using a number of analytical techniques. The methods used in this work made use of x-ray diffraction (XRD) for identification and quantification of crystalline phases and the

amount of bulk amorphous material in fly ash. In addition, scanning electron microscopy (SEM) using energy-dispersive spectroscopy (EDS) to analyze the composition of the fly ash provided further characterization. The analytical techniques are described in the following sections.

2.6.1 X-ray diffraction

X-ray diffraction is an analytical technique for identifying the crystalline phases that are present in a material. Many commercial x-ray diffraction systems use Bragg-Brentano geometry for the experimental set up. This setup is well described in *Modern Powder Diffraction* (Reed 1989). Copper x-rays are commonly used for x-ray diffraction experiments. The x-rays are generated when a beam of electrons strikes a copper target, resulting in x-rays as outer-shell copper electrons drop to fill inner-shell vacancies. The x-rays then pass through a series of aligning slits that serve to focus the beam onto the plane of the specimen, which is located in the middle of a circular goniometer. The detector, the specimen, or the source move in a circular fashion, making various angles with the specimen at which the x-ray signal can be measured. The x-rays interact with the specimen and, if diffraction has occurred at that angle of interaction, the diffracted x-rays are collimated and then collected by the detector. If no diffraction has occurred, only background radiation known as Bremsstrahlung is detected, with a value near zero. A monochromator may be present in the system, which limits the x-rays that pass through to the detector to a single wavelength. This ensures that the peak is not broadened by collection of x-rays with too low energy. For a copper x-ray system, typically the Cu K-α radiation is allowed to pass, while the Cu K-β radiation is filtered out. The detector converts x-ray energy into a different form that can be recorded on a computer as

intensity values based on counts at each step. Thus, an XRD plot of Bragg-Brentano geometry appears as an x-y plot in which x is the angle of incidence and y is the intensity.

An experiment has many operator-selected factors including the angles and sizes of the collimating slits on either side of the specimen, the total angle range of the experiment, the step size (i.e. how many "slices" each degree is broken into), the dwell time, and others. Typically for a particular XRD, the collimating slits will have an optimum set up. The divergence slit function is to irradiate as much of the specimen as possible at once while avoiding irradiation of the sample holder, thus the size of the sample surface is of importance in selecting this. The angle range used in an experiment depends on the lowest and highest major peak locations along the 2θ range for the phases of interest. Due to this, some prior knowledge of the phases in the specimen is helpful. An optimal step size can minimize errors induced by smoothing, and a step value that will typically ensure that 10-20 points are taken above the full-width half-max value for a peak is 0.02° 2θ (Jenkins 1989). The dwell time is the length of time each step is held for data collection, and a higher dwell time will allow for better resolution of minor phases from the background. However, the dwell time directly influences the experiment time, so the shortest reasonable dwell time should be used if time is important.

2.6.1.1 Powder diffraction of materials

Powder diffraction is a technique that allows for the identification of crystalline compounds in a sample of finely divided material. It assumes that the randomly oriented particles offer a statistically representative sample of the crystalline phases' crystal planes such that the signature pattern is collected for each crystalline material in the specimen (Bish and Reynolds 1989). The patterns are plotted as measured intensities (counts) across the angular range of the experiment, expressed as degrees 2θ. Depending on the

material there may be few or many crystalline phases present in a specimen. The relative peak heights of the major peaks present in different phases indicate relative amounts of the phases present in the material.

The phases in a material can be identified in x-ray diffraction patterns based on the presence of their signature set of peaks. The number of peaks and location of the peaks for each phase are determined by the crystal lattice system of the crystal, while the intensity of the peaks is influenced by the atom type and by the amount of the crystal present in the material (Reynolds, Jr. 1989). The relative intensities between peaks for an individual crystalline material remain constant for that material regardless of the bulk material composition. Databases of diffraction patterns have been created for efficient phase identification using previously collected or calculated diffraction data. The main source for diffraction pattern data is The International Center for Diffraction Data (ICDD), which maintains a database of files called "PDF" or powder diffraction files. The data are now computer-based, after originating as printed handbooks, and the files contain the diffraction data, crystallographic information, and other information regarding a crystal. The data contained in the ICDD handbook are either submitted by scientists who have performed diffraction experiments on the crystalline material or who have calculated diffraction patterns from crystallographic information ascertained for a crystalline material. The main source from which ICDD obtains calculated patterns based on crystallographic data is the Inorganic Crystal Structure Database (ICSD), which maintains a database of crystal structures for inorganic materials. Although it is possible to manually identify phases using patterns that have been published in the literature, this would be time-consuming; therefore, purchasing a software package with access to these databases is the most efficient method for phase identification.

2.6.1.2 Quantitative analysis: internal standards

Internal standards are used in x-ray diffraction as a reference for quantification of crystalline phases in a specimen. The internal standard is interground with the material being characterized as a partial weight replacement of the total sample, typically using a dispersant liquid such as ethanol. Common internal standards in cementitious materials include rutile (TiO_2) (Chancey et al. 2010), corundum (Al_2O_3) (Fernández-Jiménez, de La Torre, et al. 2006; Criado et al. 2007), zincite (ZnO) (Buchwald 2006; Dombrowski, Buchwald, and Weil 2007), and fluorite (CaF_2) (R. Williams and van Riessen 2010).

Internal standards for use in x-ray diffraction have several selection criteria. First, the crystalline peaks of the internal standard should not overlap the major peaks of any phase in the raw material being analyzed. This allows for correct phase identification and is a requirement of semi-quantitative analysis methods, for which the measured peak intensities for the unknown and the internal standard are compared directly (Reynolds, Jr. 1989). Another consideration in selecting an internal standard is the linear absorption coefficient, which should be similar to that of the material in which the standard is being placed. For example, the use of a material with too great an absorption coefficient could result in lower x-ray counts for crystalline peaks due to absorption, underestimating the amount of that crystalline phase in the material. The particle size is also important, since the more similar the particle size of the internal standard and the unknown material, the better dispersed the standard material will be in the specimen.

2.6.1.3 Quantitative data analysis: the Rietveld method

The Rietveld method is a whole pattern fitting quantitative technique named after Dr. H.M. Rietveld, who developed it in the late 1960's (Rietveld 1969). The Rietveld method was revolutionary to x-ray diffraction since it allowed for the simultaneous calculation of quantities of all crystalline phases in a material, even in cases where there

were overlapping contributions from multiple phases in a single reflection (Young 1993). The method is used to compare a calculated x-ray pattern to the actual pattern collected, and the process of fine-tuning the crystal structures that make up the calculated pattern to more closely match the actual pattern is called refinement.

The essential requirement for Rietveld analysis is that a reasonable starting model for the pattern be available (Young 1993). The starting model consists of a model for the expected profile resulting from the equipment geometry, diffraction optics effects and all of the crystalline phases within the material. Rietveld refinement requires that all crystalline phases be identified prior to the commencement of the Rietveld refinement. The geometric parameters of the equipment are fixed, since they are physical values such as the radius of the goniometer, the sizes and angles of the slits on either side of the specimen, and the presence or lack thereof of a monochromator. The crystalline phases in the material are added to the refinement using electronic files that contain the crystallographic information as either crystallographic information files (CIF) or structure files (.str). While many of the crystallographic databases cost money to access, CIF files can be downloaded at no charge from the American Mineralogist Crystal Structure Database (AMCSD), accessed online[2]. The variables that form the starting model of the collected pattern are refined through the process, hence the name "Rietveld refinement." A refinement must be carried out in a step-by-step progression, and Young described a sound refinement strategy in the book *The Rietveld Method* (Young 1993).

The best way to monitor Rietveld refinements is to visually inspect the difference between the calculated and collected patterns. Alternatively, there are several variables that give a reasonable assessment of the progression of the refinement. Rietveld

[2] http://rruff.geo.arizona.edu/AMS/amcsd.php

refinements can be monitored by the continual decrease of the "weighted-pattern" residual (R_{wp}) values, which are calculated using the actual difference between the calculated and collected patterns as the numerator (Young 1993). When R_{wp} has been minimized, it is likely that the pattern has been correctly modeled. Another important parameter in Rietveld refinements is the "goodness of fit" designated S, for which a value of less than 1.3 but at least near 1 is generally considered very good (Young 1993).

The Rietveld method is a powerful tool in materials analysis and should be studied closely by anyone wishing to use the method, beginning with the study of crystallography, then experimental geometry, and finally effective refinement.

2.6.2 Scanning electron microscopy

Scanning electron microscopy (SEM) is a qualitative and quantitative technique for identifying features of microscopic material including physical traits and compositional information. Goldstein et al. (2003) provide detailed information on the topics discussed in this section, and readers are referred to that source for more detail than presented here. The microscope operates by generating electrons, which proceed through a column that uses physical apertures and electromagnetic fields to focus the electrons into a beam of small radius. The beam strikes the sample, typically in a perpendicular orientation, and electron interactions with the sample result in several types of signal: secondary electrons, backscattered electrons, and x-rays. Secondary electrons and x-rays are produced when an electron in the specimen is ejected from its position in a particular orbital of an atom within the sample. A secondary electron detector collects the ejected electron, while an x-ray is generated when an outer-shell electron drops to fill the hole left by the ejected electron; a different detector collects the x-ray. Backscattered

electrons are original beam electrons that have interacted with the specimen and been scattered back out of the sample.

Typically the secondary electron detector and x-ray detectors are mounted on the side of the chamber, while the backscatter detector is mounted directly above the sample, at the bottom of the column around the opening where the electron beam exits. Since secondary electrons are relatively low-energy, the secondary electron detector is usually surrounded by a Faraday cage, which uses a small amount of positive bias to attract the electrons. Backscattered electrons are much higher energy than secondary electrons; therefore, their detectors are not biased. In some cases, the secondary detector may be used to collect backscattered electrons, and for this the Faraday cage has slight negative bias. X-rays are collected by x-ray detectors similar to those used in XRD. The reader is referred to Goldstein et al. (2003) for further information on microscope setup and electronics.

The electron source within a SEM can be one of three types: a tungsten filament, lanthanum hexaboride (LaB_6), or a field emission source. The differences are discussed thoroughly in Goldstein et al. (2003) and are summarized here. Beam brightness is significantly higher for field emission sources, while the beam current stability is significantly better for tungsten sources than for field emission sources. Brightness is a function of the electron current, the beam area, and the angle of spread of the electrons, but it is preserved even when one of these factors changes for the particular electron source (Goldstein et al. 2003). To improve imaging, the beam area (i.e. the probe size) must be minimized, but the only way to do this without sacrificing beam current is to increase the brightness. Therefore, selecting an electron source with sufficient brightness for the task is important. For high-resolution imaging, a field emission gun is the best since it has high brightness and small probe size, but field emission guns come at a cost

of beam current stability. The beam current stability is highly important for long experiments, since the stability is a function of time. Usually long experiments are run when collecting x-ray maps, which are often not a high-resolution application. Tungsten beam sources are more stable than most types of field emission beams (Goldstein et al. 2003).

2.6.2.1 Imaging modes

The secondary electron image is a topographic image, and appears like a picture of the microscopic material. As a relatively low energy electron, the secondary electron must be attracted to the detector instead of left to find it on its own. The signal collected from the secondary electrons is then used to form a topographic grayscale image of a specimen, which is known as a secondary electron image. Such images appear like a photograph and allow researchers to look at the surface of a specimen with resolutions down to nanometer scale. These images do not give any chemical information for the composition of the fly ash but they are very useful for describing morphology.

The backscattered electron image appears as a flat grayscale image, in which the grayscale indicates relative average atomic number across the viewing area. It should be taken from a flat, polished specimen in order to result in accurate data. Backscattered electrons are of relatively high energy, having been reduced from the accelerating voltage of the electron beam by their interaction with the specimen. The less interaction an electron has with the specimen, the less energy it loses. Therefore, brighter areas are those of higher average atomic number, whereas the lighter areas are those of lower average atomic number. It is important to note that this image type is only showing differences in the average composition across the material, so no determination of the actual material composition can be made from such an image.

X-ray images are maps of locations where the element in question appears (brighter pixel) or does not appear (black or very low-value pixel). The images look similar to backscattered images, and they are also taken from flat, polished specimens. X-ray images are qualitative in nature. X-ray point analysis and line analysis are other methods using x-ray signal, and they are taken either at a point location or across a line that the microscope operator has drawn on a feature of interest in the BSE image of the sample. Point and line analyses are quantitative in nature. In any of these cases (images, point, or line analyses), the x-rays emitted from a specific orbital transition within each element have a characteristic energy, which is how the detection software attributes the signal to a particular element. There are a few energy overlaps, which are discussed in detail in Goldstein (2003).

2.6.2.2 Quantitative x-ray microanalysis

Quantitative x-ray microanalysis, known as energy dispersive spectroscopy (EDS), requires several important considerations. First, the user must decide whether to use a method of standard-based or standardless analysis. In standard-based analysis mineral, glass, or elemental standards are used as references for determining the composition of the unknown specimen. The method varies by microscope software program, but in general, the spectra for the known standards are collected and are compared to the unknown spectra either manually or by the software package. This allows for calculation of the unknown specimen's composition. In standardless analysis, the information about expected spectra for various compositions are built into the software, and a simple calibration (usually using copper) is performed prior to collection of the unknown spectra. The software package can then calculate the amount of each element present in the unknown specimen. Another consideration for the operator to

make in EDS analysis is selection of the appropriate matrix corrections which consist of ZAF corrections (where Z = atomic number, A = absorption, and F = Fluorescence) and $\Phi(\rho Z)$ corrections (a different method of determining the effect of atomic number). As discussed in Goldstein (2003), the ratio of the composition of an unknown and a known intensity theoretically equals the ratio of their intensities, according to Castaing's first approximation. However, matrix effects of the surrounding material greatly affect the actual concentrations, which is where the corrections become necessary. The corrections are very complicated and should be thoroughly researched by the SEM operator in a source such as Goldstein et al. (2003) prior to selection and data collection. Finally the operator must consider detector issues such as dead time in setting up the EDS experiment. The detector dead time is an important factor in collection of x-ray spectra, since it limits the amount of signal that can actually be collected from the specimen. Dead time is the amount of time that the detector has stopped collecting data due to its being overwhelmed by signal, and a high dead time results in poor counting statistics from which the composition is calculated. The type of detector can affect the results. Lithium-doped silicon detectors (known as Si(Li) detectors) are common in SEMs but have the disadvantage of high dead times. Silicon Drift Detectors (SDDs) are more efficient in collection, which results in lower detector dead time (Maniguet et al. 2012). The operator should adjust collection time to decrease the dead time as much as possible.

2.6.2.3 Specimen preparation

Scanning electron microscopy specimen preparation depends on the type of image desired. For secondary electron imaging, fracture surfaces or any three-dimensional specimen is acceptable. For x-ray analysis and backscattered imaging, the specimen should be microscopically flat, since the x-ray signal intensity and backscattered electron

intensity depend heavily on the geometrical condition that the beam strikes the sample at a perpendicular angle (Goldstein et al. 2003). In addition, for non-conductive materials, excess beam electrons can congregate on the surface of the specimen in a phenomenon known as charging, which is a particular problem for rough surfaces. This can result in poor images since it causes the beam to jump around due to the excess electrons. For such samples, a conductive material should be deposited on the surface in a thin layer to allow excess electrons to move off of the sample. Commonly used coatings for x-ray microanalysis are carbon, gold-palladium, and silver (Goldstein et al. 2003), and the selection mainly depends on what elements the operator is looking for in the sample. For specimens requiring compositional analysis, the x-ray signal of the coating material should not interfere with those of the elements of interest in the specimen.

2.6.2.4 Data analysis: Multispectral Image Analysis (MSIA)

Multispectral image analysis (MSIA) began as a technique used for analyzing satellite images collected for geographical information systems and was expanded into mineralogical specimens by (Lydon 2005). The premise behind MSIA is that multiple data sets that encompass the same spatial area are overlaid, allowing the contribution from the information contained in each of the many layers to be analyzed holistically. The number of layers in a multispectral image depends on how much relevant information is available, but the layers can range from just a few to thousands. Images with large numbers of layers are typically referred to as hyperspectral.

Multispectral image analysis was described for use in geological samples by Lydon (2005), who outlined a set of methods for mineral phase analysis using two free computer programs, ImageJ[3] and Multispec[4]. This type of data analysis has been used in

[3] ImageJ http://rsbweb.nih.gov/ij/
[4] Multispec https://engineering.purdue.edu/~biehl/MultiSpec/

cement phase analysis (Stutzman 2004) and in fly ash phase analysis (Chancey et al. 2010). The elements in the material should be identified prior to collection of the x-ray map data, so that the correct x-ray maps are collected. The maps comprise the multispectral image stack and are digitally overlaid for a computer program to analyze each pixel location. The pixels with similar characteristics from all of the overlaid maps are grouped with other like pixels, which can be accomplished with or without operator supervision. Mathematical functions are used in the software's decision-making process as to which phase each pixel falls within.

The x-ray map data typically need to be pre-processed in order to minimize noise and make particle and phase edges as clear as possible. This is accomplished through the use of filters, which change the pixel values based on the surrounding pixels. ImageJ is one program that can be used for this task, and full details of the algorithms are found in its documentation. The median filter examines each of a pixel's nearest neighbors in the radius selected by the user and replaces the pixel with the median value of the neighboring pixels. This is a smoothing filter. The generic "smooth" filter within ImageJ is simply a median, radius 3 filter. Sometimes the median filter is too strong, particularly for very small features in the image. The thresholded blur plug-in is a useful tool in such instances. It allows the user to exclude values that are more than a particular amount larger or smaller than the pixel in question and to apply a strength multiplier to the filter. This plug-in must be downloaded separately from the installation of the program. Finally, noise in regions known to contain no data (i.e. carbon epoxy), is best removed from the image. This cannot be accomplished with ImageJ, so instead MATLAB can be used to read in images and replace any pixel values below the noise threshold with zero values.

There are two types of multispectral image analysis, supervised and unsupervised analyses. In a supervised cluster analysis, the operator selects regions of pixels called "training classes" to define each of the phases in the material. Once all of the phases have been identified and the training classes defined, the pixels in the image can be applied to a class. There are mathematical formulas used for this. Multispec contains several pixel-assignment procedures including Quadratic likelihood, Fisher Linear Likelihood, Minimum Euclidean Distance, Echo Spectral-Spatial, Correlation (SAM), Matched Filter (CEM), and Parallel Piped. Lydon suggested that for geological samples that the Minimum Euclidean Distance, Fisher Linear Discriminant, and the CEM (Constrained Energy Minimization) methods give the best results (Lydon 2005). In an unsupervised phase analysis, the operator selects either a single-pass or Isodata algorithm, defining the number of clusters, the minimum cluster size, and the area to be classified (typically the whole image). The operator also selects the percentage agreement that the phases must be to consider the clustering complete. Multispec's reference manual provides full details on both of these methods.

2.6.3 Dissolution methods for materials characterization

Selective dissolution is a chemical method for determining the bulk composition of fly ash glasses that are soluble, and uses acids such as hydrofluoric, acetic, and oxalic acids (Hemmings and Berry 1988), and caustics such as sodium hydroxide (Pietersen 1993; Aughenbaugh et al. 2013) to dissolve the glassy phases. The crystalline phases are assumed to be unaffected, with the exception of calcium-containing phases, such as lime, anhydrite, belite, etc., that are known to be reactive. (Hemmings and Berry 1987). The material remaining after dissolution is typically weighed to find the mass change, which correlates to the amount of glass dissolved. By using chemical mass balances, the bulk

glass composition may be estimated (Hemmings and Berry 1987). Secondary electron SEM images of particles in the residue after selective dissolution have revealed the etching of glasses to leave inner shells of crystalline products such as mullite and quartz, which indicates that the solutions selectively dissolve glassy phases.

2.6.3.1 Acid dissolution (hydrofluoric, hydrochloric)

One method for testing the reactive silica in fly ash is hydrofluoric acid dissolution. In the method, which is a standard Spanish procedure (UNE 80-225-93), the fly ash is placed in a platinum crucible, a few drops of water are added, then 10 mL of hydrofluoric acid is added along with a few drops of sulfuric acid. The mixture is heated under a fume hood to 175° C, until the sulfur trioxide has all evaporated (white fumes disappear). The resulting residue is weighed, and the weight is compared to the original specimen, with the calculations reporting the amount of "pure silica" in the specimen (Fernández-Jiménez, de La Torre, et al. 2006).

Acid dissolutions can also be used to test for degree of reaction, which is related to fly ash reactivity, by continuously mixing hardened geopolymer pastes with 1:20 diluted hydrochloric acid at room temperature for several hours (Fernández-Jiménez, de la Torre, et al. 2006; Dombrowski, Buchwald, and Weil 2007). The residue is then separated from the HCl to be tested for composition. In the HCl method, the hydrochloric acid reacts with geopolymer reaction product, and dissolves it to leave the unreacted fly ash particles. By comparing the data for the fly ash residue to that collected for the original fly ash, the dissolved (i.e. reactive) portion of the fly ash is characterized.

2.6.3.2 Caustic dissolution (NaOH, pore solutions)

Caustic dissolution methods have also been used in fly ash reactivity studies. Cementitious pore solutions and sodium hydroxide solutions have been used to dissolve

soluble species from the fly ash to determine the amount of fly ash that is dissolved under those conditions (Pietersen 1993; Chancey 2008; Aughenbaugh et al. 2013). Elevated temperatures of 70° C have been used to expedite the experiment (Buchwald 2006), with the duration of the experiment lasting only a few hours. Other work has used a different approach and allowed the dissolution to continue for the same amount of time as compressive strength of a concrete would typically be tested, such as 1 day, 3 days, 28 days, etc. (Chancey 2008; Aughenbaugh et al. 2013). In general, the steps to these caustic methods were to mix the solid with the caustic liquid in very dilute proportions and to stir or rotate the mixture continuously until the time of testing. At the time of testing, both the solid and liquid material were analyzed for composition. A mass balance allowed for the calculation of the dissolved ionic species from the aluminosilicate, when compared against the raw material properties.

2.7 LIMITATIONS OF PREVIOUS RESEARCH

A major challenge in using fly ash as the sole geopolymer precursor material for concrete is that it is difficult to determine whether a given fly ash will react sufficiently with the activating solution. One chemical method for testing reactivity is hydrofluoric acid dissolution, which measures the reactive silica content of the fly ash by comparing the weight of the treated material to the original sample weight (Fernández-Jiménez, de La Torre, et al. 2006). However, the acid requires extreme care in handling, and it does not represent the highly caustic environment that the fly ash is subjected to in geopolymer formation. Analytical methods of fly ash characterization include x-ray diffraction (XRD) and scanning electron microscopy (SEM). In a method previously applied by Chancey et al. (2010) a comprehensive characterization of fly ash glassy phases was completed for two fly ashes meant for use as portland cement replacements. The same

method may be applicable to fly ashes for use in geopolymer cements, for which the reactivity is difficult to assess.

It is known that there are multiple glassy phases within a fly ash sample, and it is important to identify these glasses since they can react differently when exposed to caustic solutions. While studies have been done to assess the reactivity of fly ash in terms of how much silicon and aluminum dissolve under caustic conditions (Buchwald 2006; Chen-Tan et al. 2009), they do not attribute the source of the silicon and aluminum to particular phases in the fly ash. It is known that how the silica and alumina are bound within the fly ash is also of importance. Point compositional analysis has been used to measure the composition of the various glasses within fly ash in an attempt to better understand its internal structure and potential for reactivity (P. Williams et al. 2005). However, in order to estimate how much of a particular phase is in the fly ash, they should be coupled with x-ray maps, which show the distribution of the phases in the fly ash within and across individual particles (Chancey et al. 2010).

Chapter 3: Materials & Methods

3.1 RAW MATERIALS

The raw materials in these experiments included fly ash, alkali solution, and graded Ottawa sand, which are described in the following sections.

3.1.1 Fly ash

Ten fly ashes were used in this study and of those, eight were Class F (ASTM C618-12) and two were Class C (ASTM C618-12).

3.1.1.1 Fly ash compositions

The fly ashes selected for this work were sourced from several locations around the United States. The fly ashes were selected to include a variety of compositions based solely on oxide analyses provided by the fly ash producer. Three ashes were selected to be similar to the compositions of fly ashes investigated by Lloyd (2008) in Australia that were found to result in favorable geopolymer strengths. The remaining seven ashes rounded out a wide compositional spectrum.

The oxide contents of the fly ashes were provided by the manufacturer (Table 3.1), and in some cases do not add up to 100% because of unmeasured impurities in the specimen.

Table 3.1: Fly ash oxide analyses based upon a single mill sheet report provided by each manufacturer, expressed as mass percent for the ten fly ashes selected for study.

Oxide	Bell River (mass %)	Boral Class C (mass %)	Big Brown Raw (mass %)	Coleto Creek (mass %)	Atikokan (mass %)	Centralia (mass %)	LEGS (mass %)	Martin Lake (mass %)	Fontana (mass %)	Belews Creek (mass %)
Al_2O_3	17.04	17.2	18.43	20.98	21.58	16.36	17.8	19.92	25.14	30.5
SiO_2	33.16	35.7	48.36	48.15	47.66	54.06	54.14	54.75	59.36	55.81
CaO	27.06	25.3	14.14	12.77	12.3	11.16	10.7	9.37	5.63	1.19
Fe_2O_3	4.91	5.85	7.97	4.85	4.21	6.01	7.74	8.66	5.56	4.6
K_2O	0.78	0.604	1.14	1.2	0.89	1.86	1.43	1.13	0.97	2.26
MgO	5.06	5.94	2.16	3.42	2.7	4.14	2.31	2.43	0.94	0.72
Na_2O	4.2	1.96	0.64	1.53	1.93	1.18	0.45	0.64	0.15	0.28
SO_3	2.87	1.72	0.4	0.32	1.2	0.64	0.4	0.46	0.37	0.08
TiO_2	1.11	1.24	1.18	1.04	0.97	0.98	1.2	n/a	1.09	-
LOI	0.58	n/a	0.46	0.81	0.76	0.24	0.09	0.14	0.16	n/a

3.1.1.2 Particle size distributions

The particle size distributions (PSD) of the fly ashes were analyzed using a Spraytec by Malvern Instruments, Inc. laser particle size analyzer with Spraytec software, and the results are shown in Figure 3.1. The fly ashes were mixed with isopropyl alcohol (99% purity) prior to testing. The d_{50} value for each of the fly ashes is highlighted by a red line in Figure 3.1. The d_{50} values for each fly ash are given in Table 3.2. While the d_{50} value represents the median particle size, the overall particle size distribution is important. This point is illustrated by comparing the curves for ashes with approximately the same d_{50} value. The finest material is shifted to the left in a particle size analysis, while the coarsest material is shifted furthest to the right on the plot. The finest fly ash in the study, based on d_{50} value, was the Coleto Creek ash, followed by the Centralia and Martin Lake fly ashes. However, while the Centralia fly ash had a steeper slope curve above the d_{50} indicating that it had a narrower particle size range above d_{50} and a smaller maximum particle size, the Coleto Creek fly ash had a more gradual curve indicating a

wider distribution of particle sizes above the d_{50} size and a larger maximum particle size. The Bell River, Boral, Atikokan, and LEGS fly ashes had very similar d_{50} sizes to each other and comprised the middle of the PSD results. The remaining ashes, Big Brown Raw, Belews Creek, and Fontana, had approximately the same d_{50}, and were the coarsest three fly ashes in the study.

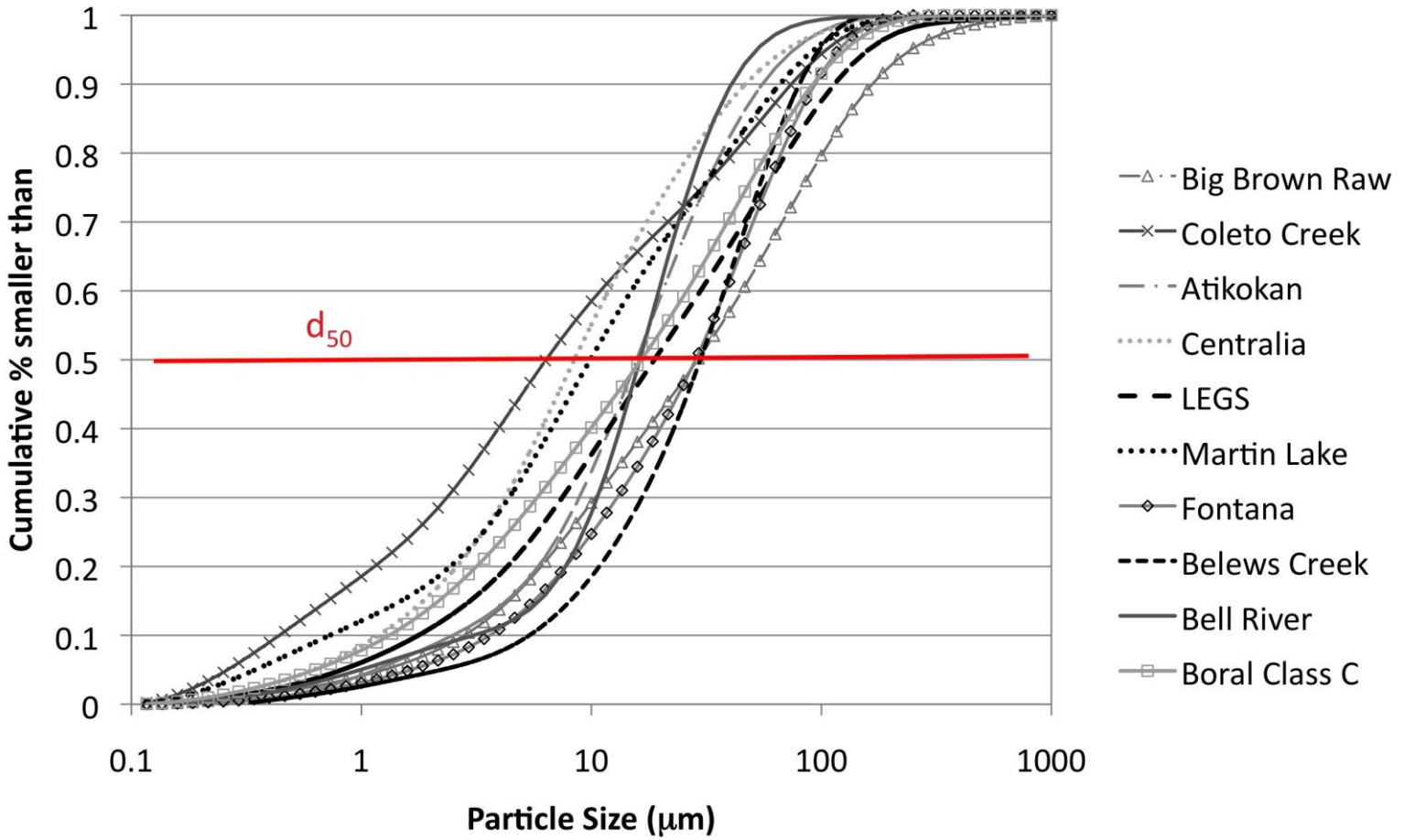

Figure 3.1: Laser particle size analysis curves for each of the ten fly ashes

Table 3.2: Tenth (d_{10}), fiftieth (d_{50}), and ninetieth (d_{90}) percentile particle sizes for the ten fly ashes in this study as measured by laser particle size analysis by a single measurement

Fly ash	d_{10} (μm)	d_{50} (μm)	d_{90} (μm)
Atikokan	2.5	15. 8	54.1
Belews Creek	5.9	31	84.2
Bell River	3.4	15.8	39.8
Big Brown Raw	2.9	29.3	158.5
Boral Class C	1.4	15.8	85.8
Centralia	1.2	8.6	46.4
Coleto Creek	0.5	6.3	73.6
Fontana	4.0	29.3	100
LEGS	1.8	18.5	116.6
Martin Lake	0.7	10	63.1

3.1.2 Activating solutions

Sodium hydroxide activating solution (8M) was used for all specimens in this work, similar to the work of other researchers who found that this solution was successful in fly ash activation (Fernández-Jiménez and Palomo 2005; Fernández-Jiménez, de la Torre, et al. 2006; Dombrowski, Buchwald, and Weil 2007). The NaOH solution was made one of two ways: by diluting 50 wt/wt% reagent grade NaOH solution with ultrapure water (resistivity of 18 MΩ-cm) to the desired concentration or by weighing reagent grade NaOH pellets and dissolving them in ultrapure water. The solution was allowed to rest until all heat was dissipated and stored in capped non-reactive Nalgene jugs prior to use.

3.1.3 Other materials

Mortar cubes were made according to ASTM C109 (2009) using graded Ottawa sand. The sand was certified to meet the "graded sand" standard (ASTM C778).

3.2 METHODS

The methods used throughout the work presented in this dissertation are described in this section including specimen preparation and equipment operating conditions.

3.2.1 Mortar cubes

Mortar cubes were made for compressive strength analysis of all ten fly ashes mixed using the same proportions and curing regimes. These data were used as an indicator of fly ash reactivity, with the assumption that increased strength indicated increased reactivity of the fly ash. The method given in ASTM C109 (2007) was followed (with some modification) for mixing, placing, and curing the specimens. The solution-to-powder (s/p) ratio (by mass) was not determined individually for each fly ash as the method suggested; rather, a s/p that was appropriate for all ten fly ashes was determined through trial mixing small amounts of mortars until a mixture that was not too dry and not too runny was obtained for all ten ashes. This s/p value turned out to be 0.485, the same as that recommended for use in portland cement mortars. This was done in an effort to compare fly ashes mixed with the same amount of sodium hydroxide solution. In addition, while portland cement mortars should be stripped from the molds at 1 d, this was determined too short an interval for most fly ash-based geopolymers, so the mortars remained in their molds for 7 d. Finally, instead of storage in limewater, the mortar cubes to be tested at 28 d were patted surface dry and placed in sealed plastic bags and stored in a room at 23 °C. Mortar cubes were made for testing at 7 d and 28 d for each of the ten fly ashes.

3.2.2 X-ray diffraction

Quantitative x-ray powder diffraction (XRD) was used to qualitatively and quantitatively analyze the fly ashes for crystalline and bulk amorphous content. The

following sections discuss the internal standard used for quantitative x-ray diffraction analysis, the methods for specimen preparation, and the methods of data analysis.

3.2.2.1 Zincite as an internal standard

In order to perform quantitative analysis on the fly ashes, an internal standard was interground with the powder specimens. The internal standard analysis for x-ray powder diffraction is described by (Klug and Alexander 1974). Knowledge of the proportions of the crystalline and amorphous content of an internal standard is import for appropriate estimates of the crystalline and amorphous mass fractions. This may be accomplished using a certified reference material or through creation of a secondary reference standard using a certified reference material. Zincite (ZnO, ACS reagent grade from Acros Organics) was selected for a secondary reference internal standard in this study as was used by other researchers for fly ash quantitative analysis (Dombrowski, Buchwald, and Weil 2007). In order to use an ACS reagent grade material instead of a standard reference material, the purity was assessed by running an x-ray diffraction scan on the powder and identifying zincite as the only crystalline phase. Next, x-ray diffraction was completed with a blend of the zincite and National Institute of Standards and Technology (NIST) Standard Reference Material® (SRM) 676, which was the corundum polymorph of Al_2O_3. Two blends, 25% SRM/ 75% ZnO and 10% SRM/ 90% ZnO were used. Rietveld analysis was performed on the zincite/SRM blends, since the crystal structure data were known for the SRM, which allowed for refinement of the structure file for zincite. The NIST SRM certified corundum mass percent of 99.02% was used to estimate the mass fraction of zincite and residual amorphous content of the secondary reference powder. The refined structure file could then be used in Rietveld analysis of the fly ash specimens for which the zincite was used as an internal standard.

Characteristics important to appropriate internal standard selection were discussed previously in section 2.6.1.2.

3.2.2.2 XRD specimen preparation & experimental procedure

The ZnO internal standard was interground with the fly ash in an agate mortar and pestle at 10% by mass replacement using ethanol as a dispersing lubricant. The mixing process was complete when the powder was free-flowing in the mortar, indicating that all of the ethanol had evaporated. The specimens were placed in a 38 °C oven until they were dry. The powdered specimens were pressed into the plastic XRD sample holders using a glass plate such that the plane of the specimen surface was even with the edge of the specimen holder. These steps to properly set specimen height ensured that the face of the specimen was in the focusing circle of the powder diffractometer employing Bragg-Brentano geometry (Reynolds, Jr. 1989).

The x-ray diffraction analysis was performed using a Siemens D500 x-ray diffractometer. The Cu x-ray source produced Ni-filtered Cu-Kα radiation, operating at 40 kV and 30 mA. A dwell time of 6 seconds per step was used for all specimens to increase the x-ray counts at each step for better resolution of phases. The scans were run from 13°-67° 2θ with a step size of 0.02° 2θ. The XRD was configured with a 1º divergence slit, a 4º soller slit, and a 1º anti-scatter slit on the beam side and a 1º anti-scatter slit, a 4º soller slit, a 0.15 mm receiving slit, and a 0.6 mm detector slit. The detector also included a graphite monochromator to remove Cu K-β radiation prior to reaching the detector.

3.2.2.3 XRD data analysis

The crystalline phases in the fly ashes were identified using files from the inorganic crystal structure database[5] and Jade software package[6], and Rietveld analysis was completed with TOPAS Academic version software (Coelho Software, Brisbane, Australia). Rietveld analysis of XRD data allowed for calculation of the amount of bulk glassy phase in the fly ash by first calculating the amounts of all crystalline phases in the material and then subtracting the sum from 100%. For Rietveld analysis, many structure files were previously transcribed as the necessary .str files used by the computer program by former researchers in our lab including Ryan Chancey and Irvin Chen, and some were obtained from Paul Stutzman (unpublished data). Additional files were obtained from the AMCSD[7] online. The refinement strategy outlined by Young was used to complete refinements (Young 1993).

Rietveld analysis assumes that the specimen is 100% crystalline, thus it apportioned the crystalline phases to sum to 100%. Because of this, the Rietveld results showed that the internal standard spike was greater than the 10 mass % that was known to be in the sample. To calculate the amount of bulk amorphous phase in the fly ash, the results were normalized to the known spike amount following the procedure reported by Chancey et al. (2010):

$$P_i' = P_i\left(\frac{I'}{I}\right) \qquad (1)$$

where P_i' is the mass percentage of phase i in the spiked sample, P_i is the mass percentage of phase i as determined directly by Rietveld analysis, I' is the mass percentage of the internal standard, and I is the mass percentage of internal standard as identified in Rietveld analysis (Chancey et al. 2010).

---

5 FIZ/NIST Inorganic Crystal Structure Database (ICSD)http://www.nist.gov/srd/nist84.cfm

6 http://www.materialsdata.com/

7 http://rruff.geo.arizona.edu/AMS/amcsd.php

Since the calculated amounts of each crystalline phase plus the amorphous phase ($P_i^{'}$) still contained the 10 weight % spike of zincite, the values were then renormalized to 90% of the total mass in order to include only those phases found in the fly ash. See Chancey (2010) for further details.

3.2.3 Scanning Electron Microscopy (SEM)

Scanning electron microscopy (SEM) was used to characterize the glassy phases in fly ash. The backscattered electron images are compositional images with brightness proportional to the average atomic number of the materials. This facilitates identification of the constituent phases within a multiphase particle and of particle edges. The x-ray maps were used to image element spatial distribution and relative concentration. Stacking the x-ray maps as a multispectral image allowed interactive display of the chemical composition of the particles.

3.2.3.1 SEM specimen preparation procedures

The specimen preparation methods for SEM specimens followed those of Chancey which were outlined briefly in (Chancey et al. 2010) and in further detail in (Chancey 2008). First, a specimen holder of 32 mm diameter and 10 mm. thickness was prepared using Epotek 353ND epoxy[8]. This was cured for 24 hours at 38 °C and allowed to cure for another 24 h at room temperature. Each specimen holder typically housed 4 to 8 powder samples in wells that were drilled using a drill press with a 3/8 in. bit (9.525 mm). The powder samples were prepared by mixing the powder with the Epotek epoxy at a 2:1 mass ratio, respectively, and placing the mixture into the predrilled wells of the specimen holder. The same curing regimen was used as for the specimen holders. A picture of a specimen is shown in Figure 3.2.

[8] Epoxy Technology Inc., Billerica, MA

Figure 3.2: Coated, polished, epoxy-embedded SEM powder specimen ready for imaging

The polishing process involved several stages of dry grinding with silicon carbide paper followed by several stages of polishing using diamond pastes. All grinding and polishing was completed by hand. First, the slightly mounded specimens were ground to the level of the specimen holder plane using #180 paper. Next, the sample was further ground using papers of #600 and #1200. A light microscope aided the grinding process; using the light microscope, the scratches in the sample surface caused by the grinding process could be monitored to ensure that sufficient material was removed before moving to a finer grinding stage. The specimens were cleaned between each stage of grinding using ethanol and dried with compressed air or a twill polishing cloth[9]. The diamond paste polishing was completed using a polishing wheel rotating at 100 rpm (0.104 rad/s). The diamond paste polishing compound was applied to a dry twill polishing cloth that was secured to the rotating platen of a polishing table using an adjustable hoop. The first stage of diamond paste was 6 μm fineness (Ted Pella 895-9, Redding, CA), followed by 3 μm (Ted Pella 895-8, Redding, CA), 1 μm (Ted Pella 895-7, Redding, CA), and ¼ μm (Ted Pella 895-5, Redding, CA). Each step lasted approximately 5 minutes, after which

[9] Ted Pella 812-2, Redding, CA

the specimen was examined with a light microscope to assess the progress. The specimens were cleaned between each polish using an ultrasonic bath with ethanol to remove any remaining polishing media. The length of ultrasonication was typically done in 10 s increments until no trace of polishing compound remained (based on visual inspection).

Carbon coating was the last step in specimen preparation. This step ensured that electrons from the microscope could be dissipated from the specimen surface, since the specimen itself was non-conductive. The coating was applied using an evaporation coater and the thickness of the coating was measured using the brass substrate method (Kerrick, Bminhizer, and Villaume 1973). Approximately 25-30 nm of carbon was applied to each specimen such that the brass substrate appeared blue to indigo-red.

3.2.3.2 SEM data collection procedures

Scanning Electron Microscopy (SEM) work[10] was completed at 10 kV accelerating voltage, and the electron beam current was maintained at 2.5 nA and monitored between data sets using a Faraday cup.

Backscattered electron images were collected for each fly ash using a 2-pole solid state backscattered detector mounted directly above the specimen. The BSE images were collected along with the x-ray images using the same operating conditions. The dual EDS detectors increased the count rates significantly from a single-detector system. X-ray maps and BSE images were collected using a slow 256 μs dwell time per pixel and line averaging of 2 with a 1024 x 768 map size. Each sweep required approximately 6 min to collect with four sweeps summed to complete data collection, requiring approximately 24 min for each data set. The data were saved as 16-bit tiff files, which

[10] FEI Quanta 600 (tungsten filament) and Bruker Quantax x-ray microanalysis and imaging system with dual silicon-drift detectors

allowed for preservation of the actual x-ray counts for each element at each pixel. Maps of Ca, Si, Al, Fe, Na, Mg, K, Ti, O, S, and C were collected for each fly ash.

To quantitatively determine the composition at specific points throughout the specimens, standards-based EDS analysis was completed. Three reference standards, the NBS 1716 glass, NIST K412 glass, and rhyolite mineral[11] from the Smithsonian, were used as to quantify the chemical composition of selected points. The collection conditions were 45 s (real time) collection time at each point, and automatic ZAF correction (Goldstein et al. 2003) and analysis after acquisition. A complete reference on x-ray microanalysis and correction schemes may be found in Goldstein et al. 2003. The software allowed for interactive multi-point designation and spectra collection, such that the operator could pre-select many points on the field of view for analysis and the program would automatically move from point to point collecting and analyzing the data. The software also had the capability to auto-select the points for analysis using a grid of points (i.e. in a fully unsupervised point selection regime), but this resulted in too many locations on the epoxy (and non-useful data) such that the operator-selected option was more useful.

3.2.3.3 SEM data analysis procedures

Multispectral image analysis has been described for minerals (Lydon 2005) and fly ash (Chancey et al. 2010) and is discussed here briefly, following a description of how the images were prepared for analysis. Every effort was made to collect high quality x-ray data by using optimum microscope operating conditions. However, in some cases, the data contained noise that precluded the identification of the features of interest (i.e. particles). In order to improve the analysis, the data required pre-processing before

[11] NIST K412 was part of now out of stock SRM 470 glasses for microanalysis. K1716 was a trial reference glass and the rhyolite glass was obtained from the Smithsonian microbeam reference collection as USNM 72854.

multispectral image analysis. The main goals of pre-processing were to remove noise and improve resolution of the fly ash particles.

The x-ray maps were preprocessed using ImageJ[12] and MATLAB[13]. The images were saved as 16-bit tiff files to preserve raw data values and were converted to 8-bit tiff files using MATLAB. Pixel value scaling was unnecessary since no pixel value in any x-ray map exceeded 255, which is the maximum value for 8-bit pixels. It is important to note that ImageJ contains a function to convert 16-bit to 8-bit images as well, but it rescales the data, which was undesirable. MATLAB was a better choice for this operation. The images often looked black when opened in ImageJ, despite data being present, and this appearance was due to the low pixel vales. To view the images, the display image could be modified in ImageJ by using Image → adjust brightness/contrast and adjusting the high end from 255 down to the maximum pixel value in the image. This did not change the raw data values. ImageJ was used to perform any smoothing operations necessary to make particle edges more clear and remove noise from the images. Often, a median filter of radius = 1 was used for this purpose. This filter replaced all pixel values in the image by finding the median value of pixels at a user-defined neighborhood surrounding each pixel. Thus, for a radius = 1 median filter, the software only looked at the pixels immediately touching the center pixel. The thresholded blur filter (available as a plugin) was another smoothing filter, and it was similar to the median filter but included additional parameters in recalculating pixel values. Thresholded blur allowed for more control over the strength of the filter. Finally, the low-end pixels deemed noise were replaced with 0 values using MATLAB code. The noise cutoff value was determined visually using ImageJ and the adjust

[12] ImageJ, http://rsbweb.nih.gov/ij/
[13] Mathworks http://www.mathworks.com/products/matlab/

brightness/contrast function. These steps were used only as necessary on an image-by-image basis, and the minimum pre-processing was used.

The images were stacked digitally using Multispec[14]. Three maps were viewed simultaneously as red, green, and blue channels; by changing which elemental maps were turned on, the user gained familiarity with the composition of the fly ash. Groups of pixels were then selected in regions of different composition (based on appearance of the 3-channel RGB image) and were defined as the training field for various phases in the fly ash. The Multispec program then assigned every pixel in the image to the most likely of the defined fields from which an area percentage of each phase was calculated. If the volume of spherical fly ash particles is assumed equal to the area (Bentz and Remond 1997); after converting area percents to volume percents, published densities can be used to calculate weight percentages of each phase present, but this was not done in the study described here.

3.2.4 Dissolution study of phase reactivity

The glassy phase reactivity was determined using a dissolution method. The specimens were subjected to the same caustic solution as was used for activation (8 M NaOH) and continuously agitated.

3.2.4.1 Dissolution specimen preparation

The dissolution method was performed as follows: 2 g fly ash was mixed with 10 mL 8 M NaOH solution, similar to the procedures used by Chancey and others for simulated cement pore solutions (Chancey 2008; Aughenbaugh et al. 2013). The samples were mixed in non-reactive plastic vials, sealed with a screw-cap lid, and placed on a laboratory rotisserie (LabQuake) that rotated the samples end-over-end at approximately

[14] Multispec, https://engineering.purdue.edu/~biehl/MultiSpec/

10 rpm until the desired time had elapsed. The rotisserie was located in a room that was maintained at 23 °C. At 7 d and 28 d, the sample was removed from the rotisserie and the solid material was separated from the liquid under vacuum using a 2.7 μm non-reactive filter paper and a Buchner funnel. The solid material was dried for no more than one hour in air, then scraped from the paper into a vial and placed in a vacuum desiccator for complete drying.

The dried powder was examined using x-ray diffraction and scanning electron microscopy. To prepare the specimens for x-ray diffraction, the same procedure was used as outlined in Section 3.2.2.2. Similarly, the same procedure was used for SEM specimen preparation of powdered samples as outlined in Section 3.2.3.1.

3.2.4.2 Dissolution specimen data analysis

Data analysis in x-ray diffraction consisted of phase identification using the ICDD powder diffraction database. Often, the phases were not identifiable, since they consisted of undocumented zeolite species (Oh et al. 2010), and Rietveld analysis was not performed unless all phases were identified. Glassy phase analysis for the reactivity samples consisted of the same MSIA analysis as described in section 3.2.3.3. The results were compared to the phase compositions determined for the raw fly ash and conclusions were drawn as to the reactivity of the phases in the fly ashes. More details are given in the pertinent chapters.

Chapter 4: Results: Fly ash characterization

Ten fly ashes were analyzed for composition using x-ray diffraction and scanning electron microscopy. The fly ash bulk oxide compositions are given in Table 3.1 in the previous chapter. The ashes were characterized for crystalline phases using quantitative x-ray diffraction and the Rietveld method, discussed in section 4.1. The ashes were also characterized for composition using scanning electron microscopy x-ray mapping and multispectral image analysis (SEM-MSIA), discussed in section 4.1.

4.1 CRYSTALLINE PHASE ANALYSIS

The fly ashes were analyzed for crystalline material content using an internal standard and Rietveld quantitative analysis. The phases were identified using Jade[15] software and the ICDD listings built into it. The Rietveld analysis was completed using the academic version of TOPAS[16] combined with jEdit[17]. Quantitative results are presented for each fly ash. The results are reported with a precision of 0.1 mass %; however; the error in Rietveld analysis may be higher than this, therefore the reporting of very small amounts of a phase indicates that the phase was identified in the XRD scan but the amount reported may be within the error. A test result is defined as three replicate determinations to estimate a mean and an uncertainty, expressed as a single standard deviation for each data set. The eight Class F fly ashes are presented first, followed by the two Class C fly ashes. Finally, a discussion of the crystalline and bulk amorphous contents for the fly ashes is made. An XRD scan for each fly ash is shown in Appendix A.

[15] Materials Data, Inc. http://www.materialsdata.com/index.html
[16] Coelho Software http://www.topas-academic.net/
[17] jEdit http://www.jedit.org/

4.1.1 Atikokan fly ash Rietveld analysis results

The Atikokan fly ash contained crystalline phases of quartz, mullite, hematite, anhydrite, and periclase.Table 4.1 shows the results of Rietveld analysis for the Atikokan fly ash. The amorphous material was a very high proportion of the fly ash at an average of 88.5 % of the three samples tested. Quartz and mullite comprised the major crystalline phases, and each was present at approximately 5 mass % of the material. Hematite, anhydrite, and periclase were present in trace amounts of < 1 mass % of the specimens.

Table 4.1 Atikokan fly ash Rietveld analysis results expressed as mass percent with an uncertainty expressed as a single standard deviation (s) of n = 3.

Phase	Relative Amounts in Samples			Mean (mass %)	Std. deviation (mass %)
	Sample 1	Sample 2	Sample 3		
Amorphous	90.0	88.3	87.4	88.6	1.4
Quartz	5.7	3.9	7.3	5.6	1.7
Mullite	2.7	6.7	3.9	4.5	2.1
Hematite	0.7	0.4	0.6	0.6	0.1
Anhydrite	0.4	0.2	0.2	0.3	0.1
Periclase	0.5	0.5	0.7	0.6	0.1

4.1.2 Belews Creek fly ash Rietveld analysis results

The Belews Creek fly ash contained only three crystalline phases: quartz, mullite, and hematite. The results of the Rietveld analysis are shown in Table 4.2. The amorphous portion was 76.5 % by mass. There was a large amount of mullite in the fly ash, which was present at an average of 18.5 mass % of the material in the three samples tested. Quartz was present at around 4 mass %, and hematite was present in a trace amount of < 1 mass %.

Table 4.2 Belews Creek fly ash Rietveld analysis results expressed as mass percent with an uncertainty expressed as a single standard deviation (s) of n = 3.

Phase	Relative Amounts in Samples (mass %)			Average (mass %)	Std. Deviation (mass %)
	Sample 1	Sample 2	Sample 3		
Amorphous	80.0	74.0	75.7	76.6	3.1
Quartz	4.4	4.8	3.7	4.3	0.6
Mullite	14.9	20.8	19.9	18.5	3.2
Hematite	0.8	0.4	0.7	0.6	0.2

4.1.3 Big Brown Raw fly ash Rietveld analysis results

The Big Brown Raw fly ash contained six crystalline phases: quartz, mullite, magnetite, anhydrite, periclase, and lime. Table 4.3 presents the quantitative crystalline results for the Big Brown Raw fly ash. The Big Brown Raw fly ash had an amorphous content of around 79 mass %. The quartz and mullite were present at around 4 mass % each, while trace amounts of magnetite, anhydrite, periclase, and lime were identified in the fly ash. Two samples were tested for this fly ash.

Table 4.3: Big Brown Raw fly ash Rietveld analysis results expressed as mass percent with an uncertainty expressed as a single standard deviation (s) of n = 2.

Phase	Relative Amounts in Samples (mass %)			Average (mass %)	Std. Deviation (mass %)
	Sample 1	Sample 2	Sample 3		
Amorphous	73.4	83.9	-	78.7	7.5
Quartz	3.6	5.0	-	4.3	1.0
Mullite	3.9	3.2	-	3.6	0.5
Magnetite	0.3	0.0	-	0.2	0.2
Anhydrite	0.1	0.4	-	0.3	0.2
Periclase	1.4	0.6	-	1.0	0.5
Lime	0.1	0.0	-	0.0	0.1

4.1.4 Centralia fly ash Rietveld analysis results

The Centralia fly ash contained seven crystalline phases: quartz, mullite, hematite, maghemite, and anhydrite as identified in three samples. Periclase was identified in one replicate. The quantitative results are shown in Table 4.4. Centralia fly ash was highly

amorphous with an average of 87 mass % amorphous phase. Quartz was the most prevalent crystalline material at approximately 8 mass %, followed by mullite, which was calculated to make up approximately 3 mass% of each sample. Hematite, maghemite, and anhydrite were present in trace amounts of < 1 mass%. The periclase identified in a single replicate was calculated to amount to approximately 1.3 mass % of the sample.

Table 4.4: Centralia fly ash Rietveld analysis results expressed as mass percent with an uncertainty expressed as a single standard deviation (s) of n = 3.

Phase	Relative Amounts in Samples (mass %)			Average (mass %)	Std. Deviation (mass %)
	Sample 1	Sample 2	Sample 3		
Amorphous	85.6	89.2	87.5	87.4	1.8
Quartz	10.5	6.1	6.9	7.8	2.3
Mullite	1.5	3.5	3.9	2.9	1.3
Hematite	0.5	0.7	0.8	0.7	0.1
maghemite	0.4	0.2	0.6	0.4	0.2
anhydrite	0.3	0.4	0.4	0.4	0.0
periclase	1.3	-	-	1.3	n/a

4.1.5 Coleto Creek fly ash Rietveld analysis results

The Coleto Creek fly ash was found to contain six crystalline phases: quartz, mullite, hematite, magnetite, anhydrite, and periclase. Table 4.5 shows the results of Rietveld quantitative analysis for the Coleto Creek fly ash. The amorphous portion of the fly ash amounted to approximately 85 % of the fly ash mass. Quartz was the crystalline material present in the highest amount at nearly 10 % by mass. The mullite was the second greatest amount of crystalline material, at 4 % by mass. The remaining phases (hematite, magnetite, anhydrite, and periclase) existed at less than 1 mass % of the fly ash. Magnetite was identified on the basis of its peaks in the diffraction pattern; however, magnetite was identified in amounts below the 0.1 % detection limit.

Table 4.5: Coleto Creek fly ash Rietveld analysis results expressed as mass percent with an uncertainty expressed as a single standard deviation (s) of n = 3.

Phase	Relative Amounts in Samples (mass %)			Average (mass %)	Std. Deviation (mass %)
	Sample 1	Sample 2	Sample 3		
Amorphous	83.9	89.6	81.7	85.1	4.1
quartz	9.8	7.6	10.4	9.3	1.5
mullite	5.4	0.9	6.5	4.3	3.0
hematite	0.1	0.7	0.3	0.4	0.3
magnetite	0.0	-	-	0.0	n/a
anhydrite	0.1	0.4	0.3	0.3	0.2
periclase	0.8	0.8	0.8	0.8	0.0

4.1.6 Fontana fly ash Rietveld analysis results

The Fontana fly ash contained six crystalline phases: quartz, mullite, hematite, maghemite, anhydrite, and lime. The results of Rietveld analysis are shown in Table 4.6. The bulk amorphous portion of the fly ash was only 61 mass %, which was significantly lower than any other fly ash. Mullite was the crystalline phase present in the greatest amount at approximately 20 % by mass. Quartz was the second greatest crystalline phase at 14 % by mass. The remaining crystalline phases were present in very small amounts of near 1 % by mass.

Table 4.6: Fontana fly ash Rietveld analysis results expressed as mass percent with an uncertainty expressed as a single standard deviation (s) of n = 3.

Phase	Relative Amounts in Samples (mass %)			Average (mass %)	Std. Deviation (mass %)
	Sample 1	Sample 2	Sample 3		
Amorphous	60.5	58.9	64.6	61.4	2.9
Quartz	16.1	15.7	11.6	14.5	2.5
Mullite	19.5	19.7	21.3	20.2	1.0
Hematite	0.9	1.0	0.9	0.9	0.1
Maghemite	1.3	1.6	0.8	1.2	0.4
Anhydrite	2.6	0.4	0.3	1.1	1.3
Lime	1.5	0.6	0.4	0.8	0.6

4.1.7 LEGS fly ash Rietveld analysis results

The LEGS fly ash contained five crystalline phases: quartz, mullite, magnetite, anhydrite, and periclase. The Rietveld quantitative analysis results are shown in Table 4.7. The bulk amorphous content was approximately 80 % by mass. Quartz was present in the greatest quantity at around 14 mass %. Mullite was present in second-highest quantity at approximately 4 mass %. The magnetite phase was present around 1 mass %, while the two remaining phases, anhydrite and periclase, were present in trace amounts well under 1 mass %.

Table 4.7: LEGS fly ash Rietveld analysis results expressed as mass percent with an uncertainty expressed as a single standard deviation (s) of n = 3.

Phase	Relative Amounts in Samples (mass %)			Average (mass %)	Std. Deviation (mass %)
	Sample 1	Sample 2	Sample 3		
Amorphous	78.4	81.0	82.2	80.5	1.6
Quartz	16.3	13.5	12.0	13.9	1.8
Mullite	3.4	4.2	4.5	4.0	0.5
Magnetite	1.2	0.9	1.0	1.0	0.1
Anhydrite	0.5	0.4	0.3	0.4	0.1
Periclase	0.3	0.2	0.0	0.1	0.1

4.1.8 Martin Lake fly ash Rietveld analysis results

The Martin Lake fly ash contained four crystalline phases: quartz, mullite, maghemite, and anhydrite. The Rietveld analysis results are shown in Table 4.8. The bulk amorphous content was approximately 78 % by mass, and the crystalline material present in greatest quantity was quartz at approximately 14.6 mass %. Mullite was calculated as being present at around 6 % by mass, while maghemite was near 1 mass %. Anhydrite was present in a trace amount at 0.2 % by mass.

Table 4.8: Martin Lake fly ash Rietveld analysis results expressed as mass percent with an uncertainty expressed as a single standard deviation (s) of n = 3.

Phase	Relative Amounts in Samples (mass %)			Average (mass %)	Std. Deviation (mass %)
	Sample 1	Sample 2	Sample 3		
Amorphous	78.5	77.4	78.4	78.1	0.6
Quartz	14.9	14.8	14.2	14.6	0.4
Mullite	6.3	5.9	5.5	5.9	0.4
Maghemite	0.3	1.5	1.7	1.2	0.8
Anhydrite	0.1	0.3	0.2	0.2	0.1

4.1.9 Bell River fly ash Rietveld analysis results

The Bell River fly ash contained eleven crystalline phases, many in very small quantity. The bulk amorphous content of the fly ash was calculated to be approximately 79 % by mass. Merwinite ($Ca_3Mg(SiO_4)_2$) was identified as the crystalline phase present in highest quantity, at approximately 6% by mass. The second greatest crystalline phase was quartz at nearly 5 % by mass, followed by mullite at nearly 4 % by mass. Gehlenite (C_2AS), was identified at 2 mass %. Two portland cement phases, tricalcium aluminate (C_3A) and C_2S (belite), were identified at approximately 1 %. The remaining phases were present in trace quantities under 1%.

Table 4.9: Bell River fly ash Rietveld analysis results expressed as mass percent with an uncertainty expressed as a single standard deviation (s) of n = 3.

Phase	Relative Amounts in Samples (mass %)			Average (mass %)	Std. Deviation (mass %)
	Sample 1	Sample 2	Sample 3		
Amorphous	73.38	83.92	79.29	78.86	5.28
Quartz	3.63	4.97	5.39	4.67	0.92
Mullite	3.90	3.21	4.17	3.76	0.50
Magnetite	0.29	0.04	0.01	0.11	0.15
Anhydrite	0.11	0.39	0.29	0.26	0.14
Periclase	1.36	0.61	0.86	0.95	0.38
Lime	0.07	0.00	0.00	0.02	0.04
Merwinite	3.65	6.83	8.00	6.16	2.25
Gehlenite	6.07	0.03	0.14	2.08	3.45
C_3A	1.95	0.00	1.38	1.11	1.00
C_2S	3.70	0.00	0.47	1.39	2.01
Calcite	1.90	0.00	0.00	0.63	1.10

4.1.10 Boral Class C fly ash Rietveld analysis results

The Boral Class C fly ash contained seven crystalline phases: quartz, mullite, maghemite, anhydrite, periclase, lime, and merwinite. The bulk amorphous content was calculated as 77 % by mass of the fly ash. Merwinite was the crystalline phase present in the highest amount at approximately 10 % by mass. Quartz was the next phase at approximately 6 % by mass. Mullite was present at approximately 2.5% by mass, and anhydrite was nearly 2 %. The remaining crystalline phases were present in very small amounts.

Table 4.10: Boral Class C fly ash Rietveld analysis results expressed as mass percent with an uncertainty expressed as a single standard deviation (s) of n = 3.

Phase	Relative Amounts in Samples (mass %)			Average (mass %)	Std. Deviation (mass %)
	Sample 1	Sample 2	Sample 3		
Amorphous	75.05	78.43	77.62	77.03	1.77
Quartz	6.73	4.59	6.37	5.90	1.15
Mullite	4.35	1.08	2.25	2.56	1.66
Maghemite	0.19	0.09	0.01	0.10	0.09
Anhydrite	2.23	1.72	1.19	1.71	0.52
Periclase	1.98	2.36	1.97	2.10	0.23
Lime	0.54	0.54	0.62	0.57	0.04
Merwinite	8.92	11.18	9.98	10.03	1.13

4.1.11 Comparison and Discussion: Crystalline phases in fly ash

The number of crystalline phases identified in the fly ashes ranged from a low of three crystalline phases identified up to a high of eleven. In general, the Class F fly ashes had a lower number of phases present than the Class C fly ashes. The two fly ashes with the lowest calcium content (Belews Creek and Fontana) had the greatest amount of mullite and least number of phases. The Martin Lake fly ash, which had the third-lowest CaO amount (9%), also had few phases identified, but it did not have high mullite content. This fly ash was more similar in composition to the remaining Class F fly ashes with higher CaO content.

The amorphous content of fly ash is considered the most reactive portion, with the exception of portland cement calcium silicate and calcium aluminate phases that are in crystalline form (Hemmings and Berry 1987). Figure 4.1 presents the results for bulk-amorphous content of all ten fly ashes, so that they may be compared to each other. The lowest amount of bulk amorphous content was determined to be in the Fontana fly ash with just 61 % amorphous phase by mass. The highest amount of bulk amorphous phase was found in the Atikokan fly ash, which was calculated as 89 % amorphous by mass. The Centralia and Coleto Creek fly ashes were similarly high to the Atikokan. The remaining fly ashes were between 77 and 80 mass % of amorphous phase. No minimum

amount has been suggested for optimum reactivity, but given these results, it is hypothesized that the Atikokan, Centralia, and Coleto Creek fly ashes may have high reactivity in an alkaline solution, while the Fontana fly ash would have low reactivity. This hypothesis was tested and results are reported in Chapter 5.

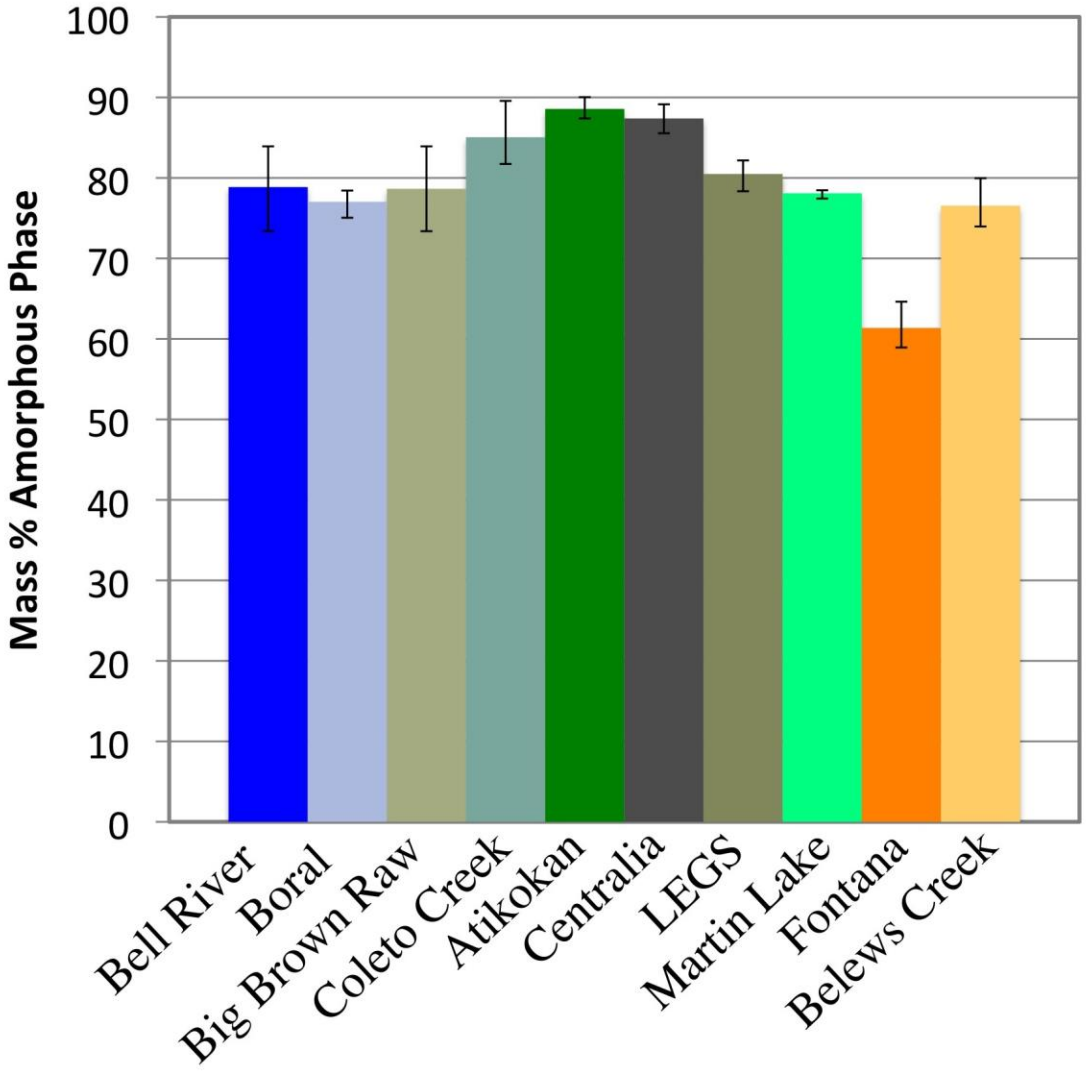

Figure 4.1: Bulk amorphous content of the fly ashes as calculated by quantitative x-ray powder diffraction with uncertainties expressed as a ± 1s for n=3.

It has also been reported in the literature that the location of the maximum of the amorphous phase hump is indicative of the composition of the glassy phases and that a higher location of the 2θ maximum indicates less reactive glass (Kilgour and Diamond 1987). The location of the amorphous hump maximum can be read from the XRD scans, which are shown in Appendix A.

4.1.12 SiO_2/Al_2O_3 ratios

Previous work has suggested optimum relationships between the major constituent elements or oxides in geopolymer cements for the best geopolymer reaction, which ranged from 3.3 - 4.5 (Davidovits 1982; Barbosa, MacKenzie, and Thaumaturgo 2000; Rowles and O'Connor 2003; Duxson et al. 2005; Fletcher et al. 2005; Duxson, Mallicoat, et al. 2007; Chindaprasirt et al. 2012). The method for calculating these ratios is to subtract the crystalline portion from the bulk oxide analysis and to consider only the amount of the elements or oxides in the amorphous phase. For example, Davidovits recommended a SiO_2/Al_2O_3 of 4.0 in defining geopolymer materials in his 1982 patent. The molar ratios of SiO_2/Al_2O_3 calculated for each of the ten fly ashes in the study presented herein are shown in Table 4.11. Based on the recommendations from the literature, the fly ashes with SiO_2/Al_2O_3 between 3.3 and 4.5 would be the most reactive: these include Atikokan, Bell River, Coleto Creek, LEGS, and Martin Lake. Further discussion of this topic is given in the next chapter with the reactivity results.

Table 4.11: Molar ratio of silica to alumina in the fly ashes after subtraction of the crystalline components from the bulk chemical analyses

Fly Ash	SiO_2/Al_2O_3
Atikokan	3.79
Belews Creek	4.99
Bell River	3.75
Big Brown Raw	4.84
Boral Class C	3.03
Centralia	5.52
Coleto Creek	3.64
Fontana	7.2
LEGS	4.24
Martin Lake	4.29

4.2 MULTISPECTRAL IMAGE ANALYSIS (MSIA)

The fly ashes were studied using multispectral image analysis (MSIA) to determine the mineral and glassy phase composition and distribution. X-ray maps of silicon, aluminum, calcium, iron, sodium, magnesium, and potassium were collected for each fly ash for use in MSIA. Additional elements of interest included oxygen, sulfur, and titanium, which were collected but not used for MSIA.

One of the most critical problems when processing digital microscope images and performing MSIA is the rescaling of images by the digital image processing software, both in the microscope and during later processing. Unless avoided or rigorously accounted for, rescaling leads to false expression and subsequently an inconsistent interpretation of the element intensities and approximate concentration at each pixel. In this work, the rescaling was rigorously monitored, as discussed next.

Many microscope software programs rescale the data such that it is visible to the eye when displayed on a monitor but do not provide information on how they were

rescaled. Monitors display 8 bits of color for each channel, which means that each pixel can have a value between 0 and 255 for each color (red, green, blue), resulting in a 24-bit color spectrum. In this work, the x-ray map pixel values collected for major constituents were on the order of 0-70 and for minor constituents were on the order of 0-10 or less; in the former case, the higher value pixels can be seen when displayed on the 0-255 scale, but for the lower intensities and in the latter case, the entire image appears black when displayed on the 0-255 scale. To counteract this, the data collection software might scale the data to visible values, but without giving the scaling factor. It is clear that when the images are stacked using random scaling factors, the visible colors cannot be compared since the ratios of signal from each channel are different. In this work, to avoid this problem, 16-bit tiff images were the preferred data type since they preserved pixel values of raw intensity counts. The microscope manufacturer confirmed that images saved as text files were matrices of the raw data, and Paul Stutzman (personal communication) confirmed that the pixel values of the data saved as 16-bit tiff files were the same as for when the images were saved as text files. Therefore, all data presented were saved as 16-bit tiff files and modified as needed to be visible on the screen.

The first step of MSIA was to pre-process the raw data to make the particle edges more clear and to smooth the intensities in individual particles. First, the image type was changed from 16-bit to 8-bit, preserving the true pixel intensity values, using MATLAB to read in and output the images. This saved space since the file sizes were smaller, and it meant that the true pixel values could be displayed in ImageJ. When 16-bit files were used, ImageJ rescaled the display image, causing confusion on the actual intensities. The display image is merely how the image is displayed, so no data values were rescaled, but it caused user confusion and was, thus, avoided. In the 16-bit to 8-bit conversion, all pixel values were preserved. In nearly every case, the data were smoothed using a

median filter with a radius of 1 pixel. The program inspected the surrounding pixels to the pixel in question at a radius specified by the user. The median value from the surrounding pixels was used to replace the pixel in question. The median filter preserves edge definition while smoothing the image. The filters are fully explained in ImageJ documentation[18]. Another step that was used on many of the fly ashes was to remove the low-end noise pixels from the images. Particularly in maps of elements that were low in concentration, the resolution of signal to background noise was often low, so it was useful to remove the background. Frequently, this occurred in the parts of the image that were known to only contain carbon because they were the epoxy void space between particles. This operation was completed using MATLAB and was analogous to a "find and replace" function: MATLAB found pixels with values below the operator-defined value and replaced them with the value 0. This aided in the segmentation process.

After the raw images were pre-processed, Multispec was used to stack the images virtually and to classify the pixels to phases. An example of this process is given in Appendix B and is described here. Only the maps that were necessary for the segmentation process were used. In some cases, very low concentration elements were left out of the stack due to their poor quality maps. This did not likely change the results, as the very low concentration elements would not have segmented into a separate phase. The phases were defined by selecting training sets of pixels for each of the phases that was identified in a supervised cluster analysis process. The training set is simply a group of pixels (typically selected as a rectangle) that the user defines as a particular phase. For instance, quartz is typically obvious in these specimens, so the user would select a group of pixels in a quartz particle and tell the program "this is quartz" by naming the training set "quartz". The process is repeated for all of the different phases

[18] http://rsbweb.nih.gov/ij/docs/index.html

identified in the image. The pixels in the entire image are then compared to each of the training sets to determine which phase they belong to. The training sets were manually selected. The other type of cluster analysis, unsupervised clustering, required the operator to select the number of expected phases; this meant that the operator had to visually inspect the data and determine the number of phases. Since this step of visual inspection was also part of the supervised cluster analysis, the supervised method was used, which allowed the most operator control.

Once the training classes were selected for each image set, the Fisher linear likelihood method was used for pixel phase assignment. This is one of the methods recommended by Lydon (2005), and it resulted in the best phase classification for these data sets when compared to other methods that Lydon also recommended, which were the minimum Euclidean distance and quadratic likelihood methods. A phase assignment image was also output to an image, with pseudo colored pixels representing the phase to which the pixel was assigned. Multispec output information also included the phase name and the percentage of pixels that were assigned to that particular phase. The area percentage data were normalized to remove the measured void space (i.e. the epoxy in which the solid material was mounted). This was accomplished using the equation 4.1:

$$A_2 = \left(\frac{A_1}{1 \quad -0A_v} \right) * 1 0 \qquad \text{Equation 4.1}$$

where A_2 is the phase area in the residue, A_1 is the phase area percent as calculated in Multispec, and A_v is the area of voids as calculated in Multispec.

For each fly ash, the phase composition table, the phase assignment image, and the relative phase amount pie chart are provided in this chapter. Phase amounts (or phase areas) were selected for reporting since they give a representation of the volume of each phase in the material. Bentz and Remond (1997) reported that area is equal to volume for such generally spherical materials, so conversion to volume should be straightforward.

Phase masses are not reported because the density of the phases is needed for this conversion and this information is not known for the glassy phases.

The phase assignment image (also referred to as the phase map) given for each fly ash is not an SEM image. It was generated by Multispec after each pixel in the image stack was assigned to a compositional phase as defined by the researcher. Therefore, the phase map pixels are colored to represent the phase in which they were classified and are based on the SEM data, but are not the direct SEM data.

The average and standard deviation of the phase compositions for each fly ash are shown in tables in each section. Point compositional information was taken for each field of view using a standard-based analysis algorithm built into the EDS detector operating software. Sixty points were analyzed for composition and were matched to their phases by identifying the point's phase in the phase assignment image (as closely as possible). For most phases, at least five points were gathered from points classified into that phase, but if not, this is noted in the table. Five points were used because Chancey et al. (2010) used five points per phase to identify the composition in their prior work. In the work presented herein, the only cases in which points that were classified into a particular phase were not included in the average was if the standard deviation was greater than the average and an obvious outlier could be identified. The outlier was removed and the average and standard deviation recalculated in order to more accurately define classes, but it was not a standard statistical method. Given the inherent compositional variability of the glassy phases in fly ash, variability is to be expected in the analyses.

Also provided in this chapter for each fly ash is phase amount pie chart, which consists of the area data from multispectral image analysis (i.e., the percentage of pixels in each class compared to all pixels in the image area), renormalized to leave out the

voids. The pie chart colors were selected to match the constituent phase from the phase maps.

For aluminosilicate and calcium aluminosilicate phases, the same designations were given to phases across all ten fly ash data sets; designations were based upon the average amounts of each element in the phase and element ratios. Both the amount of the element and the ratio were important to phase segmentation; for example, the aluminosilicate phases all had low calcium but their silicon to aluminum ratios varied. Table 4.12 gives phase designations and ranges of each major constituent element in those phases. Calcium, silicon and aluminum were used to define the aluminosilicate and calcium aluminosilicate phases since these summed to greater than 35 mass % of the fly ash, which, when added to the amount of oxygen (between 30 and 50 % by mass for all phases), made up the majority of the composition. The groupings used for phase designations are presented visually in Figure 4.2, which plots the average for calcium, aluminum, and silicon for each phase, from each fly ash, on a ternary diagram. Each point on the ternary diagram represents the average composition of a clustered phase from each of the fly ashes, and those for which the averages were compositionally similar were given the same A-S or C-A-S designation. An obvious reason for attempting to use the same designation for similar phases across fly ashes is to highlight the phases that apparently appear in multiple ashes, and then assess whether these phases have good or bad reactivity. A second reason for attempting to match phases across fly ashes was due to the limited number of distinct colors available for designating phases. There are few colors from which to choose that are easily discernible by the eye as different, and I wanted to make it easy to identify similar phases across fly ashes.

Table 4.12: Compositions of designated MSIA phases (ranges of elemental mass % are reported for calcium, silicon and aluminum only)

	Phase composition (range of elemental mass%)		
	Calcium	Silicon	Aluminum
A-S 1	< 5	29-32	10-15
A-S 2	< 5	25-33	13-22
A-S 3	< 1.3	21-25	26-29
A-S 4	1.3-2.3	35-44	5-9
C-A-S	32-40	9-11	4
C-A-S 1	32-37	6-12	7-11
C-A-S 2	24-30	9-14	7-10
C-A-S 3	27	16	7
C-A-S 4	26-30	4-14	11-14
C-A-S 5	22-26	18-20	8-10
C-A-S 6	5-9	31-35	5-11
C-A-S 7	6-12	21-30	9-14
C-A-S 8	9-15	21-26	10-14
C-A-S 9	7.3	23-24	16-20

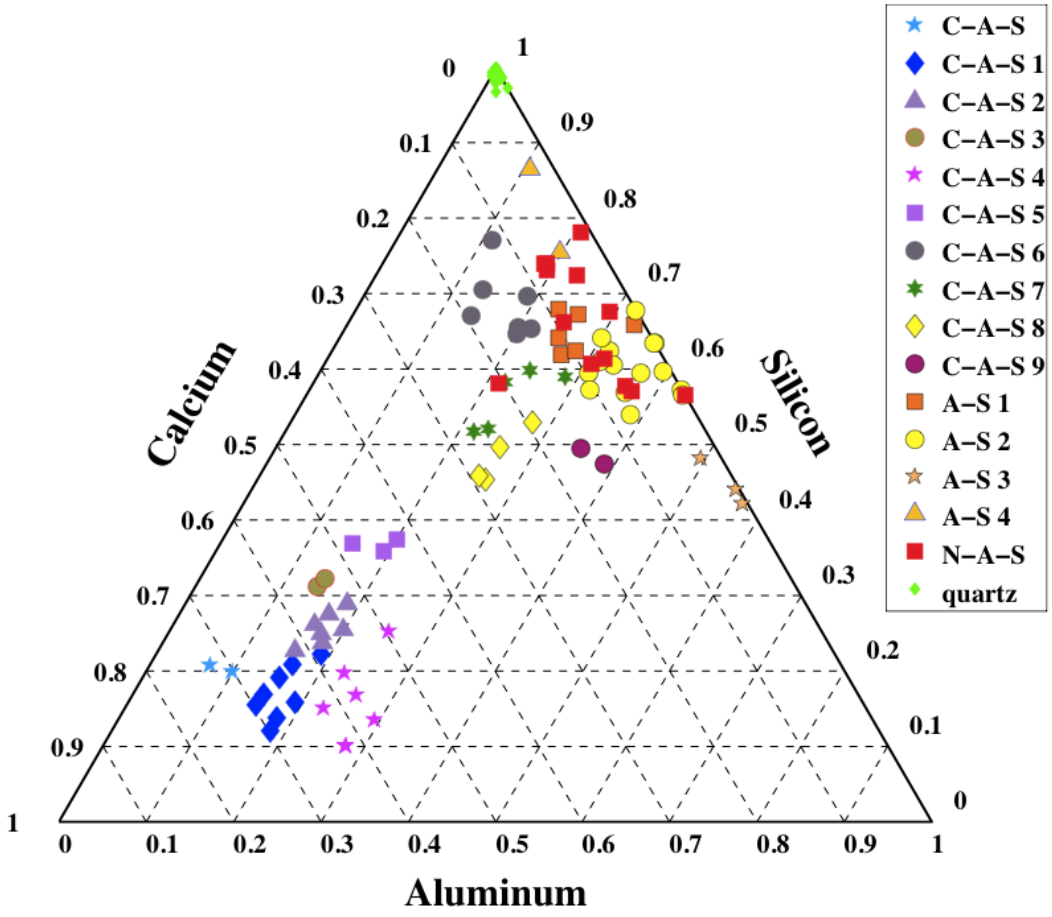

Figure 4.2: Average compositions (mass % Ca-Al-Si) of the calcium-modified aluminosilicate (C-A-S) and aluminosilicate (A-S) phases identified across all samples; plotted on a ternary diagram

The other phases that were commonly identified in the fly ashes included N-A-S (sodium-modified aluminosilicate), K-A-S (potassium-modified aluminosilicate), Fe-rich (an iron-rich phase) which is likely hematite, magnetite or maghemite, and Mg-rich (a magnesium-rich phase) which is probably periclase. The phase designations were selected while selecting the training classes to designate regions that had high concentrations of these elements relative to the rest of the image area; therefore, after the compositions were known, it was determined that the actual composition varied widely across specimens. This point is made so that the reader realizes that for these four

phases, the designation does not mean the same thing from one fly ash to another. The ranges for the calcium, silicon, aluminum, iron, sodium, magnesium, and potassium are given in Table 4.13. Another note is that the Mg-rich phase (when present) was assumed to be crystalline periclase, as identified by RQXRD. The Fe-rich phase was likewise assumed to contain any crystalline iron-containing phase identified by RQXRD.

Table 4.13: Compositions of designated MSIA phases (relevant elements only)

	Phase Composition (element mass %)						
	Calcium	Silicon	Aluminum	Iron	Sodium	Magnesium	Potassium
K-A-S	0-5	30-36	9-12	-	-	-	5-11
N-A-S	0-4*	22-37	9-19	-	3-7	-	-
Mg-rich	3-27	3-10	0-14	-	-	4-47	-
Fe-rich	0-19	0-22	0-10	16-73	-	-	-

*One specimen contained 8 % calcium and was considered an outlier

For each fly ash shown in the following sections, the phases identified in the fly ash are given in the phase assignment image. The compositions of the phases in the specific fly ash are shown in a table in the corresponding section, and they can be compared to the overall phase designations given in Tables 4.12 and 4.13. It is also of note that the colored regions of the images (usually round in shape) are fly ash particles, while the black area is the epoxy in which they are embedded. An attempt was made to include approximately similar amounts of particles for all of the fly ash specimens by using a constant ratio of fly ash to epoxy (2:1, by mass) when making the specimens and a constant magnification for all images.

4.2.2 Class F fly ash: Atikokan

The Atikokan fly ash x-ray maps were processed using a median filter of radius 1 for each of the x-ray maps. The potassium map was excluded from the segmentation process, since it was found to be < 1 mass % by XRF analysis and it did not result in good quality x-ray map data. The single sample of Atikokan fly ash was found to be

composed of aluminosilicate phases intermixed with calcium- and sodium-modified aluminosilicates and crystalline-containing particles. Six phases were identified in the Atikokan fly ash using SEM-MSIA: aluminosilicate (A-S 2); quartz; magnesium-rich, calcium-aluminosilicate (C-A-S 1); sodium aluminosilicate (N-A-S); iron-rich and voids. The compositions of these phases are listed in Table 4.14. Table 4.12 can be used as a reference for the compositional range of each of the phases.

Table 4.14: Phase compositions and uncertainties (s) for a single sample of Atikokan fly ash; a minimum of three measurements was used, else the number of points tested is specified

		Mass % element							
		Ca	Si	Al	Fe	Na	Mg	K	O
C-A-S 1	**average**	**33.3**	**9.7**	**8.0**	**7.6**	**0.5**	**5.2**	**0.0**	**34.09**
	std. deviation	3.6	4.4	2.1	2.2	0.1	2.7	0.0	1.8
N-A-S	**average**	**1.4**	**31.2**	**13.5**	**2.3**	**5.3**	**0.3**	**0.9**	**44.9**
	std. deviation	1.3	4.8	3.9	1.0	1.3	0.4	0.3	1.8
periclase	**single point**	**8.6**	**3.6**	**0.0**	**2.2**	**0.0**	**47.1**	**0.0**	**38.6**
quartz	**average**	**0.5**	**49.0**	**0.4**	**0.0**	**1.0**	**0.0**	**0.0**	**49.5**
	std. deviation	0.0	0.8	0.1	0.0	0.0	0.0	0.0	2.2
Fe-rich	**single point**	**1.5**	**0.0**	**3.9**	**61.2**	**0.8**	**1.1**	**0.0**	**31.5**

The phase map showing the spatial distribution of the phases designated in Table 4.13 is shown in Figure 4.3, and the amount of each phase in the fly ash is depicted in Figure 4.4. The N-A-S phase is the most prevalent at more than 50 area % of the specimen and is colored red. Quartz, shown in green, also makes up a substantial portion of the fly ash, along with a calcium aluminosilicate phase C-A-S 1, shown in blue. The aluminosilicate phase shown in yellow was just one particle with misshapen morphology and vesicular texture in the sample (point compositional analysis was not obtained for this A-S phase). Mg-rich and iron-rich phases were also a very small proportion of the fly ash and were observed included in very small particles.

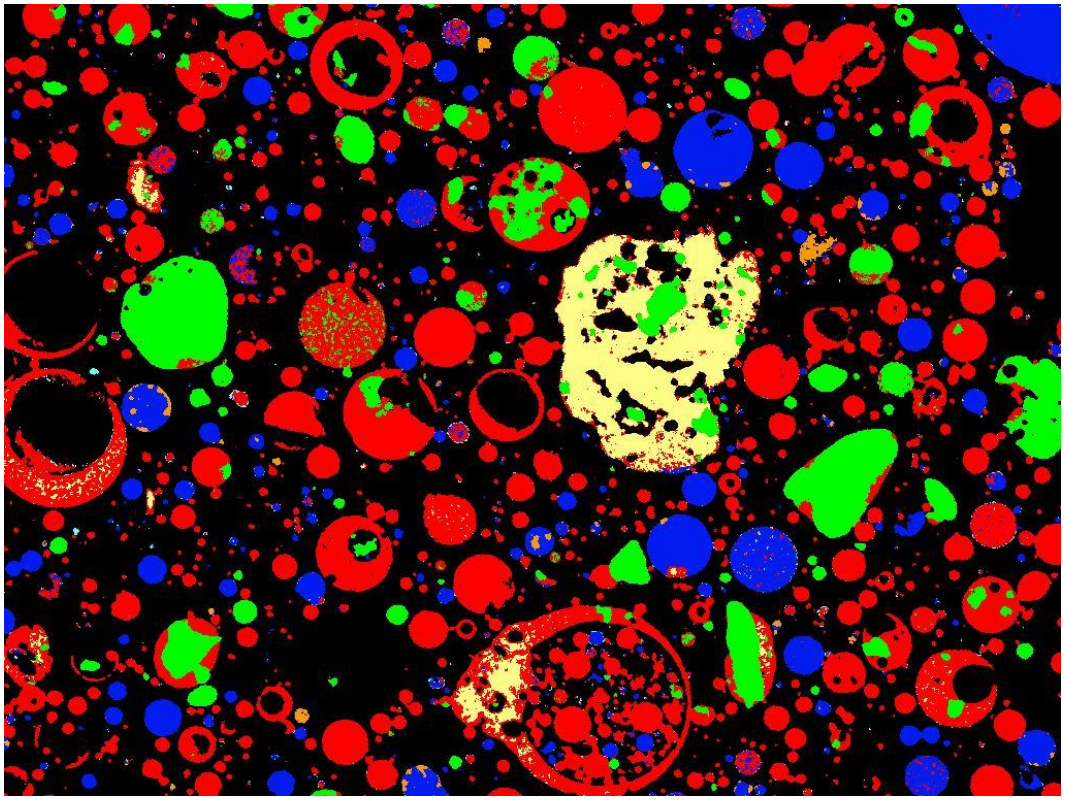

Figure 4.3: Phase assignment image of Atikokan fly ash

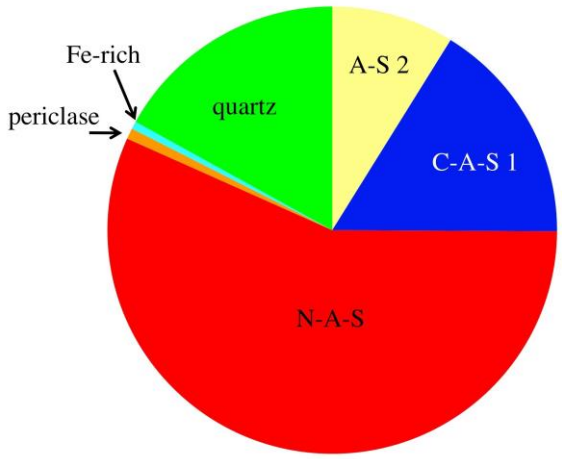

Phase	Area %
A-S 2	8.83
C-A-S 1	16.26
N-A-S	56.63
periclase	0.79
Fe-rich	0.56
quartz	16.94

Figure 4.4: Area distribution of phases in Atikokan fly ash for the single map shown in Figure 4.3

4.2.3 Class F fly ash: Belews Creek

The Belews Creek x-ray maps were pre-processed with a median 1-pixel radius filter. The images were thresholded to eliminate low-end signal using MATLAB. The sodium and magnesium maps were not used in segmentation, since these two elements were not present in sufficient quantity (<1 mass % oxide) to result in good quality mapping data. The Belews Creek fly ash was found to contain four phases: two aluminosilicate phases (A-S 1 and A-S 2), an iron-rich phase, and quartz. Table 4.15 presents the compositions of the phases identified in the fly ash; the phase compositions for this particular fly ash can be compared to the overall compositional range for each phase, which were given in Table 4.12.

Table 4.15: Phase compositions and uncertainties (s) for a single sample of Belews Creek fly ash; a minimum of three measurements was used, else the number of points tested is specified

		Mass % element								
		Ca	Si	Al	Fe	Na	Mg	K	O	Ti
A-S 1	**average**	**0.5**	**30.4**	**15.2**	**2.8**	**0.1**	**0.6**	**1.9**	**47.2**	**1.3**
	std. deviation	0.7	2.5	2.4	2.1	0.2	0.4	0.6	0.7	1.1
A-S 2	**average**	**0.1**	**27.2**	**20.7**	**1.4**	**0.0**	**0.3**	**1.4**	**48.4**	**0.4**
	std. deviation	0.3	2.4	2.8	1.1	0.0	0.4	0.6	2.3	0.5
Fe-rich	**single point**	**0.0**	**5.5**	**1.8**	**60.8**	**0.0**	**0.0**	**0.0**	**31.9**	**0.0**
quartz	**single point**	**0.0**	**46.7**	**1.3**	**0.3**	**0.0**	**0.0**	**0.5**	**50.5**	**0.7**

The phase assignment image for Belews Creek fly ash is shown in Figure 4.5. The area amount of each phase is given in Figure 4.6. It is evident that the two aluminosilicate phases are the main constituents of the material and they were often observed to coexist in the same multi-phase particle. The phases are shown in yellow (A-S 2) and orange (A-S 1) in the pixel assignment image. These two phases were distinguished by their differing Si/Al ratio; A-S 1 had Si/Al of 2, while A-S 2 had Si/Al of 1.35, as shown in Table 4.13. In addition, the particles themselves varied widely in size and morphology. Round, solid and cenosphere particles were observed as well as vesicular, irregularly-shaped particles. Quartz is easily identifiable as green-colored angular particles, and some of the quartz was contained within particles of other composition. There are a few iron-bearing particles in the specimen, distinguished by their aqua color. The iron-containing particles were typically small and round.

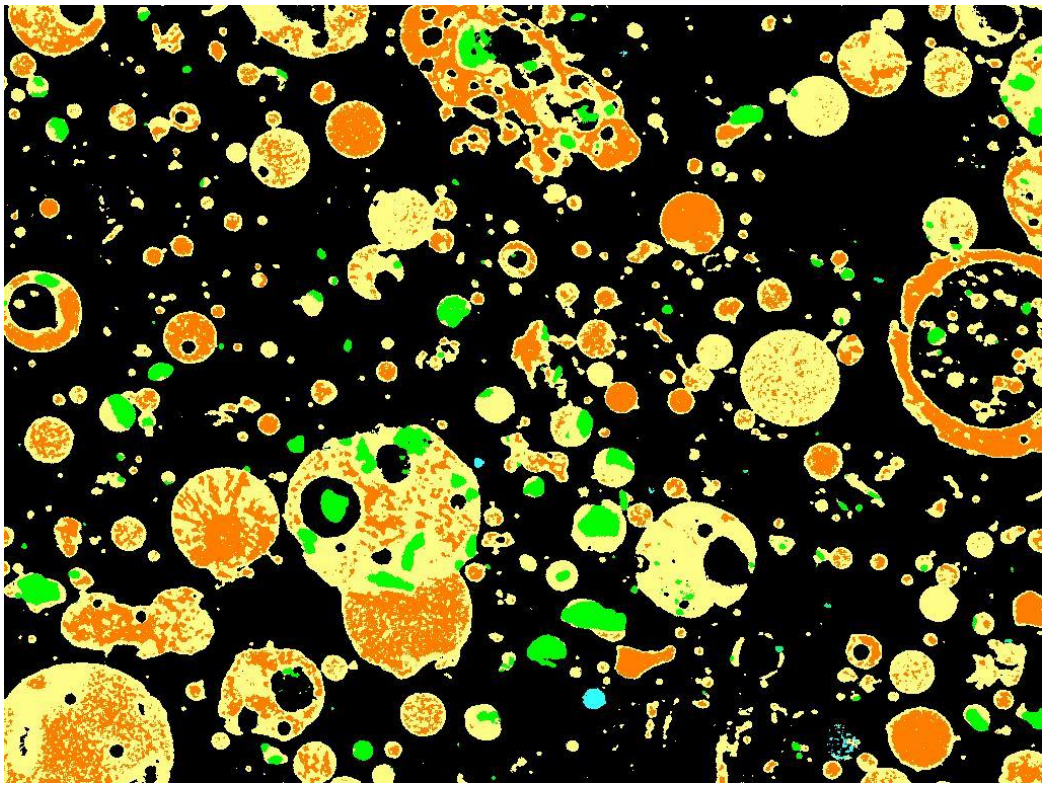

Figure 4.5: Phase assignment image of Belews Creek fly ash

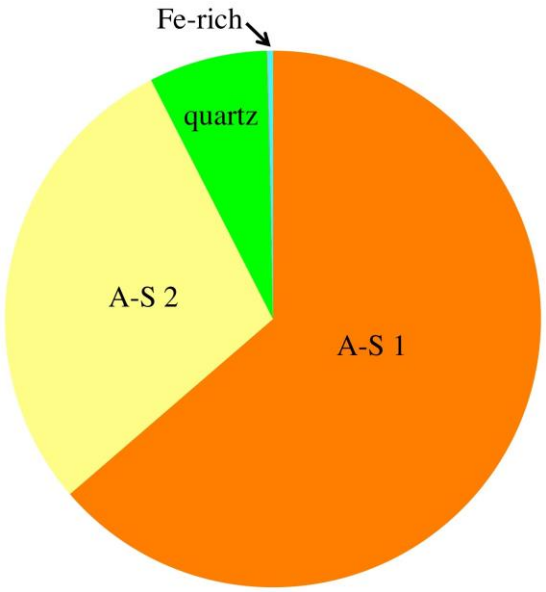

Phase	Area %
A-S 1	63.68
A-S 2	28.81
quartz	7.16
lime	0.08
Fe-rich	0.27

Figure 4.6: Area distribution of phases in Belews Creek fly ash for a single phase map shown in Figure 4.5

4.2.4 Class F fly ash: Big Brown Raw

The Big Brown Raw fly ash x-ray images were all pre-processed using a median filter of radius 1. Each image was also thresholded to remove low-end signal that was deemed to be noise. The sodium map was left out of the segmentation, since sodium oxide was present in less than 1 wt % according to XRF analysis, and the resultant x-ray map was of poor quality. The Big Brown Raw fly ash contained six phases including A-S 2, C-A-S 4, C-A-S 6, Mg-rich, Fe-rich, and quartz. The phase compositions are given in Table 4.16. The phase compositions for the Big Brown fly ash can be compared to the compositional range for each phase, given in Table 4.12.

Table 4.16: Phase compositions and uncertainties (s) for a single sample of Big Brown Raw fly ash; a minimum of three measurements was used, else the number of points tested is specified

		Mass % Element								
		Ca	Si	Al	Fe	Na	Mg	K	O	Ti
A-S 2	**average**	**3.7**	**26.3**	**18.7**	**1.4**	**3.1**	**0.8**	**0.9**	**44.1**	**1.1**
	std. deviation	3.2	2.0	3.4	0.7	1.5	0.9	0.8	1.9	1.6
C-A-S 4	**average**	**29.0**	**9.9**	**11.6**	**5.6**	**0.3**	**4.7**	**0.0**	**36.5**	**2.1**
	std. deviation	6.8	6.7	4.6	2.3	0.7	4.1	0.0	2.2	4.8
C-A-S 6	**average**	**7.0**	**31.4**	**9.6**	**2.3**	**3.6**	**1.6**	**1.1**	**42.9**	**0.7**
	std. deviation	4.5	5.3	4.1	1.2	2.3	1.0	0.9	2.0	0.8
quartz	**average**	**0.7**	**46.6**	**0.8**	**0.9**	**0.8**	**0.0**	**0.5**	**49.5**	**0.2**
	std. deviation	0.9	3.0	1.1	1.3	1.0	0.0	0.8	1.7	0.4

The phase assignment image for Big Brown Raw fly ash is shown in Figure 4.7, and the area amounts of the phases are shown in Figure 4.8. The A-S 2 phase, shown in yellow, was characterized by low calcium and a Si/Al ratio of approximately 1.35, and was approximately 15 % of the image area. The C-A-S 4 phase, shown in bright purple, had high calcium of nearly 30 mass %, with approximately equal amounts of silicon and aluminum, which were near 10 mass %. The C-A-S 4 and C-A-S 6 phases comprised the bulk of the material, summing to around 70 % by volume. The C-A-S 6 phase, shown in gray-purple, contained very high silicon of around 30 mass % with similar calcium and aluminum amounts of near 10 mass % each. The quartz phase comprised approximately 12 % of the image area. The Mg-rich phase, shown in magenta, was not characterized quantitatively for composition in the point analysis, nor was the Fe-rich phase, shown in aqua. These were present in very small amount in the specimen, as can be seen in Figure 4.8.

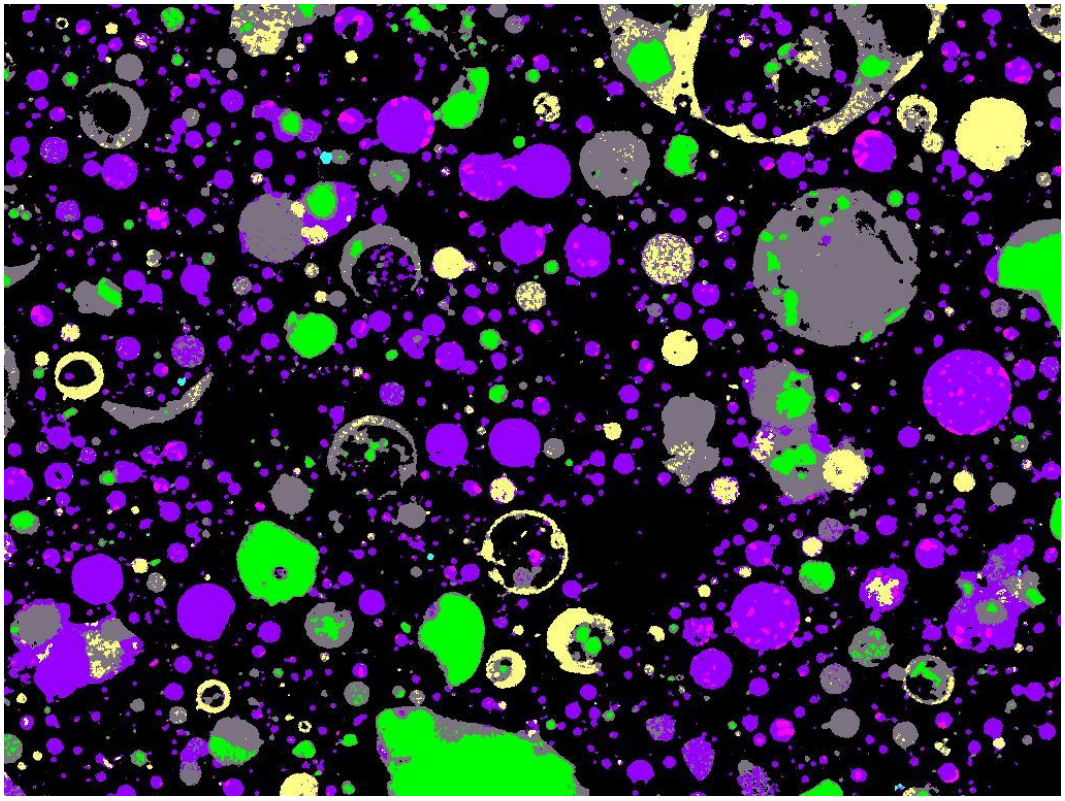

Figure 4.7: Phase assignment image of Big Brown Raw Fly ash

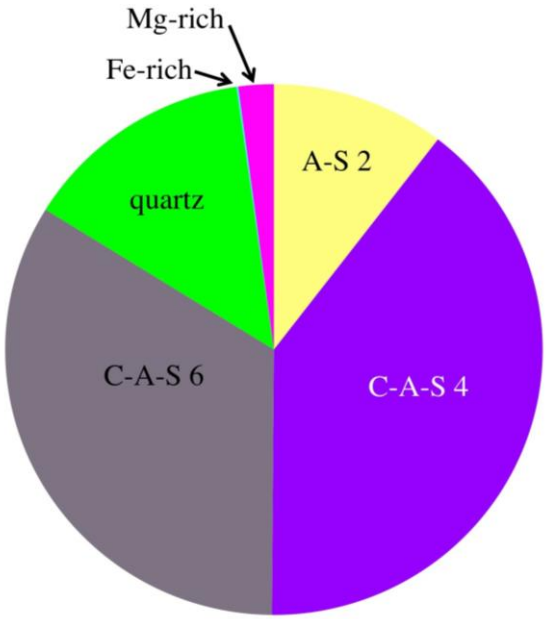

Phase	Area %
A-S 2	10.45
C-A-S 4	39.67
C-A-S 6	33.73
quartz	13.93
Fe-rich	0.11
Mg-rich	2.13

Figure 4.8: Area distribution of phases in Big Brown Raw fly ash for a single phase map shown in Figure 4.7

4.2.5 Class F fly ash: Centralia

The x-ray images for the Centralia fly ash were all pre-processed with a median filter of radius 1. They were also thresholded to remove low-end noise using MATLAB. The iron x-ray map was smoothed using a median filter of radius 3 and turned into a binary map to effectively classify the iron-containing particles. The Centralia fly ash consisted of six phases: an aluminosilicate phase (A-S 2), a calcium-aluminosilicate phase (C-A-S 2), a sodium-aluminosilicate phase (N-A-S), an iron-rich phase, a magnesium-rich phase and quartz. The phase compositions for the single data set collected for Centralia fly ash are shown in Table 4.17; the phase compositions for the Centralia fly ash may be compared to the compositional ranges for each phase given in Table 4.12.

Table 4.17: Phase compositions and uncertainties (s) for a single sample of Centralia fly ash; a minimum of three measurements was used, else the number of points tested is specified

		Mass % Element								
		Ca	Si	Al	Fe	Na	Mg	K	O	Ti
A-S 2	**average**	**2.6**	**28.5**	**14.6**	**3.5**	**3.8**	**1.2**	**3.1**	**42.4**	**0.3**
	std. deviation	2.4	3.5	3.9	1.7	1.2	0.9	1.2	1.0	0.4
C-A-S 2	**average**	**28.4**	**14.2**	**8.8**	**5.7**	**0.3**	**4.3**	**0.0**	**35.6**	**1.7**
	std. deviation	5.8	6.3	3.9	2.0	0.5	1.9	0.0	1.8	3.3
N-A-S	**average**	**3.5**	**34.9**	**8.8**	**3.2**	**3.0**	**1.0**	**2.5**	**43.0**	**0.1**
	std. deviation	7.7	8.1	2.1	3.1	1.0	1.1	1.1	3.2	0.3
Fe-rich	**average of 2 points**	**18.9**	**11.1**	**7.7**	**24.7**	**1.5**	**1.3**	**0.6**	**33.9**	**0.3**
quartz	**average**	**0.0**	**50.2**	**0.2**	**0.2**	**0.1**	**0.0**	**0.1**	**49.2**	**0.0**
	std. deviation	0.0	0.8	0.6	0.4	0.2	0.0	0.3	0.6	0.0

The phase assignment image for Centralia fly ash is shown in Figure 4.9, and the amount of each phase is depicted in Figure 4.10. The A-S 2 phase, shown in yellow, had a small amount of calcium with a Si/Al ratio of approximately 2 and made up a large portion of the fly ash. The C-A-S 2 phase, shown in lavender, contained around 30 mass % calcium and smaller amounts of silicon and aluminum, around 14 mass % and 9 mass %, respectively. The N-A-S phase, shown in red, contained a small amount of calcium and a small amount of sodium (approximately 3 mass % each), with around 35 mass % silicon and around 10 mass % aluminum. These three phases made up around 80 % of the total fly ash by area as depicted in Figure 4.10, while the iron-rich phase, magnesium-rich phase, and quartz made up the remainder. The tiny portion of Mg-rich phase, shown in magenta, was not measured quantitatively, but the iron-rich phase, shown in aqua, was a blend of many elements with approximately 25 mass % iron, calculated from an average of two samples.

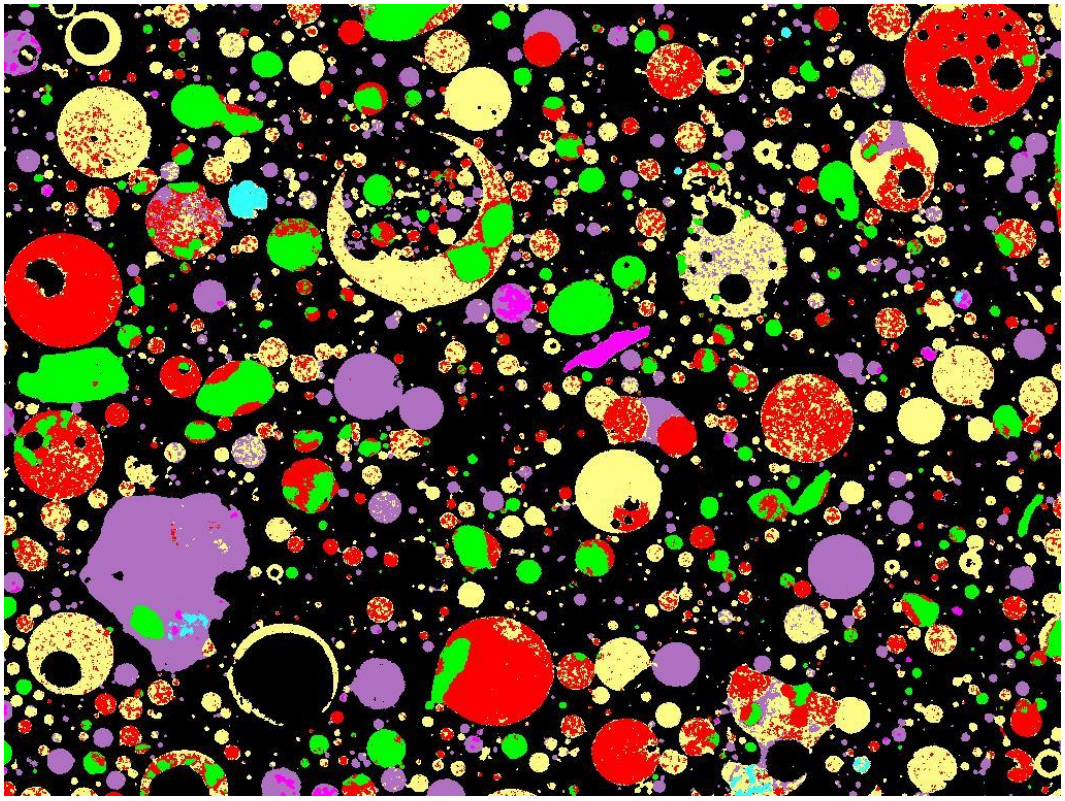

Figure 4.9: Phase assignment image of Centralia fly ash

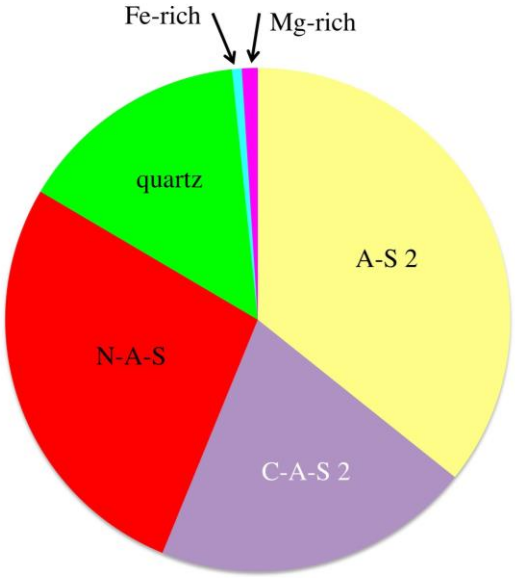

Phase	Area %
A-S 2	35.75
C-A-S 2	20.41
N-A-S	27.33
quartz	14.86
Fe-rich	0.63
Mg-rich	1.01

Figure 4.10: Area distribution of phases in Centralia fly ash for a single phase map shown in Figure 4.9

4.2.6 Class F fly ash: Coleto Creek

The Coleto Creek fly ash maps were smoothed using a median filter of radius 1. All of the maps required thresholding to remove noise. The seven maps collected were used in the segmentation process. The Coleto Creek fly ash contained eight phases including an aluminosilicate (A-S 2), three calcium-aluminosilicates (C-A-S 1, C-A-S 5, and C-A-S 7), a potassium-aluminosilicate, an iron-rich phase, periclase, and quartz. The phase compositions are given in Table 4.18 for the single data set collected for the fly ash. The phase compositions for the Coleto Creek fly ash can be compared to the compositional ranges for each phase using Table 4.12.

The phase assignment image is shown in Figure 4.11, and the relative amounts of each phase are given in Figure 4.12. The A-S 2 phase, shown in yellow, contained minimal calcium and had a Si/Al ratio of approximately 1.6. The C-A-S phase had similar amounts of calcium and silicon around 20 mass %, with approximately half as

much aluminum. The C-A-S 1 phase, shown in blue, contained over 30 mass % calcium with similar amounts of silicon and aluminum of around 8 mass % each. The C-A-S 5 phase, shown in bright lavender, had a high amount of silicon at around 30 mass % with similar amounts of calcium and aluminum, near 10 mass % each. The C-A-S 7 phase, shown in dark green, contained around 30 mass % silicon, 12% aluminum and only 8 % calcium. The iron-rich phase, shown in aqua, contained mainly iron with small amounts < 5% calcium, silicon, and aluminum. The quartz phase shown in green consisted of silicon and oxygen, with a trace of aluminum.

Table 4.18: Phase compositions and uncertainties (s) for a single sample of Coleto Creek fly ash; a minimum of three measurements was used, else the number of points tested is specified

		Mass % Element								
		Ca	Si	Al	Fe	Na	Mg	K	O	Ti
A-S 2	**average of 2 points**	**1.9**	**31.0**	**19.2**	**1.0**	**0.0**	**0.5**	**0.3**	**45.5**	**0.6**
C-A-S 1	**average**	**35.7**	**7.9**	**7.7**	**8.2**	**0.0**	**3.2**	**0.0**	**35.2**	**1.3**
	std. deviation	3.5	4.0	2.6	3.2	0.0	1.6	0.0	1.0	0.8
C-A-S 5	**average**	**21.8**	**19.2**	**10.3**	**5.4**	**0.0**	**3.4**	**0.0**	**38.6**	**1.3**
	std. deviation	5.9	7.8	3.5	1.4	0.0	1.0	0.0	2.2	1.4
C-A-S 7	**average**	**7.8**	**29.1**	**11.8**	**4.4**	**0.9**	**1.8**	**0.8**	**42.7**	**0.8**
	std. deviation	6.0	4.0	3.6	1.5	0.7	0.6	0.7	1.9	0.6
K-A-S	**single point**	**5.4**	**30.4**	**11.8**	**2.3**	**0.8**	**1.3**	**5.1**	**42.9**	**0.0**
Fe-rich	**average**	**4.6**	**2.1**	**2.1**	**61.3**	**0.0**	**0.5**	**0.0**	**29.3**	**0.2**
	std. deviation	3.3	1.1	1.1	6.9	0.0	0.6	0.0	1.1	0.3
quartz	**average**	**0.0**	**49.9**	**0.3**	**0.0**	**0.0**	**0.0**	**0.0**	**49.8**	**0.0**
	std. deviation	0.0	1.1	0.4	0.0	0.0	0.0	0.0	1.0	0.0

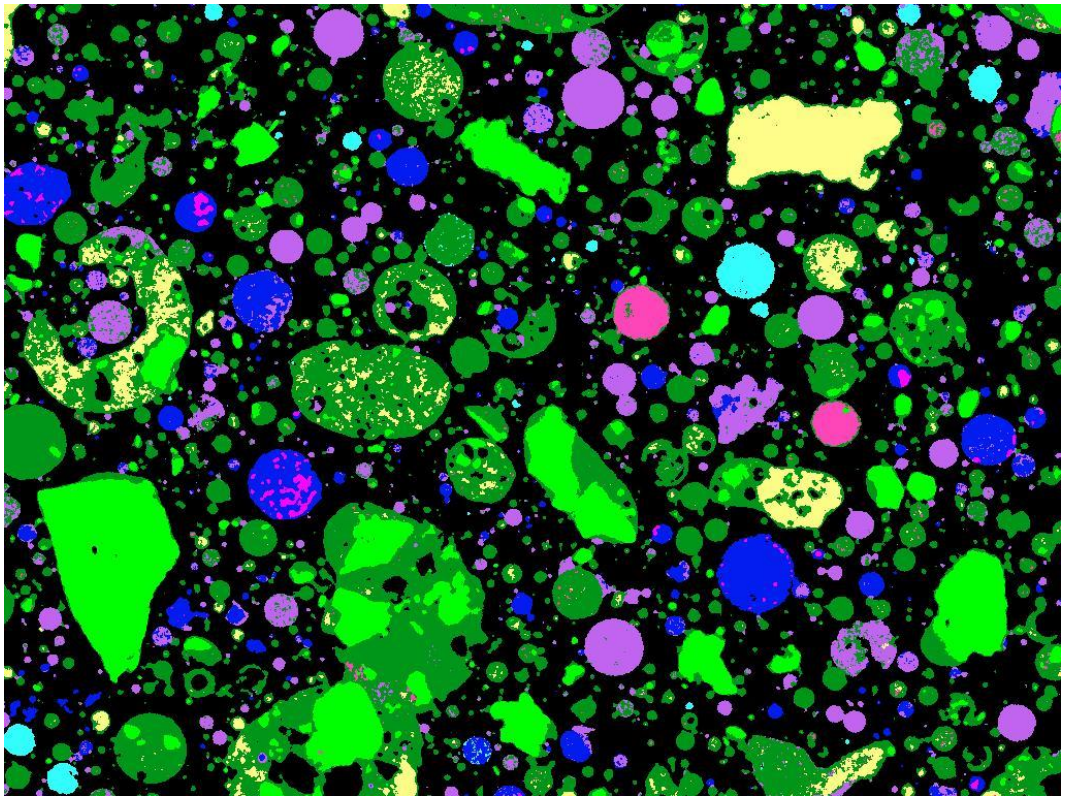

Figure 4.11: Phase assignment image of Coleto Creek fly ash

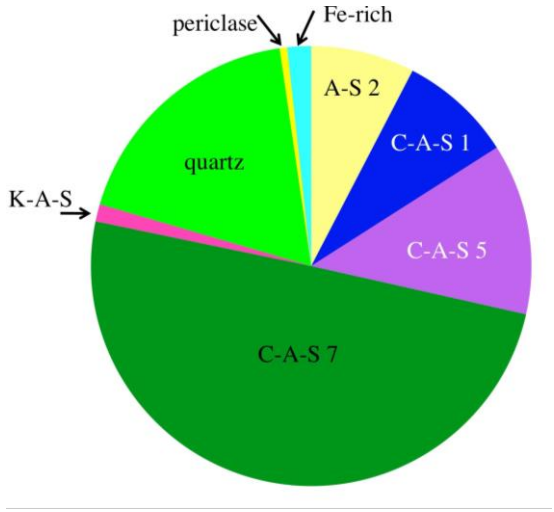

Phase	Area %
A-S 2	7.62
C-A-S 1	8.34
C-A-S 5	12.57
C-A-S 7	49.74
K-A-S	1.28
quartz	18.17
periclase	0.55
Fe-rich	1.74

Figure 4.12: Area distribution of phases in Coleto Creek fly ash for a single phase map shown in Figure 4.11

4.2.7 Class F fly ash: Fontana

The Fontana fly ash composition was relatively simple, containing few phases. The data were pre-processed with a median filter of radius 1. Sodium, magnesium, and potassium were left out of the phase analysis since they were present in very small quantities. The phases were identified as two aluminosilicate phases (A-S 1 and A-S 2), quartz, a high-calcium phase (most likely lime), and an iron-rich phase. The compositions of the phases are given in Table 4.19; the phase compositions for the Fontana fly ash may be compared to the compositional ranges for each phase given in Table 4.12.

Table 4.19: Phase compositions and uncertainties (s) for a single sample of Fontana fly ash; a minimum of three measurements was used, else the number of points tested is specified

		Mass % Element								
		Ca	Si	Al	Fe	Na	Mg	K	O	Ti
A-S 2	**average**	**3.2**	**27.8**	**17.8**	**1.4**	**0.1**	**1.0**	**0.3**	**46.9**	**1.5**
	std. deviation	2.4	1.8	2.0	0.4	0.2	0.4	0.5	0.9	1.9
A-S 1	**average**	**4.1**	**31.6**	**10.9**	**3.5**	**0.7**	**1.0**	**2.2**	**45.5**	**0.5**
	std. deviation	5.2	6.7	2.6	5.8	0.9	1.0	3.3	2.8	0.5
quartz	**average**	**0.0**	**48.3**	**0.4**	**0.0**	**0.0**	**0.0**	**0.0**	**51.4**	**0.0**
	std. deviation	0.0	0.6	0.7	0.0	0.0	0.0	0.0	0.2	0.0
"lime"	**single point**	**38.0**	**9.7**	**3.9**	**1.9**	**0.0**	**0.6**	**0.0**	**37.2**	**7.6**
Fe-rich	**single point**	**0.0**	**1.9**	**0.7**	**66.9**	**0.0**	**0.0**	**0.0**	**30.6**	**0.0**

The phase assignment image is shown in Figure 4.13, and the amount of each phase is shown in Figure 4.14. The two major components of the fly ash were the two aluminosilicate phases A-S 1 and A-S 2, identified by their differing Si/Al ratios. The mullite, which was calculated to be present at 20 mass % in Rietveld analysis was assumed to be contained within the particles of the two A-S phases that were identified. These phases were widespread throughout the sample with many particle sizes and morphologies. Quartz was identified by its strong silicon intensities, as were iron-rich particles, likely hematite (use XRD results for phase). The total iron-containing phases amounted to 1.7 area % in just a few particles. Anhydrite and lime, present in very small quantities, were not observed by MSIA. A phase designated "lime" in the training class selection process was noted in MSIA, but it also contained silicon and aluminum impurities and is not actually lime but a high-calcium phase (see Table 4.19).

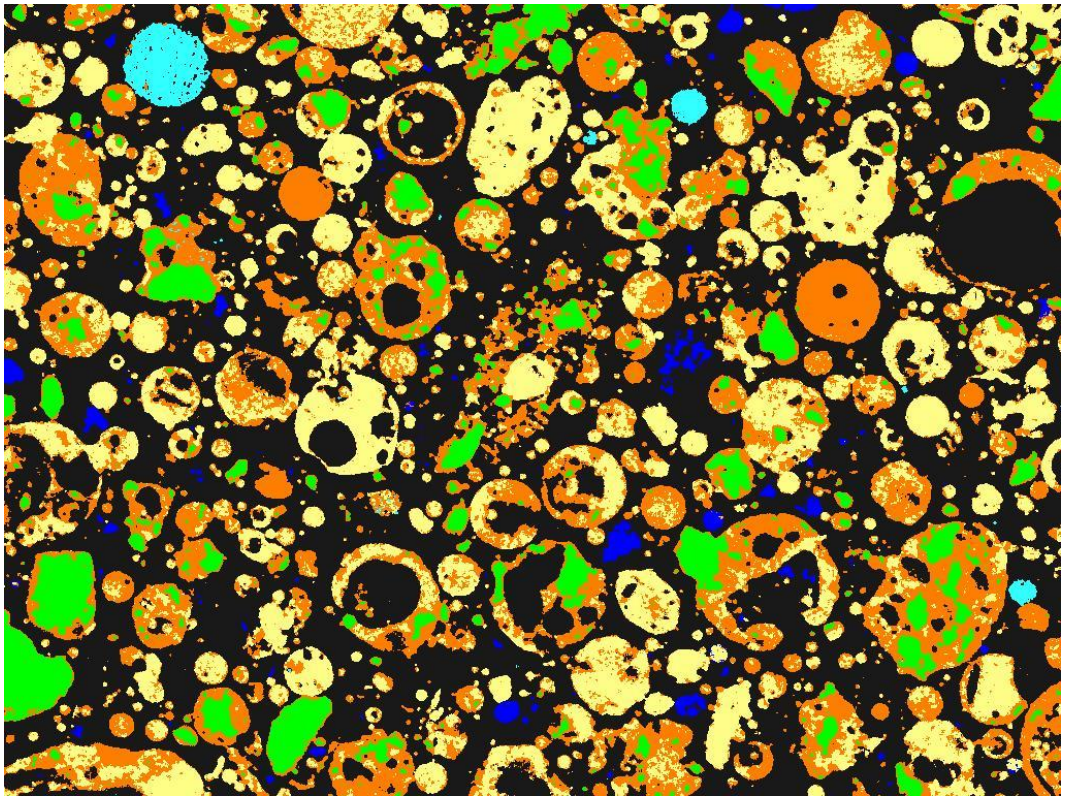

Figure 4.13: Phase assignment image of Fontana fly ash

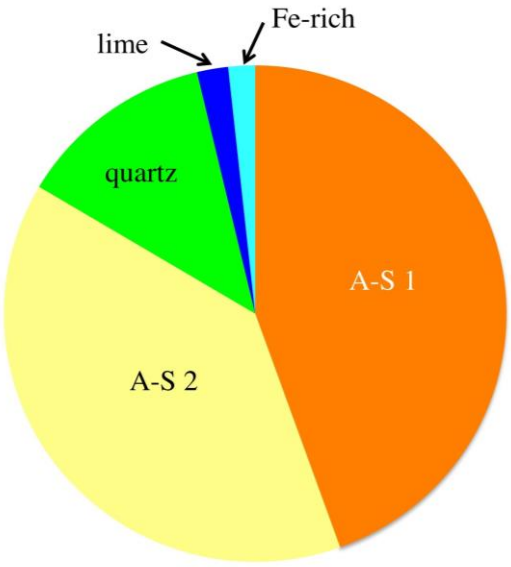

Phase	Area %
A-S 1	44.51
A-S 2	39.03
quartz	12.74
lime	2.01
Fe-rich	1.72

Figure 4.14: Area distribution of phases in Fontana fly ash for a single phase map shown in Figure 4.13

4.2.8 Class F fly ash: LEGS

The LEGS fly ash x-ray maps were pre-processed using a median filter of radius 1. The low-end signal was thresholded using MATLAB for each map. All seven of the standard maps were used in the segmentation process. Eight phases were identified in the fly ash including five calcium-aluminosilicates, quartz, an iron-rich phase, and periclase. The compositions of the phases measured quantitatively using point analysis are given in Table 4.20; the phase compositions for the LEGS fly ash may be compared to the compositional ranges for each phase given in Table 4.12.

Table 4.20: Phase compositions and uncertainties (s) for a single sample of LEGS fly ash; a minimum of three measurements was used, else the number of points tested is specified

		Mass % Element								
		Ca	Si	Al	Fe	Na	Mg	K	O	Ti
C-A-S	**average**	**40.2**	**11.5**	**3.9**	**6.5**	**0.0**	**1.5**	**0.0**	**34.3**	**0.8**
	std. deviation	4.4	6.0	1.7	5.6	0.0	1.4	0.0	1.2	0.5
C-A-S 2	**average of 2 points**	**29.2**	**16.1**	**10.3**	**3.8**	**0.0**	**3.9**	**0.0**	**36.3**	**0.4**
C-A-S 5	**average**	**25.6**	**19.7**	**8.1**	**4.8**	**0.0**	**3.6**	**0.0**	**37.0**	**1.1**
	std. deviation	3.6	4.7	2.6	2.3	0.0	0.7	0.0	1.6	0.9
C-A-S 7	**average**	**9.6**	**28.5**	**10.7**	**6.4**	**0.4**	**2.3**	**0.5**	**41.0**	**0.7**
	std. deviation	4.7	4.8	3.4	6.0	0.5	2.6	0.7	2.0	0.5
C-A-S 8	**average**	**14.6**	**23.1**	**13.4**	**4.6**	**0.8**	**2.0**	**0.9**	**39.7**	**1.0**
	std. deviation	14.0	9.0	2.8	1.3	0.9	1.0	0.9	3.5	0.9
quartz	**average of 2 points**	**0.0**	**50.2**	**0.0**	**0.0**	**0.0**	**0.0**	**0.0**	**49.8**	**0.0**
Fe-rich	**single point**	**0.8**	**0.6**	**0.0**	**72.5**	**0.0**	**0.0**	**0.0**	**26.1**	**0.0**

The phase assignment image is shown in Figure 4.15, and the amounts of each phase are given in Figure 4.16. The C-A-S phases made up most of the fly ash composition, around 86 %. The C-A-S 7 phase was the most prevalent, followed by C-A-S 8, C-A-S 5, C-A-S and C-A-S 2. All of the C-A-S phases appeared to be present in particles with morphologies approaching aspect rations of 1 (circular morphology). The quartz was present in small amount and noticeably angular particles, while the iron-rich phase was present in small amount primarily in circular particles. Periclase was noted in the MSIA data, but it was not identified quantitatively. It was a very small portion of the fly ash at < 1 area %.

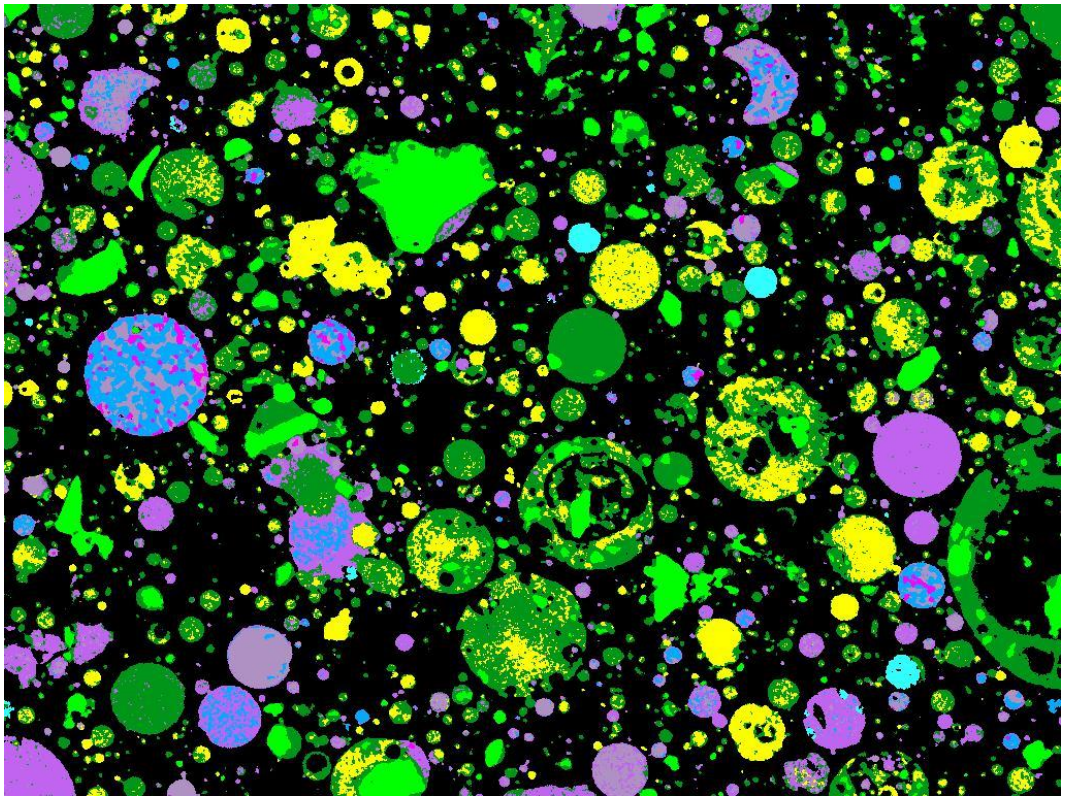

Figure 4.15: Phase assignment image of LEGS fly ash

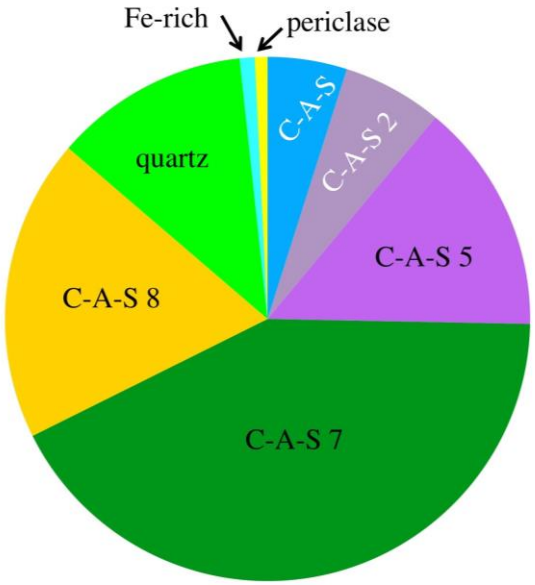

Phase	Area %
C-A-S	4.89
C-A-S 2	6.16
C-A-S 5	14.26
C--AS 7	42.34
C-A-S 8	18.66
quartz	12.00
Fe-rich	0.92
periclase	0.78

Figure 4.16: Area distribution of phases in LEGS fly ash for a single phase map shown in Figure 4.15

4.2.9 Class F fly ash: Martin Lake

The Martin Lake fly ash raw images were pre-processed using a median filter of radius 1. Some of the maps required thresholding, in which the low intensity values were replaced by 0 values using MATLAB. All seven maps collected were used for the segmentation process. The Martin Lake fly ash was found to contain six phases, including an aluminosilicate phase (A-S 2), three calcium-aluminosilicate phases (C-A-S 5, C-A-S 6, and C-A-S 8), iron-rich phase and quartz.

The phase compositions are given in Table 4.21; the phase compositions for the Martin Lake fly ash may be compared to the compositional ranges for each phase given in Table 4.12.The A-S 2 phase had a Si/Al mass ratio of approximately 2, with < 5 mass % calcium. The C-A-S phases contained varied amounts of calcium, aluminum, and silicon. C-A-S 5 contained similar amounts of calcium and silicon with less aluminum, while C-A-S 6 contained a low amount of calcium, high amount of silicon, and a

moderate amount of aluminum. The C-A-S 8 phase contained similar amounts of calcium and aluminum with much higher silicon. The iron-rich phase contained mostly iron (56 mass %), but it also contained around 8 mass % silicon and 4 mass % aluminum. The quartz contained impurities of calcium, aluminum, iron, and potassium.

Table 4.21: Phase compositions and uncertainties (s) for a single sample of Martin Lake fly ash; a minimum of three measurements was used, else the number of points tested is specified

		Mass % Element								
		Ca	Si	Al	Fe	Na	Mg	K	O	Ti
A-S 2	**average**	**4.0**	**32.3**	**16.6**	**3.5**	**0.7**	**1.0**	**1.7**	**39.9**	**0.4**
	std. deviation	3.1	4.9	5.7	1.6	0.6	1.0	0.5	1.0	0.6
C-A-S 5	**average**	**23.4**	**18.8**	**10.1**	**7.5**	**0.1**	**3.9**	**0.3**	**35.1**	**0.7**
	std. deviation	12.0	11.3	2.4	3.0	0.2	1.6	0.7	3.3	0.7
C-A-S 6	**average**	**7.3**	**33.5**	**11.7**	**3.4**	**0.4**	**2.1**	**1.6**	**39.6**	**0.6**
	std. deviation	9.2	9.6	4.0	1.4	0.4	1.7	1.2	3.0	0.6
C-A-S 8	**average**	**15.2**	**24.0**	**13.2**	**5.7**	**0.1**	**3.0**	**0.3**	**36.8**	**1.8**
	std. deviation	7.0	5.5	3.0	2.5	0.2	1.1	0.6	2.6	2.7
Fe-rich	**average of two points**	**3.0**	**8.1**	**4.1**	**55.2**	**0.0**	**1.0**	**0.0**	**28.4**	**0.3**
Quartz	single point	0.7	47.7	4.4	0.6	0.0	0.0	1.3	45.3	0.0

The phase assignment image for Martin Lake fly ash is given in Figure 4.17. The phase amounts are shown in Figure 4.18. It is obvious that the major component of this fly ash is the gray C-A-S 6 phase, which makes up more than half of the fly ash. The phase was present in a wide range of particle sizes and morphologies, although it is noted that some very large, vesicular particles were comprised of this C-A-S phase. The C-A-S 8 phase shown in gold is the second most prevalent phase in the material, followed by the A-S 2 phase shown in light yellow. The C-A-S 8 phase was present in a variety of particle sizes and largely independent of other phases, while the A-S 2 phase appeared in some small particles and also as regions of particles that contained C-A-S 6. The quartz, shown in green, and the C-A-S 5 shown in purple were present in similar amounts. The quartz was scattered throughout the specimen and was sometimes embedded in larger

particles and sometimes present as discrete particles. The iron-rich phase was present in the smallest amount and was noted in small, round particles.

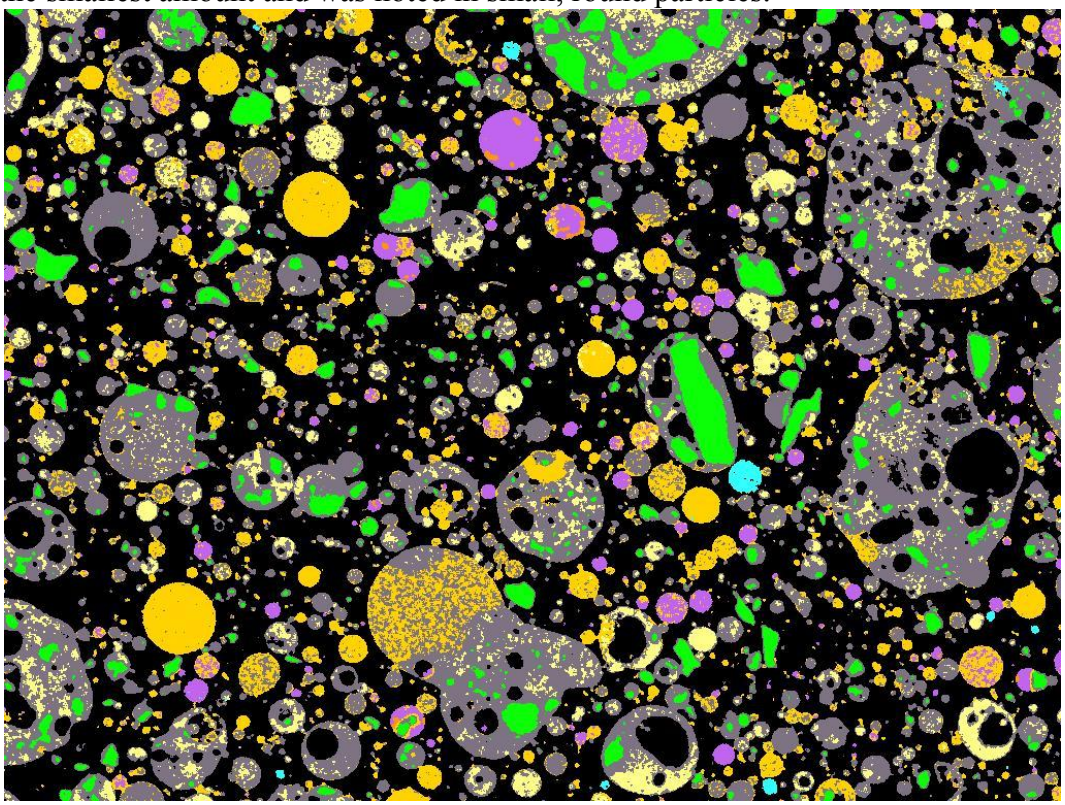

Figure 4.17: Phase assignment image of Martin Lake fly ash

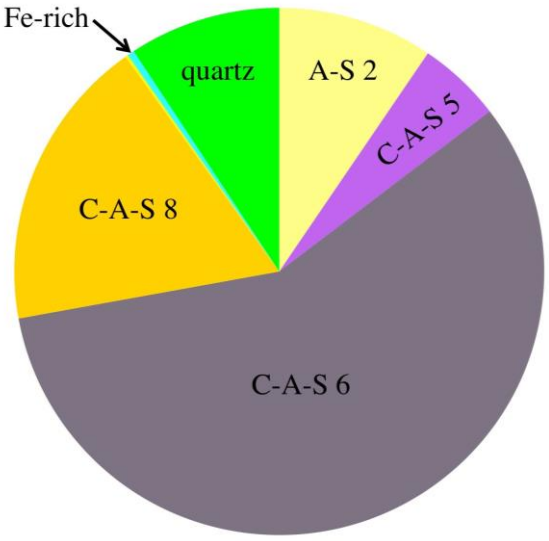

Phase	Area %
A-S 2	9.48
C-A-S 5	5.13
C-A-S 6	57.53
C-A-S 8	18.00
periclase	0.17
Fe-rich	0.43
quartz	9.26

Figure 4.18: Area distribution of phases in Martin Lake fly ash for a single phase map shown in Figure 4.15

4.2.10 Class C fly ash: Bell River

The Bell River fly ash element maps were pre-processed using a median filter of radius 1. They were all thresholded to remove low-end signal using MATLAB. The potassium image was left out due to its low concentration in the specimen and poor data quality for the x-ray map. The Bell River fly ash was a Class C fly ash and had two C-A-S phases, K-A-S, N-A-S, a calcium silicate phase, Mg-rich, quartz, and Fe-rich.

Table 4.22 shows the compositions of phases identified in the Bell River fly ash; the phase compositions for the Bell River fly ash may be compared to the compositional ranges for each phase given in Table 4.12. Eight phases were identified, including two C-A-S phases, K-A-S, N-A-S, calcium silicate, Mg-rich, quartz, and Fe-rich.

Table 4.22: Phase compositions and uncertainties (s) for a single sample of Bell River fly ash; a minimum of three measurements was used, else the number of points tested is specified

		Mass % Element								
		Ca	Si	Al	Fe	Na	Mg	K	O	Ti
C-A-S 1	**average**	**36.0**	**8.7**	**10.6**	**7.1**	**0.0**	**2.4**	**0.0**	**33.1**	**1.4**
	std. deviation	4.5	3.8	2.2	2.5	0.0	1.0	0.0	1.5	2.0
C-A-S 6	**average**	**7.7**	**33.8**	**6.4**	**2.4**	**4.3**	**1.5**	**0.8**	**41.8**	**1.5**
	std. deviation	7.0	8.8	4.5	1.1	1.2	1.5	0.5	2.5	1.5
K-A-S	**single point**	**0.0**	**36.2**	**9.7**	**0.0**	**1.4**	**0.0**	**10.2**	**42.5**	**0.0**
N-A-S	**average**	**3.2**	**29.0**	**15.0**	**1.8**	**6.2**	**0.5**	**1.2**	**42.7**	**0.4**
	std. deviation	2.7	3.4	2.7	1.2	1.1	0.5	0.7	1.9	0.8
calcium silicate	**single point**	**52.4**	**15.2**	**0.6**	**0.0**	**0.0**	**1.0**	**0.0**	**30.8**	**0.0**
Mg-rich	**average**	**26.7**	**9.5**	**13.0**	**5.9**	**0.8**	**6.7**	**0.0**	**35.2**	**1.3**
	std. deviation	4.4	5.5	1.8	1.8	1.2	3.7	0.0	1.7	0.7
quartz	**average**	**0.1**	**50.8**	**0.5**	**0.1**	**0.3**	**0.0**	**0.1**	**48.2**	**0.0**
	std. deviation	0.2	1.3	0.6	0.3	0.7	0.0	0.2	0.8	0.0
Fe-rich	**single point (was classified as N-A-S)**	**7.1**	**8.0**	**4.2**	**45.7**	**1.6**	**2.8**	**0.0**	**30.7**	**0.0**

The phase assignment image for Bell River is given in Figure 4.19 and the amounts of each phase present are shown in Figure 4.20. The phases C-A-S 1, C-A-S 6, and N-A-S made up the majority of the fly ash, and they were all found in particles of many sizes. The morphologies of most of the particles in the Bell River fly ash were circular, although the particles of K-A-S phase were noted as being irregular in shape and contained air voids, exhibiting a vescicular texture. The Fe-rich phase was mostly identified in a few dispersed particles; however, the phase was also erroneously attributed to pixels that should have been classified as voids, such as at the inside edges of N-A-S cenospheres. This was likely due to noise in the image maps. Fe-rich was determined to have been very slightly over-estimated in the image.

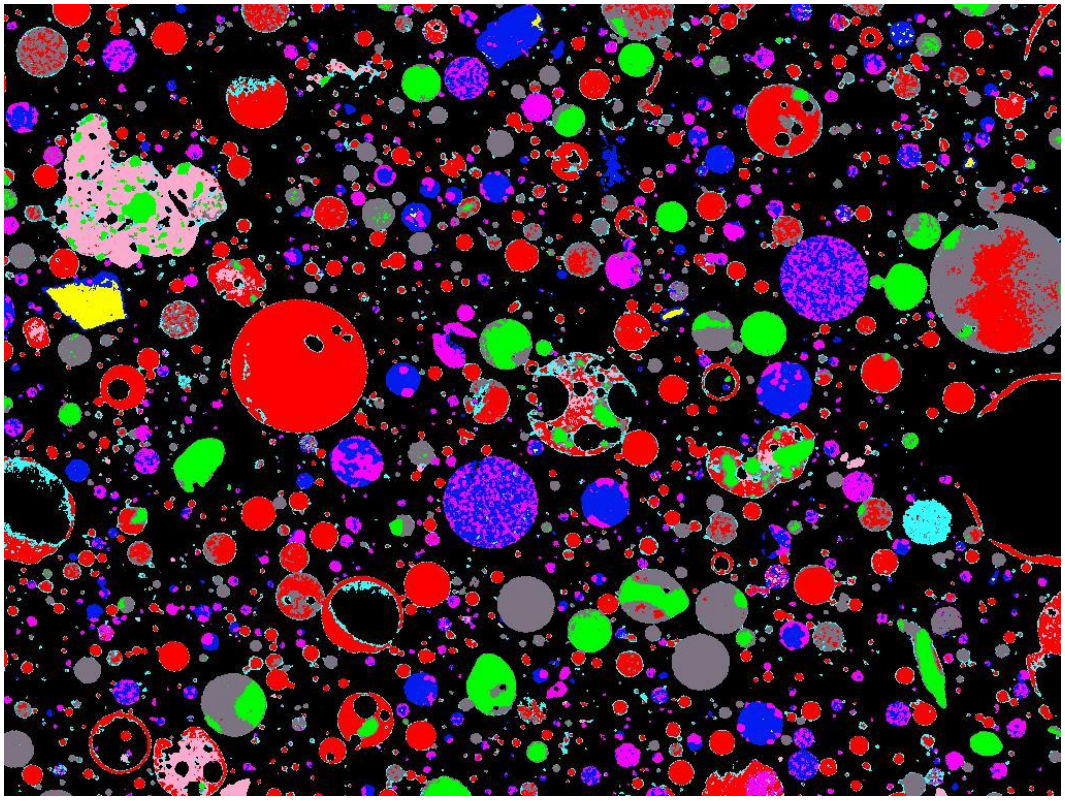

Figure 4.19: Phase assignment image of Bell River fly ash

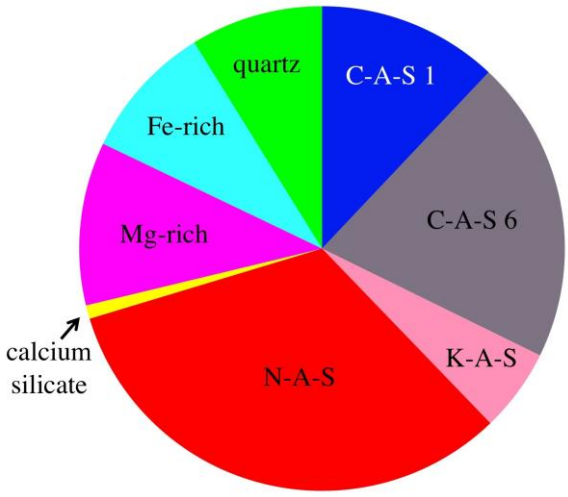

Phase	Area %
C-A-S 1	12.04
C-A-S 6	20.22
K-A-S	5.54
N-A-S	32.51
calcium silicate	0.90
Mg-rich	10.89
Fe-rich	9.06
quartz	8.82

Figure 4.20: Area distribution of phases in Bell River fly ash for a single phase map shown in Figure 4.15

4.2.11 Boral Class C fly ash

The Boral Class C fly ash raw images were pre-processed using a median filter of radius 1. The images were thresholded to remove noise. The potassium map was left out of the segmentation due to its small amount in the fly ash, which resulted in poor quality map data. The Boral Class C fly ash was found to contain five phases: A-S 4, C-A-S 4, N-A-S, N-A-S 2, iron-rich, and periclase.

The compositions of the phases identified in the fly ash are given in Table 4.23; the phase compositions for the Boral Class C fly ash may be compared to the compositional ranges for each phase given in Table 4.12. The A-S 4 phase was of very different composition than other A-S phases in other fly ashes, with a Si/Al ratio of over 8, with approximately 44 % by mass silicon and 5 % by mass aluminum. The C-A-S 4 phase was very high calcium with approximately half the amount of silicon and aluminum (a Si/Al ratio of 1) as A-S 4. The N-A-S phase was low-calcium, but it had one of the highest sodium contents at nearly 6 % by mass. The silicon was approximately 29 % by mass, while the aluminum was approximately 18 % by mass for a Si/Al ratio of 1.6. A second N-A-S 2 phase was identified with much higher silicon and lower aluminum for a Si/Al ratio of 3.8.

Table 4.23: Phase compositions and uncertainties (s) for a single sample of Boral Class C fly ash; a minimum of three measurements was used, else the number of points tested is specified

		Mass % Element								
		Ca	Si	Al	Fe	Na	Mg	K	O	Ti
A-S 4	**average**	**1.4**	**43.5**	**5.3**	**1.8**	**2.6**	**0.0**	**1.8**	**43.1**	**0.6**
	std. deviation	1.5	5.1	4.0	1.1	0.7	0.0	2.0	2.1	1.0
C-A-S 4	**average**	**26.8**	**13.5**	**13.6**	**5.9**	**1.0**	**3.3**	**0.0**	**34.0**	**1.2**
	std. deviation	6.0	6.2	3.9	4.3	1.3	1.3	0.0	2.1	1.2
N-A-S	**average**	**3.1**	**28.8**	**17.9**	**1.7**	**5.9**	**0.5**	**1.0**	**40.6**	**0.5**
	std. deviation	3.1	3.0	2.6	1.1	1.5	0.6	0.2	2.3	0.4
NAS 2	**single point**	**3.8**	**36.4**	**9.6**	**0.9**	**4.2**	**0.0**	**3.0**	**40.6**	**1.5**
quartz	**average**	**0.0**	**52.9**	**0.0**	**0.0**	**0.2**	**0.0**	**0.0**	**46.9**	**0.0**
	std. deviation	0.0	0.4	0.0	0.0	0.4	0.0	0.0	0.4	0.0

The phase assignment image is given in Figure 4.21, and the amount of each phase is presented in Figure 4.22. The A-S 4, C-A-S 4, and N-A-S phases were present in similar amounts and collectively comprised about 90 % of the image area on a void-free basis. The N-A-S 2 and quartz were present in low concentrations, while the iron-rich and periclase phases were nearly indistinguishable due to their low concentrations. The phases were all present in varied particle sizes and morphologies. The N-A-S 2 consisted of a single particle that was irregularly shaped and somewhat large.

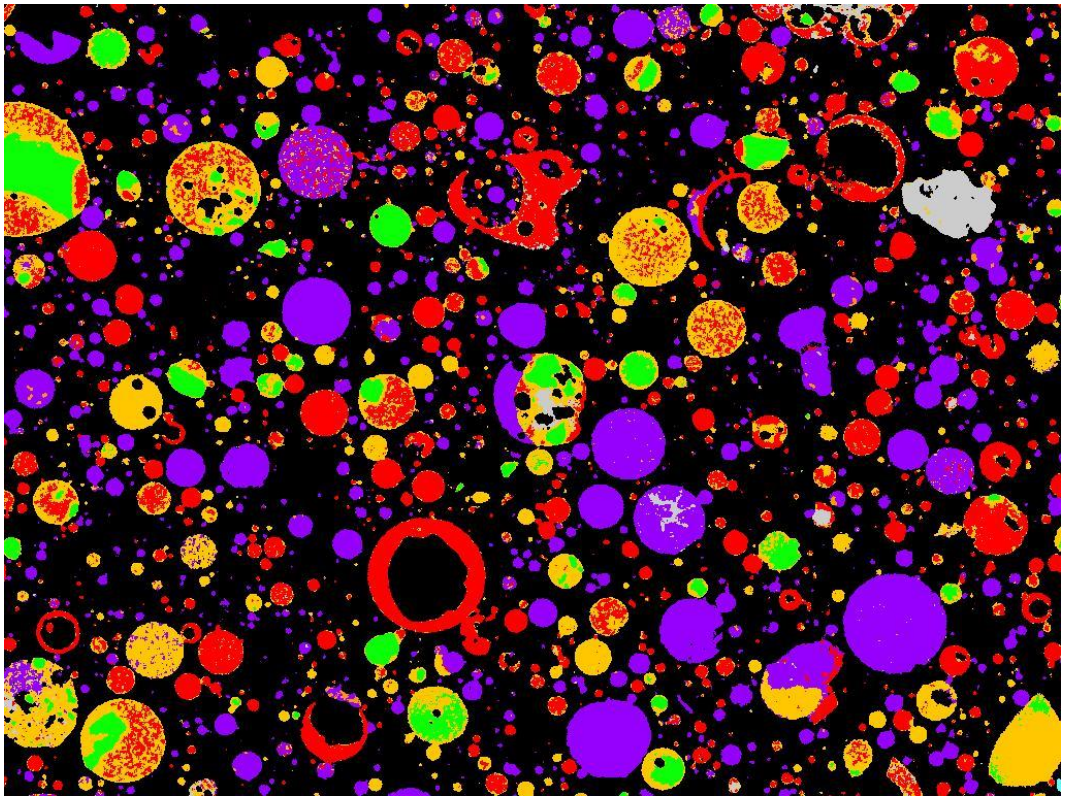

Figure 4.21: Phase assignment image of Boral Class C fly ash

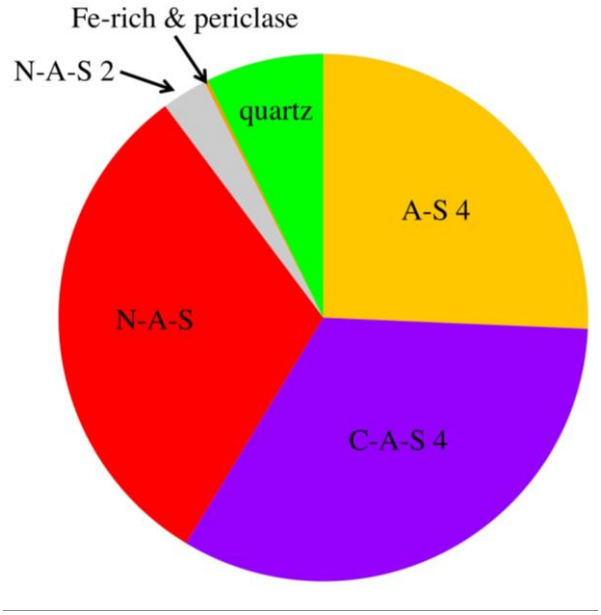

Phase	Area %
A-S 4	25.68
C-A-S 4	32.99
N-A-S	31.14
N-A-S 2	2.76
Fe-rich	0.02
periclase	0.23
quartz	7.18

Figure 4.22: Area distribution of phases in Boral Class C fly ash for a single phase map shown in Figure 4.15

4.2.12 Discussion: MSIA results

The MSIA results characterized the fly ash composition, both glassy and crystalline phases. However, as discussed in Section 4.1, most of the material in the fly ash was in a glassy form. Crystalline phases were often identified in the XRD data by the presence of characteristic peaks but most were quantified at under 1 % by mass, with the exception of quartz. Further, it is unlikely that most crystalline phases in higher amounts would be identified visually, since they often form as finely-disseminated grains within a glassy matrix as micro- or nano-crystalline materials (Hemmings and Berry 1987). Therefore, it is unlikely that such trace materials would be identified in MSIA. Quartz was the only crystalline phase that was identified through MSIA with any reliability due to its distinct inclusions, relatively large grains and unique chemical signature. The remaining crystalline phases were generally unable to be matched to the MSIA phases. Therefore, while the majority of the MSIA phase results are considered glassy phase,

they do contain the crystalline phases that were previously identified through Rietveld quantitative analysis.

4.2.12.1 Oxide analysis and phase identification

There were few observations that could be made to relate the bulk oxide composition and MSIA results. One clear observation from MSIA was that for the two fly ashes with the least amount of calcium, Belews Creek (1 % CaO by XRF) and Fontana (5.6 % CaO by XRF), and as a result the highest silicon and aluminum, the least number of phases were identified in MSIA. Further, they also had few crystalline phases (only mullite, quartz and an iron-bearing crystalline phase of hematite or maghemite), and the amount of mullite in these two very low-calcium fly ashes was much higher than for the other eight fly ashes. Hemmings and Berry (1987) observed that larger particles tend to quench more slowly, allowing time for crystallization, so this result was not surprising since Belews Creek and Fontana were among the three coarsest fly ashes in the study (see Figure 3.1). It has been noted in other work that low calcium content in fly ashes often resulted in a small number of crystalline phases (McCarthy 1987), and this work shows that the same holds true for the glassy phases, i.e. there were a small number of glassy phases in these low-Ca fly ashes.

The C-A-S phases were identified only in the eight fly ashes with highest calcium contents in the study. The CaO contents were between 9-27 % for those ashes. There were not any obvious correlations between the fly ash bulk (CaO) and the specific C-A-S phases formed, however. As in the low-calcium fly ashes, for which there were few phases, there was no obvious correlation in the moderate-to-high calcium and the number of phases identified. Otherwise, for moderate-to-high calcium fly ashes (9-27 mass % CaO as per Table 3.1) no clear trends were observed.

The phase "Fe-rich" was observed in a few dispersed particles for any given fly ash. The microscope operating conditions were not ideal for iron mapping because the accelerating voltage was optimized for the other low energy elements of interest. This meant that the iron was generally only observed in MSIA maps in the particles where it was most concentrated. These particles were assumed to contain the crystalline iron, oxides since the phases such as hematite, maghemite, and magnetite contain around 70 mass % iron, which would exhibit high intensities in the iron maps. Indeed, x-rsy microanalyses of the Fe-rich phase estimated around 70 mass % iron in the LEGS fly ash, and was over 60 mass % iron on average for the Fontana, Coleto Creek, Belews Creek, and Atikokan fly ashes. In the other fly ashes that contained an Fe-rich phase (Bell River, Martin Lake, and Bell River), the iron concentration in the Fe-rich phase was much lower than 60 mass %. This could have been for several reasons. First, the crystalline phase may not have been present in the specific point location where data were collected. Alternately, the iron may have been substituted into a crystalline or glassy phase in sufficient quantity to result in a strong intensity in the x-ray map; substitution into crystalline phases such as mullite and network-former substitution in glasses frequently occurs in fly ash with elemental iron (McCarthy 1987; Hemmings and Berry 1987).

The minor elements magnesium, potassium, and sodium were often dispersed through the cross sections of the ash particles. Through visual observations of the x-ray maps, magnesium was often found within particles that were also high in calcium, and was nearly exclusively left out of aluminosilicate phases. Additionally, while a relatively large amount of other elements were observed in the iron-rich phases, magnesium rarely occurred within these grains. For the Class C fly ashes, calcium and magnesium-rich phases likely contained the merwinite, the crystalline phase that was identified in greatest

quantity in both Class C ashes. Atikokan, Centralia, Bell River, and Boral Class C contained an N-A-S phase, and these were the four highest sodium-containing fly ashes. The other phases identified in these four ashes generally had low sodium, therefore it was speculated that in those four fly ashes, the sodium preferentially occurred in aluminosilicate phases. One noted exception was the inclusion of sodium in C-A-S 6 phase in Big Brown Raw fly ash, which contained over 3 mass % sodium (for the phase); however, the C-A-S 6 phase was one of the lower calcium C-A-S phases with around 7 % calcium by mass, barely above the 5 % Ca that was the upper limit for calcium in the A-S phases. The same trend was identified with the potassium; much of the potassium was found in aluminosilicate phases or else also in the N-A-S phases.

4.2.12.2 Class designations and phase identification

The Class designations of the fly ashes as C or F per ASTM C618 were not predictive as to the number of phases identified in the fly ash. As previously discussed, the lowest calcium-containing (< 5 %) fly ashes had few phases as identified in MSIA, but for the higher calcium Class F fly ashes (9-14 % CaO, by mass), there were not obvious differences in the number of phases in the fly ashes when compared to Class C. The presence of portland cement phases occurred in one Class C fly ash but not the other. The formation of phases such as merwinite and gehlenite was also unique to the Class C fly ashes. However, the C-A-S phases identified using MSIA were common to all Class F ashes. All of the phases identified in the fly ashes are shown in Table 4.24. From this we can see that the A-S 1 and A-S 2 phases were only found in Class F fly ashes, while the A-S 4 phase was only found in a Class C fly ash. The C-A-S 1 phase was also identified in both classes of fly ash, while CAS, C-A-S 2, C-A-S 5, C-A-S 7, and C-A-S 8 were only identified in Class F fly ashes. Boral Class C fly ash contained two distinct sodium aluminosilicate phases (N-A-S and N-A-S 2), which was unique to this Class C

fly ash. Bell River also contained N-A-S, although two Class F fly ashes also contained a similar phase.

Table 4.24: Phases observed in the fly ashes by MSIA

	Phase designation																	
	A-S				C-A-S								Other					
Fly Ash	1	2	4	C-S	C-A-S	1	2	4	5	6	7	8	Fe-rich	K-A-S	Mg-rich	N-A-S	N-A-S 2	quartz
Atikokan		X				X							X	X	X	X		X
Belews Creek	X	X											X					X
Big Brown Raw		X						X		X								X
Centralia		X					X						X			X		X
Coleto		X				X			X		X		X	X				X
Fontana	X	X											X					X
LEGS					X		X		X		X	X	X					X
Martin Lake		X							X	X		X	X					X
Bell River				X		X				X			X	X	X	X		X
Boral Class C			X					X								X	X	X

4.2.12.3 Inter- and Intra-particle heterogeneity and phase morphology

It has long been known that there is intra-particle heterogeneity in fly ash (Hemmings and Berry 1987), but the phase compositions have not been reported in great detail until more recently (P. Williams et al. 2005; Chancey et al. 2010). The data collected for these ten fly ashes grouped regions of flat-polished epoxy-mounted fly ash specimens into specific compositional phases using their x-ray maps. Synthesis of the information given by the various elemental maps allows for better explanation of how the bulk composition is distributed into particles, which vary in size and morphology. Additionally, while inter-particle heterogeneity could be explained by the collection of fly ash particles over time and made by burning coal that is also inherently

heterogeneous, intra-particle heterogeneity is caused by localized differences in composition in the molten glasses. The results will be discussed by phase to relate composition to morphology and to note whether the phases that were found in particles with multiple phases had similarities in composition.

The A-S phases comprised the majority of the low-Ca fly ashes, and were also constituents in some of the moderate calcium fly ashes and one of the high-calcium fly ashes. The A-S 1 phase was identified in the Belews Creek and Fontana fly ashes. The A-S 1 phase was identified in a wide variety of particle sizes and also intermixed with the A-S 2 phase. The A-S 1 particles in Belews Creek and Fontana exhibited multiple forms as large, angular, and vesicular, and medium to small and circular. The appearance of a circular particle in cross section suggests that the likely 3-dimensional morphology is spherical, while the angular particles likely retain that angularity. The A-S 2 phase was identified in Belews Creek, Centralia, Coleto Creek, Fontana, and Martin Lake. In the Belews Creek and Fontana fly ashes, the phase was identified in many shapes and sizes and intermixed with the A-S 1 phase. In the Centralia fly ash the phase was in large, vesicular particles and very small circular particles. In the Coleto Creek fly ash, the A-S 2 phase was identified in large, irregularly shaped particles and also intermixed in small amounts with particles that were predominantly phase C-A-S 7. In the Martin Lake fly ash, the A-S 2 phase was in a few medium-small circular particles and in small amounts with C-A-S 6. The A-S 4 phase in the Boral Class C fly ash was present in larger angular particle and in some circular particles. The phase was also intermixed with N-A-S in some particles.

The A-S phases were intermixed with each other, with two different C-A-S phases, and with an N-A-S phase in the five fly ashes in which they were identified. The C-A-S phases that the A-S 2 phase intermixed with were C-A-S 6 and C-A-S 7, in two

different fly ashes. In the Martin Lake fly ash in which the A-S 2 and C-A-S 6 were intermixed, the compositions of the phases were very dissimilar indicating the existence of two different phases in the same particles. Similarly, in the Coleto Creek fly ash in which the A-S 2 phase was intermixed with C-A-S 7, the two phases were very different in composition. The A-S 4 phase was intermixed with N-A-S in the Boral Class C phase. The phase compositions for these were also significantly different, again indicating very different compositions existent in the same particle(s) within the fly ash. In summary, the A-S phases tended to be present in large, vesicular particles, medium circular particles, and small circular particles. They were also intermixed with other phases of distinctly different composition.

The C-A-S phases identified in the fly ashes included C-A-S, C-A-S 1, C-A-S 2, C-A-S 4, C-A-S 5, C-A-S 6, C-A-S 7, and C-A-S 8. C-A-S was present in one fly ash, the LEGS fly ash. It was in large to medium-sized particles and was intermixed with phase C-A-S 2. The C-A-S 1 phase was identified in Coleto Creek and Bell River fly ashes. In the Coleto Creek fly ash, the C-A-S 1 phase was identified in few medium-sized, circular particles with Mg-rich phase in small inclusions (likely periclase), also. The C-A-S 1 phase in the Bell River fly ash was in medium-to-small, circular particles, and it also had Mg-rich phase inclusions. The C-A-S 2 phase was identified in the LEGS fly ash and the Centralia fly ash. This phase was intermixed with the C-A-S phase in medium-sized, circular particles in the LEGS fly ash. In the Centralia fly ash, the (C-A-S 2?) phase was mostly found in large particles, some with angular morphology and some with circular morphology; quartz and iron-rich phases were intermixed with the C-A-S 2 phase in Centralia fly ash. The C-A-S 4 phase was identified in the Big Brown Raw and Boral Class C fly ashes. In the Big Brown Raw fly ash, this phase was in particles of all sizes and circular in shape. In the Boral class C fly ash, the C-A-S 4 phase was also

present in particles of a range of sizes and circular in shape. In neither case was this phase intermixed with another. The C-A-S 5 phase was identified in the Coleto Creek fly ash, the LEGS fly ash, and the Martin Lake fly ash. In the Coleto Creek fly ash, the C-A-S 5 phase was in medium-sized particles that were spherical in morphology. In the LEGS fly ash, the phase was identified in larger, circular particles, while in the Martin Lake fly ash, the phase was found in medium-sized spherical particles. The C-A-S 6 phase was identified in Big Brown Raw fly ash, Martin Lake fly ash and Bell River fly ash. In the Big Brown Raw fly ash, C-A-S 6 was identified in large, irregularly shaped particles. In the Martin Lake fly ash, the phase was identified in many particle types including large, angular and circular particles. The C-A-S 6 in Martin Lake was intermixed with phase C-A-S 8. In the Bell River fly ash, C-A-S 6 was identified in medium-to-large circular particles. The C-A-S 6 in Bell River was intermixed with N-A-S phase. The C-A-S 7 phase was identified in the Coleto Creek fly ash; it was present in some very large, angular particles, as well as in small particles and cenospheres. The C-A-S 8 phase was identified in the Martin Lake fly ash; it was present in large, spherical particles and was intermixed with phases C-A-S 6 and A-S 2.

Of the C-A-S phases, few were intermixed with other phases. Of those that were identified in particles with other phases, one was intermixed with another C-A-S phase, one was mixed with N-A-S, and the other was intermixed with A-S 2. C-A-S 2 and C-A-S were intermixed in the LEGS fly ash, and had very different compositions. The C-A-S 6, C-A-S 8, and A-S 2 phases were intermixed in Martin Lake, indicating particles in this fly ash with very regional composition. The C-A-S 6 phase that was intermixed with the N-A-S phase in Bell River had relatively high sodium compared to the other C-A-S 6 phases in other fly ashes (the phase was designated based on Ca, Si, and Al content only), and Bell River had high sodium relative to the other fly ashes in the study as per oxide

analysis. The phases were distinct in composition, but regional differences in the particle were noted. In summary, the C-A-S phases were of all shapes, sizes and morphologies, but they tended to be discrete phases within the particles. There were a few exceptions, which were noted and discussed.

The alkali-modified aluminosilicates, N-A-S and K-A-S, were identified in some fly ashes. The N-A-S phase was identified in Atikokan, Centralia, Bell River, and Boral Class C fly ashes. The K-A-S phase was identified in the Coleto Creek and Bell River fly ashes. The N-A-S phase in Atikokan fly ash was in varied particle sizes and circular morphology. In Centralia fly ash, the N-A-S phase was in large particles containing air voids and very small, circular particles. In the Bell River fly ash, the N-A-S 6 phase was in a wide range of particle sizes, all circular in shape, and it was intermixed with C-A-S 6 in some particles. The Boral Class C fly ash included two N-A-S phases of different compositions. The N-A-S phase was identified in large cenospheres and medium-to-small circular particles. N-A-S 2 was in a single angular particle that was large in size. The K-A-S phase was identified in Coleto Creek and Bell River fly ashes. In the Coleto Creek fly ash, two medium-sized, circular particles were noted. In the Bell River fly ash, this phase was present in a few large, angular and vesicular particles.

In general, the alkali-modified aluminosilicates did not intermix with other phases. They were present in a variety of particle sizes and included some angular or void-filled particles. The only instance in which N-A-S was identified intermixed with another phase was in Bell River fly ash, in which it was mixed with the C-A-S 6. The C-A-S 6 phase in Bell River was high in sodium (approximately 4.3 mass %) compared to C-A-S 6 in other fly ashes (0.3-3.5 mass %), so this was not entirely surprising.

The Fe-rich phase was identified in all ten fly ashes. The Fe-rich phase, which varied in composition by fly ash, was identified in only a few distinct particles in each fly

ash. Typically the particles were medium-to-small in size, and they were always circular in morphology. The Fe-rich phase was never intermixed with other phases.

The Mg-rich phase was identified in Big Brown Raw and Bell River fly ashes. The phase was identified as small inclusions in C-A-S 4 (in Big Brown Raw) and C-A-S 1 (in Coleto Creek and Bell River), both of which contained periclase as per XRD results. In the Bell River fly ash, the Mg-rich phase was also present in small, circular particles, in which a small amount of periclase was identified by XRD. The C-A-S 4 phase in which Mg-rich was included in Big Brown Raw fly ash had the highest Mg content of any of the C-A-S 4 compositions (4.7 mass %; again, C-A-S phases were defined only by Ca, Si, and Al). The C-A-S 1 phases in which Mg-rich was included in Bell River or Coleto Creek did not contain a high amount of Mg relative to the C-A-S 1 in other fly ashes.

Quartz was also identified in all ten fly ashes, and in general was heterogeneous in terms of its particle size, morphology, and dispersion. In many cases, it was included in large and small particles of other composition, while in other cases it was identified as discrete particles. The quartz was angular in morphology in all cases, though in some the edges were more rounded. Hemmings and Berry noted that the quartz can be polished by the boiler flame even though it does not reach its melting point, which would lead to the rounded edges observed in some of the data sets (Hemmings and Berry 1987).

4.3 DISCUSSION OF RESULTS AND OBSERVATIONS

Ten fly ashes were selected to study for reactivity in geopolymers. The first stage was to analyze the composition of the fly ashes for crystalline and glassy components. X-ray diffraction and Rietveld analysis were used to quantify the crystalline component and the bulk amorphous content. The fly ashes contained a variety of crystalline phases including quartz, mullite, magnetite, maghemite, hematite and melilite in greatest amount

and other phases in small amounts. The bulk amorphous content was measured to range between 62 % and 88 % for the ten fly ashes. Since it has been suggested that the amount of amorphous material is important for favorable reactivity, it is hypothesized that the Atikokan, Centralia, and Coleto Creek fly ashes may have high reactivity in an alkaline solution since they contained the three highest amounts of bulk amorphous phase, separated from the next nearest fly ashes by 5 %, while the Fontana fly ash would have low reactivity due to its low amount of amorphous phase.

Constituent ratio methods for defining geopolymer composition typically use the amorphous portion of the relevant oxides in their calculations since that is known to be the most reactive portion of the fly ash. The amount of the network-forming oxides (silica and alumina) necessary for geopolymer gel formation were calculated for each fly ash in this study by subtracting the crystalline portion of those oxides from the bulk oxide amount measured by XRF and reported in Chapter 3. SiO_2/ Al_2O_3 ratios were calculated using the amorphous-phase portions in an attempt to predict reactivity for the fly ashes when used in alkaline activation. Those closest to 4.0, the value recommended by Davidovits (1982), were hypothesized to result in the best reactivity, which included Atikokan, Bell River, LEGS, and Martin Lake.

The fly ashes were characterized with MSIA analysis to determine which had similar glassy phase composition. Three A-S phases were identified, one in only a single fly ash, one in only 2 fly ashes, and one in 6 fly ashes. Comparing the A-S phases with the fly ashes predicted to be reactive, the A-S 2 phase was identified in both fly ashes that were predicted to be reactive (Centralia, Coleto Creek, and Martin Lake) and the fly ash hypothesized to be poorly reactive (Fontana). The A-S phases also made up nearly all of the composition of the Fontana and Belews Creek fly ash. Since Fontana was predicted to be poorly reactive by the amount of bulk amorphous phase, the similarities in their

compositions by MSIA imply that Belews Creek should also be hypothesized to be poorly reactive. The shapes and sizes of the particles give no clues as to potential reactivity. The A-S 1 and 2 phases were found in Fontana and Belews Creek in a variety of sizes and shapes. In the fly ashes hypothesized to be reactive, the A-S 2 phase was noted in large particles in Coleto Creek, large and small in Centralia, and small in Martin Lake.

The C-A-S phases that were identified in the most fly ashes (3 each) were C-A-S 1, C-A-S 5, and C-A-S 6. Further, two of the three (C-A-S 1 and C-A-S 5) were only identified in fly ashes predicted to be reactive, including Atikokan, Bell River, and Coleto Creek for C-A-S 1 and Coleto Creek, LEGS, and Martin Lake for C-A-S 5. C-A-S 6 was identified in 2 fly ashes that were predicted to be reactive (Martin Lake and Bell River), while it was also identified in Big Brown Raw, for which no trends had been observed previously. The particle sizes for these three phases were similar for each of the three fly ashes in which they were identified. The C-A-S 1 phase was in medium-small particles in all three fly ashes. The C-A-S 5 phase was in medium size particles in Coleto Creek and Martin Lake, while it was noted in large particles in the LEGS fly ash. The C-A-S 6 phase was identified mainly in medium to large particles in the Big Brown Raw and Bell River fly ashes, while it was in a variety of sizes in the Martin Lake fly ash.

The N-A-S phase was identified only in fly ashes that were hypothesized to be well reactive (Atikokan, Centralia, Bell River, Boral Class C). In only one case was the phase identified solely in large particles (Centralia).

Based on these results, the following hypotheses are made regarding the fly ashes most likely to react and the phases that are likely the most and least reactive:

- Atikokan, Centralia, Coleto Creek, LEGS, Martin Lake, and Bell River are hypothesized to be the most reactive fly ashes.

- A-S 1 and A-S 2 are poorly reactive phases.
- C-A-S 1, C-A-S 5, and C-A-S 6 are hypothesized to be the reactive calcium-modified aluminosilicate glassy phases in fly ashes, but the particle size may affect this result.

Chapter 5: Results: Fly ash reactivity

Fly ash reactivity for use in geopolymer cements was examined using two methods: compressive strength testing of mortar cubes of geopolymers made from the ten fly ashes in the study and a dissolution technique that examined the composition of fly ash residue from each of the ten fly ashes after their exposure to 8 M NaOH solution in dilute proportions. The results are presented in this chapter with discussions in each section. It is important to note that while the fly ashes are given by name in these results and their reactivities are ranked as good, moderate, or poor, these results are based upon small samples from single lots of the fly ashes. Because of the inherent variability in fly ash produced over time (and across small time periods), this is not a judgment of the fly ash resulting from the power stations named. Names are given only for reproducibility of the study by other interested researchers.

5.1 COMPRESSIVE STRENGTH AS AN INDICATOR OF REACTIVITY

The ten fly ashes were initially screened for their potential reactivity using mortar cubes tested for compressive strength. The mortars consisted of fly ash mixed with 8 M NaOH solution at a 0.485 solution-to-powder ratio (by mass). The compressive strengths were tested at 7 d and 28 d. The compressive strength results for 7 d are shown in Figure 5.1, and the compressive strength results for 28 d are given in Figure 5.2. In reviewing these results, it is important to note that the goal of this study was to test the approximate reactivity of the fly ashes using strength as an indicator, not to manufacture a strong geopolymer; thus, the compressive strengths are low compared to those reported for other geopolymer mortars, which were over 30 MPa for all fly ashes tested in work reported by (Chindaprasirt, Chareerat, and Sirivivatnanon 2007).

At 7 d testing, the Bell River fly ash geopolymer had the highest compressive strength of 6.4 MPa (900 psi). The remaining 9 fly ashes were below 3.5 MPa (500 psi).

The weakest specimens at 7 d were made with Belews Creek and Fontana fly ashes and could barely be demolded without falling apart; they had the consistency of wet sand and could not be tested. The other fly ashes were easily demolded at 7 d, yet had very low strengths, under 3.5 MPa. By 28 days, the different reactivity of the fly ashes with the activating solution (8 M NaOH) was apparent by differences in the compressive strengths of the geopolymers. From these results three categories were devised for descriptive purposes of the fly ash reactivity: for compressive strength over 10 MPa (1450 psi) the fly ash was considered reactive, for compressive strength of 5-10 MPa (725-1450 psi) the fly ash was considered moderately reactive, and for compressive strength under 5 MPa (725 psi) the fly ash was considered poorly reactive. The highest strength developed was from the Big Brown Raw geopolymer, which had 20 MPa (2800 psi) compressive strength at 28 days. The Martin Lake, Bell River, Coleto Creek, Atikokan, and Centralia geopolymers also had high strengths of over 10 MPa. These six fly ashes were all considered reactive. The LEGS and Boral Class C geopolymers had 28 d compressive strength between 5-10 MPa (725-1450 psi) and were classified as moderately reactive. The Belews Creek and Fontana geopolymers had 28 d compressive strength well under 5 MPa (725 psi) and were both deemed poorly reactive under these experimental conditions and relative to the other fly ashes in the study.

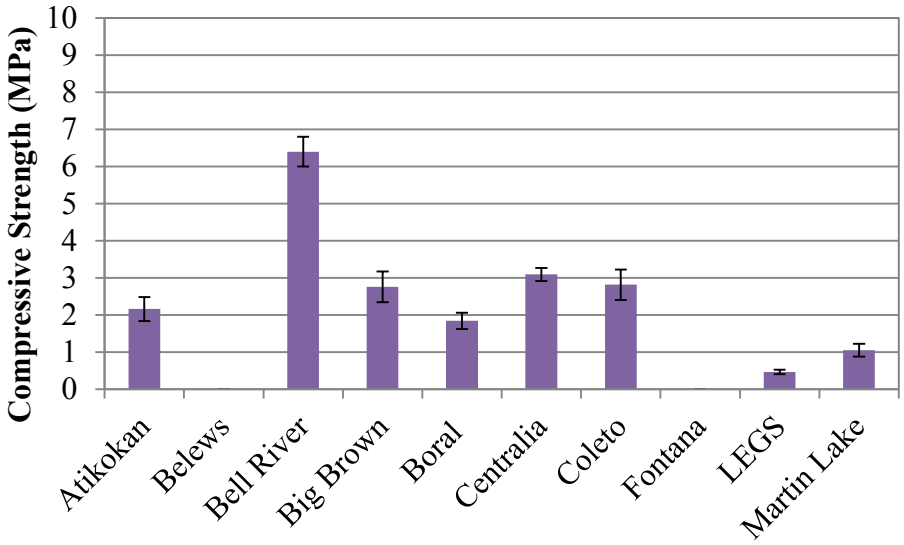

Figure 5.1: 7 d compressive strengths for geopolymer mortars made using the designated fly ash and 8 M NaOH solution at a 0.485 s/p and cured at 23° C

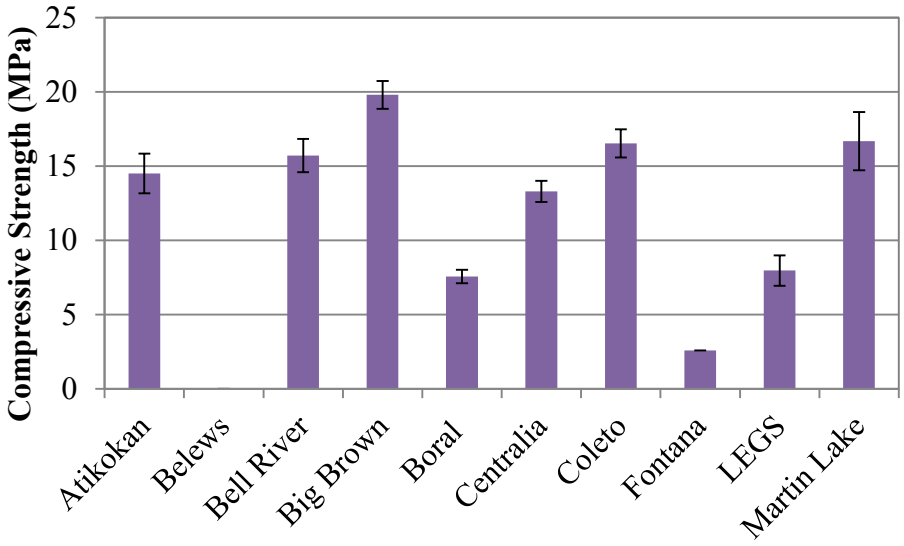

Figure 5.2: 28 d compressive strengths for geopolymer mortars made using the designated fly ash and 8 M NaOH solution at 0.485 s/p, cured at 23° C

5.1.2 Discussion of compressive strength results

The compressive strength results were reported in this section for geopolymer mortars made with each of the ten fly ashes, and by 28 d they had separated into three

distinct categories of strength/reactivity. The reactivity designations are now compared to the hypotheses for fly ash reactivity and glassy phase reactivity presented in Chapter 4. Through this, I hope to determine whether there were any obvious relationships between the phases identified in the MSIA study and the reactive, moderately reactive, and poorly reactive fly ashes.

In Chapter 4, it was hypothesized that the Atikokan, Centralia, Coleto Creek, LEGS, Martin Lake, and Bell River fly ashes would be reactive in geopolymers based upon either their high amounts of bulk amorphous phase and/or their silica to alumina ratios. The compressive strength results showed that these predictions were correct in all cases but LEGS fly ash, which was identified as moderately reactive based on compressive strengths. Also, the Big Brown Raw fly ash was identified as reactive by the compressive strength results, but it was not hypothesized as such based on its compositional analysis.

5.1.2.1 Discussion of reactivity versus particle size

The d_{50} values reported for each fly ash may give some indication of the expected reactivity, so they are compared to the compressive strength results. The reactive fly ashes all had d_{50} values under 15 μm, except for the Big Brown Raw fly ash, which had a d_{50} of 30 μm. The moderately reactive fly ashes had a d_{50} of 16-19 μm, while the poorly reactive fly ashes had d_{50} of 30 μm. Therefore, while the d_{50} value showed a trend for reactivity (finest were the most reactive, medium for the moderately reactive, and coarse for the poorly reactive), the Big Brown Raw fly ash showed that this was not an absolute trend, either.

5.1.2.2 Discussion of reactivity versus molar constituent ratios

The molar constituent ratios given in Chapter 4 for SiO_2 / Al_2O_3 of all ten fly ashes after subtraction of the crystalline phases revealed that those closest to ideal by Davidovits's definition (1982) were Atikokan, Bell River, Coleto Creek, LEGS, and Martin Lake. These fly ashes were all designated reactive based on the compressive strength results, with the exception of LEGS, which was moderately reactive. The two fly ashes that were designated poorly reactive had very high amorphous SiO_2/Al_2O_3 ratios of 4.99 (Belews Creek), and 7.2 (Fontana). However, the Centralia fly ash had a high SiO_2/Al_2O_3 of 5.52, so a strict correlation was not identified between the reactivity and bulk amorphous phase silica to alumina ratios.

The alkalis in the system are also known to affect the properties of hardened geopolymer cements, and the ratios that have been reported as important to the proportioning of geopolymers were Na_2O / Al_2O_3 and Na_2O / SiO_2. The Na_2O source in these geopolymers was primarily from the activating solution, since sodium in the fly ashes was present between 0.15 and 4.2 mass % Na_2O as measured in oxide analysis. Within that range of reported Na_2O, only one fly ash had over 2 % Na_2O, by mass, and half had under 1 % Na_2O by mass. The fly ashes were mixed into geopolymers using 8 mol/L NaOH solution with a 0.485 solution-to-powder ratio. For every 100 g of geopolymer at a 0.485 s/p, 0.108 mol of sodium was incorporated. The molar ratios of Na_2O / Al_2O_3 and Na_2O / SiO_2 are given in Table 5.1, with literature values given in the last two rows. The sodium oxide to silica ratio was generally close to the ranges established by previous work reported in the literature, with the two Class C fly ashes as outliers with their relatively high ratios of 0.42 and 0.40. Therefore, all of the Class F fly ashes were within the optimal sodium oxide to silica composition range. The sodium oxide to alumina ranges were not as aligned with recommended values. The Bell River,

Boral Class C, Centralia, and Fontana fly ashes were somewhat far from the recommended ratio value, which was near 1 in the literature (Davidovits 1982; Rowles and O'Connor 2003). Davidovits reported the alkali content in the form of M_2O, which was defined as Na_2O or K_2O, since in metakaolin systems he described, it was expected that all of the alkalis would be contributed from the activating solution. In these calculations only Na_2O was used to calculate the ratio, although some potassium may have been available from the fly ash.

Table 5.1: Molar oxide ratios of sodium oxide to silica and alumina, using only the amorphous portion of silica and alumina from each fly ash

	Molar ratios	
Fly Ash	Na_2O / SiO_2	Na_2O/ Al_2O_3
Atikokan	0.27	1.01
Belews Creek	0.2	0.99
Bell River	0.42	1.58
Big Brown Raw	0.21	1.02
Boral Class C	0.4	1.22
Centralia	0.22	1.23
Coleto Creek	0.28	1.04
Fontana	0.23	1.64
LEGS	0.25	1.05
Martin Lake	0.25	1.07
Davidovits (1982)	**0.25-0.28**	**1.0-1.14***
Rowles & OConnor (2003)	**0.32**	**0.92**

* The ratio was reported as M_2O/Al_2O_3 in Davidovits where $M_2O = (K_2O, Na_2O)/Al_2O_3$, but potassium is excluded from the current calculations

It has been reported in the literature that excess sodium would reside in pore solution if there was too much to be incorporated into the charge-balancing role of the geopolymer gel (Duxson et al. 2005). Therefore, the excess sodium was not expected to harm the formation of gel in these geopolymer mortars. However, excess sodium has been linked to carbonation at the surface of ambient-cured geopolymers (Temuujin, Williams, and vanRiessen 2009), so excess sodium can be a negative attribute. Of the

poorly reactive fly ashes, Belews Creek was slightly lower than the recommended Na_2O / SiO_2 ratio and was nearly exactly at the recommended value of Na_2O/ Al_2O_3. The Fontana fly ash was very close to the recommended Na_2O / SiO_2 and it had a high Na_2O/ Al_2O_3. However, the reactive Bell River fly ash had a similarly high Na_2O/ Al_2O_3, so this ratio did not seem to be the exact determining factor for the reactivity of the fly ashes under the conditions in this study.

5.1.2.3 Discussion of reactivity versus bulk amorphous content

In Chapter 4, it was hypothesized that the reactivity was linked to the amount of bulk amorphous phase measured in XRD, since the amorphous phases are typically considered the reactive portion of fly ashes. Atikokan, Centralia, and Coleto Creek were the three fly ashes with the highest bulk amorphous content. Upholding the hypothesis, these three ashes all fell into the "reactive" category based on their compressive strength results. They were not the three strongest geopolymers, however, indicating that they may not have had the highest reactivity of the ten fly ashes studied. The strongest fly ash as activated under these conditions was the Big Brown Raw fly ash, and the weakest was the Belews Creek fly ash. These two fly ashes fell within the 75 – 80 % bulk amorphous range, showing a great deal of similarity in bulk amorphous content with dramatically different reactivities. Therefore, it is made clear that the types of phases in the glassy portion of the fly ash must affect the reactivity more than solely the bulk amorphous content.

The fly ashes designated reactive based on compressive strength results had some phase similarities as reported for the MSIA results presented in Chapter 4. The phases identified by MSIA in each of the "reactive" fly ashes are given in Table 5.2. One similarity noted is that for all of the Class F fly ashes, the aluminosilicate phase identified was A-S 2. No aluminosilicate phase was identified in the Class C Bell River fly ash. A-

S 2 was thought to contain the mullite identified by RQXRD, and it was hypothesized to be poorly reactive in Chapter 4. One possible reason for its seeming link to reactive phases could be the amount in the fly ashes. It did not make up the majority of the fly ash composition for these fly ashes. C-A-S 1 and C-A-S 6 were identified in three ashes each and were hypothesized to be reactive glassy phases in the fly ash in Chapter 4, and the hypothesis was upheld by the compressive strength results. C-A-S 5, which was also hypothesized reactive in Chapter 4, was present in 2 fly ashes designated reactive, including Coleto Creek and Martin Lake. Since the other fly ash containing C-A-S 5 was designated "moderately reactive" the hypothesis is inconclusive. However, one possible explanation is that the C-A-S 5 phase was identified in smaller particles in the Coleto Creek and Martin Lake fly ashes, which may have improved its dissolution due to the increased surface area of smaller particles compared to larger ones. N-A-S, although a designation given to a wide range of compositions, was identified in three of the reactive fly ashes, while a fourth contained K-A-S. Chancey et al. (2010) grouped these two phases together in their work, since they were typically somewhat minor, and they also noted that they were completely soluble in caustic conditions. Table 5.3 shows the average compositions of the N-A-S and K-A-S phases as identified in the reactive specimens, and it is notable that they are very similar and cover only a small range of mass % for each element. Therefore, if these phases were reactive, they could be one key in predicting reactivity in fly ashes.

Table 5.2: Phases identified in the fly ashes designated "reactive" based on compressive strengths of their geopolymer mortar cubes at 28 d

Fly Ash					
Atikokan	**Big Brown**	**Bell River**	**Centralia**	**Coleto**	**Martin Lake**
A-S 2	A-S 2	C-A-S 1	A-S 2	A-S 2	A-S 2
C-A-S 1	C-A-S 4	C-A-S 6	C-A-S 2	C-A-S 1	C-A-S 5
N-A-S	C-A-S 6	K-A-S	N-A-S	C-A-S 5	C-A-S 6
periclase	Mg-rich	N-A-S	Mg-rich	C-A-S 7	C-A-S 8
Fe-rich	Fe-rich	calcium silicate	Fe-rich	K-A-S	periclase
quartz	quartz	Mg-rich	quartz	periclase	Fe-rich
		Fe-rich		Fe-rich	Quartz
		quartz		quartz	

Table 5.3: N-A-S and K-A-S compositions for the reactive fly ashes

			Mass % Element							
Fly Ash	Phase	Data Type	Ca	Si	Al	Fe	Na	Mg	K	O
Atikokan	N-A-S	average	1.4	31.2	13.5	2.3	5.3	0.3	0.9	44.9
Bell River	N-A-S	average	3.2	29.0	15.0	1.8	6.2	0.5	1.2	42.7
Centralia	N-A-S	average	3.5	34.9	8.8	3.2	3.0	1.0	2.5	43.0
Coleto	K-A-S	single point	5.4	30.4	11.8	2.3	0.8	1.3	5.1	42.9

The phases identified in the moderately reactive fly ashes, Boral Class C and LEGS, are listed in Table 5.4. There were no similarities between the two fly ashes other than quartz. The Boral Class C contained an aluminosilicate phase, which had very high silicon of 44 mass % with a Si/Al ratio of 8 (see Table 4.23). The Boral fly ash also contained an N-A-S phase and an N-A-S 2 phase, while the LEGS fly ash did not contain an aluminosilicate or sodium-modified aluminosilicate. The LEGS fly ash contained a large number of C-A-S phases, five in total, which was a greater number of phases than the single C-A-S 4 phase identified in the Boral fly ash. In summary, the comparison of phases identified in these two moderately reactive fly ashes was inconclusive as to why these fly ashes were only moderately reactive when mixed into a geopolymer. They shared no common phases with each other, and they shared many similar phases with the

reactive fly ashes (N-A-S, C-A-S 4, C-A-S 2, C-A-S 5, C-A-S 7, C-A-S 8). One factor may be that even for a reactive phase present in the fly ash, it may be present in small amounts in these fly ashes and therefore unable to contribute significantly to strength. Another possible factor is that the particle sizes of the phases being too large, and despite dissolution occurring, there was too little surface area to allow a high amount of dissolution before precipitation occurred, slowing the reaction (Chen et al. 2011).

Table 5.4: Phases identified in fly ashes designated "moderately reactive" based on compressive strengths of their geopolymer mortar cubes at 28 d

Fly ash	
Boral Class C	LEGS
A-S 4	CAS
C-A-S 4	CAS 2
N-A-S	C-A-S 5
NAS 2	CAS 7
quartz	CAS 8
Fe-rich	quartz
	Fe-rich
	periclase

The poorly reactive fly ashes were interesting because they contained nearly the same phases (Table 5.5). They each contained A-S 1, A-S 2, quartz, Ca-rich, and an iron-rich phase. The A-S 1 phase was only identified in these poorly-reactive fly ashes. Since A-S 2 was identified in the reactive fly ashes and it was also identified in the poorly reactive fly ashes, it is hypothesized that for the reactive fly ashes, this phase did not contribute to the reactivity necessary to obtain the high compressive strengths of the reactive phase. A-S 2 was present in large amount in each of the poorly reactive fly ashes; therefore if it were significantly reactive, these fly ashes would likely have had better reactivity in the compressive strength results. The calcium-rich phase was identified as a very small amount, so even if it were reactive, it would not likely have

been able to contribute much to strength. It is also of interest that the Fontana fly ash had the lowest amount of bulk amorphous phase and it was classified as poorly reactive by compressive strength testing. This suggests that very low bulk amorphous contents (such as the 55% calculated for the Fontana fly ash) may actually correlate to poor reactivity. Also, these poorly reactive fly ashes were very coarse. Coarseness in a fly ash may indicate poor reactivity, as well, as previous works have shown that grinding is necessary to improve strengths in coarse fly ashes (Duxson and Provis 2008).

Table 5.5: Phases identified in fly ashes designated "poorly reactive" based on compressive strengths of their geopolymer mortar cubes at 28 d

Fly ash	
Belews	Fontana
A-S 1	A-S 1
A-S 2	A-S 2
quartz	quartz
Ca-rich	Ca-rich
Fe-rich	Fe-rich

5.2 DISSOLUTION STUDY USING NAOH

Geopolymer formation is a dissolution-precipitation process that is thought to occur by surface dissolution of ionic species from the aluminosilicate powder, after which reaction products precipitate from solution after a critical concentration is reached forming on the surface of nucleation sites in the mixture (Duxson, Fernández-Jiménez, et al. 2007; Chen-Tan et al. 2009; Chen et al. 2011). From this basis, a dissolution technique was selected in this work to test whether the phases identified in the fly (Chapter 4) were reactive by tracking their presence in the fly ash after 7 d and 28 d of exposure to 8 M NaOH solution in dilute proportions. The results from Chapter 4 identified phases that existed in multiple fly ashes, and when combined with the

compressive strength data presented in Section 5.1 allowed for correlations to be drawn regarding the phases present in fly ashes with the highest, medium, and lowest compressive strengths. The work presented in the following sections will attempt to more specifically link individual phases to reactivity by tracking their presence/ absence and amount over the same time periods as compressive strength was tested.

The details of the test methods are described in Chapter 3. However, some points are made here for the reader to keep in mind. First, each of the data sets is a single field of view for each fly ash at each time. Also, the same field of view size was selected for each data set, which in true size measured approximately 1 mm x 0.8 mm. Further, when epoxy-mounting the residue specimens, the solid-to-epoxy mass ratio was intended to be the same for each specimen, which would result in a similar amount of solid material in each field of view. This did not always occur due to the increased liquid demand in many of the reacted samples, which was attributed to the increased surface area that would be associated with reaction product formation as compared to the smooth, spherical particles typical of the original fly ashes. Because of the disparity in amount of solid material due to the increased liquid demand from many of the samples, the data were normalized to remove the epoxy from the relative amounts of each phase. This way the data were compared as solid material to solid material at each time step.

The compositional results for the fly ash residues after 7 d and 28 d of exposure to 8 M NaOH are described in the following sections and compared to the results for the fly ashes prior to NaOH exposure that were presented in Chapter 4. The phase compositions for each phase in the fly ash residues are described in terms of element mass %, not the oxide form. The designations given to each of the phases were selected from the same criteria given in Table 4.12 from the previous chapter. One aspect of this method that must be kept in mind is that for each fly ash, a single field of view was selected for each

fly ash at each time period. Sometimes the results did not follow the pattern that was expected, which was: identification in the reacted sample of all or some of the same phases as in the fly ash prior to treatment, plus the addition of a reaction product (in cases where measureable compressive strengths were recorded). The lack of continuity could be explained by sampling error due to the heterogeneity of fly ash, which is well established (Hemmings and Berry 1987). Sampling error may also occur when a phase is present in very small amount, in discrete particles that may not have been included in the field of view selected for data collection. Another possibility is that the phases may have changed in composition due to leaching of ions to solution. It is known that even after a reaction product has formed on the surface of a fly ash, dissolution continues for the particle inside (Chen et al. 2011); therefore, leaching of one phase from the original fly ash may have resulted in another phase identified in the dissolution results. Quantitatively documenting such behavior was beyond the scope of this work but is noted when it is a possible explanation.

The dissolution results are presented in the order that the ashes were grouped based on compressive strengths: reactive, moderately reactive and poorly reactive. In each section the phase assignments, phase compositions, and amount of each phase at 7 d and 28 d are given. Figures showing the relative composition of the fly ashes at each time period (original, 7 d of exposure to NaOH, and 28 d of exposure to NaOH) are given. The reaction product is normalized out of the compositions for the comparison figure, so that the original fly ash composition is compared to the residue composition. The phases present in very small amounts (< 1 % area) were omitted, therefore the total does not always add up to 100 %. Only the obvious changes are discussed. A large increase or decrease (around 20%) in a phase is considered significant, so it is discussed, otherwise the phase is left out of the discussion.

5.2.1 Crystalline component of dissolution residues

XRD scans of the fly ash residues at 7 d and 28 d were collected for each fly ash. However, in some cases, crystalline zeolites formed that were not identifiable, which hindered the ability to complete Rietveld analysis. The XRD scans are given in Appendix A.

5.2.2 Atikokan fly ash

The Atikokan fly ash (Class F, ASTM C618) was considered reactive based on the compressive strength results shown in section 5.1. The changes in Atikokan fly ash from the raw material to 7 and 28 d of NaOH exposure followed a logical pattern of similar phases being identified, decreasing over time, and in some cases differing compositionally after exposure to NaOH solution. In this data set, a reaction product was clearly identified in both the 7 and 28 d samples, it was easily segmented, and it increased in the field of view for the two reactivity specimens studied.

Six phases were identified in the Atikokan fly ash as discussed in Section 4.2.2, including A-S 2, C-A-S 1, N-A-S, periclase, Fe-rich, and quartz. After 7 d of exposure to 8 M NaOH solution, the fly ash residue contained all of these phases, except periclase, and one new phase, a reaction product. The Atikokan 7 d results are based upon a single data set. The phases and their compositions are given in Table 5.6. The phase compositions can be compared to Table 4.12, which gave the compositional ranges for each phase. The compositions of the phases at 7 d were nearly identical to the original fly ash phases and are not described. The phase assignment image for the Atikokan solid residue after 7 days of exposure to NaOH is given in Figure 5.3, and the relative amounts of each phase are shown in Figure 5.5. The A-S 2 phase (yellow) was identified in larger particles with void inclusions. The C-A-S 1 phase (blue) was present mainly in circular particles (presumably spherical in three dimensions) of medium-to-large sizes. The N-A-

S phase (red) was present in a range of sizes but exclusively in circular morphology. Quartz (lime green) was angular in morphology, although several spherical particles were identified for this phase. The iron-rich phase (aqua), which was a very minor phase in the raw material, was also very minor at 7 days. The periclase (light orange) identified in the raw material was not identified in the 7 d specimen, but this is considered a sampling error. Finally, a reaction product (teal blue) was identified in the 7 d specimen. It surrounded many of the fly ash residue particles and was particularly visible on particles of C-A-S 1 composition.

The 28 d specimen also contained many of the same phases as the raw fly ash and 7 d sample. The phase compositions are given in Table 5.7, and the phase assignment image is given in Figure 5.4. The phase compositions can be compared to Table 4.12, which gave the compositional ranges for each phase. The A-S 2 phase (yellow) identified in both prior samples remained, while the C-A-S 1 phase was not identified but two other C-A-S phases were identified in its place: C-A-S 3 (tan) and C-A-S 4 (bright purple). These two C-A-S phases contained less calcium than the C-A-S 1 phase and, and C-A-S 3 had increased silicon to aluminum ratio, while C-A-S 4 had a decreased Si/Al. The C-A-S 3 phase and C-A-S 4 phase contained approximately 27% by mass calcium. They differed in silicon and aluminum: C-A-S 3 had 16% silicon and 7% aluminum (average), while the C-A-S 4 had 4% silicon and 12% aluminum, single point. The N-A-S phase (red) at 28 d had 4.5 % sodium, while the silicon was measured at 25 % by mass and the aluminum at 9% by mass. While the silicon and calcium remained similar or slightly increased in the N-A-S phase compared to 7 d, the aluminum was strikingly lower implying aluminum dissolution from this phase. Periclase was identified in MSIA of the 28 d specimen after not appearing at 7 days, but this was likely a sampling error. Its composition was not measured quantitatively.

The reaction products identified in the 7 d and 28 d specimen are described separately, since they were not intended as the main focus of this study. The reaction product identified in the 7 d specimen was high in calcium at 23 % by mass, and low in silicon and aluminum at 6.5 and 9.7 mass %, respectively. The reaction product iron content was 12.5%. Sodium and magnesium were also present in the reaction product in small amounts of 2-3% by mass. Two reaction products were identified in the 28 d specimen, and they were different in composition from the 7 d reaction product. Whereas the 7 d reaction product had calcium of 23% by mass, both 28 day reaction products had calcium of around 10 mass %. The 28 d reaction product phase (teal) contained silicon at around 25 % by mass and aluminum at 11 % by mass, while reaction product 2 (dark purple) had silicon of around 9 % and aluminum of under 5 % by mass. It is also of note that reaction product 2 was identified on the surface of the particles and the reaction product phase surrounded the reaction product 2. The reaction product 2 phase was also mainly identified surrounding the C-A-S 4 phase or as particles of its own. The BSE image (Figure 5.6) shows the morphology of the reaction products surrounding the fly ash residue particles.

Table 5.6: Phase compositions and uncertainties (s) for a single sample of Atikokan fly ash after 7 d exposure to 8 M NaOH solution; a minimum of three measurements was used, else the number of points tested is specified

		Mass % element							
Phase	Data type	Ca	Si	Al	Fe	Na	Mg	K	O
A-S 2	**single point**	**0.0**	**33.6**	**19.3**	**0.7**	**2.8**	**0.0**	**1.3**	**42.3**
C-A-S 1	**average**	**31.9**	**12.1**	**10.2**	**8.0**	**0.7**	**3.0**	**0.0**	**32.8**
	std. deviation	8.3	6.2	4.3	3.8	1.1	1.5	0.0	2.1
N-A-S	**average**	**2.9**	**29.0**	**18.9**	**0.9**	**4.3**	**0.3**	**0.8**	**42.1**
	std. deviation	2.1	1.8	3.5	0.8	1.5	0.5	0.0	1.2
Quartz	**single point**	**0.0**	**52.4**	**0.5**	**0.0**	**0.0**	**0.0**	**0.0**	**47.2**
Fe-rich	**single point**	**1.0**	**14.0**	**9.6**	**41.0**	**2.1**	**0.0**	**0.0**	**32.3**
Reaction product	**average**	**22.6**	**6.5**	**9.7**	**12.2**	**2.1**	**3.5**	**0.0**	**41.9**
	std. deviation	6.3	1.1	2.7	3.3	1.0	3.2	0.0	5.0

Table 5.7: Phase compositions and uncertainties (s) for a single sample of Atikokan fly ash after 28 d exposure to 8 M NaOH solution; a minimum of three measurements was used, else the number of points tested is specified

		Mass % element							
Phase	Data type	Ca	Si	Al	Fe	Na	Mg	K	O
A-S 2	**single particle**	**0.0**	**29.4**	**21.9**	**0.0**	**2.9**	**0.0**	**0.8**	**44.9**
C-A-S 3	**average**	**27.2**	**16.4**	**7.3**	**3.2**	**0.8**	**4.1**	**0.0**	**40.2**
	std. deviation	4.6	3.5	5.2	1.6	0.8	2.4	0.0	2.6
C-A-S 4	**2 sample average**	**27.4**	**4.4**	**12.3**	**14.0**	**0.4**	**3.9**	**0.0**	**35.8**
N-A-S	**average**	**8.9**	**25.3**	**9.3**	**3.0**	**4.5**	**1.4**	**1.1**	**45.3**
	std. deviation	7.5	10.7	3.1	3.0	1.4	1.3	1.4	3.9
Quartz	**average**	**0.1**	**48.5**	**0.5**	**0.6**	**0.7**	**0.0**	**0.2**	**49.4**
	std. deviation	0.3	2.4	1.1	1.1	0.9	0.0	0.4	1.4
Reaction product	**average**	**8.1**	**25.1**	**11.0**	**3.4**	**5.1**	**1.5**	**0.1**	**44.3**
	std. deviation	7.4	5.3	3.5	1.5	1.1	1.4	0.2	4.5
Reaction product 2	**average**	**13.9**	**9.3**	**4.8**	**12.0**	**3.5**	**4.4**	**0.0**	**49.3**
	std. deviation	1.1	2.2	1.6	2.5	1.9	1.2	0.0	3.3

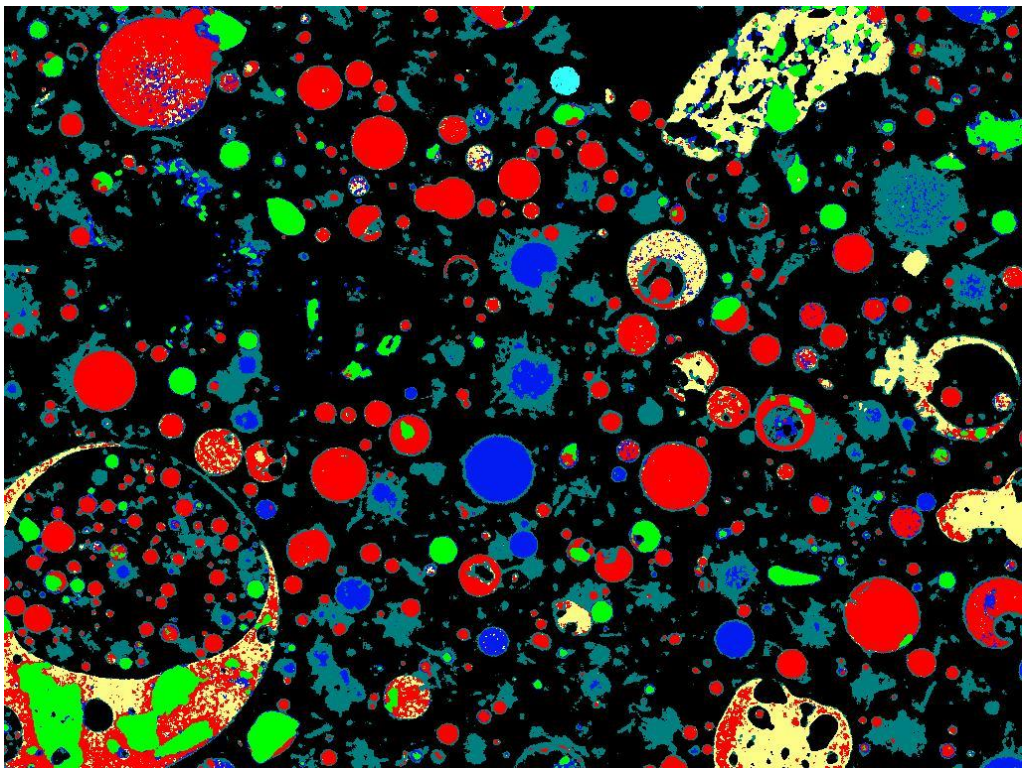

Figure 5.3: Phase assignment image of Atikokan fly ash residue after 7 d exposure to 8 M NaOH solution

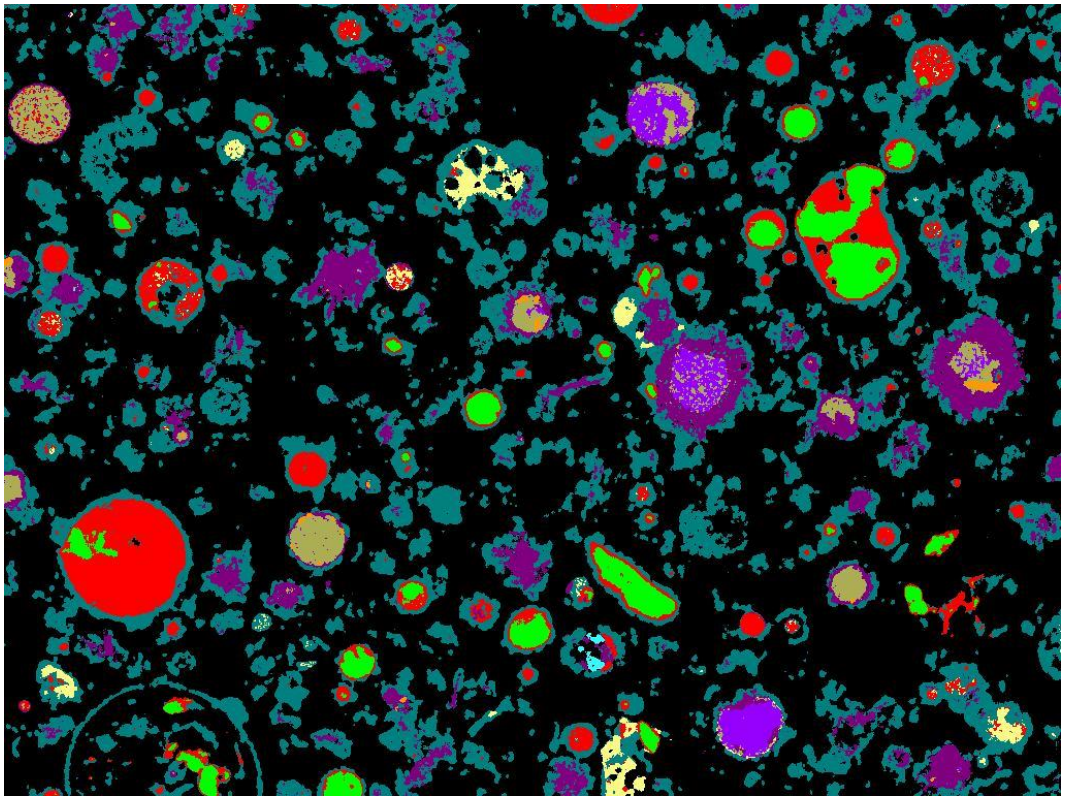

Figure 5.4: Phase assignment image of Atikokan fly ash residue after 28 d exposure to 8 M NaOH solution

a)

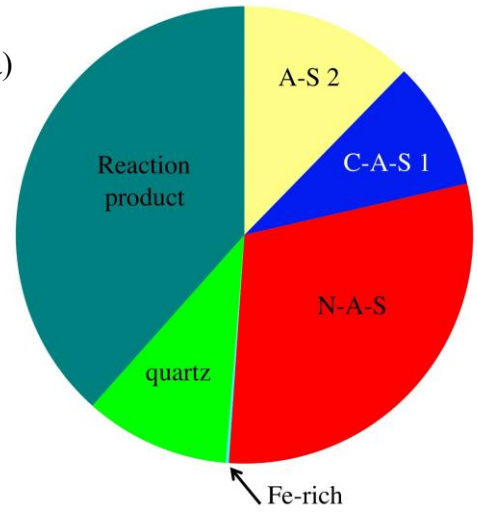

Phase	Area %
A-S 2	12.30
C-A-S 1	9.09
N-A-S	29.70
Fe-rich	0.22
quartz	10.26
reaction product	38.43

b)

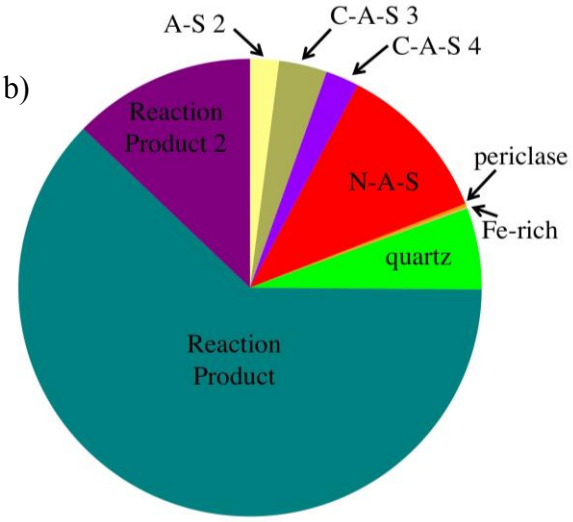

Phase	Area %
A-S 2	2.02
C-A-S 3	3.36
C-A-S 4	2.33
N-A-S	11.31
periclase	0.23
Fe-rich	0.11
quartz	5.76
reaction product	62.10
reaction product 2	12.78

Figure 5.5: The phase distribution of Atikokan fly ash after 7 d (a) and 28 d (b) exposure to 8 M NaOH solution; each based on a single sample

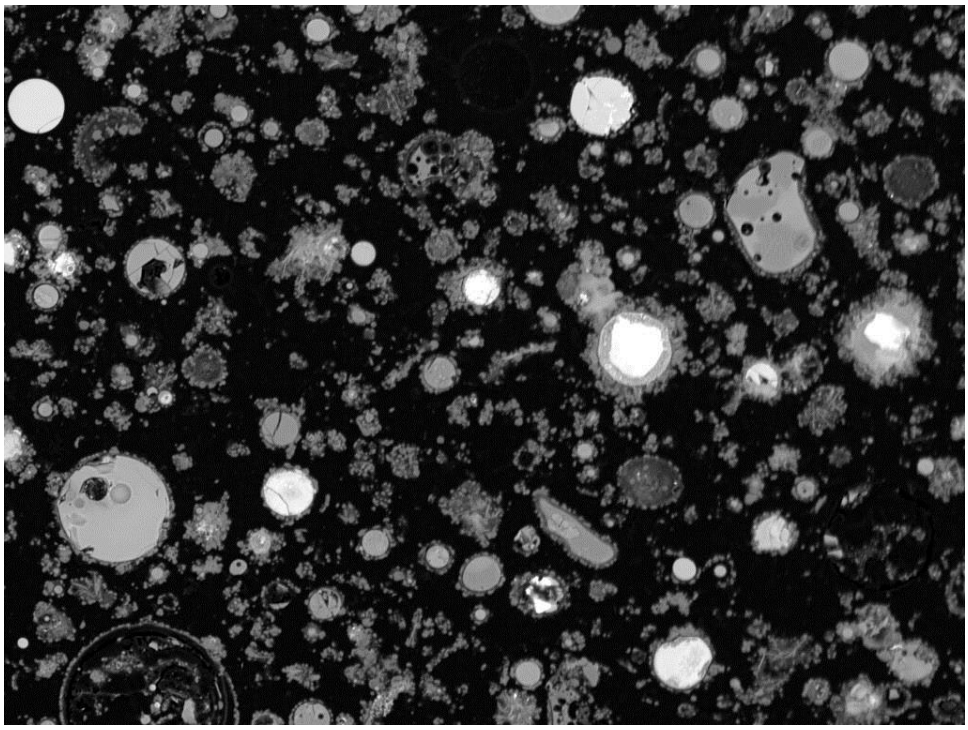

Figure 5.6: Backscattered electron image of Atikokan fly ash residue after 28 d exposure to 8 M NaOH solution

The compositional changes over time for all three data sets are shown in Figure 5.7, renormalized after removal of the reaction products so that only fly ash phases are shown. The Atikokan fly ash changed little over the time periods measured. It is interesting that the C-A-S 1 phase disappears prior to 28 d of exposure to NaOH solution. Two other C-A-S phases were identified in its place, C-A-S 3 and C-A-S 4. The C-A-S 1 phase contained 32 % by mass calcium, 12 % by mass silicon, and 10 % by mass aluminum. The C-A-S 3 phase and C-A-S 4 phase contained approximately 27% by mass calcium, but they differed in silicon and aluminum: C-A-S 3 had 16% silicon and 7% aluminum (average), while the C-A-S 4 had 4% silicon and 12% aluminum, single point. From these results it is possible that calcium, silicon, and aluminum leached from the C-A-S 1 phase to result in the C-A-S 3 and C-A-S 4 phases. This fly ash was designated reactive based on compressive strength results, but it is not clear from these data why the fly ash was reactive. The fly ash looks very similar at each time step. Given that reaction product, formed, though, dissolution did occur, but it is difficult to determine which phases were the most soluble.

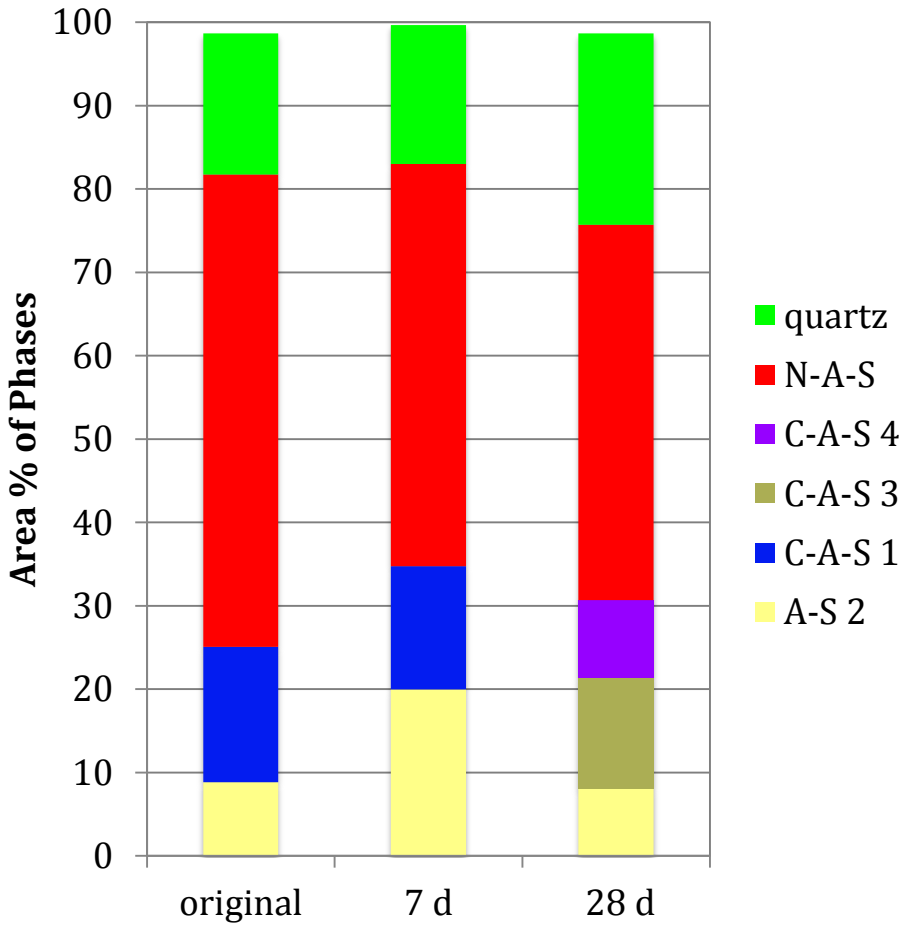

Figure 5.7: Atikokan fly ash: relative composition of fly ash before and after exposure to 8 M NaOH solution

5.2.3 Bell River fly ash

The Bell River fly ash was a Class C fly ash that was categorized as reactive based on the 28 d compressive strength results given in Section 5.1. The fly ash contained eight phases in its original form including C-A-S 1, C-A-S 6, K-A-S, N-A-S, calcium silicate, Mg-rich, Fe-rich, and quartz. The fly ash followed a logical pattern from 0 to 28 d when considering its compressive strength results, which showed it formed by far the strongest geopolymer at 7 d and was among the strongest at 28 d. By 7 d approximately 2/3 of the image area was reaction product, an amount that only slightly

increased after 28 d of 8 M NaOH exposure. The calcium silicate phase identified in the fly ash was no longer identified at 7 d or 28 d, and the C-A-S 6 and K-A-S phases likewise disappeared after NaOH exposure. The reactivity of K-A-S was noted by Chancey (2010) in his assessment of the LEGS fly ash, in which he identified K-A-S that was dissolved by a less concentrated NaOH solution used in the experiment. Conversely, an aluminosilicate phase was identified at 7 d and 28 d, although in only a few particles, that was not identified in the original fly ash. C-A-S 7 phase was identified in 7 d and 28 d results and the C-A-S 2 phase was identified at 28 d. These results are discussed in more detail next.

At 7 d, the fly ash residue contained aluminosilicate (composition not identified), C-A-S 1, C-A-S 7, N-A-S, Mg-rich, quartz, Fe-rich, and reaction product. The phase compositions are presented in Table 5.8. The phase compositions can be compared to Table 4.12, which gave the compositional ranges for each phase. The phase assignment image is given in Figure 5.8. The aluminosilicate phase and C-A-S 7 phase were the two phases identified in this sample that were not found in the original fly ash. C-A-S 7 was moderate in calcium, with around 11 mass %, and higher in silicon around 22 mass %, and moderate in aluminum at 9 % by mass. The aluminosilicate phase was unable to be quantitatively defined, since no point analysis data were taken in any of its particles.

At 28 d, the fly ash residue contained aluminosilicate, C-A-S 2, C-A-S 7, N-A-S, quartz, Mg-rich, and reaction product. The phase compositions are given in Table 5.9, while the phase assignment image is presented in Figure 5.9. The phase compositions can be compared to Table 4.12, which gave the compositional ranges for each phase. The C-A-S 1 phase identified in both previous time intervals was not found in the 28 d sample. However, the C-A-S 2 phase was newly identified at 28 d. It contained 26 % by mass calcium, 11 % by mass silicon, and 8 % by mass aluminum as well as nearly 4 mass

% each of iron and magnesium. The aluminosilicate phase in this specimen was not quantitatively defined by point analysis like in the 7 d sample. However, the intensity ratios of the training classes defined at 7 d and 28 d revealed similar Si/Al ratios and zero calcium content in both aluminosilicates, so they are thought to be the same phase and that it was poorly reactive. The aluminosilicate phase was found in large, vesicular particles intermixed with the N-A-S phase.

The reaction products found in the two fly ashes had very different compositions. The reaction product after 7 d was high in calcium at 19 % by mass compared to the 28 d reaction product, which contained 5 % by mass calcium. The silicon was lower at 7 d and higher at 28 d, while the aluminum was similar for both time periods. These results suggest calcium dissolution and precipitation early with greater silicon dissolution and precipitation at later time stages. Aluminum dissolution may have mostly occurred by 7 d, with little increase by 28 d.

Table 5.8: Phase compositions and uncertainties (s) for a single sample of Bell River fly ash after 7 d exposure to 8 M NaOH solution; a minimum of three measurements was used, else the number of points tested is specified

		Mass % Element								
Phase	Data type	Ca	Si	Al	Fe	Na	Mg	K	O	Ti
C-A-S 1	**average**	**36.2**	**7.3**	**9.6**	**4.9**	**1.0**	**3.9**	**0.0**	**35.6**	**0.8**
	std. deviation	11.7	3.6	6.1	3.1	0.2	2.7	0.0	2.3	0.7
C-A-S 7	**average of two points**	**11.2**	**21.8**	**9.1**	**8.9**	**4.0**	**2.9**	**0.4**	**40.2**	**1.5**
N-A-S	**average**	**4.1**	**30.3**	**11.4**	**1.2**	**6.0**	**1.0**	**1.5**	**44.0**	**0.5**
	std. deviation	3.9	5.9	2.6	0.9	1.4	0.8	0.9	2.0	0.7
Mg-rich	**average**	**31.1**	**5.6**	**15.6**	**6.5**	**0.9**	**4.9**	**0.0**	**34.5**	**0.6**
	std. deviation	3.8	3.2	2.0	2.5	0.3	2.4	0.0	1.2	0.6
Quartz	**average**	**0.4**	**49.2**	**0.1**	**0.3**	**0.8**	**0.0**	**0.2**	**48.9**	**0.0**
	std. deviation	0.6	1.2	0.2	0.7	1.3	0.0	0.4	1.6	0.0
Reaction product	**average**	**18.9**	**10.3**	**8.7**	**3.9**	**6.7**	**3.2**	**0.4**	**46.8**	**0.6**
	std. deviation	11.8	11.7	2.8	3.2	7.7	2.2	0.8	8.0	0.6

Table 5.9: Phase compositions and uncertainties (s) for a single sample of Bell River fly ash after 28 d exposure to 8 M NaOH solution; a minimum of three measurements was used, else the number of points tested is specified

		Mass % Element								
Phase	Data type	Ca	Si	Al	Fe	Na	Mg	K	O	Ti
C-A-S 2	**single point**	**25.8**	**11.2**	**7.9**	**3.6**	**1.8**	**3.8**	**0.0**	**30.2**	**0.4**
C-A-S 6	**average**	**5.2**	**34.0**	**4.9**	**1.1**	**4.3**	**0.6**	**0.5**	**40.2**	**0.9**
	std. deviation	3.9	3.3	3.5	1.0	0.7	0.7	0.5	3.3	1.9
N-A-S	**single point**	**0.0**	**21.7**	**16.7**	**0.0**	**7.2**	**0.0**	**0.9**	**38.0**	**0.0**
Reaction product	**average**	**4.5**	**15.0**	**8.6**	**2.1**	**4.1**	**2.3**	**0.0**	**30.4**	**0.4**
	std. deviation	5.0	5.0	4.3	3.0	0.6	2.6	0.0	2.9	0.7

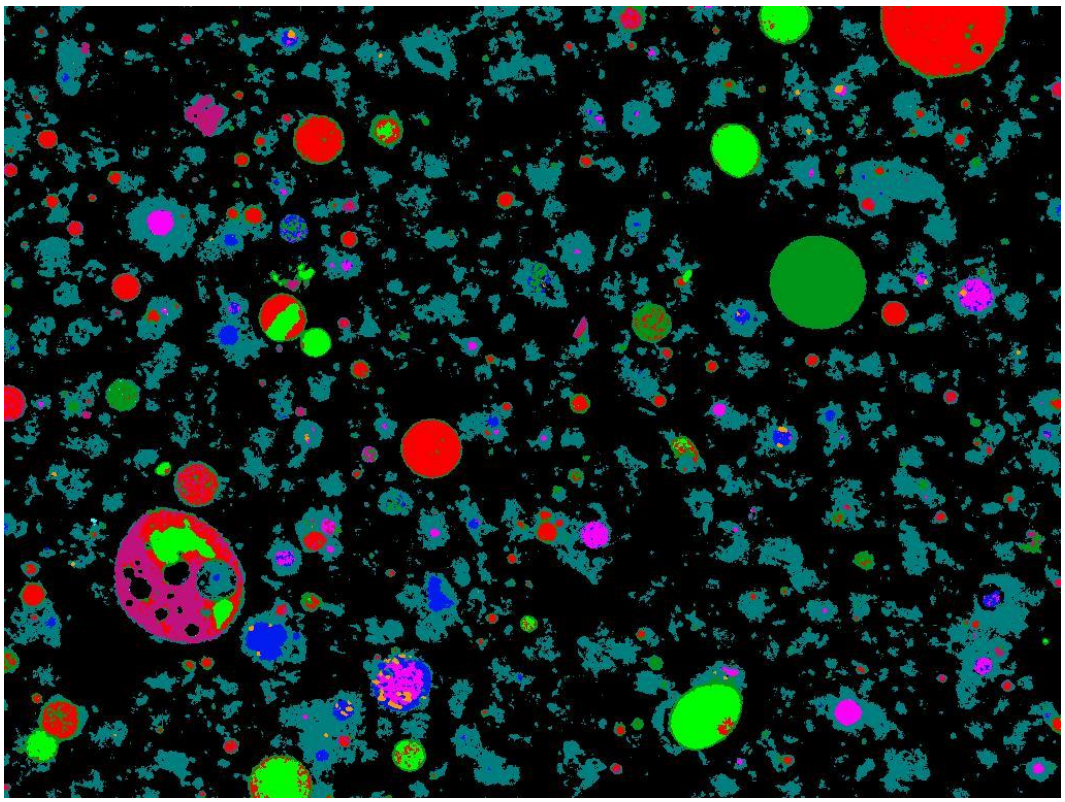

Figure 5.8: Phase assignment image of Bell River fly ash residue after 7 d exposure to 8 M NaOH solution

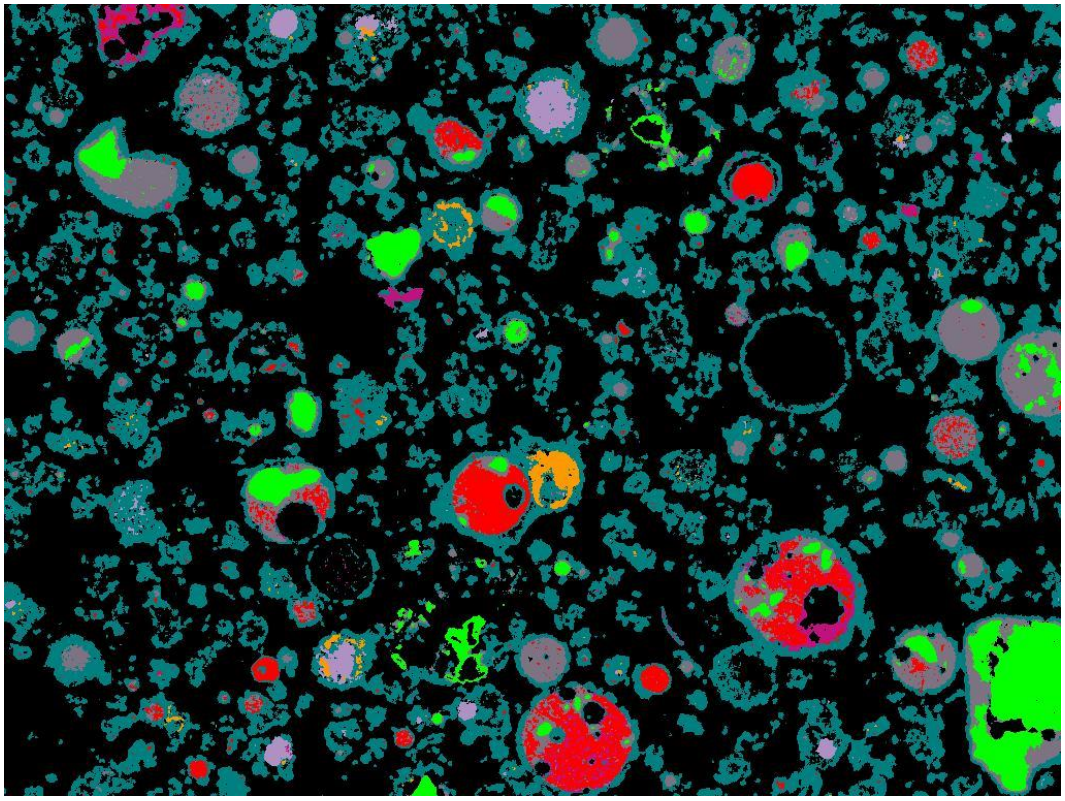

Figure 5.9: Phase assignment image of Bell River fly ash after 28 d of exposure to 8 M NaOH solution

a)

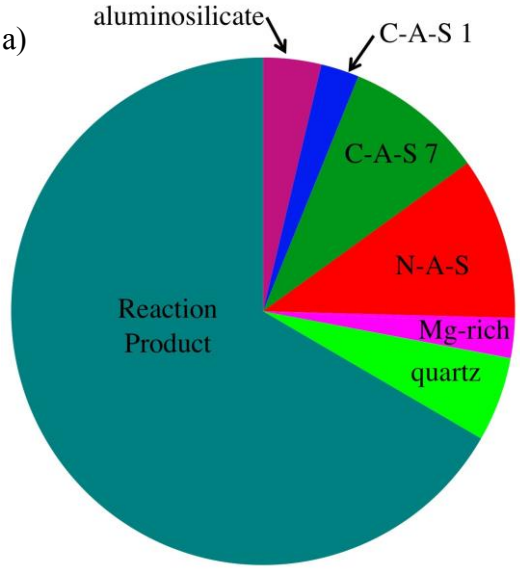

Phase	Area %
aluminosilicate	3.73
C-A-S 1	2.45
C-A-S 7	8.89
N-A-S	10.34
Mg-rich	0.36
Mg-rich	2.19
Fe-rich	0.02
quartz	5.37
reaction product	66.64

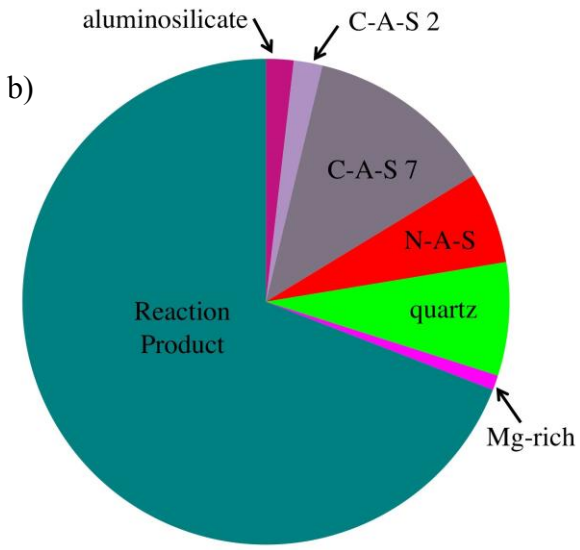

Phase	Area %
aluminosilicate	1.83
C-A-S 2	1.90
C-A-S 6	12.55
N-A-S	6.10
quartz	7.54
Mg-rich	0.99
reaction product	69.08

Figure 5.10: The phase distribution of Bell River fly ash after 7 d (a) and 28 d (b) exposure to 8 M NaOH solution; each based on a single sample

The Bell River fly ash changed somewhat significantly across the time steps, mainly in the C-A-S phases as shown in Figure 5.11. The Bell River fly ash original sample did not add to 100 % due to the non-inclusion of the iron-rich phase, which was high in the original sample due to a single particle inclusion. It was not identified in high amount in the 7 d and 28 d samples, but this change is attributed to sampling error and not reactivity of the iron-rich phase. One unexpected change over time was that the total amount of all C-A-S phases increased over time, which was not expected since these phases were thought to be soluble. However, the fly ash is a high-calcium fly ash, which could have meant that the low-calcium glasses still had slightly higher calcium than for lower calcium fly ashes. One possible explanation for the C-A-S phase increase results from examining the composition of the C-A-S 6 phase that was identified at 28 d in large amounts, since it was compositionally similar to the aluminosilicate phases that were presumed to be poorly reactive; the main difference in composition was the C-A-S 6 phase contained around 7 % calcium, which was slightly higher than the A-S phases

which were defined as having less than 5 % calcium. Therefore, it is possible that the calcium content was not sufficient to alter the glassy structure enough to result in high reactivity. The C-A-S 6 phase was identified in the original fly ash and the 28 d residue. It is unclear why the phase was not present in the 7 d sample. The C-A-S 7 phase that was present in highest amount at 7 d was somewhat similar in composition to C-A-S 6, with slightly higher silicon content. The C-A-S 1 phase disappeared after 7 d, and it was assumed to have dissolved. The Bell River fly ash was designated reactive by compressive strength testing. It appears that the C-A-S 1 phase dissolved after 7 d, and the C-A-S 7 phase appeared and dissolved after 7 d. These two phases appeared to be reactive in the Bell River fly ash. C-A-S 1 was hypothesized to be reactive and these results uphold that hypothesis.

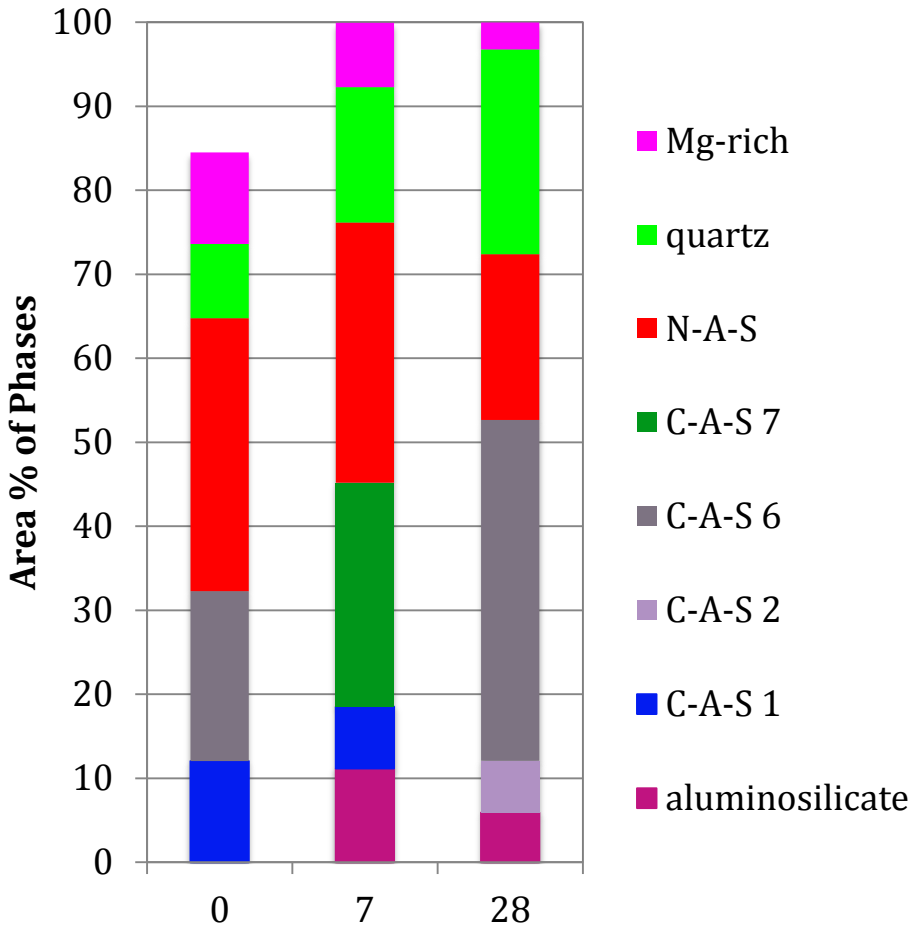

Figure 5.11: Bell River fly ash: relative composition of fly ash before and after exposure to 8 M NaOH solution

5.2.4 Big Brown Raw

The Big Brown Raw fly ash (Class F, ASTM C618) was considered reactive based upon its 28 d compressive strength shown in Section 5.1. Prior to exposure to NaOH the Big Brown Raw fly ash contained A-S 2, C-A-S 4, C-A-S 6, quartz, iron-rich phase and Mg-rich phase. 7 d quantitative compositional data were not available for this specimen since the point map that allowed for matching the phase to the compositional point data was lost; therefore, the 28 d fly ash residue data were directly compared to the fly ash data. The results showed that the aluminosilicate phase identified in the raw fly

ash changed from A-S 2 (Si/Al= 1.3) to A-S 1 (Si/Al = 2.3). The C-A-S phases originally identified (C-A-S 4 and C-A-S 6) were not found in the 28 d residue, but C-A-S 1 was identified. Quartz, Mg-rich phase and iron rich phase were identified in both samples. By 28 d, a reaction product had formed in the specimen, which was not surprising given the reactivity of the fly ash in the mortar cube study. These phases will serve as references to the changes observed in the samples over time.

As previously mentioned, 7 d data were collected for the fly ash; however, the point compositional analysis data could not be matched with phases because the point map was not recorded for this data set. In an attempt to name the phases segmented qualitatively by MSIA, the intensity values for the BBR 7 d training classes were compared to the intensity values in the training classes for other fly ashes to estimate what phases were present. The same microscope operating conditions were used for all data sets; therefore the intensities for each element should have been similar for similar phases, with some variation based on effects of the bulk fly ash composition. It was hypothesized that the 7 d specimen contained A-S 3, C-A-S 1, C-A-S 3, quartz, iron-rich, Mg-rich, and reaction product phases. The phase assignment image is given in Figure 5.12.

The 28 d specimen of Big Brown Raw fly ash consisted of A-S 1, C-A-S 1, quartz, iron-rich phase, and periclase. Reaction product made up the bulk of the image area at approximately 64 %. The point compositional data showed that two aluminosilicate phases that were classified as separate phases in MSIA were compositionally the same, as shown in Table 5.10 for the two A-S 1 phases. The phase compositions can be compared to Table 4.12, which gave the compositional ranges for each phase. As shown in the phase assignment image in Figure 5.13, A-S 1 is colored orange, and the particles in the phase were similar in size, shape, and texture; most were

larger-sized and most had irregular shapes and vesicular texture. The A-S 1 phase had lower Si/Al mass ratio than A-S 2, at approximately 2.4 compared to the Si/Al of 1.4 for the A-S 2 in the raw material. The C-A-S 1 phase was high in calcium (34 mass %), and low in silicon and aluminum (8.45 mass % and 7.5 mass %, respectively). This phase was identified in few particles, and it was typically surrounded by the reaction product phase. The Mg-rich phase was interspersed with the C-A-S 1 phase in several particles, and it contained magnesium, iron, aluminum, silicon, and calcium, in order of decreasing amount.

Table 5.10: Phase compositions and uncertainties (s) for a single sample of Big Brown Raw fly ash after 28 d exposure to 8 M NaOH solution; a minimum of three measurements was used, else the number of points tested is specified

		Mass % Element								
Phase	Data type	Ca	Si	Al	Fe	Na	Mg	K	O	Ti
A-S 1	**average**	**5.4**	**29.0**	**12.5**	**4.2**	**1.5**	**1.6**	**1.0**	**44.4**	**0.3**
	std. deviation	3.2	2.3	1.2	1.1	0.6	0.5	0.9	2.5	0.4
A-S 1	**average**	**4.5**	**29.3**	**13.1**	**3.8**	**2.6**	**1.3**	**1.0**	**44.1**	**0.3**
	std. deviation	2.8	4.9	3.4	1.5	3.9	0.7	0.8	1.1	0.4
C-A-S 1	**average**	**34.1**	**8.5**	**7.5**	**5.6**	**0.2**	**5.3**	**0.0**	**37.2**	**0.5**
	std. deviation	3.3	8.1	4.5	3.5	0.3	3.7	0.0	2.5	0.4
Mg-rich	**single point**	**3.3**	**5.9**	**9.0**	**8.9**	**2.3**	**18.2**	**0.0**	**51.5**	**1.0**
Reaction product	**average**	**17.1**	**16.0**	**6.1**	**6.8**	**5.2**	**3.0**	**0.0**	**44.8**	**1.0**
	std. deviation	5.4	4.4	1.0	1.6	2.2	1.2	0.0	3.8	0.3
Quartz	**single point**	**0.0**	**48.6**	**0.0**	**0.0**	**0.0**	**0.0**	**0.0**	**51.4**	**0.0**

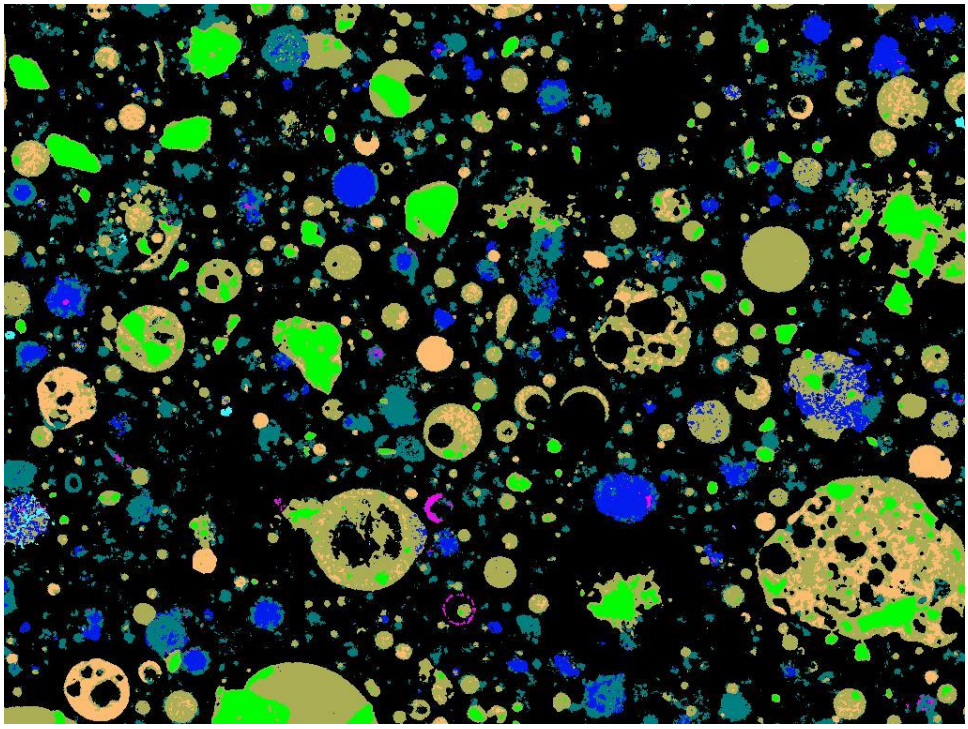

Figure 5.12: Phase assignment image of Big Brown Raw fly ash residue after 7 d exposure to 8 M NaOH, phase assignments made based upon training class intensities instead of point compositional data

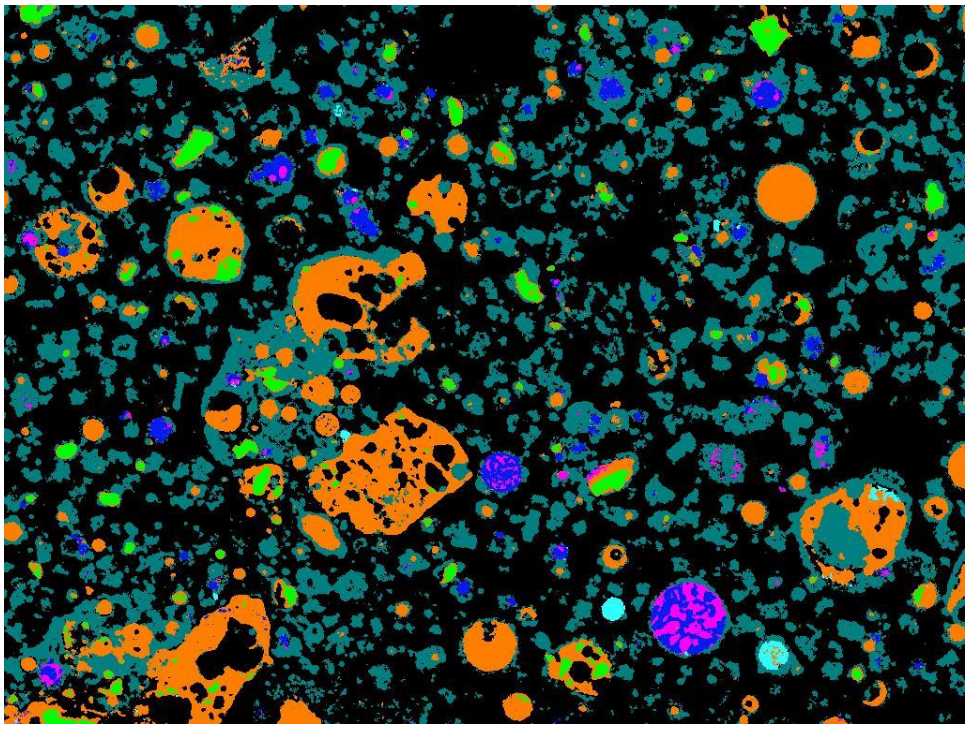

Figure 5.13: Phase assignment image of Big Brown Raw fly ash residue after 28 d exposure to 8 M NaOH solution

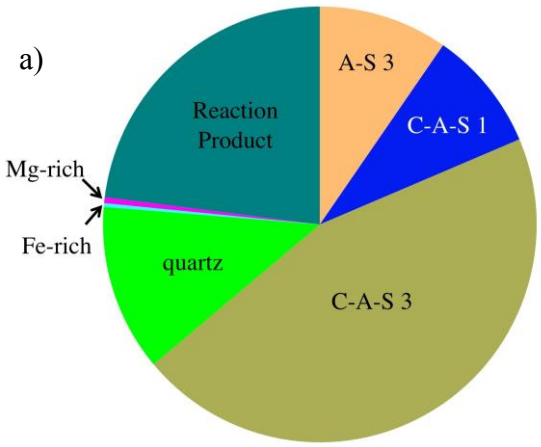

Phase	Area %
A-S 3	9.63
C-A-S 1	8.98
C-A-S 3	45.29
quartz	12.37
Fe-rich	0.28
Mg-rich	0.43
reaction product	23.00

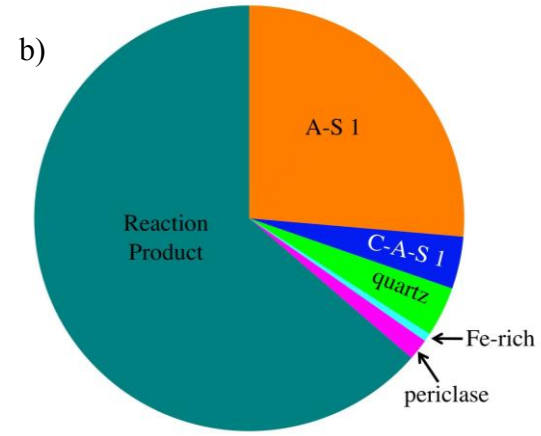

Phase	Area %
A-S 1	11.58
A-S 1	14.79
C-A-S 1	3.97
quartz	3.79
Fe-rich	0.63
Mg-rich	1.62
reaction product	63.59

Figure 5.14: The phase distribution of Big Brown Raw fly ash after 7 d (a) and 28 d (b) exposure to 8 M NaOH solution; each based on a single sample

The reaction product identified in the 28 d specimen had similar amounts of calcium and silicon (17 %, by mass) and similar aluminum, iron and sodium amounts (6 %, by mass).

The compositional changes over time for all three data sets are shown in Figure 5.15. The Big Brown Raw fly ash had an expected result in that it was originally comprised of several C-A-S phases and quartz, but after 28 d, it was mainly comprised of the aluminosilicate phase A-S 1. It is important to note that the 7 d results were hypothesized based on intensities, so these may not be the accurate phase designations.

Comparing the original fly ash to 28 d is more likely to explain the results accurately. Since the aluminosilicate phases were not hypothesized to react significantly, the increase in aluminosilicate signifies that the C-A-S phases were reactive in this fly ash. Only a small amount of C-A-S 1 remained in the 28 d residue. The many changes in the C-A-S phases cannot be explained with certainty, although it is hypothesized that C-A-S 4 was soluble and C-A-S 6 was soluble, since they each disappeared by 7 d. The appearance of C-A-S 1 (37 % calcium, 9 % silicon, 8 % aluminum, by mass) at late age was somewhat surprising, but it is possible that C-A-S 4 (29 % calcium, 10 % silicon, and 12 % aluminum, by mass) was leached of aluminum, resulting in this phase. The release of sufficient aluminum in solution is essential to geopolymer formation (Duxson and Provis 2008), so if that occurred, this fly ash being the highest in compressive strength at 28 d may be explained. This fly ash was designated reactive in the compressive strength testing, and it is very clear for this fly ash that the C-A-S phases were dissolved such that the 28 d residue was nearly entirely low-to non-reactive aluminosilicate glass.

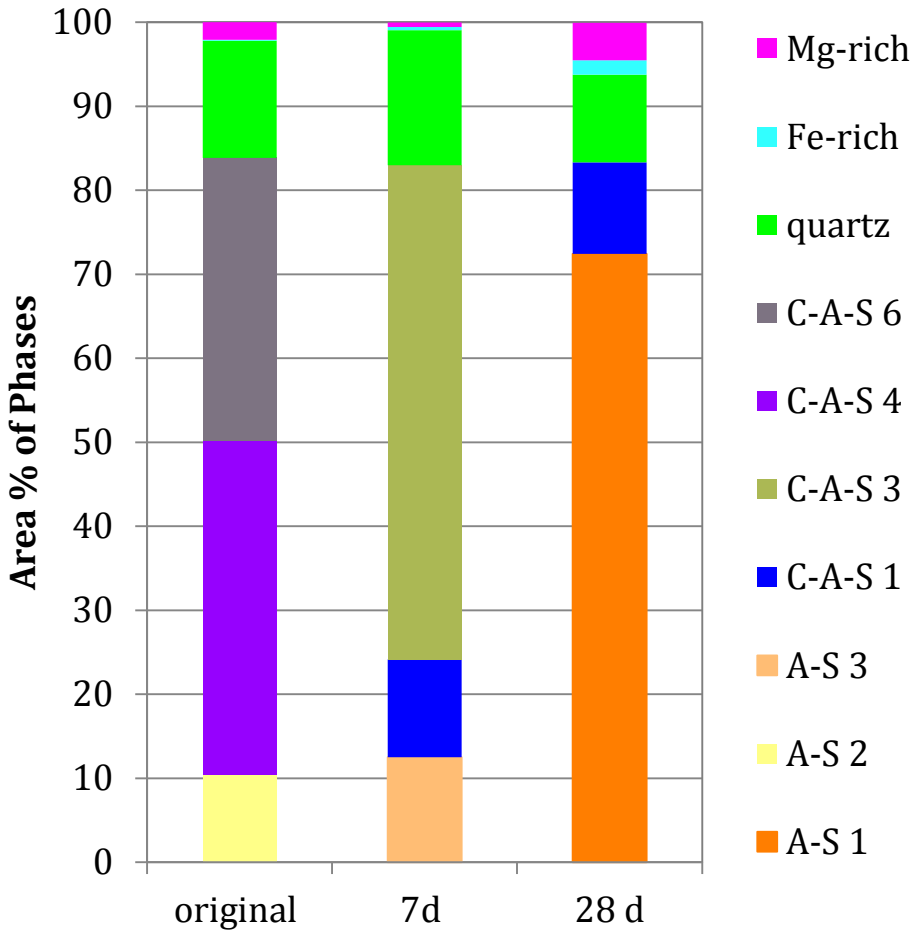

Figure 5.15: Big Brown Raw fly ash: relative composition of fly ash before and after exposure to 8 M NaOH solution

5.2.5 Centralia fly ash

The Centralia fly ash (Class F, ASTM C618) was considered a reactive fly ash based upon the compressive strength results presented in Section 5.1. The composition changed over time from the raw material to the residues at 7 d and 28 d. Prior to exposure to NaOH the following phases were identified in the Centralia fly ash: A-S 2, C-A-S 2, N-A-S, quartz, iron-rich, and Mg-rich phases. The 7 d sample had no aluminosilicate, two C-A-S phases, N-A-S, quartz, iron-rich, and Mg-rich. By 28 d there were three C-A-S phases, N-A-S, quartz, and iron-rich. Reaction product was identified

after 7 d and 28 d of exposure, which was not surprising given the reactivity of the fly ash as determined in the mortar cube experiment.

The Centralia fly ash after 7 d of exposure did not contain an A-S phase. The phase compositions are given in Table 5.11, while the phase assignment image is given in Figure 5.16. The phase compositions can be compared to Table 4.12, which gave the compositional ranges for each phase. The relative amounts of the phase are given in Figure 5.18. C-A-S phases identified were of different composition than the C-A-S phase identified in the raw fly ash. C-A-S 4 (bright purple) contained approximately 30 % calcium by mass, 9 % silicon, and 13 % aluminum, with iron and magnesium making up most of the remainder, while C-A-S 9 (berry pink) contained 7 % calcium by mass, 24 % silicon by mass, and 17 % aluminum by mass and included small amounts of iron, sodium, magnesium, and potassium. The C-A-S 4 phase was similar in composition to the C-A-S 2 phase, and it was also present in particles of similar morphology. The C-A-S 9 phase was compositionally similar to the A-S 2 phase identified in the raw fly ash and its particle morphology of medium-to-large particle size was similar, as well. It is possible these two phases were mis-classified using the point averages or that the raw material phases dissolved slightly to change composition, resulting in these phases at 7 d. N-A-S (red) was compositionally the same as in the raw material, but its proportion had changed. The iron-rich (aqua), magnesium rich (magenta), and quartz (lime green) phases were all identified at both ages. Reaction product (teal) was also identified at 7 d.

By 28 days, there were different phases identified including C-A-S 1 (blue), C-A-S 2 (lavender), C-A-S 8 (yellow), N-A-S (red), quartz (lime green), Fe-rich (aqua), and reaction product (teal). The compositions of the phases are given in Table 5.12, and the phase assignment image is given in Figure 5.17. The phase compositions can be compared to Table 4.12, which gave the compositional ranges for each phase. The

relative amounts of each phase are shown in Figure 5.18. No aluminosilicate phase was identified in the 28 d specimen as in the 7 d sample; however, the C-A-S 8 particle morphology was similar to A-S 2 particles from the raw material and the Si/Al ratios and amounts of Si and Al were similar, although C-A-S 8 phase calcium content was significantly higher (10 mass % versus 3 mass %). The A-S 2 phase identified in the raw material also had one of the highest sodium contents, so some A-S 2 could have been classified as N-A-S in this specimen. The N-A-S phase had Si/Al of 3, and the sodium content was low compared to other N-A-S phases (defined for each fly ash in its respective section) at 3% by mass. The phase was nearly identical in composition to the N-A-S phase identified in the raw material and at 7 d.

Table 5.11: Phase compositions and uncertainties (s) for a single sample of Centralia fly ash after 7 d exposure to 8 M NaOH solution; a minimum of three measurements was used, else the number of points tested is specified

		Mass % Element								
Phase	Data type	Ca	Si	Al	Fe	Na	Mg	K	O	Ti
C-A-S 4	average	29.6	8.6	13.3	7.1	0.0	3.9	0.0	34.9	2.3
	std. deviation	5.2	4.7	5.8	3.6	0.0	2.6	0.0	1.8	1.6
C-A-S 9	average of 2 points	7.3	23.3	16.5	3.5	4.0	2.1	1.4	41.9	0.0
N-A-S	average	3.3	34.2	8.7	3.1	3.0	1.4	2.4	43.1	0.8
	std. deviation	2.6	2.0	3.2	0.7	0.9	0.4	1.0	1.0	1.8
Fe-rich	single point	3.9	9.4	3.3	48.8	0.7	2.2	0.0	31.9	0.0
quartz	single point	0.0	51.8	0.0	0.0	0.0	0.0	0.0	48.2	0.0
reaction product	average of 2 points	33.9	7.0	8.2	8.2	0.4	2.5	0.0	35.5	1.6

Table 5.12: Phase compositions and uncertainties (s) for a single sample of Centralia fly ash after 28 d exposure to 8 M NaOH solution; a minimum of three measurements was used, else the number of points tested is specified

		Mass % Element								
Phase	Data type	Ca	Si	Al	Fe	Na	Mg	K	O	Ti
C-A-S 2	average of 2 points	26.9	12.6	9.8	6.3	0.0	5.5	0.0	38.0	0.9
C-A-S 8	average of 2 points	10.5	21.1	10.9	5.4	2.0	1.9	0.4	41.7	6.0
N-A-S	average	1.9	31.9	10.2	3.3	3.2	1.3	3.2	44.6	0.5
	std. deviation	1.1	3.2	1.7	1.4	0.5	0.8	1.5	0.7	0.6
Fe-rich	single point	6.7	22.1	7.3	15.9	3.0	1.7	0.9	40.1	2.3
quartz	average	0.0	48.7	0.4	0.1	0.3	0.0	0.2	50.3	0.0
	std. deviation	0.0	1.6	0.8	0.2	0.5	0.0	0.6	1.0	0.0
Reaction product	average	10.5	18.0	6.4	9.8	4.5	5.5	0.2	44.0	1.2
	std. deviation	2.6	3.0	3.3	3.4	1.4	1.7	0.3	5.1	0.5

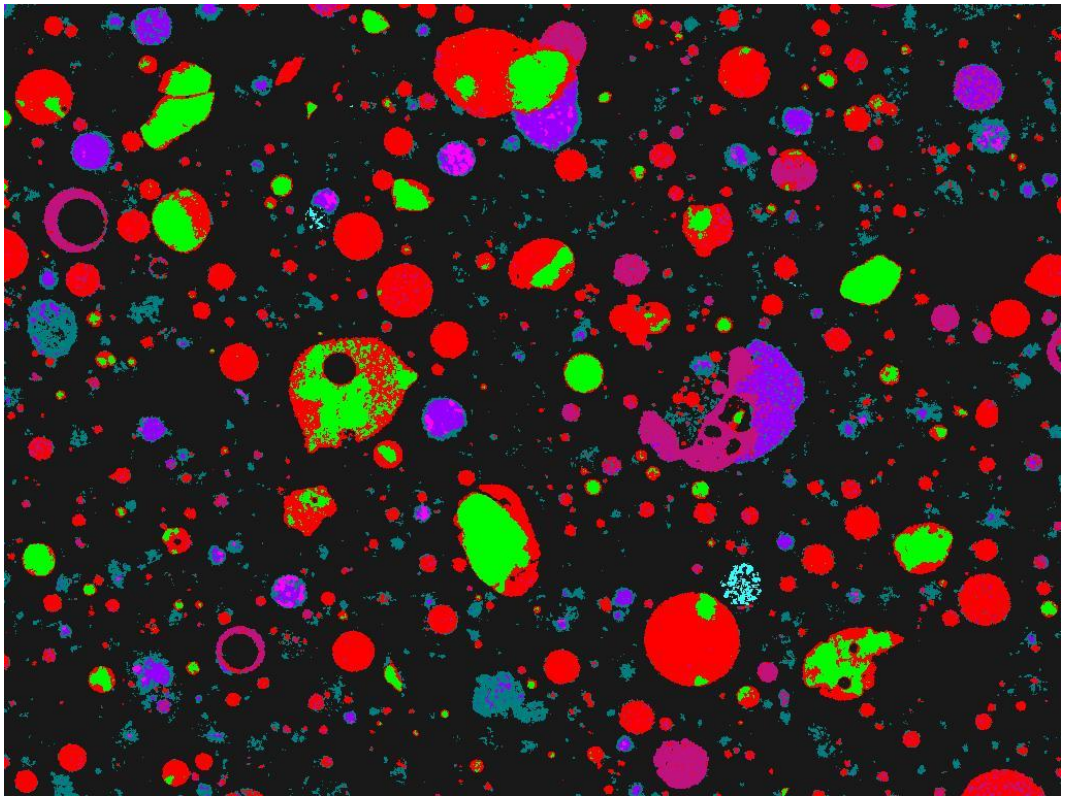

Figure 5.16: Phase assignment image of Centralia fly ash residue after 7 d exposure to 8 M NaOH solution

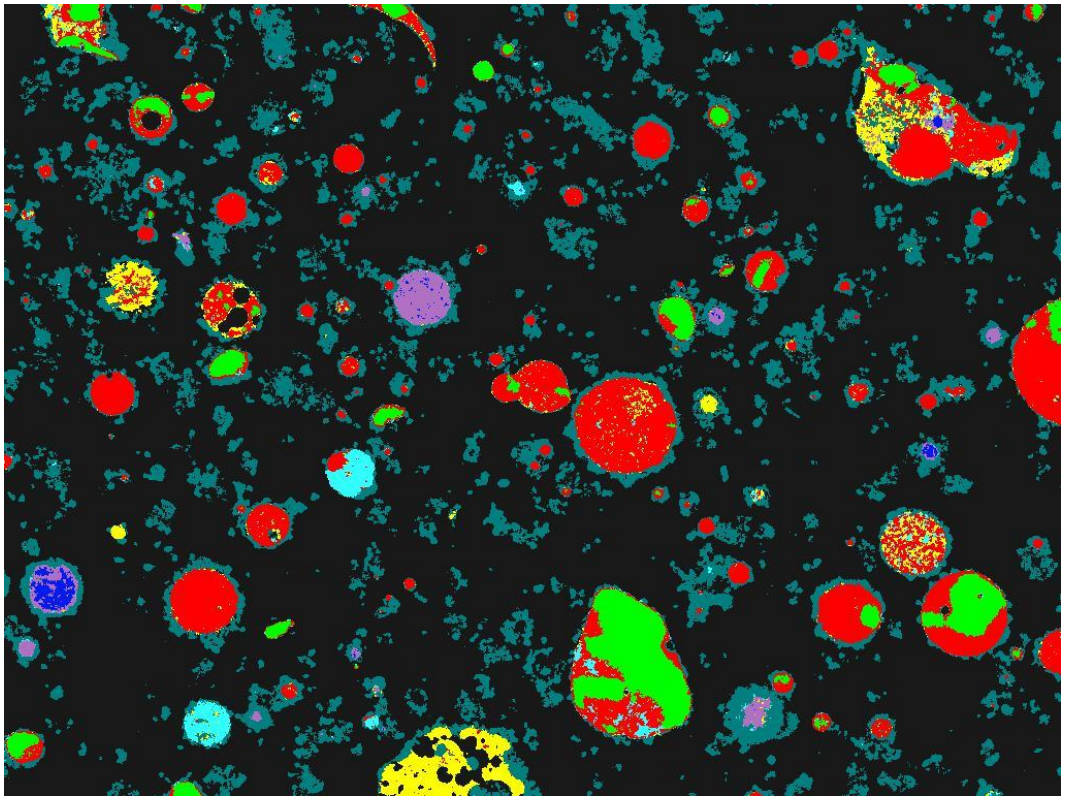

Figure 5.17: Phase assignment image of Centralia fly ash residue after 28 d exposure to 8 M NaOH solution

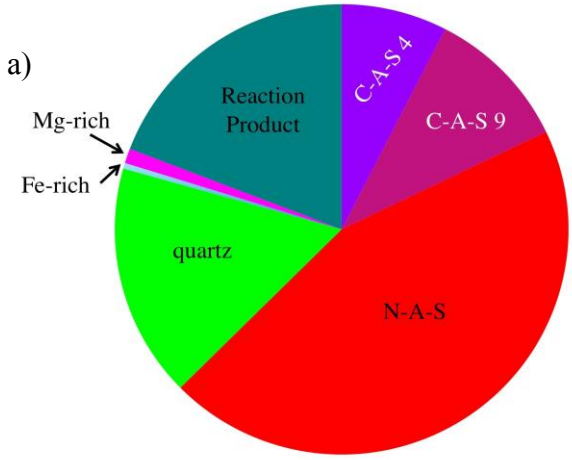

Phase	Area %
C-A-S 4	7.55
C-A-S 9	10.32
N-A-S	44.72
quartz	16.78
Fe-rich	0.41
Mg-rich	1.06
Reaction Product	19.17

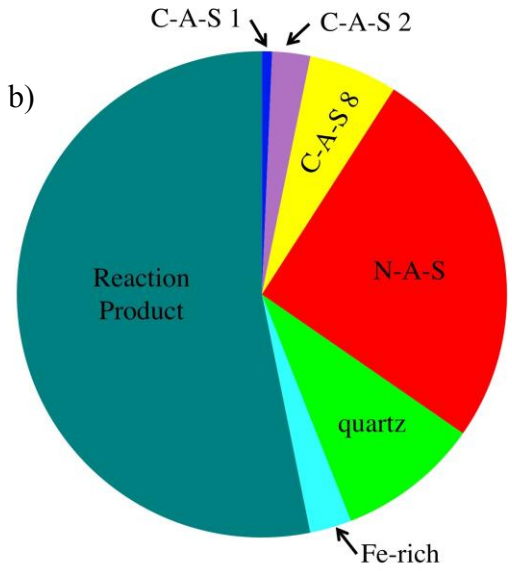

Phase	Area %
C-A-S 1	0.67
C-A-S 2	2.52
C-A-S 8	5.86
N-A-S	25.64
quartz	9.40
Fe-rich	2.75
Reaction Product	53.17

Figure 5.18: The phase distribution of Centralia fly ash after 7 d (a) and 28 d (b) exposure to 8 M NaOH solution; each based on a single sample

The fly ash residues each contained reaction products. At 7 d, the Centralia fly ash residue contained high calcium (33 % by mass) and relatively low silicon and aluminum (around 8 % each, by mass). Iron was present at nearly the same amount as silicon and aluminum, while sodium was exceptionally low. This reaction product composition implies high dissolution of calcium prior to 7 d with slower silicon, aluminum, and iron dissolution. At 28 d, the element present in the greatest amount was silicon at 18 % by mass, while calcium was measured at 10 % by mass, iron at 10 % by mass, sodium at 5 % by mass, and nearly 6 % magnesium by mass. These results showed that silicon dissolved between 7 and 28 d at a higher amount than in the first 7 d.

The relative compositions of the fly ash at all time intervals are shown in Figure 5.19. The Centralia fly ash results showed a decrease of the total amount of C-A-S phases by 28 d, while the N-A-S phase increased. This result implied that the C-A-S phases in the Centralia fly ash dissolved in solution, while the N-A-S was poorly soluble. The lack of an A-S phase at 7 d may be attributed to N-A-S phase, since the content of

the modifier Na was only around 3 % in the N-A-S phases at 7 d and 28 d, which was approximately the same as for the A-S and N-A-S phases in the original fly ash. It appears from examining the phase compositions that the only distinction between A-S 2 and N-A-S in the raw fly ash was differences in the amounts of Al and Si, which were 28 % and 15 %, by mass, in the A-S 2 phase and 35 and 9 %, by mass, in the N-A-S phase, respectively. Since the compositions of N-A-S phases are consistent at all data collection times, perhaps aluminum leached from the A-S 2 phase, resulting in its grouping with N-A-S at later ages. This fly ash was considered reactive, and the trends are somewhat unclear as to why the fly ash was classified this way, since it seemed to mostly consist of poorly soluble N-A-S and A-S phases; however, if aluminum was leached early from the A-S 2 phase, this could explain the favorable strength results since the rate of aluminum available at early age is known to improve reactivity for geopolymers (Duxson and Provis 2008).

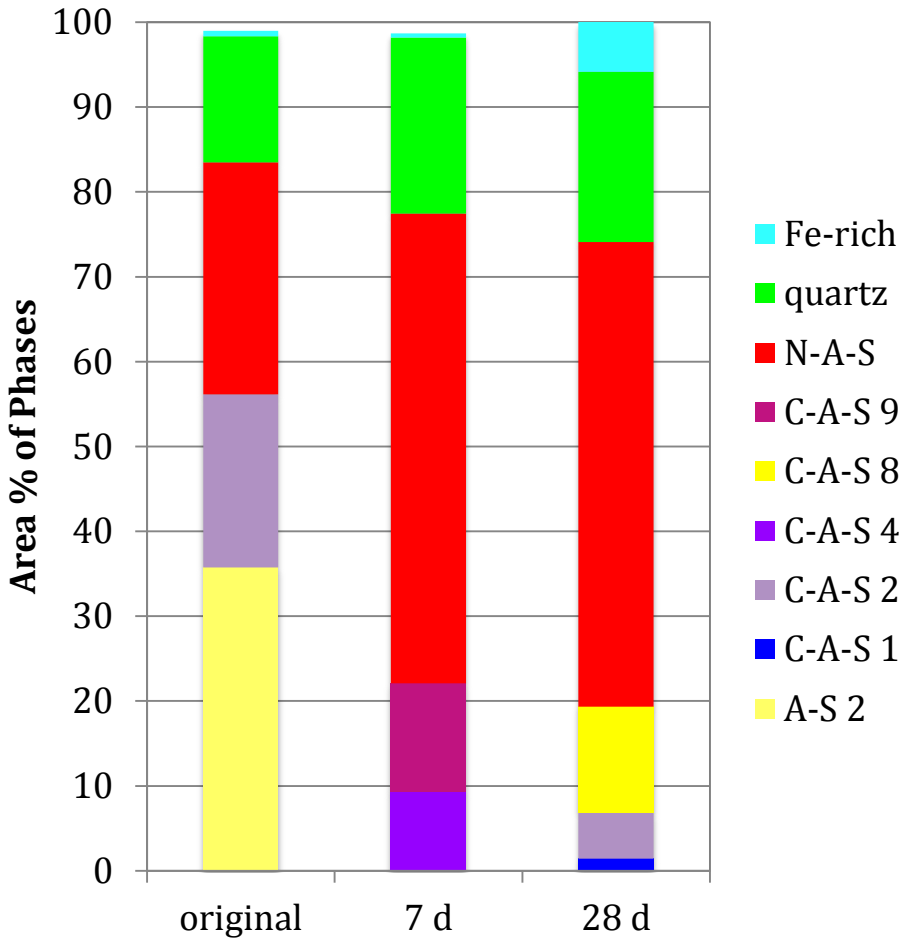

Figure 5.19: Centralia fly ash: relative composition of fly ash before and after exposure to 8 M NaOH solution

5.2.6 Coleto Creek fly ash

The Coleto Creek fly ash (Class F, ASTM C 618) was considered a reactive fly ash based on the results of the compressive strength shown in Figure 5.1. The Coleto Creek fly ash consisted of eight phases prior to its exposure to the NaOH solution including A-S 2, C-A-S 1, C-A-S 5, C-A-S 7, K-A-S, quartz, periclase and an iron-rich phase. After 7 d of NaOH exposure, the A-S phases identified included A-S 1 and A-S 4, while there was only one C-A-S phase, which was C-A-S 4. The K-A-S phase was not identified in the 7 d sample. Quartz and reaction product were also identified at 7 d. By

28 d, the A-S 1 phase remained, and two different C-A-S phases (C-A-S 3 and C-A-S 6) were identified. The K-A-S phase identified in the raw material was again identified at 28 d; however, this was a designation issue, as the main particle in question was actually remnant alkali feldspar that passed through the boiler. A few other particles were also classified into this phase that were likely actually K-A-S glasses. Periclase was also found again at 28 d after being absent at 7 d, and it was considered a sampling error. Reaction product was observed at 28 d. The reaction products at 7 and 28 d were as expected given the reactivity determined in compressive strength testing presented in Section 5.1.

By 7 d, the Coleto Creek fly ash residue consisted of A-S 1, A-S 4, C-A-S 4, an aluminate phase, and quartz. The phase compositions are given in Table 5.13 and the phase assignment image is shown in Figure 5.20. The phase compositions can be compared to Table 4.12, which gave the compositional ranges for each phase. The aluminosilicate glasses in the fly ash residue were of the form A-S 1 and A-S 4, instead of the A-S 2 phase identified in the fly ash. The A-S 1 (orange) phase was identified using the intensity ratios of the phase, since point compositional data were not taken in any particles classified in the phase. The particle morphology for A-S 1 particles was varied, with some large, irregular particles and some medium-sized round particles. The A-S 4 phase (bright yellow) was highly siliceous (30 mass %) with approximately 10 % by mass aluminum and around 2 % by mass calcium. The morphology of the A-S 4 (yellow) particles tended to be round and large-diameter particles. There were only two C-A-S phases in the residue instead of the three identified in the fly ash. The C-A-S 4 phase (purple) had slightly lower calcium than the C-A-S 1 phase identified in the fly ash, but it had similar amounts of silicon and slightly higher aluminum. This phase was in medium-sized circular particles dispersed through the specimen. The C-A-S 8 phase was

near 10 mass % calcium with 26 mass % silicon and 14 mass % aluminum. The aluminate phase was exclusive to this specimen and was 40 mass % aluminum and 6 mass % each iron and magnesium. This phase was identified in a single particle. The Fe-rich phase was not identified in the 7 d residue.

At 28 days, six phases were identified in the Coleto Creek fly ash residue including A-S 1, C-A-S 3, C-A-S 6, K-A-S, quartz, Mg-rich, periclase, and reaction product. The phase compositions are given in Table 5.14, and the phase assignment image is shown in Figure 5.22. The phase compositions can be compared to Table 4.12, which gave the compositional ranges for each phase. The aluminosilicate phase remained as A-S 1, and the A-S 4 phase was no longer identified. The C-A-S 6 phase was similar in composition to A-S 4, with slightly greater calcium content at 5 % by mass compared to the A-S 4, which contained 2 % calcium by mass. A-S 1 and C-A-S 6 tended to be identified in the same particles, and their morphology was larger-size and round, typically with air voids noted in the particle. C-A-S 3 was the other C-A-S phase identified. The C-A-S 3 phase had similar amounts of calcium and aluminum to C-A-S 1, but the silicon was significantly higher. The C-A-S 3 class was found in few medium-sized round particles. The K-A-S phase was identified in one particle after being absent from the 7 d sample. The phase was in a single large particle, and the angular morphology and composition implied that this was an alkali feldspar material that was a remnant from the parent coal material (McCarthy et al. 1989). The quartz decreased slightly from the raw material, and Mg-rich and periclase phases were identified in very small amounts. The iron-rich phase was not identified after NaOH exposure.

Table 5.13: Phase compositions and uncertainties (s) for a single sample of Coleto Creek fly ash after 7 d exposure to 8 M NaOH solution; a minimum of three measurements was used, else the number of points tested is specified

		Mass % Element								
Phase	Data type	Ca	Si	Al	Fe	Na	Mg	K	O	Ti
Aluminate	**single point**	**2.9**	**2.8**	**40.3**	**6.2**	**1.0**	**6.4**	**0.0**	**39.2**	**1.2**
A-S 4	**average**	**2.3**	**35.6**	**9.2**	**1.6**	**1.6**	**0.7**	**1.7**	**45.3**	**2.0**
	std. deviation	2.8	5.4	4.5	0.9	0.4	0.7	0.9	2.3	5.6
C-A-S 4	**average**	**29.7**	**7.1**	**10.9**	**6.5**	**0.2**	**4.1**	**0.0**	**37.5**	**0.8**
	std. deviation	5.0	2.7	3.3	2.6	0.5	2.1	0.0	4.5	0.5
C-A-S 8	**average**	**9.6**	**26.1**	**13.7**	**3.5**	**1.2**	**2.4**	**0.4**	**42.2**	**0.6**
	std. deviation	5.7	2.4	3.6	1.1	0.9	1.1	0.7	1.4	0.5
Quartz	**average**	**0.0**	**49.7**	**0.6**	**0.0**	**0.0**	**0.0**	**0.0**	**49.7**	**0.0**
	std. deviation	0.0	1.2	0.8	0.0	0.0	0.0	0.0	0.9	0.0
Reaction product	**average**	**22.3**	**7.2**	**9.1**	**8.0**	**2.1**	**5.2**	**0.1**	**45.5**	**0.4**
	std. deviation	6.4	6.0	1.1	2.9	1.4	4.1	0.3	5.4	0.3

Table 5.14: Phase compositions and uncertainties (s) for a single sample of Coleto Creek fly ash after 28 d exposure to 8 M NaOH solution; a minimum of three measurements was used, else the number of points tested is specified

		Mass % Element								
Phase	Data type	Ca	Si	Al	Fe	Na	Mg	K	O	Ti
A-S 1	**average**	**3.2**	**31.4**	**12.1**	**2.6**	**2.5**	**1.2**	**1.4**	**45.3**	**0.5**
	std. deviation	2.2	5.8	4.2	1.0	0.7	0.6	0.4	1.9	0.4
C-A-S 3	**average**	**27.4**	**15.6**	**7.0**	**5.0**	**0.0**	**5.2**	**0.0**	**38.2**	**0.9**
	std. deviation	5.3	6.3	2.7	0.7	0.0	1.5	0.0	1.8	0.1
C-A-S 6	**average**	**5.3**	**32.4**	**8.8**	**3.3**	**3.6**	**2.1**	**0.6**	**42.7**	**1.1**
	std. deviation	4.2	6.8	4.2	2.1	3.7	2.2	0.5	4.6	1.3
K-A-S	**average of 2 points**	**0.0**	**35.8**	**9.6**	**0.0**	**0.6**	**0.0**	**10.9**	**43.2**	**0.0**
Mg-rich	**average of 2 points**	**25.3**	**7.9**	**14.0**	**5.2**	**0.6**	**5.6**	**0.0**	**38.0**	**1.0**
Quartz	**average of 2 points**	**0.0**	**49.4**	**0.4**	**0.0**	**0.3**	**0.0**	**0.0**	**50.0**	**0.0**
Reaction product	**average**	**7.1**	**19.8**	**12.0**	**4.1**	**6.6**	**2.2**	**0.1**	**46.5**	**0.7**
	std. deviation	5.9	6.3	6.2	0.8	2.4	1.6	0.2	2.9	0.4

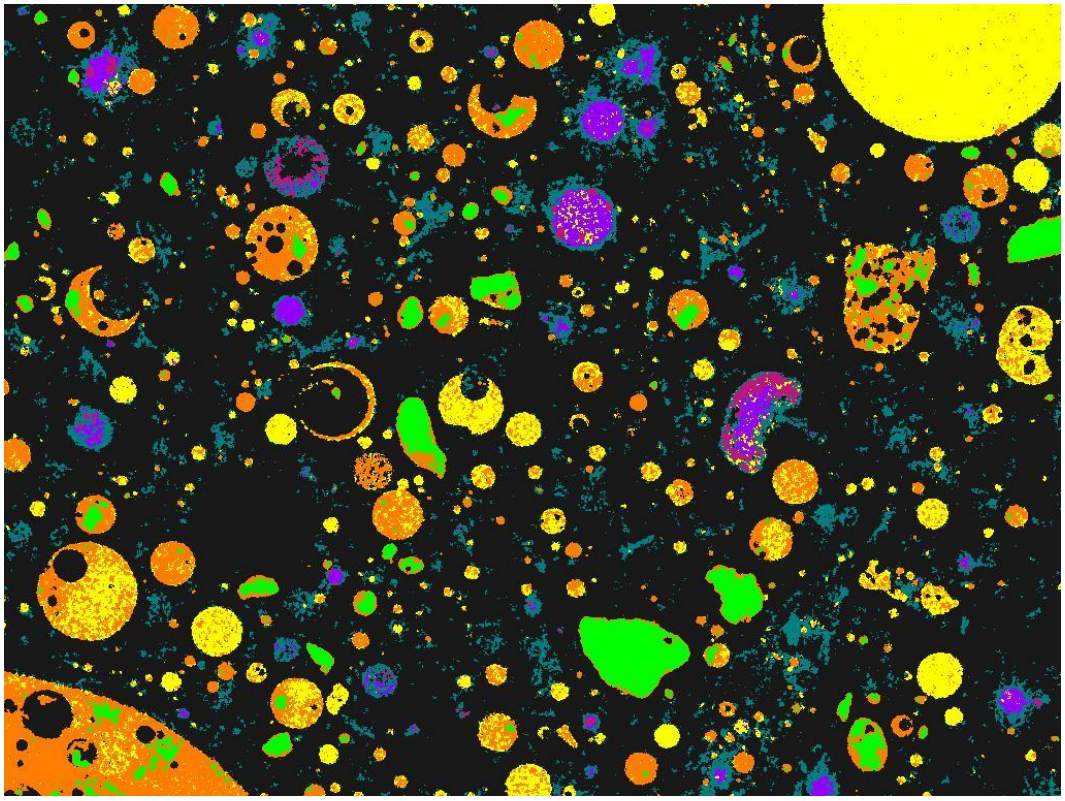

Figure 5.20: Phase assignment image of Coleto Creek fly ash residue after 7 d exposure to 8 M NaOH solution

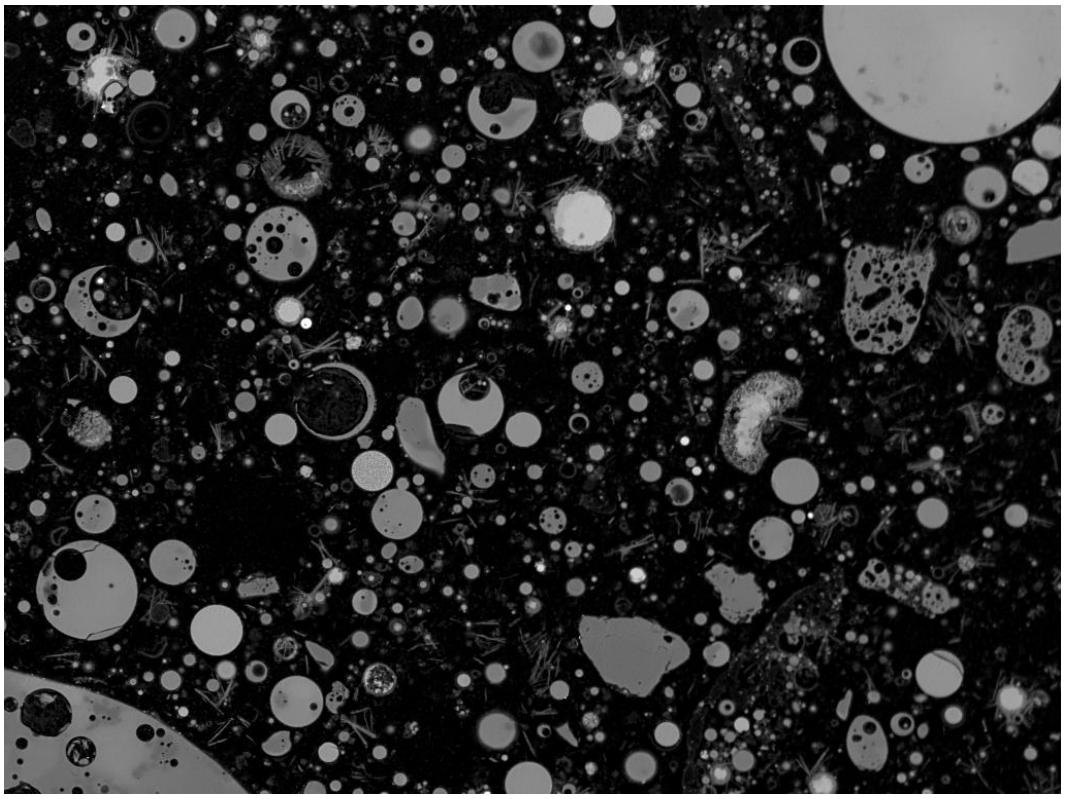

Figure 5.21: Backscattered electron image of Coleto Creek fly ash residue after 7 d exposure to 8 M NaOH solution

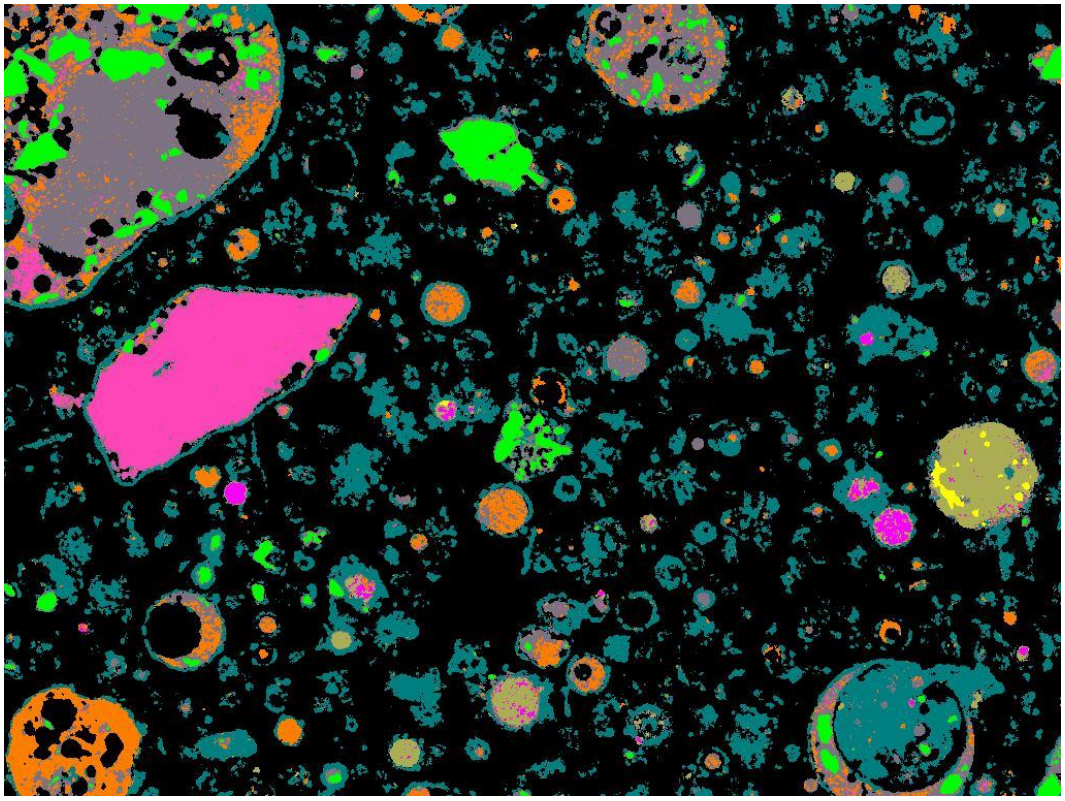

Figure 5.22: Phase assignment image of Coleto Creek fly ash residue after 28 d exposure to 8 M NaOH solution

a)

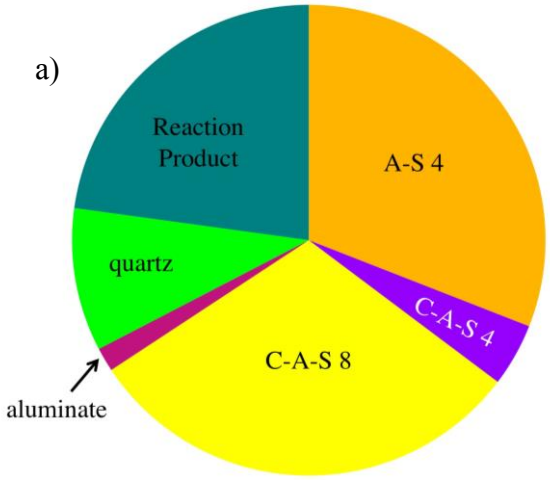

Phase	Area %
A-S 4	30.95
C-A-S 4	4.33
C-A-S 8	30.40
aluminate	1.65
quartz	9.83
reaction product	22.81

b)

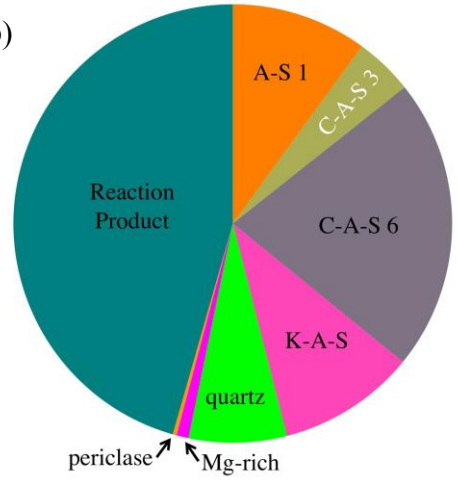

Phase	Area %
A-S 1	10.02
C-A-S 3	4.31
C-A-S 6	21.55
K-A-S	10.15
quartz	7.21
Mg-rich	0.89
periclase	0.29
reaction product	45.59

Figure 5.23: The phase distribution of Coleto Creek fly ash after 7 d (a) and 28 d (b) exposure to 8 M NaOH solution; each based on a single sample

The reaction products identified in the two specimens after 7 d and 28 d of NaOH exposure had different compositions. The 7 d reaction product was high in calcium at around 30 % by mass, with lower, similar amounts of silicon and aluminum (7 % by mass and 9 % by mass, respectively). The sodium content was low in the 7 d reaction product also, at around 2 % by mass. These compositional results showed that the calcium leached more easily in the first 7 d than silicon or aluminum. In addition, sodium, which was readily available in the activating solution, did not charge balance the reaction product, likely due to the positive charge of calcium. The 28 d reaction product had much lower calcium content (8 % by mass) than the 7 d reaction product, with high silicon (29 % by mass) and moderate aluminum (12 % by mass). The sodium was higher than the 7 d specimen at 6.5 % by mass. The 28 d reaction product showed that the silicon dissolved in much greater amount between 7 and 28 d.

The Coleto Creek fly ash compositional changes followed an expected pattern of increasing A-S phases over the time periods in the experiment. The comparisons of composition at each time step are given in Figure 5.24. The C-A-S 7 phase that was

present in large amounts in the raw material did not appear in the dissolved samples. The C-A-S 7 phase is hypothesized to have leached calcium, which would make its composition very similar to the A-S 4 phase at 7 d, which was present in simialar amount. C-A-S 7 had only 8% calcium, by mass, while the A-S 4 phase had 2.3. The silicon increased from 29 - 36 %, while the aluminum remained approximately constant when considering a change from C-A-S 7 to A-S 4. The A-S 4 phase (7 d) and C-A-S 6 phase (28 d) had nearly the same Si/Al ratio of 3.8 with the C-A-S 6 phase having slightly less silicon and aluminum overall, so it is hypothesized that A-S 4 and C-A-S 6 were the same phase, with the difference in calcium amount causing them to be classified as different phases. This implies that from 7 d to 28 d, silicon and aluminum leached from the A-S 4 phase. The Coleto Creek fly ash was considered reactive by compressive strength testing. This was generally upheld by the fact that it contained calcium-modified aluminosilicates at early age and mostly aluminosilicate phases at late age, with the exception of the relatively low-calcium C-A-S 6 phase.

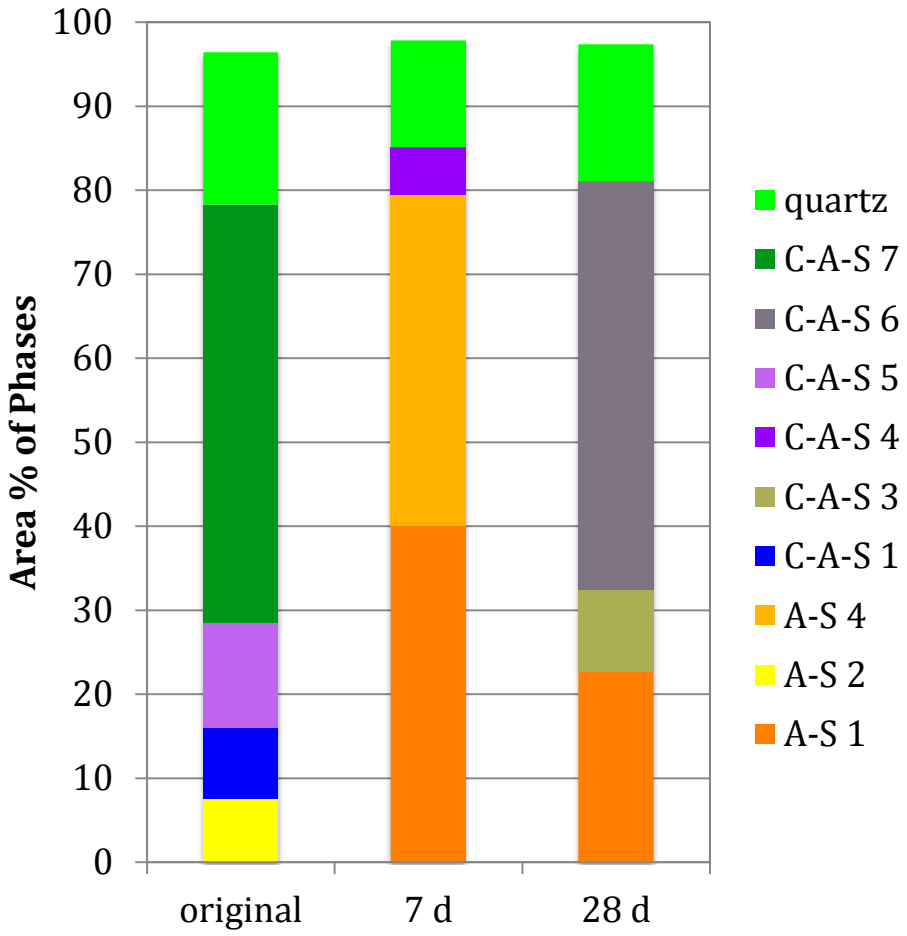

Figure 5.24: Coleto Creek fly ash: relative composition of fly ash before and after exposure to 8 M NaOH solution

5.2.7 Martin Lake fly ash

The Martin Lake fly ash was a Class F fly ash that was considered reactive based on its compressive strength results shown in Figure 5.1. The Martin Lake fly ash consisted of six phases in its original state, including A-S 2, C-A-S 5, C-A-S 6, C-A-S 8, iron-rich and quartz. The C-A-S 5 and C-A-S 6 phases were not identified in the 7 d sample or the 28 d sample. The A-S 2 phase was not identified in the 7 d sample, but it was identified at 28 d. The iron rich and quartz phases were consistently identified in all specimens. Also, reaction product was identified in both 7 d and 28 d specimens. The 7

d specimen had little reaction product, which was not very surprising given that this fly ash was barely reactive at 7 d. The reaction product was more visible and more easily segmented in the 28 d image.

The 7 d data was difficult to classify in MSIA, thus the results are of limited use in assigning the particles to phases. The segmentation difficulty was due to a poor-quality calcium map. Nevertheless, the MSIA phase assignment results for the fly ash residues are described here. The 7 d specimen contained C-A-S 2, C-A-S 7, iron-rich, magnesium-rich, quartz, and a small amount of reaction product. The compositions are given in Table 5.15, and the phase assignment image is presented in Figure 5.26. The phase compositions can be compared to Table 4.12, which gave the compositional ranges for each phase. The relative amounts of each phase are shown in Figure 5.28. The aluminosilicate phase was not identified in the 7 d sample. However, the morphology of some particles classified as C-A-S 7 (olive green) had similarities to the A-S 2 particles identified in the Martin Lake fly ash, so it appears that some particles may have been classified incorrectly. Further, the large standard deviation for the phase indicated that there may have been some points incorrectly classified into this class, which was revealed in inspection of the point data: the Ca content in the 11 points measured ranged from 1.02 to 18.87 mass %. (see appendix for the point compositional data). Therefore, it seems that the MSIA did not classify this phase reliably. The C-A-S 2 phase (lavender) had much better agreement between the five points analyzed and was high in calcium at 30 % by mass, with 12 % silicon by mass, and 10 % aluminum by mass. This phase had little in common with the compositions of the phases in the raw fly ash sample. It was identified in medium-sized circular particles. The iron-rich phase (aqua) was identified in dispersed, small particles and contained iron, calcium, silicon, and aluminum. The Mg-rich phase (magenta) was classified based on the magnesium signal in the point map,

but it had small amounts of magnesium and high calcium based upon the composition of a single point.

After 28 days of exposure to NaOH solution, there were two A-S phases identified (A-S 1 and A-S 2, orange and yellow, respectively). The phase compositions are given in Table 5.15 and the phase assignment image is shown in Figure 5.27. The phase compositions can be compared to Table 4.12, which gave the compositional ranges for each phase. A third aluminosilicate phase was identified, but it was not quantified with point quantitative analysis, and it is called "aluminosilicate" and is colored raspberry. A single C-A-S phase (C-A-S, light blue) was noted. The composition of this phase was high calcium of around 30 % by mass, with 10 % silicon and 5 % aluminum, by mass. The iron-rich phase remained at 28 days, but it was in a few small, dispersed particles and had composition that included iron, calcium, silicon, aluminum, and magnesium. The quartz had decreased somewhat at 28 days.

Table 5.15: Phase compositions and uncertainties (s) for a single sample of Martin Lake fly ash after 7 d exposure to 8 M NaOH solution; a minimum of three measurements was used, else the number of points tested is specified

		Mass % Element								
Phase	Data type	Ca	Si	Al	Fe	Na	Mg	K	O	Ti
C-A-S 2	**average**	**30.0**	**12.3**	**9.6**	**5.3**	**0.0**	**5.9**	**0.0**	**36.0**	**0.9**
	std. deviation	0.9	1.2	0.8	0.8	0.0	0.7	0.0	0.4	0.7
C-A-S 7	**average**	**6.3**	**29.4**	**14.3**	**3.7**	**0.7**	**1.8**	**1.4**	**41.8**	**0.7**
	std. deviation	5.9	6.3	2.2	0.9	0.5	0.7	1.0	1.6	0.5
Fe-rich	**single point**	**5.9**	**15.8**	**3.7**	**41.2**	**0.0**	**1.3**	**0.0**	**32.2**	**0.0**
Mg-rich	**single point**	**22.7**	**6.0**	**6.5**	**11.9**	**1.8**	**3.8**	**0.0**	**45.9**	**1.5**
Quartz	**average of 2 points**	**0.0**	**49.1**	**0.7**	**0.0**	**0.0**	**0.0**	**0.3**	**49.9**	**0.0**
Reaction Product	**single point**	**12.9**	**23.6**	**16.9**	**5.9**	**1.1**	**3.6**	**0.5**	**34.5**	**1.0**

Table 5.16: Phase compositions and uncertainties (s) for a single sample of Martin Lake fly ash after 28 d exposure to 8 M NaOH solution; a minimum of three measurements was used, else the number of points tested is specified

		Mass % Element								
Phase	Data type	Ca	Si	Al	Fe	Na	Mg	K	O	Ti
A-S 1	**average**	**5.2**	**31.1**	**12.2**	**2.7**	**1.1**	**1.5**	**1.3**	**44.2**	**0.7**
	std. deviation	2.8	2.1	1.8	0.7	0.8	0.5	0.9	1.3	0.6
A-S 2	**average**	**5.1**	**27.4**	**15.4**	**3.4**	**0.9**	**1.7**	**1.1**	**44.3**	**0.7**
	std. deviation	1.2	1.5	2.5	1.2	0.3	0.7	0.4	0.5	1.0
C-A-S	**average**	**32.5**	**9.1**	**4.6**	**4.3**	**2.4**	**2.6**	**0.0**	**43.1**	**1.2**
	std. deviation	5.0	3.1	4.4	2.5	2.1	1.4	0.0	7.9	1.1
Fe-rich	**single point**	**4.7**	**6.8**	**5.0**	**45.3**	**0.7**	**5.0**	**0.0**	**32.1**	**0.4**
Quartz	**average**	**0.0**	**49.4**	**0.2**	**0.0**	**0.0**	**0.0**	**0.0**	**50.4**	**0.0**
	std. deviation	0.0	0.6	0.4	0.0	0.0	0.0	0.0	0.5	0.0
Reaction Product	**average**	**7.7**	**24.9**	**11.8**	**7.1**	**6.0**	**1.7**	**0.5**	**39.4**	**0.9**
	std. deviation	5.1	6.6	7.6	4.0	3.0	0.9	0.5	3.7	0.6

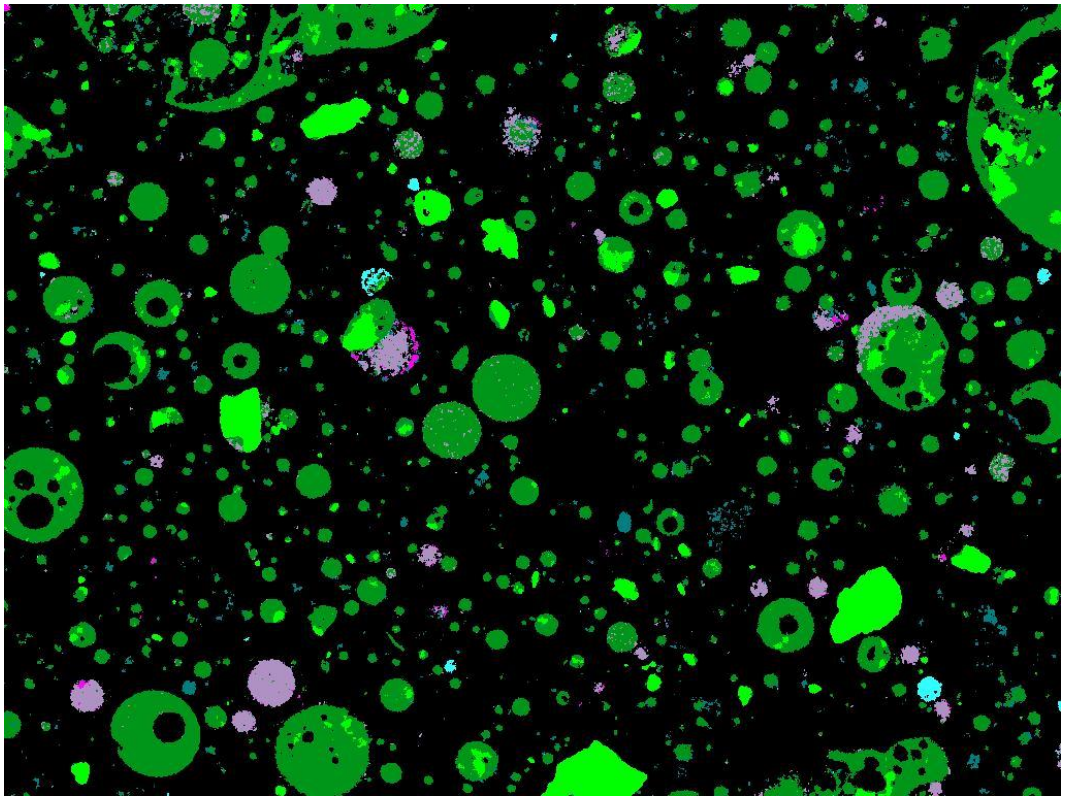

Figure 5.25: Phase assignment image of Martin Lake fly ash residue after 7 d exposure to 8 M NaOH solution

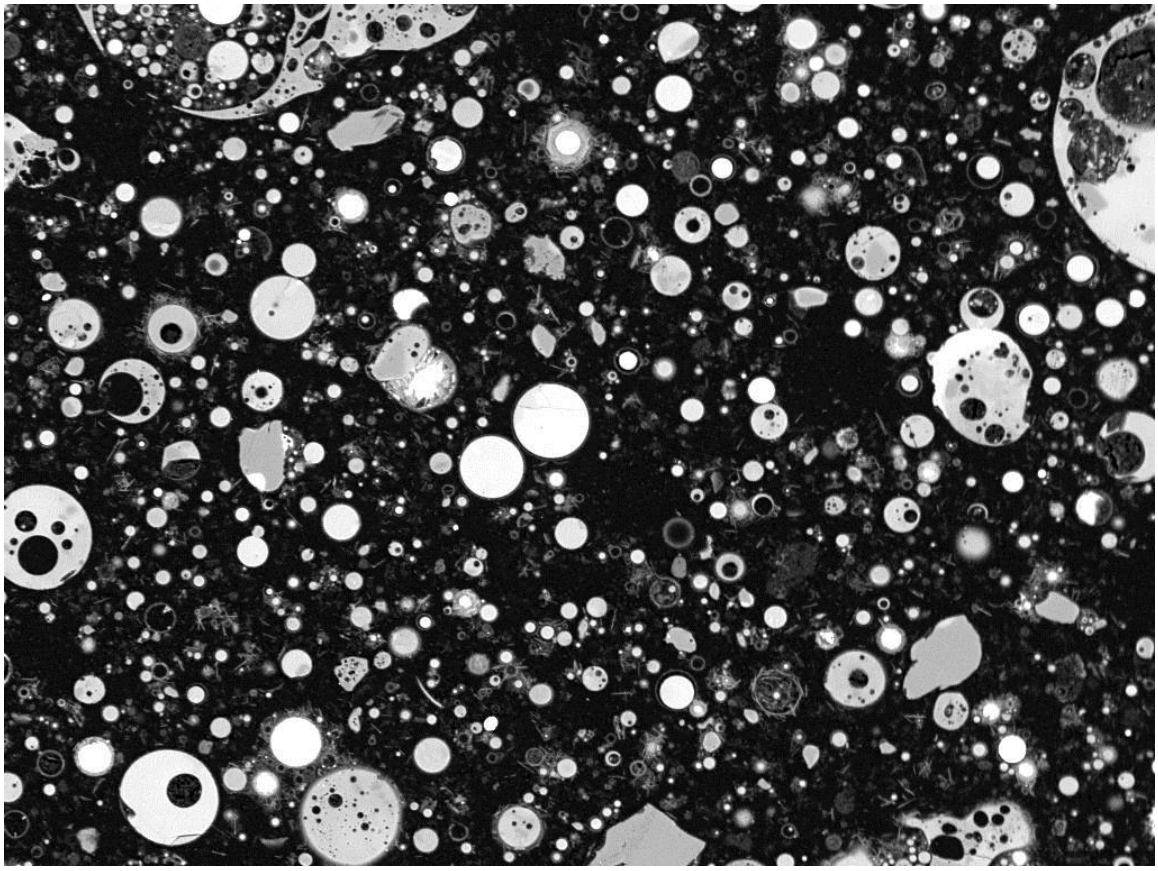

Figure 5.26: Backscattered electron image of Martin Lake fly ash residue after 7 d exposure to 8 M NaOH solution

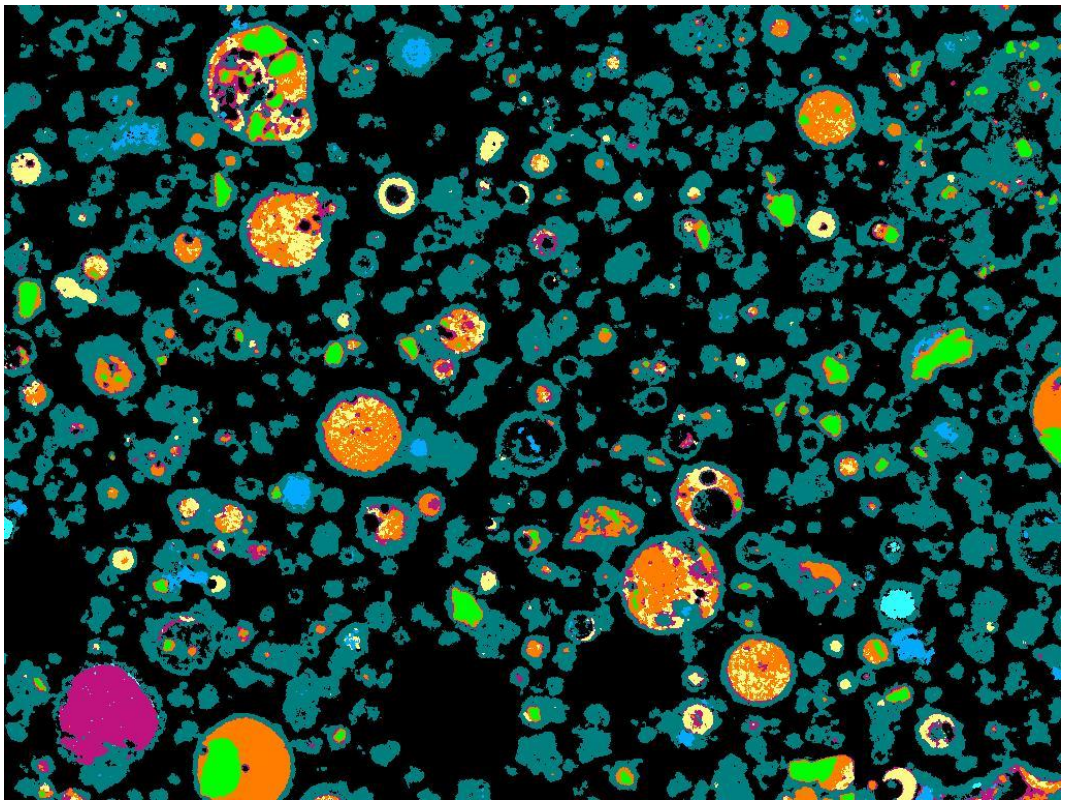

Figure 5.27: Phase assignment image of Martin Lake fly ash residue after 28 d exposure to 8 M NaOH solution

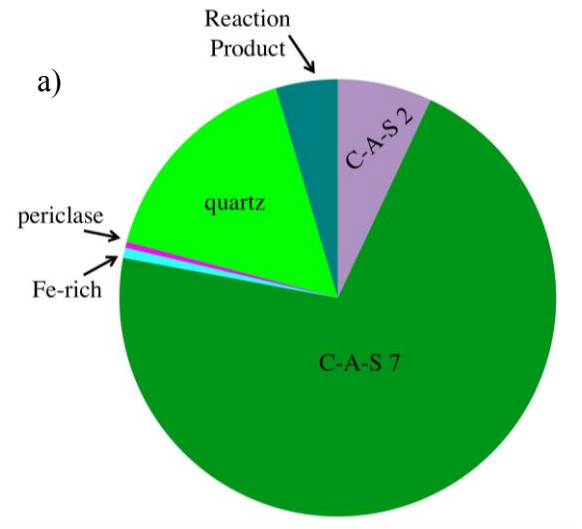

Phase	Area %
C-A-S 2	7.00
C-A-S 7	70.93
Fe-rich	0.76
Mg-rich	0.44
quartz	16.29
reaction product	4.58

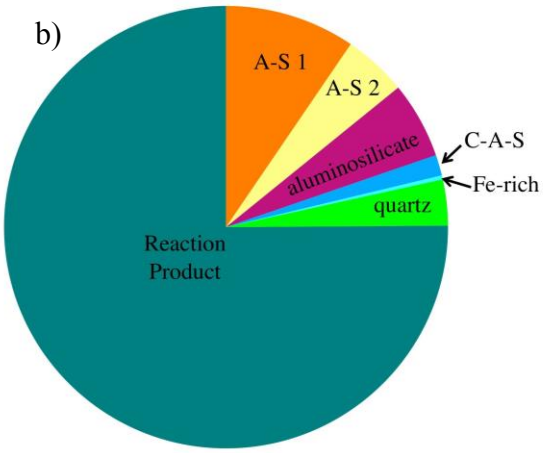

Phase	Area %
A-S 1	9.50
A-S 2	4.63
aluminosilicate	5.59
C-A-S	1.51
Fe-rich	0.30
quartz	3.35
reaction product	75.13

Figure 5.28: The phase distribution of Martin Lake fly ash after 7 d (a) and 28 d (b) exposure to 8 M NaOH solution; each based on a single sample

The reaction product was not well classified at 7 d, likely due to its wispy, needle-like morphology, which was not easily separated from noise in x-ray maps. However, a single point composition analysis represented the phase composition of reaction product at 7 d as 13 % calcium, 24 % silicon, and 17 % aluminum with significant amounts of iron (6%) and magnesium (4%). Sodium was rather low at 1 % by mass. The reaction product was only about 5 % of the image area. The 28 d sample reaction product was around 75 % of the image area, upholding the designation of the fly ash as reactive based on the compressive strength results at 28 d presented in section 5.1. The reaction product composition was high in silicon at 25 % by mass, moderate aluminum at 12 % by mass, and somewhat low calcium at around 8 % by mass. There were also iron (7 %) and sodium (6 %) identified in the reaction product at 28 d. Although there was little calcium in the reaction product, the C-A-S phase in the fly ash had nearly disappeared by 28 d. The calcium must have remained in solution as these reaction products formed. Since the amount of sodium in the reaction product increased from 7 d to 28 d, it is hypothesized that the sodium became the preferable charge-balancing cation instead of calcium. Also

of note, the Martin Lake reaction products at 7 d and 28 d were closer in composition than for other fly ashes studied in the work.

The relative composition of the Martin Lake fly ash changed significantly over time, although the one major trend was the increase in aluminosilicate phases coupled with decrease in C-A-S phases over time. The results are shown in Figure 5.29. By 28 d, the fly ash had only a small amount of one C-A-S phase in it. The C-A-S 6 phase that comprised much of the raw material may have been able to leach silicon, resulting in the C-A-S 7 phase. The C-A-S 6 phase had 7 % calcium, 34 % silicon and 11 % aluminum, while the C-A-S 7 phase had 6 % calcium, 29 % silicon, and 14 % aluminum. This fly ash was considered reactive after compressive strength testing. This would mean that the C-A-S phases must have been quite soluble to enable the formation of sufficient reaction product to attain good strength, although the 28 d reactivity sample showed that the solubility of phases was likely as it contained approximately 75 area % of reaction product. Linking phases to reactivity was more difficult, however.

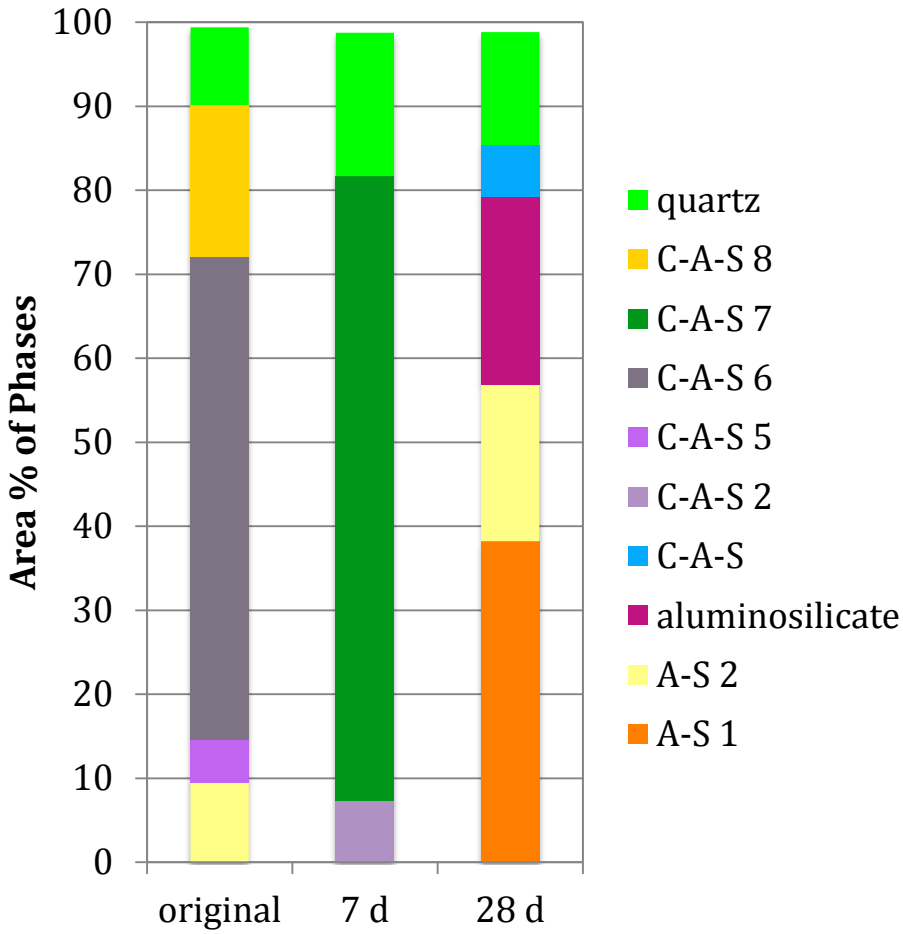

Figure 5.29: Martin Lake fly ash: relative composition of fly ash before and after exposure to 8 M NaOH solution

5.2.8 Boral Class C fly ash

The Boral Class C fly ash was classified as moderately reactive based upon its 28 d compressive strength. The phases identified in the fly ash sample in Chapter 4 included A-S 4, C-A-S 4, N-A-S, N-A-S 2, iron-rich, periclase, and quartz. After NaOH exposure, there was no A-S phase identified. The C-A-S phases identified in the 7 d sample included C-A-S 1, C-A-S 6, and C-A-S 9. Of these, C-A-S 1 and C-A-S 6 were also identified in the 28 d sample. A C-S phase was identified in both the 7 and 28 d specimens, and the N-A-S phase carried through all three specimens as well. The iron-

rich phase was not visible after 7 d, but this may be an error in sampling. The periclase and quartz phases were identified at all time intervals. Reaction product was visible at 7 d and 28 d. Since the fly ash was designated moderately reactive, this was not a surprising result.

After 7 d of exposure to 8 M NaOH solution, nine phases were identified: C-A-S 1, C-A-S 6, C-A-S 9, N-A-S, C-S 2, iron-rich, periclase, quartz, and a reaction product. The compositions of the phases are given in Table 5.17, and the phase assignment image is shown in Figure 5.30. The phase compositions can be compared to Table 4.12, which gave the compositional ranges for each phase. No A-S phase was identified after 7 d of exposure. However, A-S 4 from the original fly ash was similar in composition to the C-A-S 6 phase (gray) identified in the 7 d image, so it is possible that a change in composition occurred after NaOH dissolution. The C-A-S 1 phase (blue) in the 7 d residue was very high in calcium and was similar to the C-A-S 4 identified in the raw fly ash. C-A-S 1 had 34 % calcium, 11 % silicon, and 9 % aluminum compared to the C-A-S 4, which had 27 % calcium, 14% silicon, and 14 % aluminum. The C-A-S 9 phase (raspberry pink) was low calcium (7 % by mass) but with 25 % silicon and 20 % aluminum, by mass. A compositionally similar phase to the C-A-S 9 was not identified in the raw fly ash, so this phase is new to the 7 d residue sample, yet is not a reaction product. The N-A-S phase (red) from the raw material was similar to the one identified in the 7 d residue sample, except the aluminum was slightly decreased at 7 d. The C-S 2 phase (yellow) identified in the 7 d residue was compositionally different from any phase in the raw fly ash and it consisted of 30 % silicon and 15 % calcium with around 3 % aluminum, iron, sodium, and magnesium. The iron-rich phase (aqua) was nearly 50 % iron with impurities of calcium, silicon and aluminum, based on one point measurement. Periclase (orange) was not quantitatively analyzed by point analysis.

The 28 d fly ash residue for Boral Class C contained several phases: C-A-S 1, C-A-S 6, C-S 2, N-A-S, periclase, quartz, and reaction product. The phase compositions are given in Table 5.18. The phase compositions can be compared to Table 4.12, which gave the compositional ranges for each phase. The C-A-S 1 phase (blue) was also identified in the 7 d sample. The C-A-S 6 phase (gray) was similarly identified in the 7 d sample. The N-A-S 2 phase (light gray) was very close in composition to the raw fly ash N-A-S 2, and since it was identified in small quantity in each field of view, the lack of this phase in the 7 d residue sample was likely a sampling error. The C-S 2 phase (yellow) was present again at 28 d, and it had the same composition as at 7d.

Table 5.17: Phase compositions and uncertainties (s) for a single sample of Boral Class C fly ash after 7 d exposure to 8 M NaOH solution; a minimum of three measurements was used, else the number of points tested is specified

		Mass % Element								
Phase	Data type	Ca	Si	Al	Fe	Na	Mg	K	O	Ti
C-A-S 1	**average**	**34.2**	**11.3**	**8.9**	**6.1**	**0.1**	**4.1**	**0.0**	**33.9**	**1.0**
	std. deviation	3.9	5.8	4.5	2.2	0.2	2.4	0.0	2.2	0.7
C-A-S 6	**average**	**9.4**	**33.2**	**6.8**	**2.2**	**2.6**	**1.6**	**0.2**	**42.7**	**1.3**
	std. deviation	1.5	3.0	2.8	0.4	0.5	0.1	0.4	0.7	1.0
C-A-S 9	**single point**	**7.3**	**24.8**	**20.4**	**1.7**	**1.2**	**1.5**	**0.0**	**43.2**	**0.0**
N-A-S	**average**	**4.1**	**28.7**	**14.4**	**2.1**	**5.0**	**1.2**	**1.6**	**42.6**	**0.3**
	std. deviation	4.7	2.9	3.0	0.7	1.0	0.8	0.8	1.4	0.4
C-S 2	**average**	**14.8**	**30.2**	**3.4**	**3.6**	**2.6**	**3.2**	**0.4**	**41.3**	**0.5**
	std. deviation	7.5	6.1	1.9	0.5	1.6	1.4	0.6	4.1	0.8
Fe-rich	**single point**	**5.2**	**9.7**	**1.9**	**47.1**	**0.0**	**4.1**	**0.0**	**32.1**	**0.0**
quartz	**average**	**0.3**	**51.5**	**0.0**	**0.0**	**0.2**	**0.0**	**0.0**	**48.0**	**0.0**
	std. deviation	0.6	0.4	0.0	0.0	0.3	0.0	0.0	0.6	0.0

Table 5.18: Phase compositions and uncertainties (s) for a single sample of Boral Class C fly ash after 28 d exposure to 8 M NaOH solution; a minimum of three measurements was used, else the number of points tested is specified

		Mass % Element								
Phase	Data type	Ca	Si	Al	Fe	Na	Mg	K	O	Ti
C-A-S 1	**average**	**37.0**	**6.4**	**9.6**	**6.6**	**0.9**	**2.5**	**0.0**	**36.2**	**1.0**
	std. deviation	4.8	4.3	5.3	3.8	0.3	1.6	0.0	4.9	0.5
N-A-S 2	**single point**	**0.5**	**37.5**	**9.9**	**0.0**	**3.9**	**0.0**	**2.5**	**45.7**	**0.0**
C-S 2	**single point**	**14.8**	**32.4**	**1.7**	**2.7**	**3.2**	**2.6**	**0.0**	**41.7**	**0.9**
quartz	**single point**	**0.0**	**50.7**	**0.0**	**0.0**	**0.0**	**0.0**	**0.0**	**49.3**	**0.0**
reaction product	**average**	**21.8**	**9.5**	**8.1**	**6.3**	**2.5**	**4.2**	**0.0**	**46.8**	**0.9**
	std. deviation	3.6	1.5	0.6	0.7	0.8	1.2	0.0	1.2	0.2

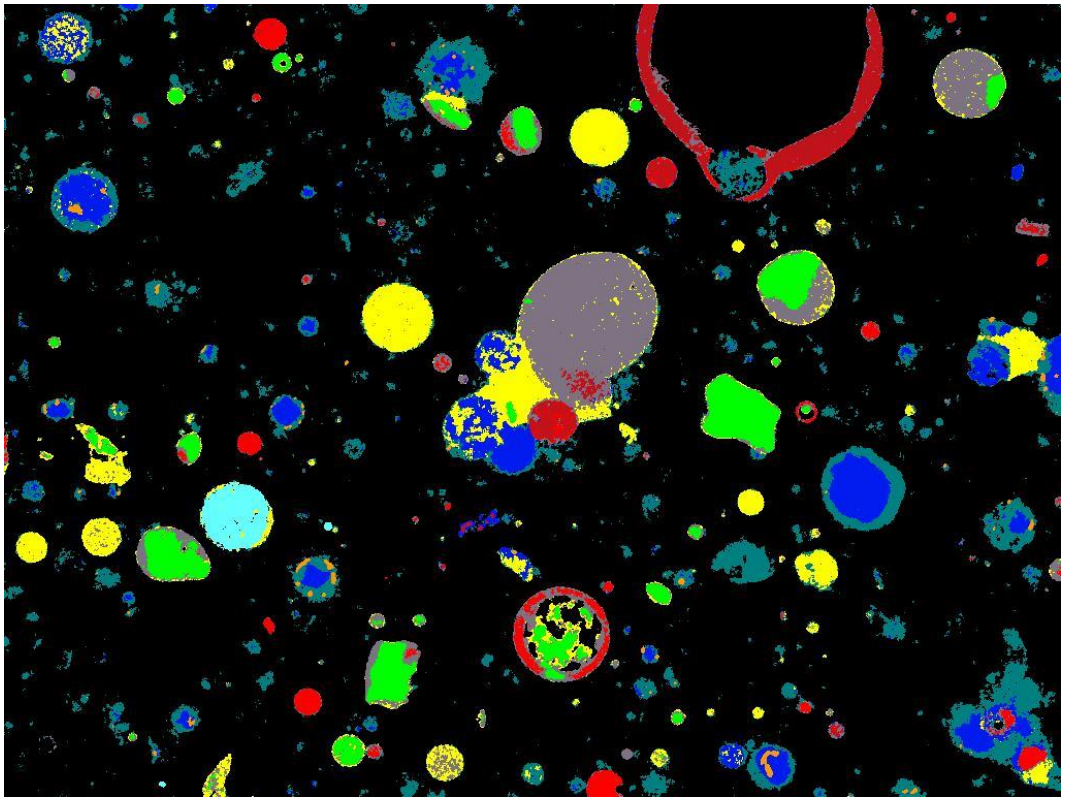

Figure 5.30: Phase assignment image of Boral Class C fly ash residue after 7 d exposure to 8 M NaOH solution

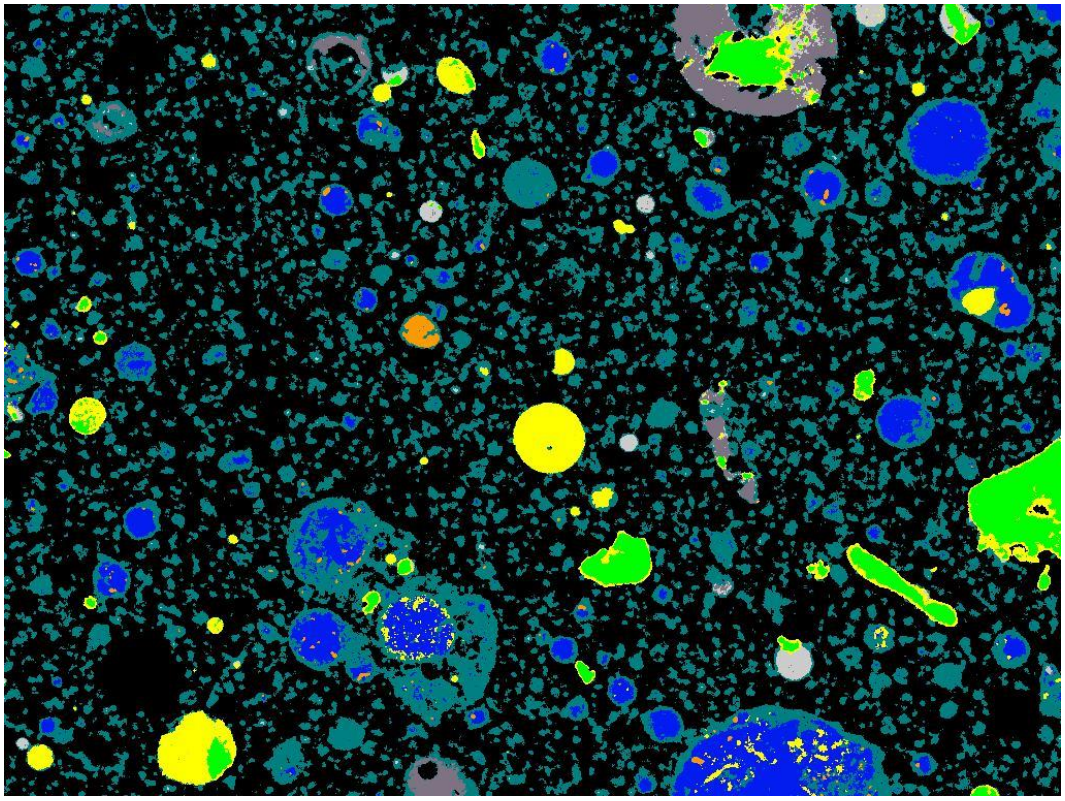

Figure 5.31: Phase assignment image of Boral Class C fly ash residue after 28 d exposure to 8 M NaOH solution

a)

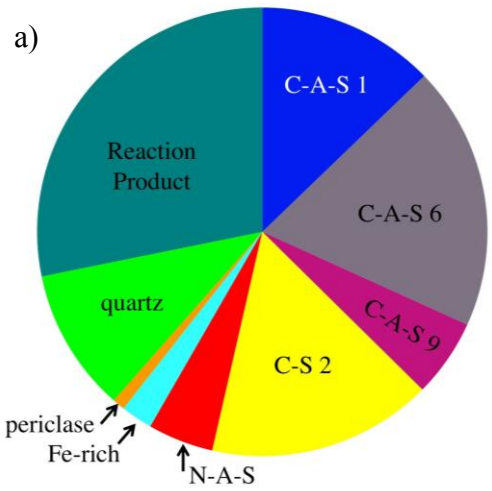

Phase	Area %
C-A-S 1	12.78
C-A-S 6	19.03
C-A-S 9	5.62
CS- 2	16.17
N-A-S	4.72
Fe-rich	2.28
periclase	0.90
quartz	10.34
reaction product	28.21

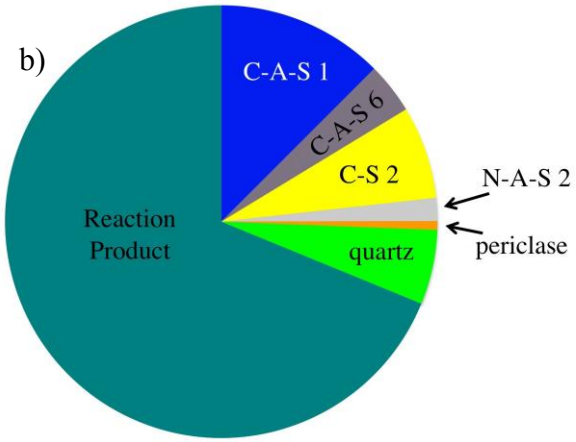

Phase	Area %
C-A-S 1	12.51
C-A-S 6	3.81
C-S 2	6.93
N-A-S 2	1.71
periclase	0.66
quartz	5.58
reaction product	68.83

Figure 5.32: The phase distribution of Boral Class C fly ash after 7 d (a) and 28 d (b) exposure to 8 M NaOH solution; each based on a single sample

The reaction product at 7 d was not measured quantitatively but was qualitatively observed and classified in MSIA. At 28 d, the reaction product was obvious, and it had approximately 22 % calcium, 10 % silicon, and 8 % aluminum, 6 % iron, 3 % sodium and 4 % magnesium. The reaction product appeared to surround the C-A-S 1 phase and was visible as individual clusters of reaction product, possibly from very tiny reactive fly ash particles that were not visible at this magnification or that were completely consumed. The high calcium content at 28 d is attributed to the fact that this fly ash was a Class C fly ash, therefore much greater amounts of calcium were available for reaction.

The relative composition of the Boral Class C fly ash changed significantly over the time periods monitored in the experiment as evidenced in Figure 5.33. The C-A-S phases increased in total amount at later age, and the N-A-S phase appeared to decrease. The fly ash being a Class C fly ash may be one reason that the C-A-S phases appear in high amount at all ages. However, no clear trends are obvious as to which phases were reactive. The highest calcium, C-A-S 1 phase increased between 7 and 28 d. The fly ash was designated moderately reactive, and there is little evidence as to why from observing the phases in the fly ash over time.

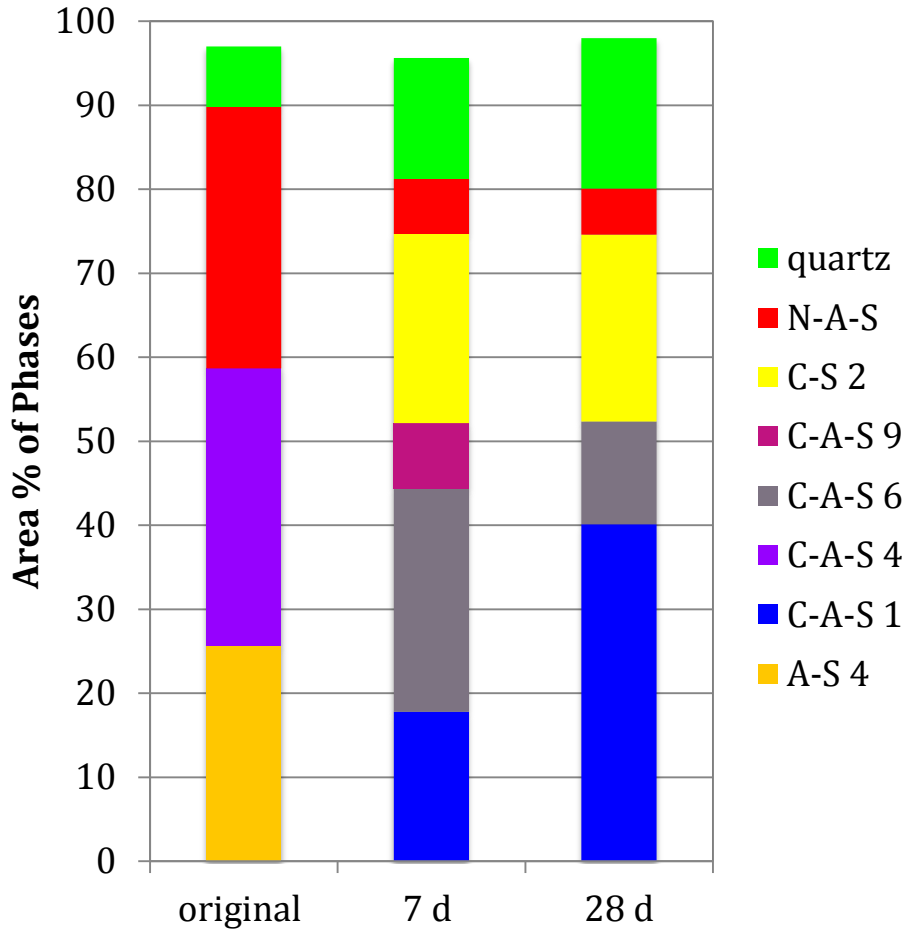

Figure 5.33: Boral Class C fly ash: relative composition of fly ash before and after exposure to 8 M NaOH solution

5.2.9 LEGS fly ash

The LEGS fly ash was a Class F fly ash that was classified as moderately reactive based upon the 28 d mortar compressive strength results presented in Section 5.1. The MSIA results for the LEGS fly ash given in Chapter 4 showed that it contained five C-A-S phases, quartz, an iron-rich phase, and periclase. The C-A-S 2 and C-A-S 7 phases were both identified after 7 d NaOH exposure. The C-A-S 2 phase was also identified in the 28 d specimen. An aluminosilicate phase (A-S 2) was found in the 7 d and 28 d

samples, while A-S 3 was identified in the 28 d sample. Quartz and iron-rich phases were identified in all three time periods, while periclase was identified in the raw material and at 7 d. Reaction products were identified at 7 d and 28 d. These results were expected since there was reasonable strength at 7 d based upon the ability of the fly ash to be demolded and tested at 7 d.

After 7 d of exposure to NaOH solution, the LEGS fly ash residue contained A-S 2, C-A-S 2, C-A-S 7, iron-rich, quartz, periclase and reaction product. The phase compositions are given in Table 5.19, and the phase assignment image is given in Figure 5.34. The phase compositions can be compared to Table 4.12, which gave the compositional ranges for each phase. The relative amounts of each phase are shown in Figure 5.36. The A-S 2 (yellow) contained approximately 30 % silicon and 14 % aluminum, by mass, with a Si/Al around 2. The C-A-S 2 (lavender) phase was identified at 7 d, and it was the same composition as in the raw material. The iron-rich phase (aqua) was a small portion of the material and only obvious on one particle, the quartz (bright green) remained generally unchanged and the periclase (orange) was present in small amount.

After 28 d of exposure to NaOH solution, two aluminosilicate phases, two C-A-S phases, quartz, an iron-rich phase, and reaction product were observed in the fly ash residue. The phase compositions are given in Table 5.20. The phase compositions can be compared to Table 4.12, which gave the compositional ranges for each phase. The A-S 2 (orange) and A-S 3 (peach) phases were identified in LEGS fly ash residue after 7 d. These phases differed in their Si/Al ratios, which was approximately 2 for the A-S 2 phase and 0.75 for the A-S 3 phase. The A-S 3 phase had a much higher aluminum than silicon and was identified as mullite. The C-A-S 2 phase (lavender) identified in the fly ash was still present at 7 days. C-A-S 4 (bright purple) was a very minor phase and was

primarily calcium with half as much aluminum and a small amount of silicon. The quartz phase (lime green) appeared unchanged, while the iron-rich phase (aqua) had increased in amount. The increase was likely due to sampling, as there was a large particle that contained a high amount of iron. The composition of the Fe-rich phase at 7 d was very close to the pre-exposure fly ash Fe-rich composition.

Table 5.19: Phase compositions and uncertainties (s) for a single sample of LEGS fly ash after 7 d exposure to 8 M NaOH solution; a minimum of three measurements was used, else the number of points tested is specified

		Mass % Element								
Phase	Data type	Ca	Si	Al	Fe	Na	Mg	K	O	Ti
A-S 2	**average**	**2.7**	**30.4**	**14.2**	**3.0**	**1.1**	**1.2**	**1.9**	**44.7**	**0.8**
	std. deviation	1.4	2.5	2.3	1.3	0.4	0.4	1.2	1.1	1.3
C-A-S 2	**average**	**27.3**	**12.4**	**7.7**	**7.9**	**1.4**	**3.8**	**0.0**	**38.5**	**1.2**
	std. deviation	2.4	3.2	2.0	3.8	1.9	1.5	0.0	3.6	0.4
C-A-S 7	**average**	**12.2**	**25.6**	**11.4**	**5.3**	**0.1**	**2.2**	**0.1**	**42.1**	**1.1**
	std. deviation	2.3	2.7	2.2	4.0	0.2	0.5	0.2	1.3	0.8
Fe-rich	**average of 2 points**	**4.8**	**4.3**	**1.2**	**69.8**	**0.3**	**0.6**	**0.0**	**19.0**	**0.0**
quartz	**average**	**0.0**	**49.2**	**0.7**	**0.0**	**0.1**	**0.0**	**0.1**	**49.9**	**0.0**
	std. deviation	0.0	1.4	1.3	0.0	0.3	0.0	0.2	0.8	0.0
reaction product	**average**	**6.0**	**17.2**	**11.0**	**7.3**	**12.6**	**3.2**	**0.0**	**41.8**	**0.7**
	std. deviation	4.6	9.9	3.3	8.1	2.6	3.4	0.0	2.2	0.8

Table 5.20: Phase compositions and uncertainties (s) for a single sample of LEGS fly ash after 28 d exposure to 8 M NaOH solution; a minimum of three measurements was used, else the number of points tested is specified

		Mass % Element								
Phase	Data type	Ca	Si	Al	Fe	Na	Mg	K	O	Ti
A-S 1	**average**	**0.3**	**21.4**	**29.1**	**0.5**	**4.6**	**0.0**	**0.0**	**44.1**	**0.0**
	std. deviation	0.5	5.0	5.4	0.5	5.1	0.0	0.0	2.4	0.0
A-S 2	**average**	**4.4**	**27.6**	**14.4**	**4.8**	**0.8**	**1.3**	**1.3**	**44.6**	**0.7**
	std. deviation	3.8	2.2	2.0	1.9	0.7	0.4	1.0	0.8	0.6
C-A-S 1	**average of 2 points**	**27.8**	**6.6**	**14.4**	**9.1**	**0.0**	**4.0**	**0.0**	**37.4**	**0.4**
C-A-S 2	**average**	**24.0**	**8.9**	**6.1**	**14.6**	**0.6**	**1.6**	**0.0**	**42.3**	**1.8**
	std. deviation	4.5	7.6	2.0	11.5	0.6	1.7	0.0	5.1	1.4
Fe-rich	**average of 2 points**	**0.8**	**3.0**	**1.4**	**64.6**	**0.0**	**0.0**	**0.0**	**30.3**	**0.0**
quartz	**average**	**0.0**	**48.4**	**0.6**	**0.2**	**0.0**	**0.0**	**0.1**	**50.7**	**0.0**
	std. deviation	0.0	1.2	1.2	0.3	0.0	0.0	0.3	0.6	0.0
reaction product	**average**	**11.0**	**19.5**	**6.4**	**8.6**	**4.0**	**4.4**	**0.4**	**43.7**	**2.0**
	std. deviation	11.7	11.4	0.4	0.7	1.9	4.4	0.5	5.9	1.1

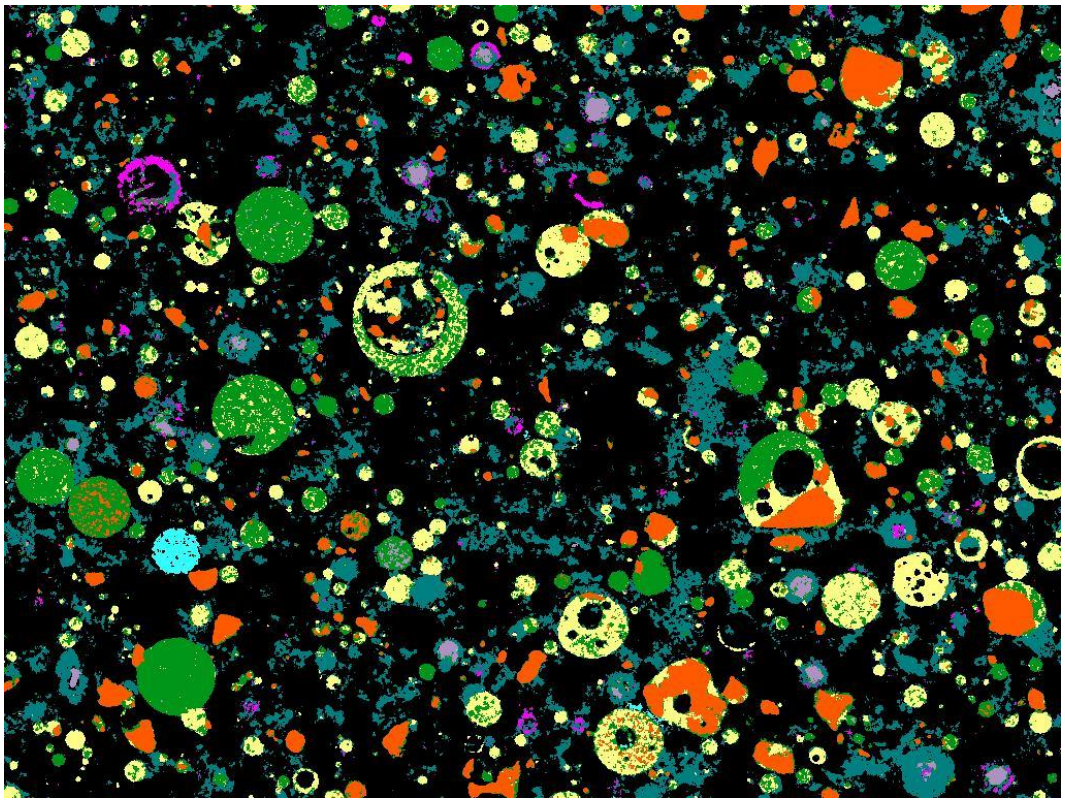

Figure 5.34: Phase assignment image of LEGS fly ash residue after 7 d exposure to 8 M NaOH solution

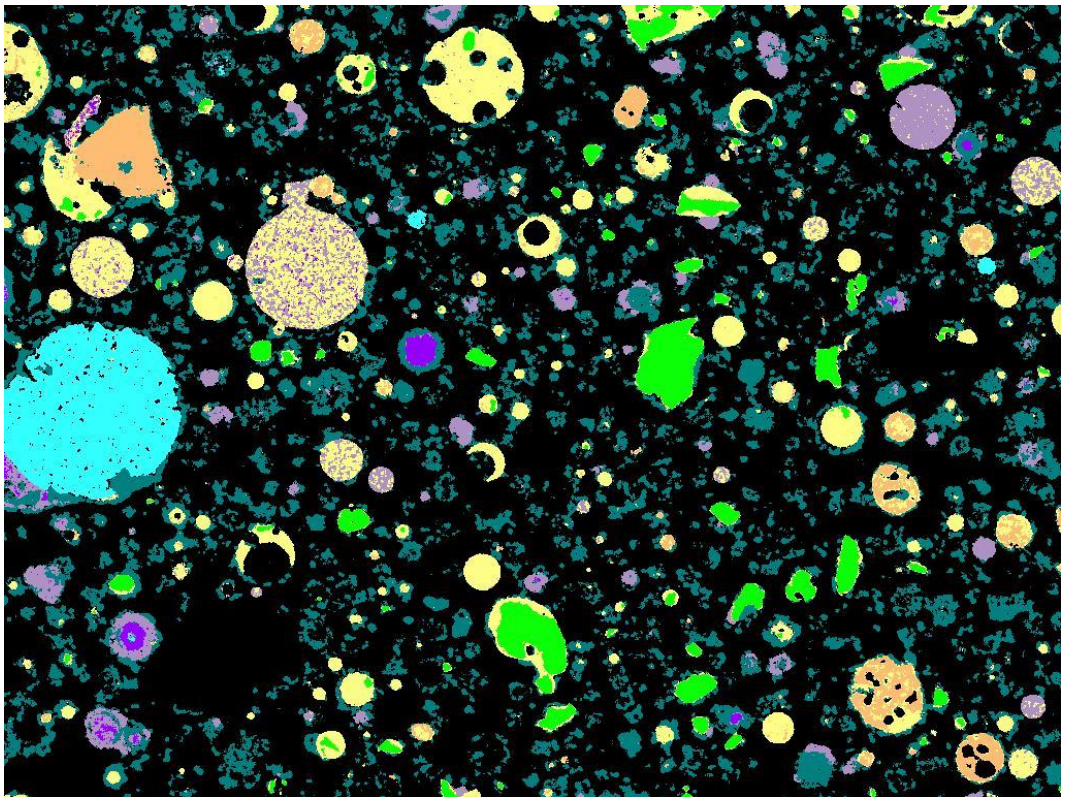

Figure 5.35: Phase assignment image of LEGS fly ash residue after 28 d exposure to 8 M NaOH solution

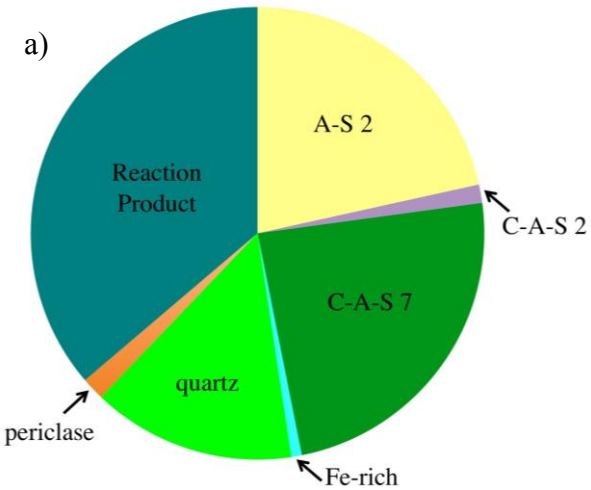

Phase	Area %
A-S 2	21.53
C-A-S 2	1.31
C-A-S 7	24.03
Fe-rich	0.75
quartz	14.49
periclase	1.65
reaction product	36.24

b)

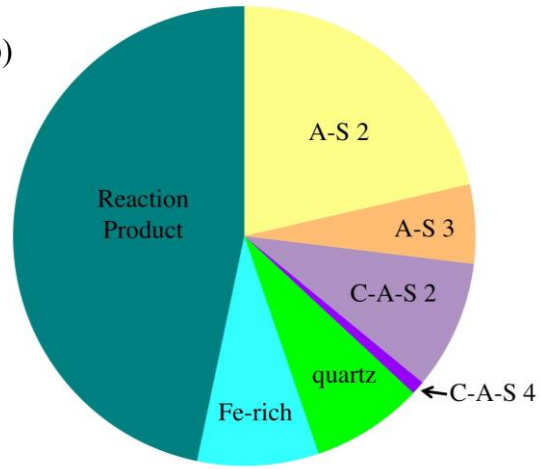

Phase	Area %
A-S 2	21.38
A-S 3	5.57
C-A-S 2	9.06
C-A-S 4	0.96
quartz	7.83
Fe-rich	8.49
reaction product	46.73

Figure 5.36: The phase distribution of LEGS fly ash after 7 d (a) and 28 d (b) exposure to 8 M NaOH solution; each based on a single sample

The reaction product at 7 d had a lower calcium content than at 28 d. At 28 days the calcium content had doubled, while the silicon content increased slightly and the aluminum content decreased by about half when compared to the 7 d composition. The iron amount was stable, while the sodium had increased greatly at 28 days from 7 days. The magnesium remained stable from 7 days to 28 days, also.

The LEGS fly ash had many relative compositional differences over time, but in general the A-S phases increased in amount, indicating dissolution of C-A-S phases over time. The compositions over time for the LEGS fly ash are given in Figure 5.37. The C-A-S 7 phase was identified in somewhat large amount in the original fly ash and at 7 d, but disappeared completely at 28 d. This phase was previously discussed for the Coleto Creek fly ash in which it was hypothesized that it could have leached calcium to become compositionally similar to A-S 4. In the LEGS fly ash, the phase may have leached to become A-S 2. C-A-S 7 had Si/Al of 2.3-2.7 in the original and 7 d samples, while the A-S 2 phase had Si/Al of 1.92. If the C-A-S 7 phase did change as such, then the calcium decreased over time, silicon stayed constant, and aluminum increased over time

(balancing the decrease in calcium). The C-A-S 2 phase increased by 28 d, which may indicate it is a poorly reactive phase. The LEGS fly ash was designated moderately reactive, and its presence of a poorly soluble C-A-S 7 phase in large proportion may have been one reason why this was true. Even for high solubilities of the other C-A-S phases, there would be too much of a slowly soluble phase to allow significant strength to form.

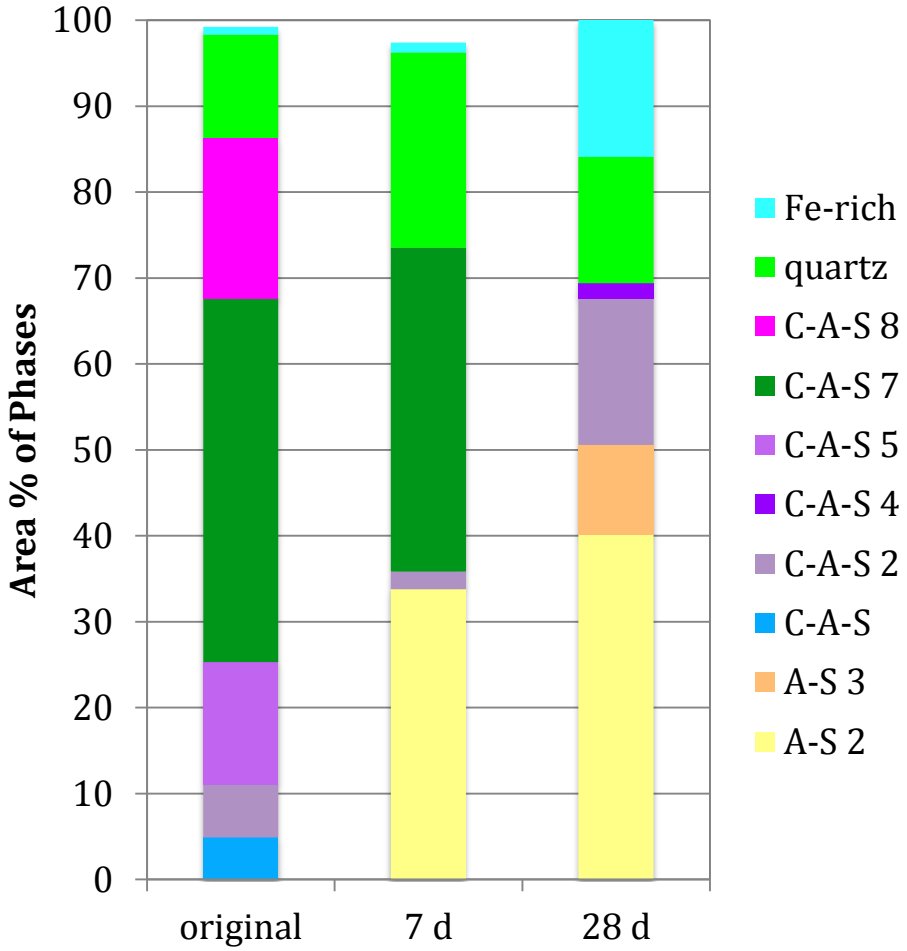

Figure 5.37: LEGS fly ash: relative composition of fly ash before and after exposure to 8 M NaOH solution

5.2.10 Belews Creek fly ash

The Belews Creek fly ash is a Class F fly ash and it was classified as poorly reactive based on the compressive strength results presented in Section 5.1. Prior to exposure to NaOH solution, the Belews Creek fly ash contained A-S 1, A-S 2, quartz, and an iron rich phase. The fly ash followed the pattern expected based on the compressive strength data (Figure 5.1) in that its composition did not change greatly after 7 d of NaOH exposure and no reaction product was identified. After 28 d of NaOH exposure, the fly ash composition had changed due to differences in the aluminosilicate phases identified. In the 28 d sample, a reaction product was noted, which had Si/Al ratio of 2.32, meaning it was very silicon-rich. This supports the assertion that silicon dissolution occurred to the sample, which was represented by the changes in the aluminosilicate phases between 7 d and 28 d.

The phase compositions for the 7 d Belews Creek fly ash residue are given in Table 5.21. The phase compositions can be compared to Table 4.12, which gave the compositional ranges for each phase. The phase assignment image is shown in Figure 5.38, and the relative amounts of each phase in the specimen are shown in Figure 5.39. After 7 d of exposure to NaOH solution the Belews Creek fly ash residue had the same A-S 1 phase (orange) and A-S 2 phase (yellow) phases as in the raw sample. These two phases differed mainly in their ratios of silicon to aluminum, with A-S 1 having a greater silicon/aluminum ratio (2.7) than A-S 2 (1.7). The A-S 1 phase was found in nearly every particle in the specimen, with the A-S 2 phase interspersed into some of the particles. The iron-rich phase (aqua) and quartz (lime green) phases remained similar in composition from 0-7 days. Unlike the previous 8 fly ashes, there was no reaction product detected for the Belews Creek fly ash at 7 d.

After 28 d of 8 M NaOH exposure, the A-S 1 phase was no longer identified, while A-S 2 (yellow) and A-S 3 (peach) made up the bulk of the Belews Creek fly ash residue. The phase compositions are given in Table 5.22, the phase assignment image is shown in Figure 5.38, and the relative amounts of each phase are given in Figure 5.39. The phase compositions can be compared to Table 4.12, which gave the compositional ranges for each phase. The A-S 2 had the lower Si/Al ratio of the two A-S phases at 1.7, while the A-S 3 had a Si/Al ratio of around 1. Quartz was noted in the specimen.

Table 5.21: Phase compositions and uncertainties (s) for a single sample of Belews Creek fly ash after 7 d exposure to 8 M NaOH solution; a minimum of three measurements was used, else the number of points tested is specified

		Mass % element								
Phase	Data type	Ca	Si	Al	Fe	Na	Mg	K	O	Ti
A-S 1	**average**	**0.0**	**28.9**	**13.7**	**1.6**	**0.1**	**0.6**	**2.7**	**39.6**	**1.5**
	std. deviation	0.0	2.9	2.9	0.5	0.2	0.3	1.1	1.9	1.6
A-S 2	**average**	**0.4**	**25.8**	**17.0**	**1.8**	**0.0**	**0.5**	**1.8**	**39.2**	**0.7**
	std. deviation	0.6	1.6	1.3	0.2	0.0	0.3	0.6	1.7	0.6
Fe-rich	**single point**	**0.7**	**13.2**	**7.2**	**35.9**	**0.0**	**0.6**	**0.0**	**30.9**	**0.6**
Quartz	**average**	**0.0**	**51.8**	**0.2**	**0.0**	**0.0**	**0.0**	**0.0**	**49.8**	**0.0**
	std. deviation	0.0	1.6	0.3	0.0	0.0	0.0	0.0	1.6	0.0

Table 5.22: Phase compositions and uncertainties (s) for a single sample of Belews Creek fly ash after 28 d exposure to 8 M NaOH solution; a minimum of three measurements was used, else the number of points tested is specified

		Mass % element								
Phase	Data type	Ca	Si	Al	Fe	Na	Mg	K	O	Ti
A-S 2	**average**	**0.1**	**31.5**	**18.1**	**2.4**	**0.1**	**0.6**	**1.8**	**44.4**	**1.0**
	std. deviation	0.3	1.9	2.3	1.4	0.2	0.4	0.4	1.2	1.0
A-S 3	**average**	**0.2**	**21.3**	**27.0**	**1.5**	**6.7**	**0.2**	**0.5**	**42.0**	**0.5**
	std. deviation	0.4	7.2	11.0	1.0	10.0	0.4	0.9	6.6	0.9
quartz	**average**	**0.0**	**51.2**	**0.7**	**0.0**	**0.0**	**0.0**	**0.0**	**48.1**	**0.0**
	std. deviation	0.0	1.1	0.2	0.0	0.0	0.0	0.0	1.1	0.0
reaction product	**single point**	**0.0**	**27.5**	**11.9**	**2.3**	**9.7**	**0.0**	**0.0**	**48.1**	**0.6**

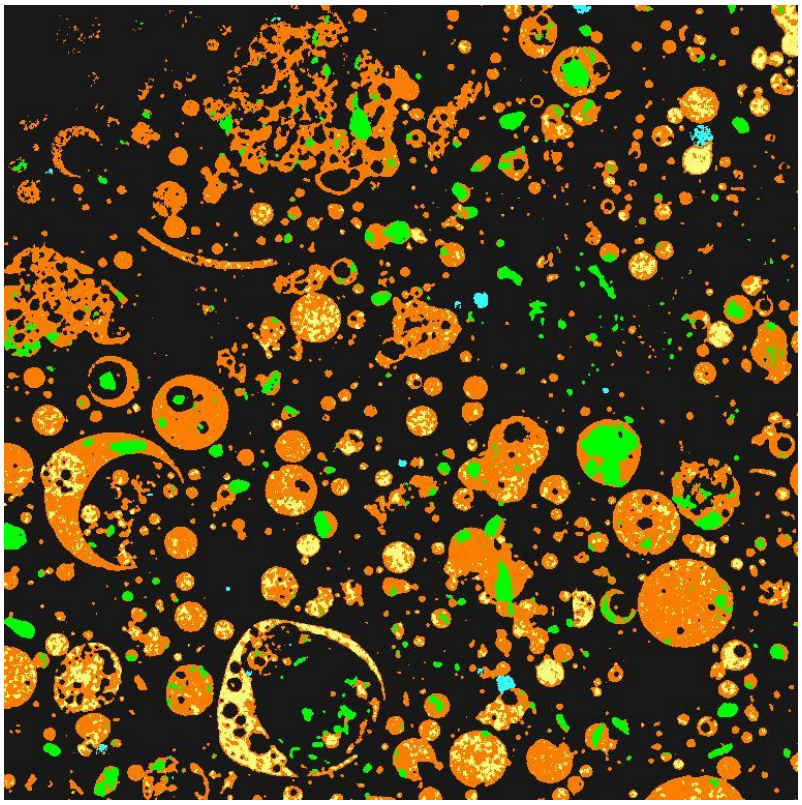

Figure 5.38: Phase assignment image of Belews Creek fly ash residue after 7 d exposure to 8 M NaOH solution (cropped due to image aberrations)

a)

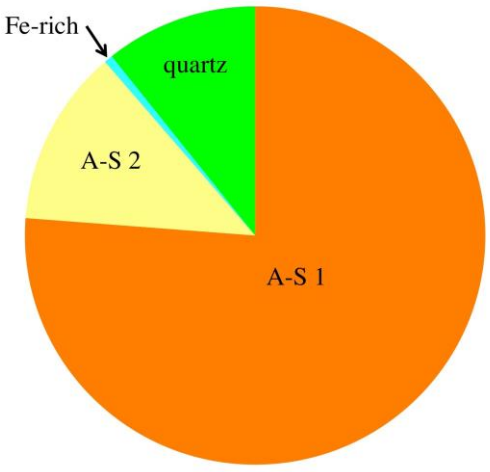

Phase	Area %
A-S 1	76.24
A-S 2	12.48
Fe-rich	0.60
quartz	10.71

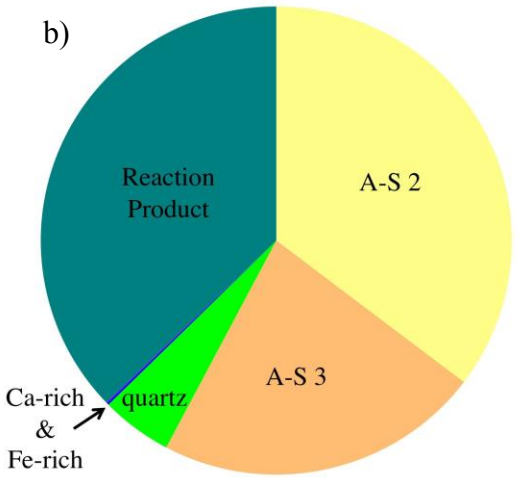

Phase	Area %
A-S 2	35.33
A-S 3	22.41
quartz	4.89
Ca-rich	0.13
Fe-rich	0.07
Reaction Product	37.18

Figure 5.39: The phase distribution of Belews Creek fly ash after 7 d (a) and 28 d (b) exposure to 8 M NaOH solution; each based on a single sample

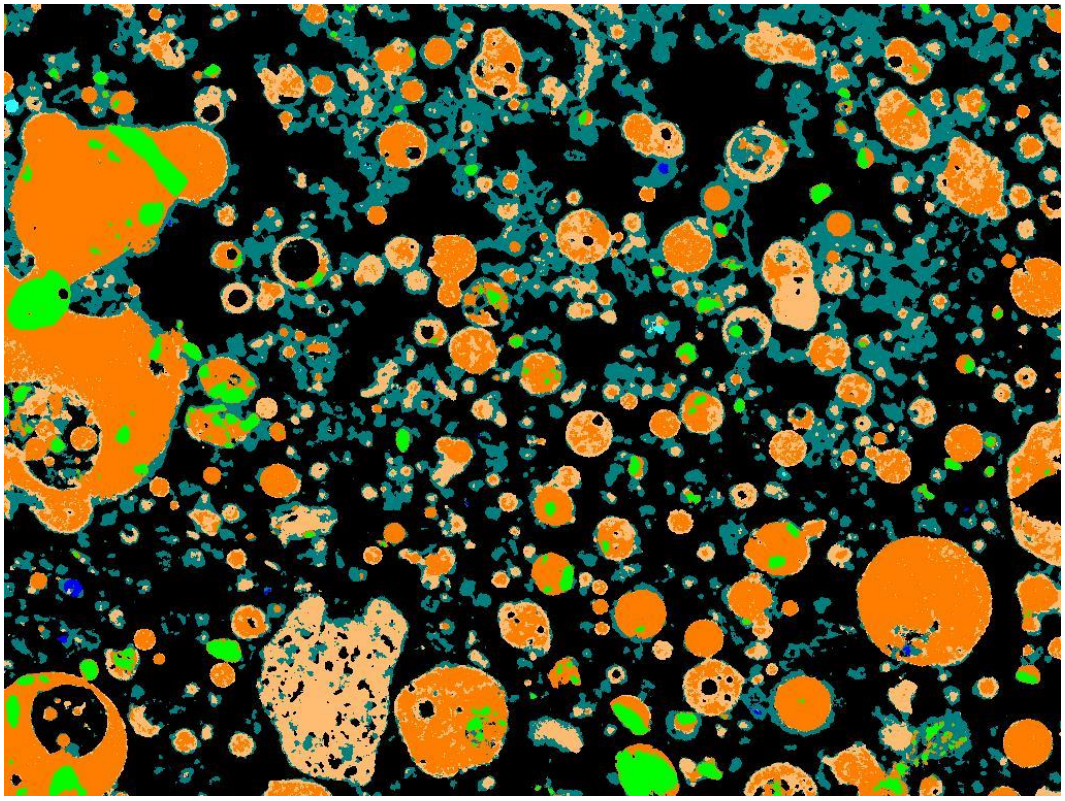

Figure 5.40: Phase assignment image of Belews Creek fly ash residue after 28 d exposure to 8 M NaOH solution

The Belews Creek fly ash was considered poorly reactive. Based on this, it was not surprising that the there was no reaction product identified in this fly ash after 7 d. A reaction product was noted in the 28 d sample, which had Si/Al ratio of 2.32, which was very silicon-rich. This supports the assertion that silicon dissolution occurred from the sample.

The Belews Creek fly ash composition changed little across the time periods measured as shown in Figure 5.41. From these data it is clear that the aluminosilicate phases stayed generally constant in the fly ash and residue across the time periods. The main difference occured at 28 d, when the A-S 1 phase disappeared entirely, and A-S 2 and A-S 3 are identified. The S/A of A-S 1 was 2.0, while the S/A of the A-S 2 phase averaged 1.5. The S/A of A-S 3 is 0.79, which meant that either the silicon decreased greatly or the aluminum increased greatly to form this phase. Since this method was most likely dissolving species from the fly ash, it is likely that silicon was leached to form A-S 3, although it is not certain which phase from the 7 d specimen was leached to form the A-S 3 at 28 d. This fly ash was designated poorly reactive in the compressive strength results, and in the dissolution study results it was shown to not have developed reaction products by 7 d. The data shown here explain this somewhat, in that the composition at 0 d and 7 d was nearly identical, whereas at 28 d (after some reaction product formed), two aluminosilicate phases were identified, but one was different than the previous two time steps. Reaction product did form by 28 d, so silicon and aluminum did leach from the sample. The appearance of reaction product was somewhat surprising since the fly ash was designated poorly reactive and had 0 compressive strength at 28 d. The results for the Belews Creek fly ash imply that the A-S phases are somewhat soluble, but they are very slowly soluble under these conditions.

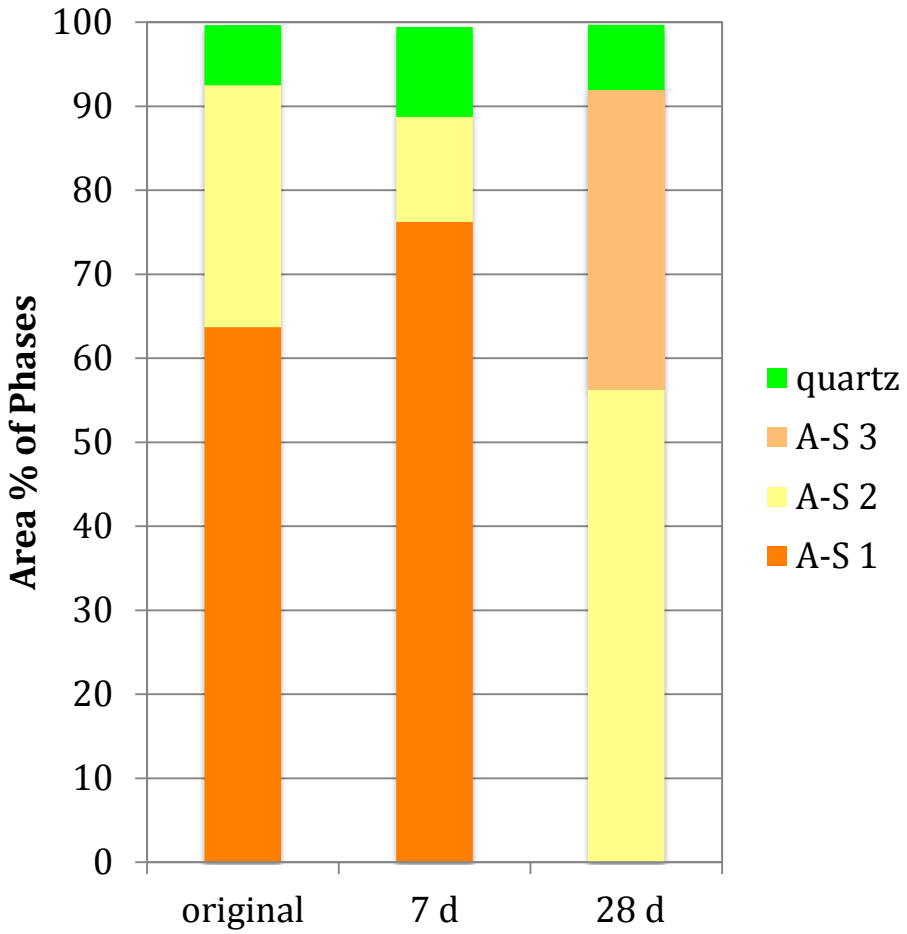

Figure 5.41: Belews Creek fly ash: relative composition of fly ash before and after exposure to 8 M NaOH solution

5.2.11 Fontana fly ash

The Fontana fly ash was considered poorly reactive based on the compressive strength testing presented in Section 5.1. The phases identified in the Fontana fly ash were A-S 1, A-S 2, quartz, a calcium-rich phase, and an iron-rich phase. Since the fly ash was poorly reactive, it was unsurprising the MSIA results showed that no reaction product formed by 7 d. One surprising result was a high-calcium phase that appeared in discrete particles in both the 7 d and 28 d samples, indicating their poor reactivity. Since the Fontana was low in Ca, these particles must have comprised much of the calcium

content in the fly ash. The crystalline composition of fly ash did not help explain these results, since the fly ash was only found to contain lime and anhydrite, both of which would be reactive under the caustic conditions of the experiments.

The phases identified in the Fontana fly ash residue at 7 d were A-S 2, quartz, an iron-silicate phase, a calcium-rich phase, an iron-rich phase and reaction product. The phase compositions are given in Table 5.23. The phase compositions can be compared to Table 4.12, which gave the compositional ranges for each phase. The phase assignment image is shown in Figure 5.42, while the relative amounts of each phase are given in Figure 5.44. The A-S 2 phase (yellow), which was the majority of the material in the image, was nearly identical to the composition of the A-S 2 identified in the raw material. The iron-silicate phase (light gray) was a somewhat large proportion of the material, and it was chiefly found in four large particles within the image. Its composition was approximately 25 % silicon, 20 % iron, and 10 % aluminum by element mass. Its appearance was considered a sampling issue, and it was not noted in either of the other two samples of this fly ash. The calcium phase (blue) had nearly 50 % calcium by mass, with small amounts of silicon, aluminum, and iron. The iron-rich phase (aqua) was 70% by mass iron, with few impurities.

After 28 days of NaOH exposure, the A-S 2 phase (yellow) had changed to A-S 3 (peach), which differed from the A-S 2 by its lower Si/Al mass ratio, which was very near to 1 on a mass basis. The compositions of the phases are given in Table 5.24, and the phase assignment image is shown in Figure 5.43. The phase compositions can be compared to Table 4.12, which gave the compositional ranges for each phase. A C-A-S phase, C-A-S 6 (gray) was identified at 28 days, which had Si/Al ratio of 3 (30 mass % Si to 10 mass % Al), while the calcium content was around 7 % by mass. The quartz phase was mostly unchanged, while the iron-rich and lime phases seemed to slightly increase.

These were most likely related to the sampling of the material, as they did not change by much. Reaction product was approximately 1/3 of the field of view at 28 d, showing that the material had reacted. The composition of the reaction product could be described as sodium-aluminosilicate with a Si/Al mass ratio of approximately 1.

Table 5.23: Phase compositions and uncertainties (s) for a single sample of Fontana fly ash after 7 d exposure to 8 M NaOH solution; a minimum of three measurements was used, else the number of points tested is specified

		Mass % Element								
Phase	Data type	Ca	Si	Al	Fe	Na	Mg	K	O	Ti
quartz	**average**	**0.0**	**50.5**	**0.6**	**0.1**	**0.0**	**0.0**	**0.1**	**48.7**	**0.0**
	std. deviation	0.0	1.3	0.6	0.3	0.0	0.0	0.3	1.4	0.0
A-S 2	**average**	**3.1**	**30.2**	**16.6**	**2.8**	**0.2**	**0.9**	**0.9**	**45.1**	**0.3**
	std. deviation	2.9	5.2	3.8	4.2	0.4	0.5	0.9	1.8	0.5
Fe-Si	**average, 2 points**	**3.7**	**24.7**	**10.0**	**19.5**	**0.0**	**0.6**	**0.4**	**40.8**	0.3
lime	**single point**	**47.6**	**3.9**	**3.4**	**3.7**	**0.0**	**0.0**	**0.0**	**40.5**	**0.9**
Fe-rich	**average**	**0.0**	**0.3**	**0.6**	**70.3**	**0.0**	**0.0**	**0.0**	**28.7**	**0.0**
	std. deviation	0.0	0.6	0.6	1.9	0.0	0.0	0.0	0.9	0.0

Table 5.24: Phase compositions and uncertainties (s) for a single sample of Fontana fly ash after 28 d exposure to 8 M NaOH solution; a minimum of three measurements was used, else the number of points tested is specified

		Mass % Element								
Phase	Data type	Ca	Si	Al	Fe	Na	Mg	K	O	Ti
quartz	**average**	**0.5**	**48.9**	**0.5**	**0.1**	**0.1**	**0.1**	**0.0**	**49.7**	**0.1**
	std. deviation	1.2	2.0	0.8	0.3	0.2	0.2	0.0	1.7	0.3
A-S 3	**average**	**1.3**	**25.3**	**26.1**	**1.2**	**1.0**	**0.3**	**0.1**	**44.0**	**0.9**
	std. deviation	1.7	4.5	7.9	0.8	0.8	0.4	0.2	2.7	0.9
C-A-S 6	**average**	**7.3**	**31.3**	**9.7**	**3.9**	**0.2**	**1.3**	**0.6**	**44.1**	**1.6**
	std. deviation	5.0	3.5	3.6	4.2	0.3	0.5	0.8	1.4	1.7
Fe-rich	**average**	**0.9**	**6.6**	**2.7**	**58.3**	**0.0**	**0.0**	**0.0**	**31.5**	**0.0**
	std. deviation	1.6	7.0	2.2	14.0	0.0	0.0	0.0	4.7	0.0
lime	**single point**	**45.9**	**2.6**	**0.6**	**0.0**	**2.4**	**0.0**	**0.0**	**48.5**	**0.0**
reaction product	**average**	**2.2**	**25.2**	**21.2**	**1.1**	**4.8**	**0.1**	**0.0**	**44.4**	**0.9**
	std. deviation	3.9	3.4	10.8	0.8	4.2	0.3	0.0	4.2	0.8

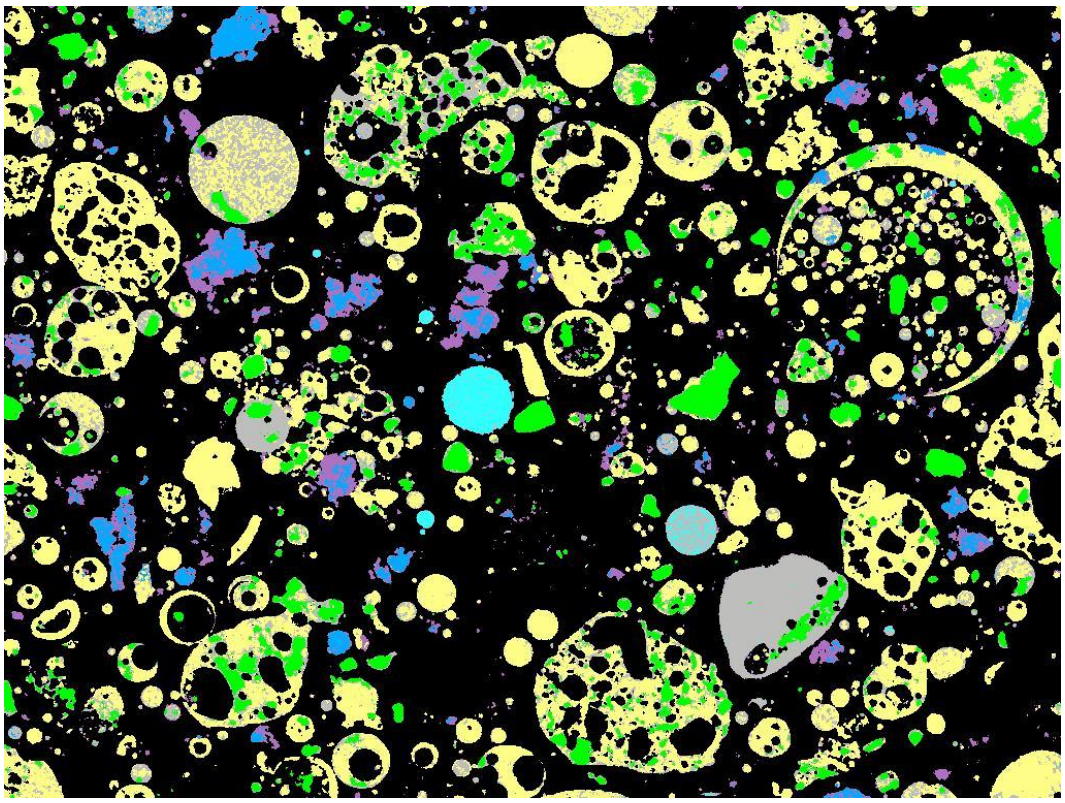

Figure 5.42: Phase assigment image of Fontana fly ash residue after 7 d exposure to 8 M NaOH solution

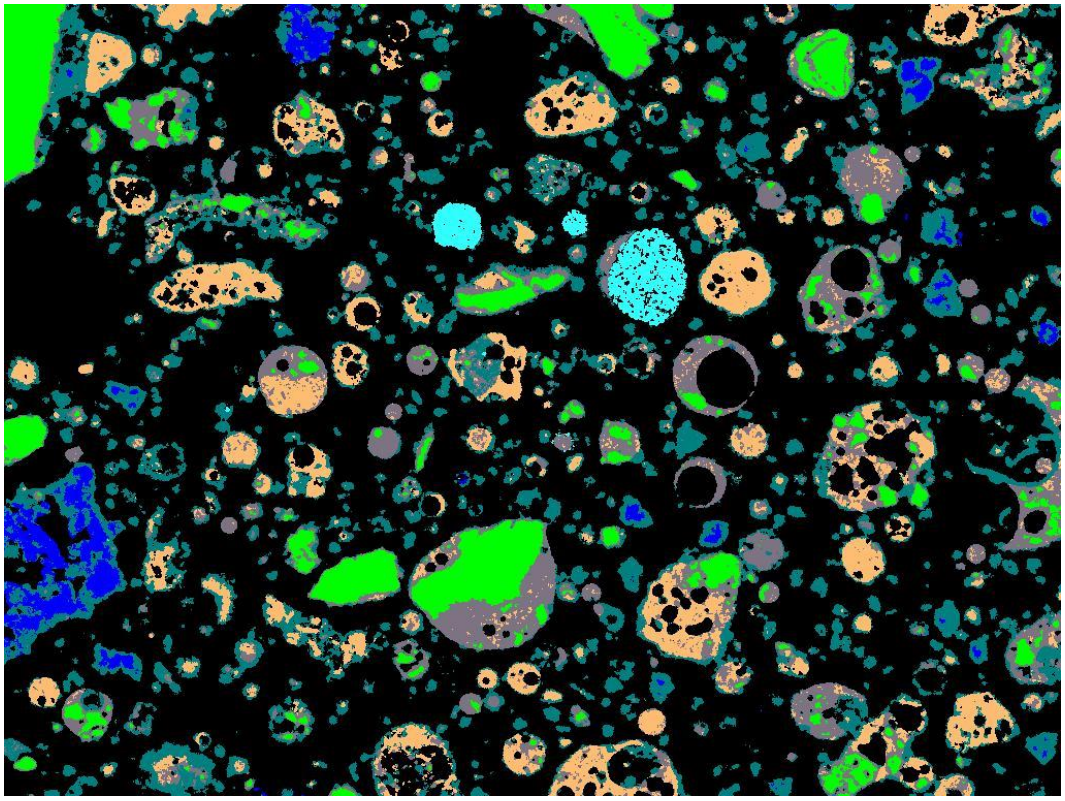

Figure 5.43: Phase assignment image of Fontana fly ash after 28 d exposure to 8 M NaOH solution

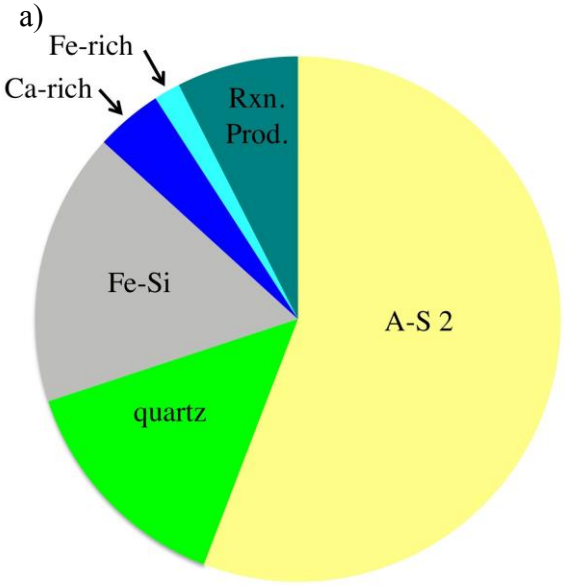

Phase	Area %
A-S 2	55.83
quartz	14.09
Fe-Si	16.84
lime	4.12
Fe-rich	1.63
Reaction Product	7.49

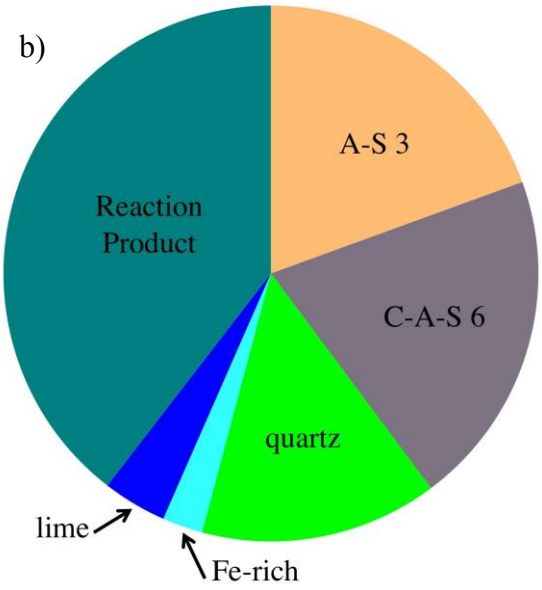

Phase	Area %
A-S 3	19.45
C-A-S 6	20.34
quartz	14.35
Fe-rich	2.45
lime	3.87
Reaction Product	39.53

Figure 5.44: The phase distribution of Fontana fly ash after 7 d (a) and 28 d (b) exposure to 8 M NaOH solution; each based on a single sample

Reaction product identified at 28 d was high in aluminum and silicon and very low in calcium (2 %, by mass), with around 5 % sodium. The composition was not analyzed at 7 d, despite the segmentation of a small amount of reaction product at that time period. The 28 d composition showed that silicon and aluminum had leached from the sample, and sodium was incorporated for charge balancing.

The Fontana fly ash contained mostly aluminosilicate phases in its original state and at 7 d. The compositions at each time are given in Figure 5.45. At 28 d, the C-A-S 6 phase was identified. This was surprising, given that the Fontana fly ash was low in calcium (approximately 5 % CaO). However, the C-A-S 6 phase is compositionally similar to the A-S 1 phase identified in the raw fly ash, sharing similar amounts of silicon and aluminum, and differing by the 7 % calcium identified in C-A-S 6. The Si/Al ratio of the C-A-S 6 phase was 3.2 versus 2.9 for the A-S 1. The Si/Al of A-S 2 was 1.82, which would not explain the identification of the C-A-S 6 phase. Since the A-S phases change

compositionally through the dissolution process, it is clear that leaching does occur from the A-S phases, which was also evidenced by the formation of reaction product at both time periods. Since the Fontana fly ash was designated poorly reactive, the results are not entirely suprising; most of the material was present in poorly soluble A-S phases, although it has just been shown that the A-S phases likely leach some amount of the network forming silicon and/or aluminum.

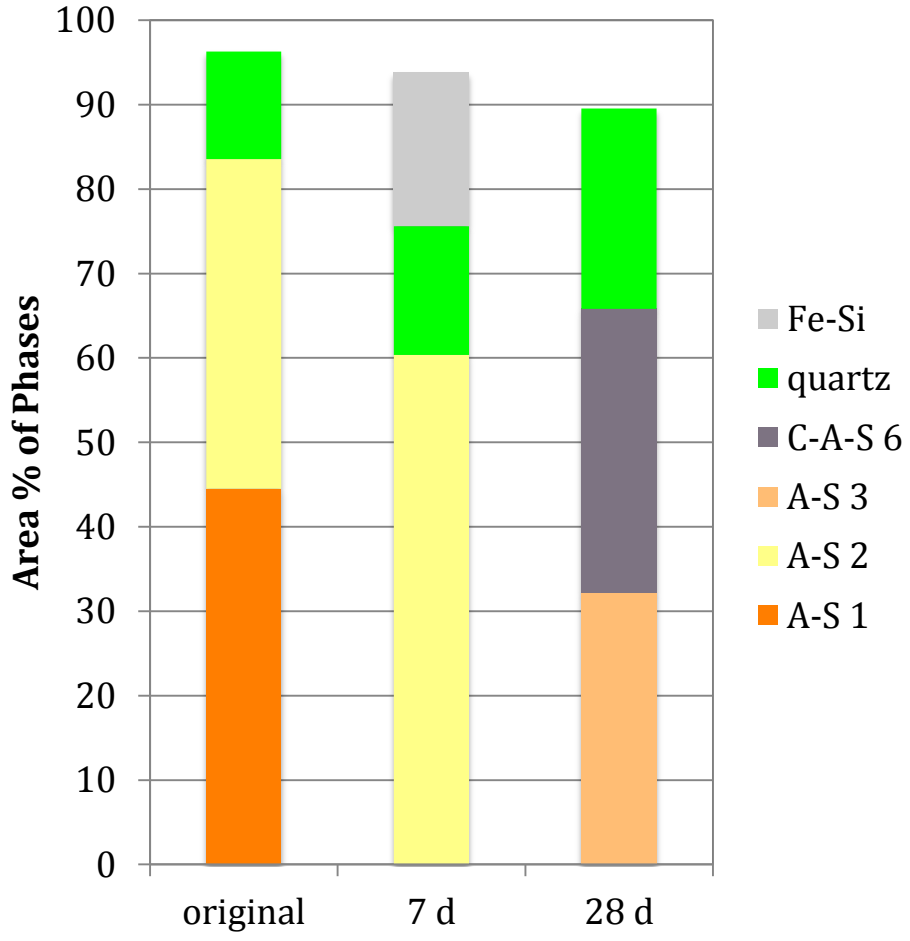

Figure 5.45: Fontana fly ash: relative composition of fly ash before and after exposure to 8 M NaOH solution

5.2.12 Discussion of dissolution testing results

In the previous sections the dissolution test results for the ten fly ashes in the study were presented with the names, compositions, and relative amounts of each phase measured at each time period given for each fly ash. It was expected that the residual fly ash phases identified in the residues would be similar to the original fly ash phase compositions, while reaction products would possibly form on the surface of particles due to the dissolution-precipitation model of geopolymer formation (Duxson, Fernández-Jiménez, et al. 2007; Chen-Tan et al. 2009; Chen et al. 2011). Since the compositions were measured away from particle edges, and the dissolution model states that the dissolution of aluminosilicates should take place at the particle surface, the hypothesis was made that the same phases would be found in the fly ashes over time (albeit in reduced quantity), with the appearance of reaction products. However, this did not happen in most cases as new fly ash phases appeared in many of the fly ashes after exposure to caustic solution.

The aluminosilicate phases were hypothesized to be mostly insoluble, since they consisted mainly of network-forming aluminum and silicon; thus, any reaction should be slow (Chen et al. 2011). The C-A-S phases were generally hypothesized to be soluble, with the degree of solubility dependent on the stoichiometry of the glasses, since they contained varying amounts of network-modifying calcium and other elements. The N-A-S phase was predicted to be insoluble, since it contained < 5 mass % sodium as a modifier in the mostly aluminosilicate composition. The Fe-rich phases were considered insoluble since iron was network forming, and in addition, the phase was also assumed to contain the slow-reacting crystalline iron phases. Quartz was also considered generally insoluble since it was of crystalline form that would likely dissolve extremely slowly if at

all under the caustic conditions of the experiments. The Mg-rich phase was thought to be soluble since magnesium is a network modifier.

As mentioned in the introduction to Section 5.2, sampling error can explain the presence and absence of phases that were identified in small quantity in any of the images. Therefore, the results for any phase that was identified in less than 5 % of the image area are omitted from the discussion.

In four of the fly ashes, the aluminosilicate phase amounts increased over time, corresponding to a decrease in the total amount of CAS phases. This occurred in the Big Brown Raw, Coleto Creek, LEGS, and Martin Lake fly ashes. Of those ashes, three were designated reactive by their mortar strengths, and the Big Brown Raw fly ash was the fly ash with the highest measured compressive strength at 28 d. Unfortunately, there are not enough similarities in the actual compositions across these fly ashes to draw conclusions on the specific C-A-S phases that may be highly reactive. Big Brown contained C-A-S 4 and C-A-S 6, Coleto Creek contained C-A-S 1, C-A-S 5, and C-A-S 7, LEGS contained C-A-S, C-A-S 2, C-A-S 5, C-A-S 7, and C-A-S 8, and the Martin Lake fly ash contained C-A-S 5, C-A-S 6, and C-A-S 8. The C-A-S 5 phase that was noted to be the only phase to consistently disappear from fly ashes is contained in these; however, the phase is not present in high amount in any of the fly ashes, so its solubility could not be the sole reason for their classification as reactive or moderately reactive.

C-A-S 1 was hypothesized to be reactive, as it appeared in Big Brown Raw, Bell River, and Atikokan fly ashes, all "reactive" fly ashes. The phase was identified in the original fly ashes and disappeared by 28 d in all of the fly ashes. Therefore, this phase was considered reactive. However, it was also identified in large amounts in the 7 d and 28 d samples of the Boral Class C fly ash, after not being identified in the original fly ash. It is noted that the Si/Al ratio for this phase at 28 d is the lowest of all of the C-A-S 1

phases (0.67), and the Ca/Si ratio is the highest at 5.78. Therefore, while the phase was classified C-A-S 1 in the Boral 28 d sample, it is a bit of a compositional outlier compared to the compositions of the other C-A-S 1.

The C-A-S 6 phase was hypothesized to be soluble and was identified in the Big Brown Raw, Bell River, and Martin Lake fly ashes. It was soluble in the Big Brown Raw and Martin Lake fly ashes, as it was not identified after NaOH exposure. However, the phase was identified in the Bell River fly ash at multiple times in similar amounts. Further, this phase appeared in several fly ashes at later age (Coleto Creek, Fontana). Therefore, the solubility of C-A-S 6 is inconclusive and the hypothesis that it was reactive was not proved.

The C-A-S 5 phase was noted as the only phase that was identified only in original fly ashes and dissolved completely from them. However, this phase was relatively minor in amount, so while it would likely cause favorable reactivity if present in large amounts it is unlikely that it caused the favorable reactivity for the fly ashes in this study.

The A-S phases were generally considered insoluble. However, the Belews Creek and Fontana fly ash results showed that although the majority of the total fly ash composition was made up of A-S phases, the compositions of the phases did change over time, particularly after reaction product was identified. This means that the A-S phases in the fly ashes did leach to some degree. Compositional similarities were identified in the lowest-calcium C-A-S phases and the A-S phases and were described for each fly ash. This was hypothesized to mean that when these low-Ca C-A-S phases (CAS 6 and CAS 7) were identified in a fly ash while little or no A-S phase was identified, that these phases likely behaved as an A-S component, i.e. were poorly reactive but exhibited some leaching behavior.

The N-A-S phase was considered insoluble, and its results upheld that hypothesis. For the fly ashes that contained N-A-S (Atikokan, Boral Class C, Bell River and Centralia), no significant differences in the amount of N-A-S were identified over time, so no conclusions could be made about its solubility. One observation made in the Atikokan fly ash was that the N-A-S phase composition changed over time such that it appeared that aluminum might have dissolved from this phase. This would be one reason why the Atikokan fly ash was reactive based on the compressive strength results.

5.2.12.1 Discussion: Reaction Product formation and composition

Reaction products formed in all of the specimens after some amount of time; for the reactive and moderately reactive specimens reaction products were visible by 7 d, while for the poorly reactive specimens reaction product was visible in Fontana at 7 d, while it was not visible in Belews Creek until 28 d. The reaction product compositions were quite varied. In some fly ashes (Atikokan, Bell River, and LEGS) the calcium content of the reaction product was higher at 7 d than at 28 d, while in other fly ashes (Coleto Creek and Martin Lake) the calcium content was higher at 28 d than at 7 d. Thus, the calcium did not follow a pattern of being high in the early stages and lower later or vice versa. When compared to the initial amount of calcium based on the oxide analysis (Table 3.1), there was no pattern observed either. The calcium content from highest to lowest was found in Bell River, Coleto Creek, Atikokan, LEGS, and Martin Lake. The Coleto Creek fly ash was the Class F fly ash with the greatest Ca yet it had low calcium in the 7 d reaction product. Based on these data, it is clear that the solubility of the calcium-containing phases was the more important factor, so that the calcium could more quickly go into solution and then exceed the saturation point, at which point it would precipitate. Fernández-Jiménez et al. (2006) described reaction products as first forming an aluminum-rich phase and then incorporating silicon, although this was at very early

age. In these data, the silicon increased from 7 d to 28 d in all cases for which compositional data was collected at both time periods. The aluminum similarly decreased in small amount in several fly ashes (Martin Lake, LEGS, Atikokan), while there was no change noticed in the Bell River. This result was not surprising, given that the Bell River already had reacted significantly by 7 d, based on the mortar cube results the amount of reacted fly ash; Bell River was no longer in early age described by Fernández-Jiménez et al. (2006) by 7 d of reaction.

The reaction products all had higher amounts of iron than would be expected since geopolymers are typically characterized as aluminosilicate composition. Additionally, the iron-rich crystalline materials were considered inert, and it has been stated that the iron-bearing aluminosilicates would be hindered from dissolving aluminum or silicon (Chen-Tan et al. 2009). However, use of a waste product such as fly ash introduces impurities such as iron, calcium, potassium, magnesium, etc. into the geopolymer composition if they are present in soluble phases. The results from my work showed that iron was contained in the reaction product, and these results were supported by results found by (Chen et al. 2011). The study by Chen et al., which was a dissolution study of fly ash mixed with KOH solution, found that iron was observed in the second time step modeled (precipitation of an early reaction product), and that gel formed on the surface of particles. The gel on the particle surfaces observed by Chen et al. (2011) also frequently contained magnesium, calcium, and titanium. A second type of reaction product was noted in the third time step modeled by Chen et al. (2011), which was the formation of an aluminosilicate gel between the thick surface layer and the fly ash. It is important to note that the model showed that there were diffusion mechanisms that allowed for continued dissolution from the fly ash through surface reaction products after the initial first order dissolution from the surface of the fly ashes. In the third time step,

they described a darker gap identified in the BSE image, which was similarly visible in thee data for fly ashes including Atikokan and Coleto 28 d samples, shown in Figures Figure 5.46 and Figure 5.47. In these images, the reaction product seemed to be separated from the particle surfaces by a gap, which may have been improperly classified as voids due to low signal in the x-ray images.

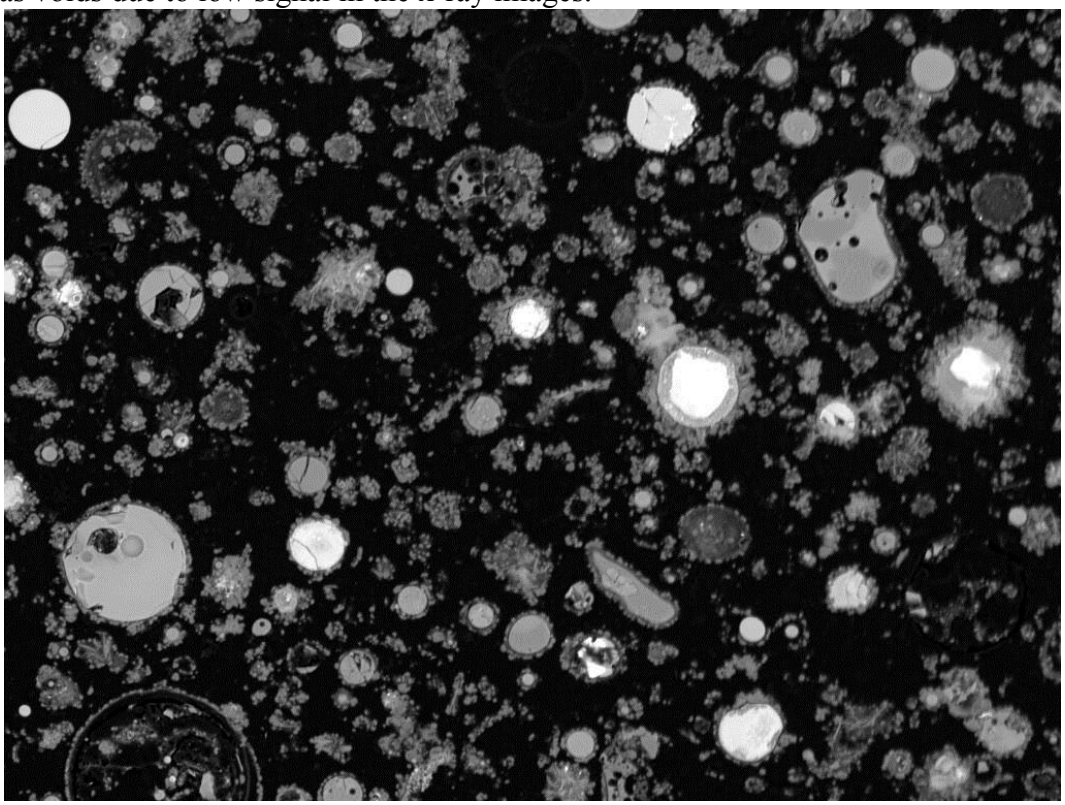

Figure 5.46: Atikokan 28 d BSE image, depicting some particles in which the reaction product appeared to gap from the particle surface

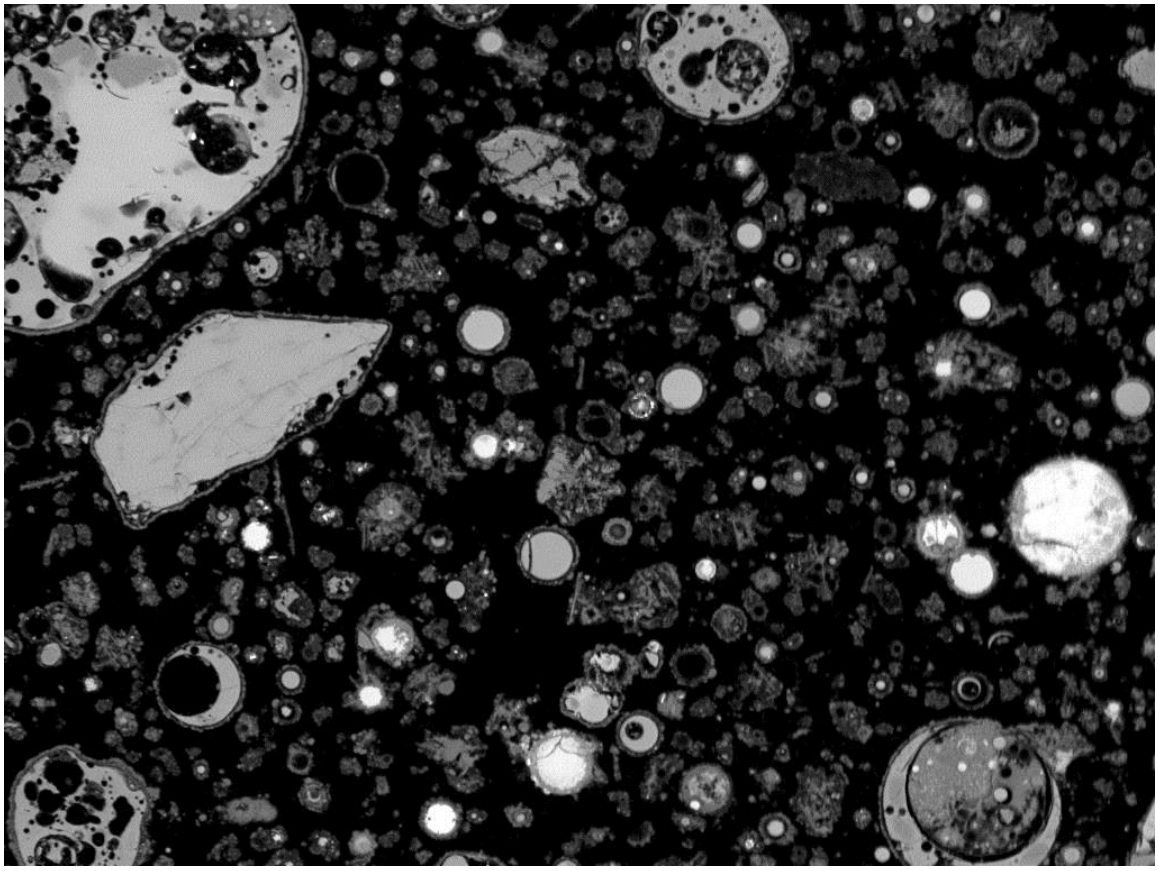

Figure 5.47: Coleto Creek 28 d BSE image, depicting some particles in which the reaction product appeared to gap from the particle surface

As mentioned briefly in each of the fly ash results sections, the compressive strength category (reactive, moderately reactive, and poorly reactive) that was given based on the 28 d results showed some correlation to the amount (area %) of reaction product; however, correlation could only be made in some cases for the reactive and poorly reactive fly ashes. The Atikokan, Bell River, Big Brown Raw, Centralia, Coleto Creek, and Martin Lake fly ashes were considered "reactive," and at 28 d they had 75 %, 69 %, 64 %, 53 %, 46%, and 75% reaction product (by area), respectively. The moderately reactive fly ashes, LEGS and Boral Class C, had 47 % and 69 % reaction product (by area), respectively. The poorly reactive fly ashes, Belews Creek and

Fontana, had the least reaction product at 37 % and 40 % (by area), respectively. These results showed that there was no clear difference in amount of reaction product for the reactive and moderately reactive fly ashes for this sample set. The two moderately reactive fly ashes had more reaction product in the image area than some of the reactive fly ashes. Since this was a dilute system (s/p = 6.4 by mass), the results were not completely representative of the availability of caustic solution to dissolve and react with the fly ash during the actual geopolymer reaction in which the s/p was 0.485, significantly lower. Therefore, from these results it is concluded that the appearance of geopolymer reaction product on the surface of particles in a dissolution study may indicate its likelihood of forming a strong geopolymer, but it is a relationship that would require further study.

5.3 REACTIVITY IN GEOPOLYMERS: RESULTS SUMMARY AND CONCLUSIONS

The hypotheses presented in Chapter 4 were tested in Chapter 5 to determine whether the fly ashes that were thought likely to be reactive actually were, and to determine whether the phases that seemed likely reactive were in fact reactive. The results showed that all but one fly ash that was hypothesized reactive was also designated reactive based on compressive strength results. Conversely, one fly ash that was not hypothesized to be reactive was designated reactive based on compressive strength results, and in fact had the highest compressive strength at 28 d. From the dissolution study results, more detailed information regarding the solubility of the phases has been revealed. The results are useful in predicting whether a fly ash is likely to be reactive in geopolymer formation.

The conclusions made from the results presented and discussed in this chapter include:

- The compressive strength results showed that the fly ashes predicted to be reactive based on bulk amorphous content SiO_2/Al_2O_3 ratios in Chapter 4 were reactive, except for one fly ash (LEGS), which was moderately reactive. The fly ash predicted to be least reactive was also poorly reactive. However, one fly ash that was not predicted to be reactive had very high strength (Big Brown Raw), and it had a similar bulk amorphous content to a fly ash that was classified poorly reactive (Belews Creek). The poorly reactive fly ash was not classified as such based on amorphous content or silica to alumina ratios. Therefore, these parameters cannot be used directly.
- The d_{50} particle size value showed a trend for reactivity (finest for the most reactive, medium for the moderately reactive, and coarse for the poorly reactive), but the Big Brown Raw fly ash showed that this was not an absolute trend due to its high reactivity and large d_{50} particle size.
- The glassy phase dissolution results showed that a decrease in soluble phases coupled with an increase in generally insoluble phases in the residue after exposure to NaOH indicated reactivity. This occurred for the Big Brown Raw, Coleto Creek, LEGS, and Martin Lake fly ashes. Of these, all but the LEGS fly ash were considered reactive based on the compressive strengths of mortars.
- For the fly ashes that followed the expected trend of decreasing C-A-S phases and corresponding relative increase in A-S phases, most did not have the same C-A-S phases at the different measurement times, so conclusions could not be drawn regarding glassy C-A-S phases that were consistently found in reactive fly ashes.
- One phase, C-A-S 1, was deemed reactive based on its identification in two reactive fly ashes (Bell River and Atikokan) at early age and disappearance by 28 d.

- The C-A-S 1 phase was identified only at late age in two fly ashes (Big Brown Raw and Boral). It was a minor phase in the Big Brown Raw, but it made up the bulk of the Boral fly ash at 7 d and 28 d. This result is thought to mean that although the C-A-S 1 phases identified across all of the ashes had compositional similarities, there was another factor besides composition alone that affected its reactivity.
- The C-A-S 5 phase was considered soluble due to its identification only in original fly ashes (Coleto Creek, LEGS, and Martin Lake); however, it was not present in high amounts that would have led to the high compressive strengths of the two reactive fly ashes, Coleto Creek and Martin Lake.
- The C-A-S 6 phase, although disappearing from some fly ashes over time, generally seemed relatively insoluble and may be more compositionally similar to the A-S phases due to its relatively low calcium amount. Therefore, it is suggested that calcium of up to 7 % should be classified as a poorly soluble aluminosilicate phase as opposed to the 5 % limit placed on the phases in this work.
- Based on the disappearance and reappearance of the same phases in different samples, it seems possible that the phases, while compositionally similar in their averages of the elements present, may have been somewhat structurally different in some cases, which altered the reactivity from one fly ash sample to another.
- There was no clear difference in amount of reaction product for the reactive and moderately reactive fly ashes, but the poorly reactive fly ashes had considerably less reaction product identified in their images. This was consistent with their low compressive strengths, since more reaction product will generally give higher compressive strengths in a cohesive cementitious material.

- The appearance of geopolymer reaction product on the surface of particles in a dissolution study may indicate its likelihood of forming a strong geopolymer, but it is a relationship that would require further study.
- The solubility of the calcium-containing phases was more important than the amount of calcium identified in the fly ash, which led to the calcium dissolving into solution more quickly and then precipitating into the reaction products.

In summary, the characteristics of fly ash such as the silica to alumina ratio and amount of bulk amorphous phase can predict whether fly ashes will perform well as geopolymers, but they do not tell the whole story. The results presented here showed that there were many glassy phases in fly ashes, of which some were more reactive than others. In addition, the total amount of the phases and particle sizes will affect the degree to which the phases can contribute silicon and aluminum to the formation of geopolymer gel when they are mixed with caustic solutions.

Chapter 6: Refinement of phase assignment strategy: K-means analysis

In Chapters 4 and 5, the results of data clustering for ten fly ashes were presented in the form of phase assignment images. The phases were defined by selecting training classes (groups of pixels) for use in a clustering algorithm. The training classes were identified after rigorous visual examination of the contributions from up to seven x-ray maps to the compositions of the fly ash particles. The clustering resulted in the phase assignment images, with regions of similar composition sharing the same color; however, while the phases could be clustered using MSIA, the actual compositions of the phases had to be measured separately using point quantitative analysis. The average composition of each phase was then calculated by assigning the point compositional data at each point to its phase as assigned in MSIA and averaging the values for each phase. Usually there were more than 5 points per phase used in the calculation of the phase composition. The results typically showed that the compositions were close for the particles assigned to the same phase, with small standard deviations, but sometimes the standard deviation was great and outliers were numerous. This led to the idea that the point compositions could be clustered so that the quantitative point compositional data could be used to select training classes, using the particles that were grouped together in the quantitative point clustering to aid in the clustering of the x-ray image data. This method could aid in selection of training classes for MSIA, instead of selecting training classes through rigorous visual examination. The k-means analysis method was investigated as an alternative method for the purpose of clustering based on quantitative compositional data. Research by Bumrongjaroen et al. (2011) used the k-means method to cluster compositional data points taken from fly ash samples in their work to develop standard glasses that represent fly ash compositions (Bumrongjaroen et al. 2011).

In this chapter, the method of k-means analysis is introduced and an example of the use of k-means analysis is presented for one fly ash, Martin Lake, and compared to the results presented for the same fly ash that were presented in Chapter 4.

6.1 BACKGROUND AND EXAMPLE: K-MEANS CLUSTERING

The k-means clustering algorithm was introduced in the 1970s and is a method in which a matrix of M points in N dimensions is clustered using K cluster centers in N dimensions (Hartigan and Wong 1979). For this work the implementation available in MATLAB was used, and the reader is referred to the help menu in MATLAB for further information on using the algorithm and the references on which the MATLAB implementation is based. The usefulness of the k-means clustering algorithm for clustering compositional data is in its ability to cluster multidimensional information, which for this dissertation is in the form of matrices of point compositional data. In the work done here, the distance parameter to be minimized for each cluster was set to use the squared Euclidean distance similar to Bumrongjaroen et al. (2011). The number of clusters, k, must be specified in the algorithm, although the code can be written such that multiple k values are run successively so that empirical observations by the researcher can then select the best value. In this work, I selected the appropriate value by observation of the results of all of the runs. The empirical nature of selecting the appropriate number of clusters was also noted by Bumrongjaroen et al. (2011).

A sample demonstration of the k-means clustering is given for a simple set of random data points, which comprised two classes. The example code given in the MATLAB help file for k-means clustering was used in this example. The data sets were comprised of two random, Gaussian-distributed classes, which had 50 points each and were centered at (-1, -1) and (1,1) on Cartesian coordinates and had a standard deviation

of 1. The data sets before clustering are shown in Figure 6.1 as a bi-plot (i.e. a 2-dimensional scatter plot) on a dimensionless (x, y) axis.

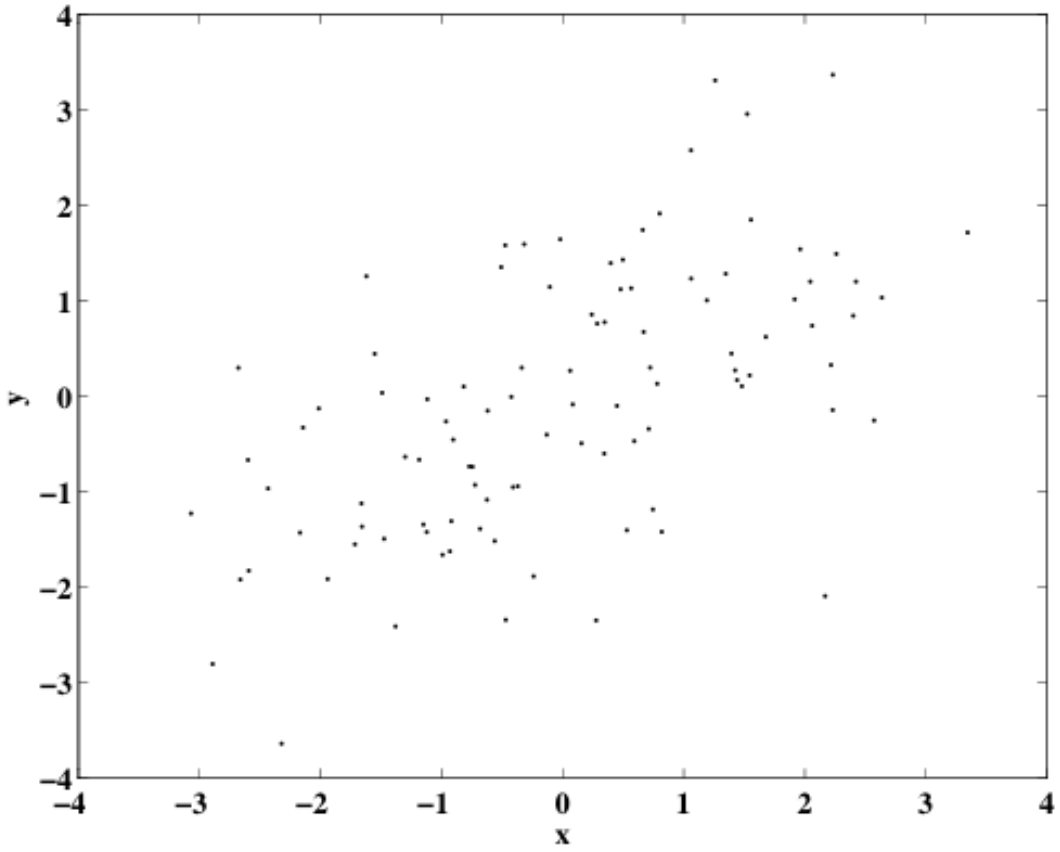

Figure 6.1: Sample data set bi-plot of two random data sets centered on (1, 1) and (-1, -1) with Gaussian distribution

The k-means clustering algorithm was applied to these data, for which the clusters are known to be the two data sets that were randomly generated. Five k-means replicates were run in an attempt to find the global minimum of clustering. Each of the 5 replicates started with different cluster centers, and the final output was the clustering result that minimized the squared Euclidean distance from the points in the cluster to the center of the cluster. After clustering, the points clustered together are known as classes. In other

words, class 1 and class 2 in this example were generated from data set 1 and data set 2. As a method for visualizing the multidimensional data classification, an N x N matrix of plots was generated in which each plot displayed the clusters projected to a two dimensional plane (x, y), called a bi-plot. In this example, N = 2, so a single plot is given, since the data can be shown by the two axes, x and y. The clusters resulting from the k-means analysis of these two data sets are given in Figure 6.2. The data sets were originally centered on (-1, -1) and (1,1), which are depicted on the clustering image as stars ("True Center" of class 1 and class 2). The centroids of the clustered classes by k-means analysis are depicted with an X for each class (Class 1 and Class 2 "centroid, k-means). The original data ares shown using the outlined markers depicted as "Class 1, true" and "Class 2, true." The newly classified k-means clusters ("Class 1, k-means" and "Class 2, k-means") show the classes.

Since the clustering algorithm is attempting to minimize the distance from the center of the cluster to each point, classification of points from one data set into the opposite phase was bound to occur, particularly at the intersection of points from the two data sets. For example, refer to Figure 6.2, and find the point at (-1.5, 1.5), which is a red dot surrounded by a blue square. This point was originally part of Class 2 (blue square), but it was classified as Class 1 (red dot) by the k-means algorithm. This means it was mathematically closer to the center of class 1 (depicted by the red X) than to the center of Class 2 (depicted by a blue X). The appropriate phase is not necessarily obvious to the eye for this particular point, but reviewing the points that fall along the intersection of the phases (near the upper left edge of the legend) shows points that are obviously closer to the opposite phase's center. This is not a misclassification, rather it shows that the points were mathematically more similar to the other class.

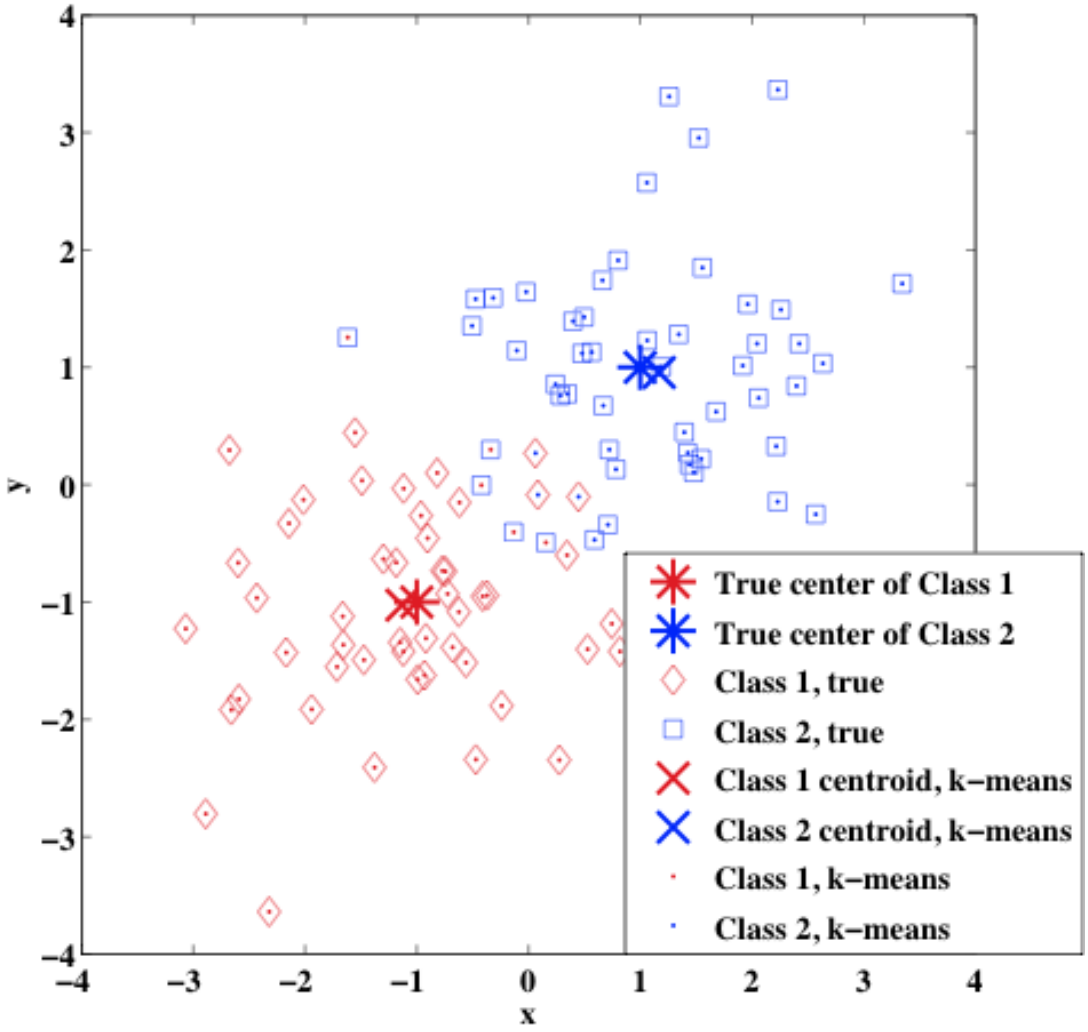

Figure 6.2: Sample data set bi-plot of two random data sets centered on (1, 1) and (-1, -1) with Gaussian distribution after clustering using the k-means method

In this example, the points were generated specifically as a Gaussian distribution around a center point. In most data sets, this is not the case, so clustering is being done without preconceived knowledge of how the points should be classified. From the example, it is shown that the known center and the k-means center were very close to each other and there were few points classified into different classes. Therefore, the

method should be relatively accurate in its assignments when used on data for which the center is unknown.

This type of clustering can be done using many more than two data sets, from which phases are identified. When applied to fly ash, the (x-y) coordinates would take on the dimensions of amount of each element in each point in the fly ash, and clustering would result in classes of similar compositional features (i.e. the phases discussed in Chapter 4 and 5). An example of a fly ash k-means analysis is presented in the next section.

6.2 EXAMPLE: MARTIN LAKE FLY ASH

K-means clustering can be used in one of two ways for the point compositional data collected for a fly ash. Some researchers have used it to comprehensively characterize the glasses in fly ash (Bumrongjaroen et al. 2011). In the present work, it was used to determine where to select training classes in multispectral images for classification of particles in an image to phases of similar composition.

The Martin Lake fly ash that was presented in Chapter 4 is revisited in this example. The k-means clustering method just described was applied to the compositional point data taken for the fly ash. The data were given to MATLAB as a matrix in which the rows corresponded to the composition at an individual point and the columns consisted of the amount of an element in the point. There were 108 data points collected in 2 Martin Lake fly ash samples, which corresponded to 108 rows (108 different point compositions), and 8 columns (Ca, Si, Al, Fe, Na, Mg, K, and O), which corresponded to the 8 elements used to classify the points compositionally. It is worth noting here that 108 data points is a small data set for comprehensive characterization of fly ash, and Bumrongjaroen et al. reported using approximately 10,000 point compositional measurements per fly ash (2011); however, the purpose of this clustering algorithm was

to aid in training set selection for multispectral image analysis, so the large number of points used in the referenced work were not necessary since full compositional characterization of the fly ash by this method was not the goal. The built-in k-means function in MATLAB was used in this work. The number of replicates was set at 1,000 to improve the chances that the global minimum was reached through the clustering. This was a high number of replicates, but the computational time was short, so it was not necessary to minimize the number of replicates. The clustering was run for 5, 6, 7, 8, 9, and 10 clusters to determine which resulted in the best classification of the data. The results of the clustering with each of these numbers of clusters were examined to determine the best result. The phases identified in the fly ash in Chapters 4 and 5 were not considered in the assessment of which number of clusters was best, although the range of possible clusters (5-10) was selected knowing that the Martin Lake consisted of 7 classes (Chapter 4). The results yielded 8 dimensions that cannot be visualized directly. Instead, each of the bi-plots shows each of the sets of clustered points in the same marker style against two-dimensional projections of the data onto a plane where the x-y axes were each an element composition percentage (i.e. Ca x Ca, Ca x Al, Ca x Si, etc.). The resulting 64 plots slice the data to every combination of pairs of elements, with redundancy above and below the diagonal. The plots were helpful in assessing how well phases were clustered and how many clusters were appropriate for the fly ash.

The matrices of bi-plots for all 6 possible numbers of clusters were examined, and the best fit was determined to be with 8 clusters. For fly ash, this means that 8 compositional phases were identified in the fly ash. The bi-plots are shown in Figure 6.3. Since these are somewhat small and the majority of the fly ash particles were clustered based on Ca, Si, and Al, the 3 x 3 Ca-Si-Al matrix of plots is given in Figure 6.4. The classes can be distinguished by how closely they cluster in bi-plots for the main elements

of interest. For example, on the potassium by silicon plot in Figure 6.1, the black crosses (class 5), appear to be somewhat separated, but on further inspection, it is clear that they are separated by only 2 %, by mass, which is a unlikely to be of great importance compositionally. Therefore, it is important to realize that when interpreting the data, in some dimensions the data may not look clustered, but if it is a minor element, then this is likely not an indication that the data were clustered incorrectly. Class 6 is the one class that appears to consist solely of several outliers, although by examining aluminum versus iron, closer agreement is obtained. This phase is the iron-rich phase in the fly ash, but its composition varied widely for the elements other than aluminum and iron. All of the remaining classes appeared to be clustered distinctly.

The compositions of points that were clustered together were listed together in Excel so that the averages and standard deviations of the phases could be calculated. Since the actual compositional data were clustered in this process, it was expected that they would have small standard deviations. Table 6.1 gives the cluster compositions by class, and shows that the standard deviations are small.

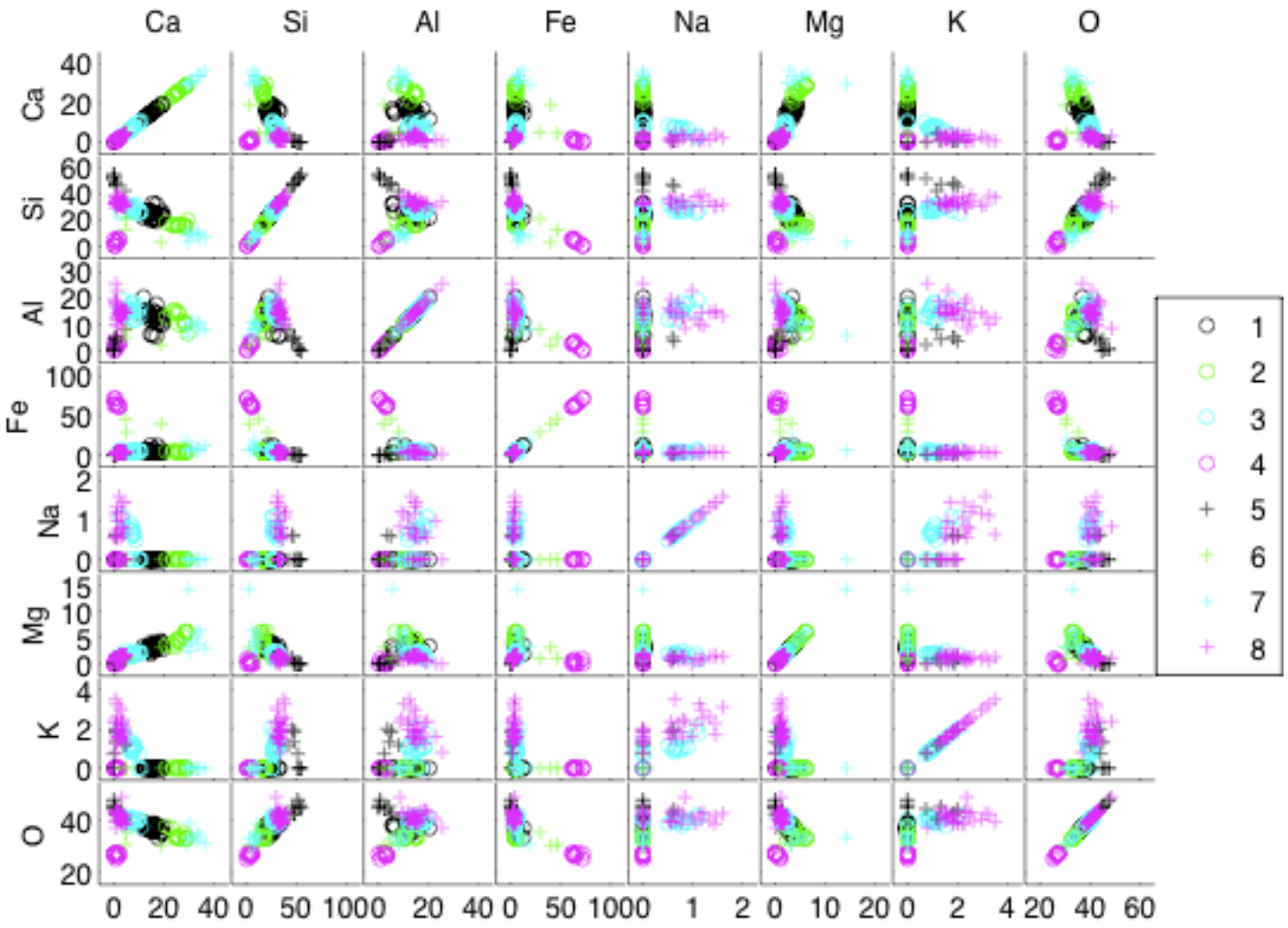

Figure 6.3: Bi-plots of clusters for Martin Lake fly ash; 8 clusters

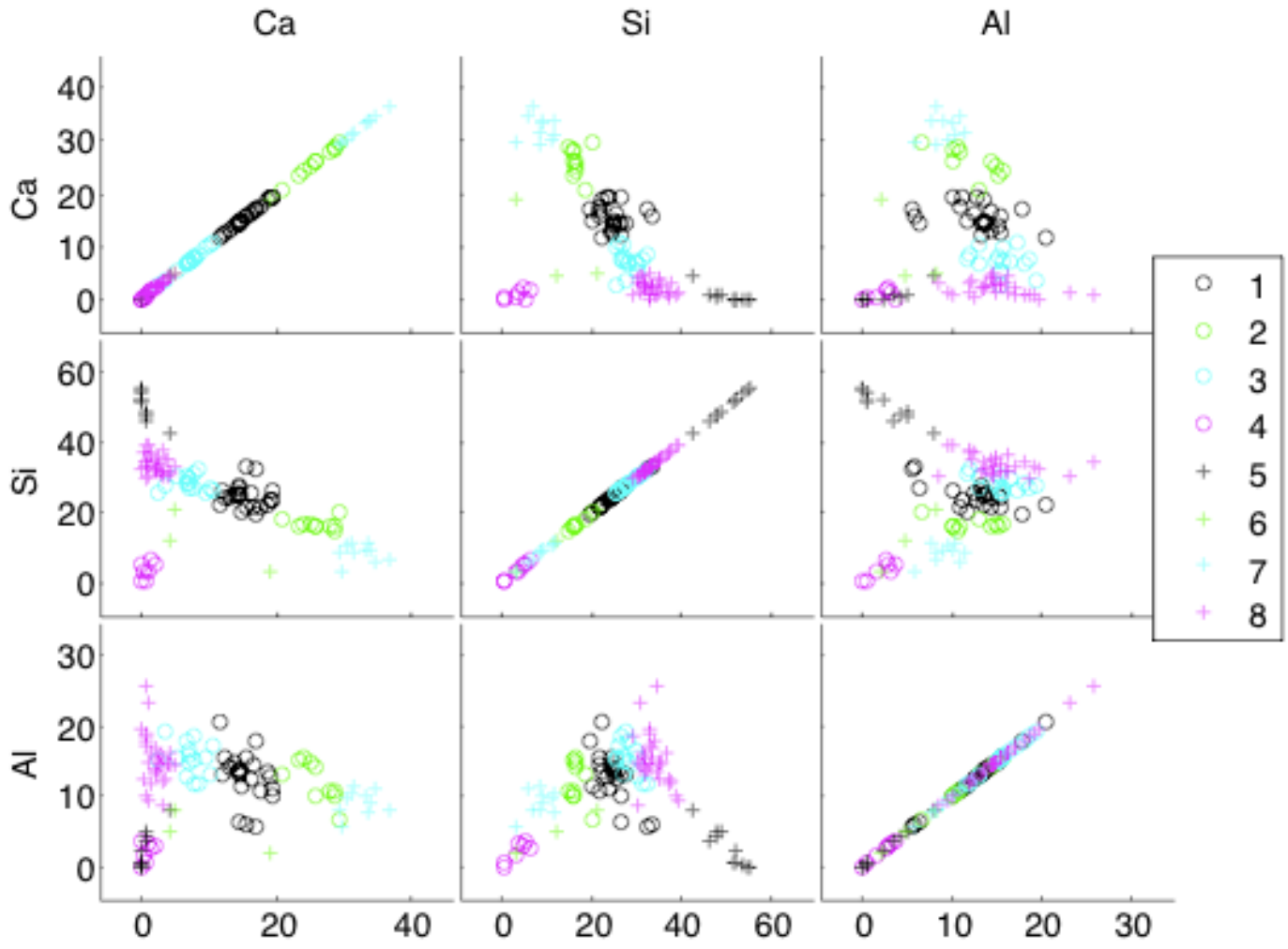

Figure 6.4: Bi-plots of clusters for Martin Lake fly ash plotted by calcium, silicon, and aluminum; 8 clusters

Table 6.1: Cluster composition averages for Martin Lake fly ash

		Mass % Element							
		Ca	Si	Al	Fe	Na	Mg	K	O
class 1	**average**	**16.0**	**25.1**	**11.4**	**6.0**	**0.0**	**3.3**	**0.0**	**36.4**
	std. deviation	2.1	3.5	2.9	3.2	0.0	0.8	0.0	1.6
class 2	**average**	**26.7**	**16.1**	**12.1**	**4.9**	**0.0**	**4.9**	**0.0**	**33.6**
	std. deviation	1.8	0.7	2.5	1.0	0.0	1.1	0.0	0.9
class 3	**average**	**7.3**	**29.3**	**15.1**	**4.9**	**0.5**	**1.9**	**1.1**	**39.3**
	std. deviation	2.5	2.3	3.0	0.3	0.4	0.6	0.6	1.5
class 5	**average**	**0.8**	**47.4**	**4.6**	**1.2**	**0.3**	**0.5**	**1.8**	**43.5**
	std. deviation	0.0	1.1	0.7	0.4	0.4	0.6	0.3	1.4
class 4	**single point**	**1.4**	**3.8**	**3.3**	**64.0**	**0.0**	**0.9**	**0.0**	**26.1**
class 6	**single point**	**4.5**	**12.5**	**5.0**	**46.4**	**0.0**	**1.0**	**0.0**	**30.6**
class 7	**average**	**33.2**	**8.0**	**9.0**	**8.2**	**0.0**	**6.1**	**0.0**	**33.2**
	std. deviation	2.2	2.7	2.0	2.0	0.0	3.8	0.0	1.3
class 8	**average**	**2.4**	**34.6**	**14.7**	**3.4**	**0.6**	**1.2**	**2.1**	**40.6**
	std. deviation	1.5	2.7	3.5	1.4	0.5	0.5	0.6	1.6

The next step after the clustering analysis was to use the clustered points to select training sets for multispectral image analysis. The point map (Figure 6.5) was used to match each compositional data point in each class to the appropriate particle, for training pixel selection. For example, in class 1, there were 11 points in the k-means cluster, so regions of pixels were selected in each particle at approximately the same location as the compositional data was collected for all 11 points. The regions selected around each of 11 points became the training pixels for Class 1. The same process was followed for each of the other 7 classes. Care was taken to avoid selecting regions within the particle that were of different composition than the location of the quantitative point analysis by observing changes in the appearance on the stacked x-ray image or the backscattered image if necessary. In this example, class 4 and class 6 were both high-iron phases, but with significantly different composition (an average of 46 % versus 64 % iron, by mass). These were combined into one phase for MSIA, due to their similar iron intensities in the x-ray map. The training class map is shown in Figure 6.6, which illustrates the large number of training pixels that were selected for each class. The Fisher Linear Likelihood method was once again used for classification, although the Minimum Euclidean Distance and

Quadratic Likelihood methods were tested; the latter two methods resulted in poor classification for the minor iron-rich phase, so they were deemed poor methods for these data.

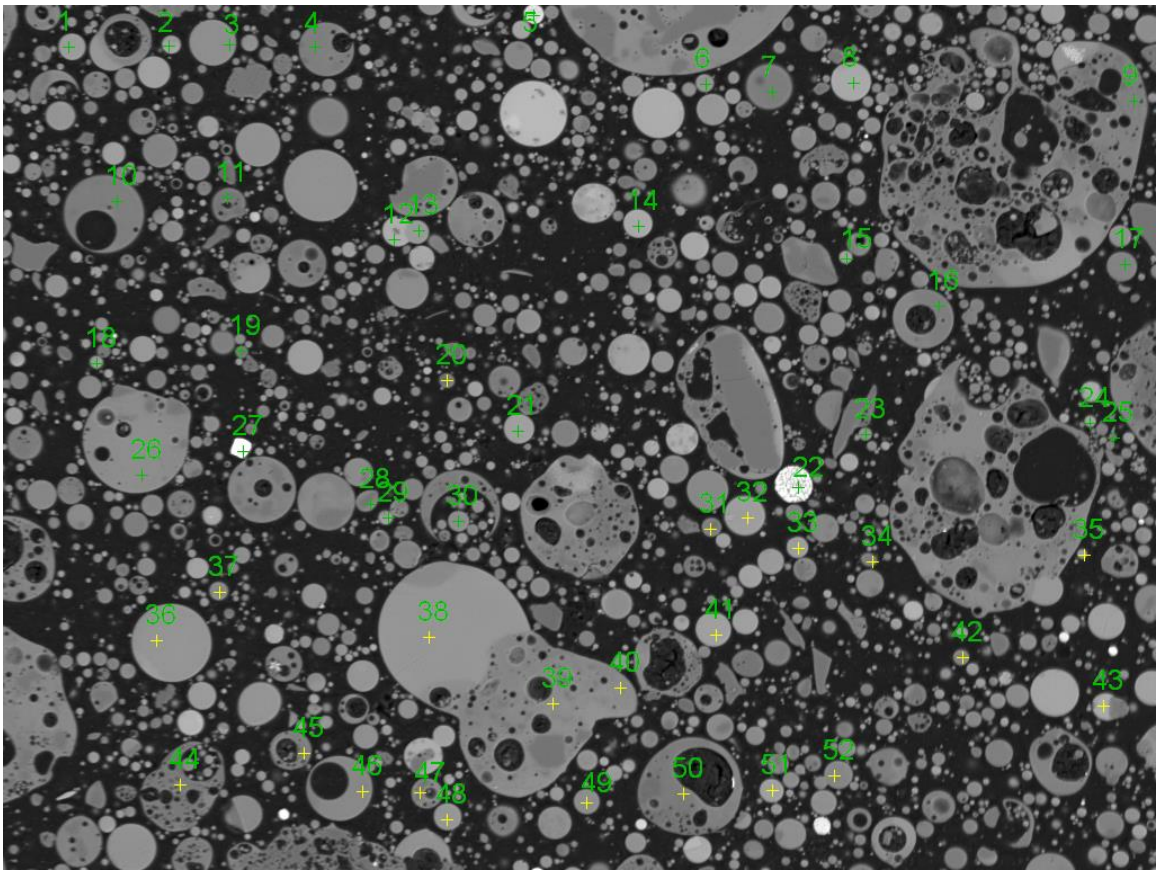

Figure 6.5: Point map for Martin Lake fly ash indicating the locations where the compositional data was collected

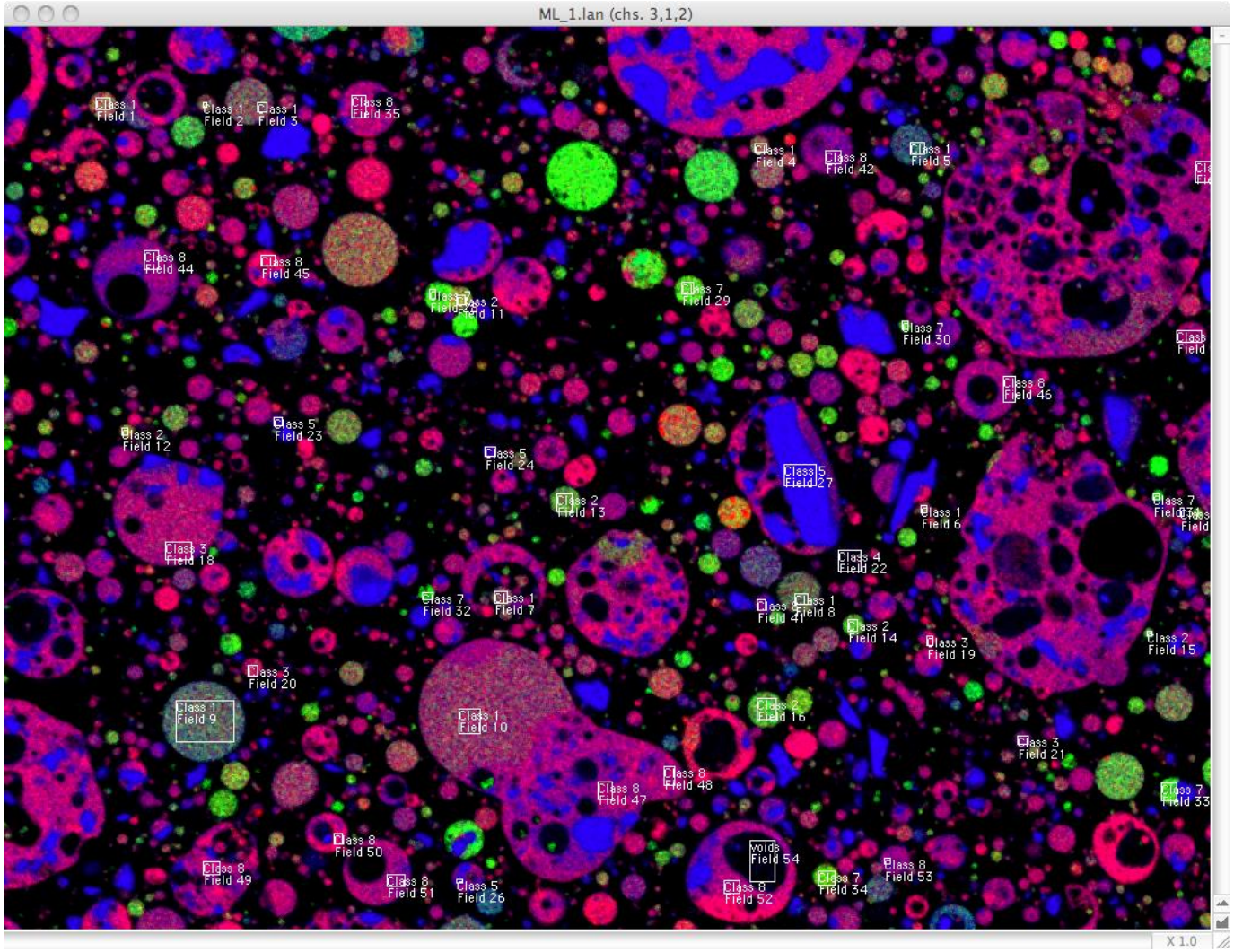

Figure 6.6: Training class selection for Martin Lake fly ash using the 8 classes identified based on compositional data

The phase assignment image was generated for the fly ash using the standard color palette from Multispec, and is given in Figure 6.7. Note that this color scheme differs from the bi-plot color scheme used in Figure 6.3 and Figure 6.4. Class 1, was high in silicon, (25 %, by mass), lower in calcium (16 % by mass) and lower in aluminum (11 %, by mass). This phase is shown in yellow in the phase assignment image. Class 2 was high calcium at approximately 27% (by mass), moderate silicon (16 % by mass), and moderate aluminum (12 % by mass). Class 2 is shown in blue in the phase assignment map. Class 3 is high silicon (30 % by mass), moderate aluminum (15% by mass), and low calcium (7 % by mass) and is shown in orange in the phase assignment image. Class 5 is very high silicon with minor other elements and is designated quartz. The quartz is shown in magenta in the phase assignment image. Classes 4 and 6 were grouped due to their similarly high iron intensities in the x-ray maps, and are shown in green in the phase assignment image. Class 7 is very high calcium (~ 30 % by mass) and low silicon (8 % by mass) and aluminum (9 % by mass). Class 7 is shown in light purple in the phase assignment image. Class 8 is high silicon (35 % by mass), moderate aluminum (15 % by mass), and very low calcium (2 % by mass). It is shown in light blue in the phase assignment image. The amounts of each phase are shown in Figure 6.8. These results will be discussed in the next section in comparison with the original classification method.

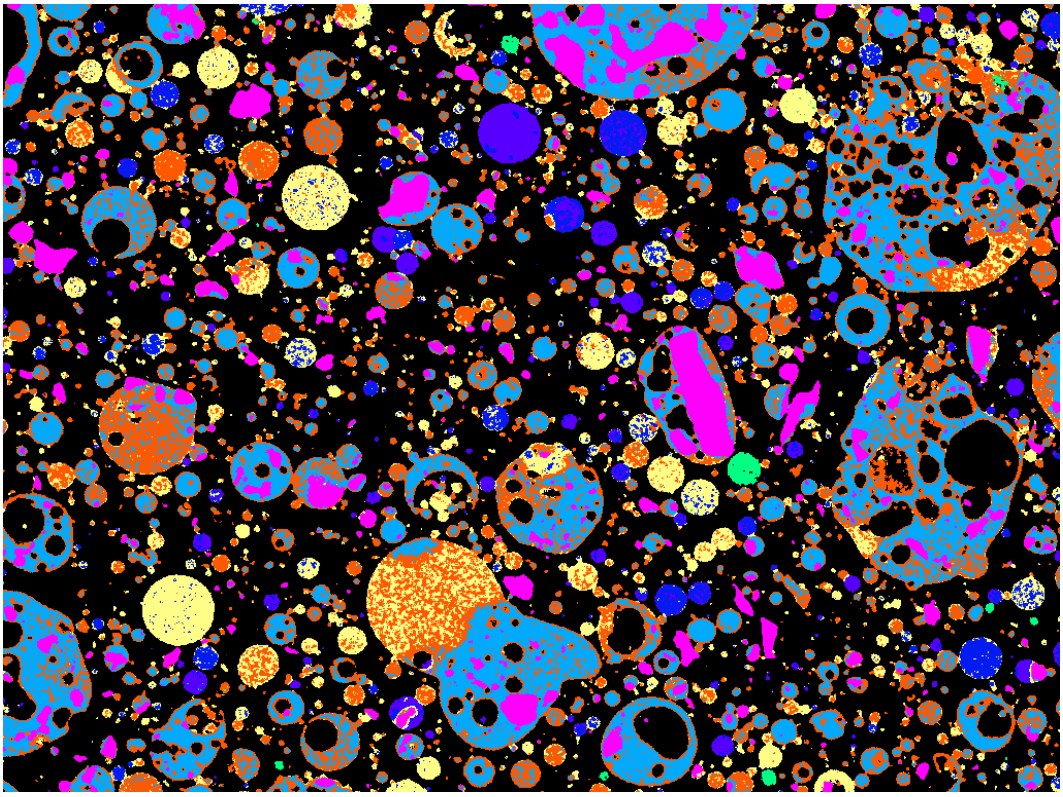

Figure 6.7: Phase assignment image after MSIA classification using training pixels for each class as identified using k-means analysis.

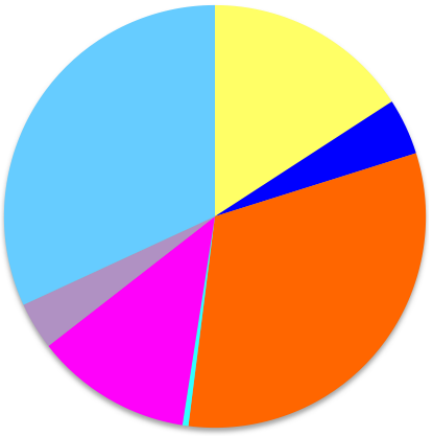

Class	Area %
Class 1	15.85
Class 2	4.31
Class 3	31.85
Class 4	0.46
Class 5	12.02
Class 7	3.63
Class 8	31.88

Figure 6.8: Phase assignment image for Martin Lake fly ash generated using the k-means clustering results to select training fields including phase distribution pie chart and amounts of each phase, by area

6.3 COMPARISON OF RESULTS FOR PIXEL SELECTION METHODS

The results presented in the previous section described the process of using k-means clustering of point compositional data to select training pixels. The results of the MSIA classification using those training pixels are compared to the results obtained using the method defined in Chapter 3 that was used in the work presented in Chapters 4 and 5 of this dissertation. The phase classification image of the Martin Lake fly ash from Chapter 4 is reprinted here for ease of reference (Figure 6.9). In comparing the images, it should be noted that the color schemes are different. However, "favorable" comparison means that the pixels were grouped into similar classes in both images. For example, the quartz is magenta in Figure 6.7 and green in Figure 6.9. Comparison of the locations of magenta pixels in Figure 6.7 and green pixels in Figure 6.9 show that they were similarly grouped in both data sets. In this class, the pixel training sets resulted in the same pixel classification regardless of the way the pixel training sets were selected. This is a favorable comparison of the two methods.

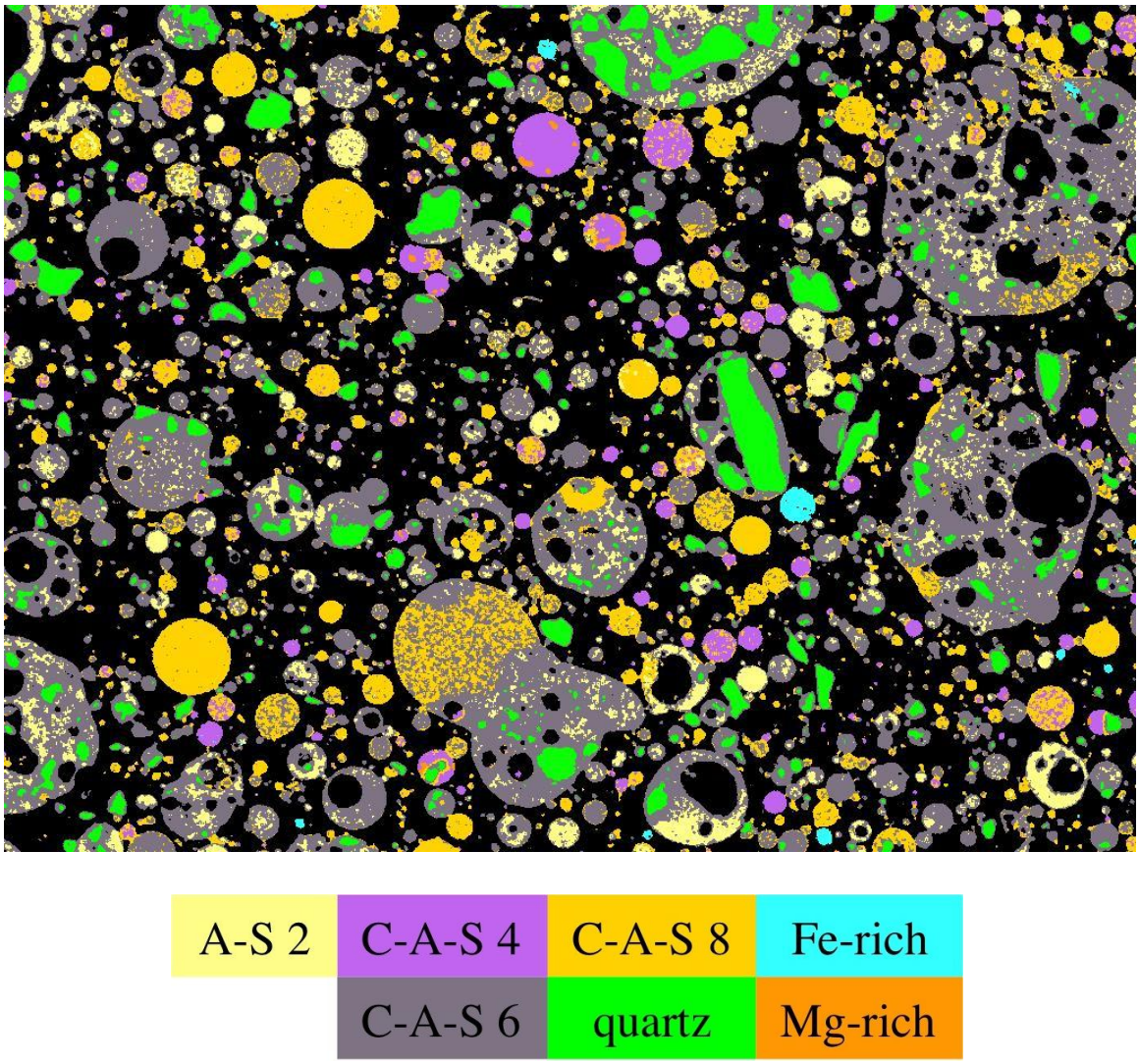

Figure 6.9: Martin Lake fly ash phase assignment image (reprinted from Chapter 4)

The appearances of the pixel assignments in the two phase assignment images compare favorably. While it is clear that some particles are relatively non-uniform, resulting in a speckled appearance in Figure 6.7, the same result was found in the previous classification given in Chapter 4, shown in Figure 6.9. The gray C-A-S 6 phase identified in Figure 6.9 was the main difference in phase classifications between the two methods, having been split into two different phases in the k-means training pixel

selection method, which were light blue and orange in color in Figure 6.8. The compositions for classes given in Table 6.1 can be assigned to phases using the same criteria presented in Chapter 4. Using the definitions established earlier, Class 1 would be C-A-S 8, Class 2 would be C-A-S 4 or 5 (its composition doesn't match either perfectly), Class 3 would be C-A-S 6, classes 4 and 6 were iron-rich, class 5 would be quartz, class 7 would be Mg-rich, and class 8 would be A-S 2. In the results using the methods as described in Chapter 3, the Martin Lake fly ash contained A-S 2, C-A-S 8, C-A-S 6, C-A-S 5, Mg-rich, and Fe-rich. The C-A-S 6 phase was split into two phases shown in light blue and orange, which can now be defined as A-S 2 and C-A-S 6.

The amounts of each phase can also be compared. Table 6.2 lists the phases and amounts of each phase for the original method of training pixel selection and the new k-means analysis method. They are listed in the same order as the classes were defined by k-means (i.e. Class 1, Class 2, Class 3, etc.). C-A-S 8 was present in similar amount using both methods. C-A-S 5 originally identified in the fly ash was classified in the same amount as the phase in the new method that was classified as C-A-S 4 or 5. C-A-S 6 was re-apportioned in the new method, and it was present in the decreased amount of 32 %, by area. The other phase that replaced a portion of C-A-S 6 was A-S 2, which was identified in about 20% more area than in the original method. Summing 32 % (C-A-S 6, new) and 20 % (increased amount of A-S 2), the result is near the 57% that was originally classified as C-A-S 6. The remaining phases were very similar in the new classes compared to the old classes. Therefore, although k-means is a mathematical method for selecting training classes, the results showed that the visual examination method used in this work resulted in the same phases in nearly the same amount.

Table 6.2: Comparison of phase amounts when phases are classified using visual examination to select training pixels versus using k-means clustering of compositions to select training pixels

Phase Name	Area % original classes	Area % new classes
C-A-S 8	18.00	15.85
C-A-S 4 or 5	5.13	4.31
C-A-S 6	57.53	31.85
iron-rich	0.43	0.46
quartz	9.26	12.02
Mg-rich	0.17	3.63
A-S 2	9.48	31.88

6.4 SUMMARY

The k-means method was applied to fly ash compositional data to aid in training pixel selection for multispectral image analysis. The results showed that the k-means method did not vary the results significantly. The original method identified 7 phases in the material, while the k-means method identified 8 phases. However, two of the phases in k-means data were similar enough in composition (high iron) that they were grouped in MSIA, leaving 7 phases for MSIA analysis. The phases identified remained the same from method to method, but the amounts of them differed in the case of two classes. C-A-S 6 was found to make up a large portion of the fly ash in the original classification, but some of the pixels were assigned to the A-S 2 phase using the new method.

The clustering results showed that the original method was quite accurate, but, the use of k-means algorithms to aid in training class selection is a promising method that can help take some subjectivity out of the MSIA process.

Chapter 7: Summary, conclusions, and suggested future research

7.1 SUMMARY OF EXPERIMENTAL PROGRAM

One of the challenges of implementing fly ash based geopolymers as an engineering material is the difficulty in identifying the reactive portion of the fly ash. The reactivity of a fly ash is critical to raw materials selection and for proper proportioning of geopolymer cements. The goal of this work was to survey ten fly ashes for their composition and to find similarities in composition across the different fly ashes in an effort to attribute composition to reactivity. The similarities in composition were linked to reactivity in the fly ashes by comparing the phases identified in the ashes to compressive strength results for geopolymers made from the fly ashes. A dissolution technique allowed the residues of the fly ashes to be examined for compositional changes from the original composition of the fly ash, giving further insights into which phases were reactive under the highly caustic conditions in geopolymer formation.

First, the ten fly ashes were characterized for crystalline and glassy composition. Rietveld quantitative analysis using an internal standard was used to calculate the crystalline and bulk amorphous content of the fly ashes. The bulk amorphous phase and amorphous ratios of silica and alumina were compared to previous work so that hypotheses could be made regarding which fly ashes were likely to be the most reactive. The fly ashes were characterized for glassy phase composition using scanning electron microscopy and point compositional analysis. X-ray maps of 7 elements were collected and were used in multispectral image analysis to identify the glassy phases and determine the amount of each identified phase in the fly ash. Point compositional analysis was used to determine the average compositions of the phases.

The reactivity of the fly ashes was tested in two ways: the fly ashes were mixed into geopolymers using identical proportioning, mixing, and curing methods, and they were tested for compressive strength at 7 d and 28 d of age. The fly ashes that resulted in the highest strength geopolymer mortars at 28 d were considered reactive, those that were at intermediate strength at 28 d were considered moderately reactive, and those that resulted in little-to-no strength at 28 d were considered poorly reactive. The results were compared to the hypotheses drawn in Chapter 4 about which fly ashes would be reactive in geopolymers, which showed that the use of amorphous amount and glassy SiO_2 and Al_2O_3 ratios generally predicted the fly ashes that would perform well, but not always. Next, a dissolution method was used to test the reactivity of the glassy phases in the fly ash. The fly ash was mixed with 8 M NaOH solution at a 6.4 solution-to-powder ratio (by mass) and placed on a laboratory rotisserie for 7 and 28 d. The fly ash residues were separated from the liquid at each time period, and the solid material was examined using the SEM point compositional analysis and MSIA methods used for the raw fly ash. The results for the compositional analysis of the fly ashes at each time period were compared to the original fly ash composition to determine which phases were the most reactive in the fly ashes.

Finally, a modification to the MSIA method was proposed for future work. This was developed due to a common criticism of the method being too subjective due to the user-selected training pixels for each phase. In the method, the point compositional data was clustered, so that particles of similar composition could be identified in the x-ray maps. The particles in which the points were clustered as similar were used to define training classes for the phase. The method also helps to determine how many distinct phases are present in the fly ash. The rest of the MSIA method remained unchanged, but the method represents an improvement in x-ray map pixel clustering.

7.2 SUMMARY OF RESULTS AND CONCLUSIONS

The results and conclusions presented in previous chapters for this study are given in the following sections. These results were obtained using single data sets from small samples of the particular fly ashes. Reactivity was assessed using a single activator (8 M NaOH solution) and ambient curing conditions (23° C). These are important considerations when interpreting the conclusions.

7.2.1 Conclusions on original fly ash compositional analysis and performance

- The bulk amorphous content was measured to range between 62 % and 88 % for the ten fly ashes. The lowest amount of glassy phase did correspond to one of the two fly ashes that did not perform well in the geopolymer reaction, and 4 of 5 of the fly ashes predicted to do well were determined to perform well in geopolymer compressive strengths. One poorly performing geopolymer was made with a fly ash that had nearly same bulk amorphous content as the geopolymer with the highest strength. The performance of these fly ashes were not properly predicted based on their amorphous amounts alone.
- Fly ashes with SiO_2/ Al_2O_3 ratios closest to 4.0, the value recommended by Davidovits (1982) included Atikokan, Bell River, LEGS, and Martin Lake. These fly ashes, with the exception of LEGS, were all found to make geopolymers with the highest compressive strengths out of the fly ashes tested. The LEGS fly ash was of moderate strength.
- The SiO_2/ Al_2O_3 ratios calculated for the poorly performing fly ashes were exceptionally high (5 or greater), which could have been an indication that very high glassy ratios indicated poorly performing fly ashes, except one reactive fly ash also had a glassy SiO_2/ Al_2O_3 ratio over 5. Therefore, the

ratio does not always indicate reactivity even when calculated using bulk glassy phase amounts.

- Three aluminosilicate (A-S) phases were identified with MSIA, one in only a single fly ash (A-S 4), one in only 2 fly ashes (A-S 1), and one in 6 fly ashes (A-S 2). The A-S 1 phase (S/A = 2.0-2.9) was only identified in fly ashes that were found to be poorly reactive, while the A-S 2 phase (S/A = 1.3-2.0) was identified in fly ashes that were reactive (Centralia, Coleto Creek, and Martin Lake) and the fly ashes that were poorly reactive (Fontana and Belews Creek).
- 8 compositionally different calcium-modified aluminosilicate (C-A-S) phases were identified in the fly ashes.
- The C-A-S phases that were identified in the most fly ashes (3 each) were C-A-S 1 (S/A = 0.7-1.2, C/S = 2.7-5.8), C-A-S 5 (S/A = 1.9-2.4, C/S = 1.1-1.3), and C-A-S 6 (S/A = 3.0-7.0, C/S = 0.15 - 0.28) and they were all identified in reactive or moderately reactive fly ashes.
- The particle sizes for the three C-A-S phases that were predicted to be reactive were similar in all of the fly ashes in which they were identified: medium-to-small in size (relative to the particles in the image area) and circular in shape.
- The N-A-S phase was identified in four fly ashes. Of these, three were reactive fly ashes and one was moderately reactive. In only one case was the phase identified solely in large particles (Centralia), while in the others it was identified in a variety of shapes and sizes.
- The d_{50} particle size value showed a trend for reactivity (finest for the most reactive, medium for the moderately reactive, and coarse for the poorly reactive), but the Big Brown Raw fly ash showed that this was not an absolute trend due to its high reactivity and large d_{50} particle size.

7.2.2 Conclusions on glassy phase reactivity

- The glassy phase dissolution results showed that a decrease in C-A-S phases coupled with an increase in A-S phases in the residue after exposure to NaOH indicated reactivity. This trend occurred for the Big Brown Raw, Coleto Creek, LEGS, and Martin Lake fly ashes. Of these, all but the LEGS fly ash were considered reactive based on the compressive strengths of mortars.
- The dissolution experiment showed that in fly ashes that were mostly comprised of A-S phases (Belews Creek and Fontana), changes in phase composition occurred over time. This means that the A-S phases were leaching, but the low compressive strengths and small amounts of reaction product identified in these fly ashes indicated that the leaching process was very slow for both A-S 1 (S/A = 2.0-2.9) and A-S 2 (S/A = 1.3-2.0).
- A-S 3 was identified in fly ashes only after leaching, and its S/A (0.7) implied that it was compositionally similar to mullite. This may have indicated that the phase surrounding mullite was leached, leaving mullite behind, which has been found experimentally by others (Hemmings and Berry 1987).
- One phase, C-A-S 1 (S/A = 0.7-1.2, C/S = 2.7-5.8), was deemed reactive based on its identification in three reactive fly ashes (Big Brown, Bell River, and Atikokan) at early age and disappearance by 28 d.
- The C-A-S 5 phase (S/A = 1.9-2.4, C/S = 1.1-1.3) was considered soluble due to its identification only in original fly ashes (Coleto Creek, LEGS, and Martin Lake); however, it was not present in enough quantity to have been solely responsible for the high compressive strengths of the two reactive fly ashes in which it was identified.

- The C-A-S 6 phase (S/A = 3.0-7.0, C/S = 0.15 - 0.28) had compositional similarities to aluminosilicate phases, particularly the A-S 4 phase (S/A 3.9-8.2). This phase may have been more appropriately characterized as an A-S phase due to its appearance in many fly ashes at late age suggesting its insolubility, and its relatively low calcium content of 7 %, by mass when compared to the other C-A-S phases. Therefore, it is concluded that glasses with calcium content up to 7 % should be considered very slightly modified A-S phases instead of C-A-S phases.
- Based on the disappearance and reappearance of the same phases in different fly ashes and after different lengths of time, it seems possible that the phases, while compositionally similar in their averages of the elements present, S/A ratios, and C/S ratios, might have been somewhat structurally different, altering the reactivity from one fly ash sample to another. One clear example of this occurrence was for the C-A-S 1 phase, which was identified as reactive in three fly ashes due to its identification in the original fly ash and disappearance by the 28 d samples, but which was also identified only at late age in the Boral Class C fly ash. However, the methods used in this study were unable to distinguish such differences in the phases.
- There was no clear difference in amount of reaction product identified in the dissolution samples for the reactive and moderately reactive fly ashes, but the poorly reactive fly ashes had considerably less reaction product identified in their images. This was consistent with their low compressive strengths, since it is expected that similar conditions occurred in the actual geopolymer mortars, resulting in decreased reaction product formation and strength.

7.3 SUGGESTIONS FOR FUTURE WORK

The study focused on a breadth of fly ashes in order to see whether similarities could be identified across fly ashes. Similar phases were identified across fly ashes based on the results. However, this came at the expense of depth in terms of comprehensive compositional analysis. Since the results did not follow a pattern in terms of the phases identified in the fly ash and residue at each time step, it is recommended that future work be completed that focuses on many more replicates and fewer fly ashes considered. Comprehensive characterization of the original fly ashes could also be used to develop model glass systems that could be tested for reactivity as is currently being investigated by Bumrongjaroen (Bumrongjaroen et al. 2011).

Results were reported for a number of different parameters that may affect the reactivity of fly ashes, and hypotheses were made regarding why the fly ashes behaved as they did. However, determining which out of all of the parameters was the most indicative of reactivity was difficult. A statistical analysis using inputs such as the particle sizes, the amount of amorphous phase, the type and amount of glassy phases, etc. may be able to predict the particular properties are the most effective for predicting whether a fly ash is a good candidate for use in geopolymers.

It is known that the composition of a fly ash changes with decreasing particle size (Hemmings and Berry 1987), and that grinding a fly ash for curing at ambient temperature can improve reactivity (Somna et al. 2011). Size fractionation and/or density fractionation of fly ashes for analysis with SEM-MSIA may result in further insights as to the reactive phases in fly ashes and these are suggested as future work. Additionally, grinding fly ashes for use in mortar cubes may increase the compressive strengths obtained, which could improve the apparent reactivity for the poorly reactive fly ashes.

Analyzing the reactivity of fly ash using a dissolution technique is a useful way to determine how well the fly ash reacts in caustic conditions, as a preliminary test for its use in geopolymers or portland cement concretes. One way to improve the results may be to use shorter durations and analyze the fly ash residues at the point just before the reaction product forms, as suggested by (Chen et al. 2011).

The results in this study found that the glasses that were characterized as compositionally similar seemed to have differing reactivity when identified in different fly ashes. This could be due to a number of factors, but one possibility is that surface properties of the fly ashes may have affected their reactivity even if the composition of the particle seemed the same from one fly ash to another. This is one factor in reactivity that should be studied in more detail in the future.

The use of k-means analysis has the potential to greatly improve the understanding of glassy phases. This method should be applied to fly ashes being analyzed in MSIA to aid in the selection of training sets. The compositional analysis of fly ashes has the potential to help select fly ashes for geopolymers that are quite reactive. However, the only way to determine approximately how much of these phases is present in the material is MSIA, so the two methods combined could be very powerful.

Appendix A: XRD Scan Data

XRD scans for one specimen of each of the fly ashes are given in this appendix. The first five fly ashes alphabetically are given in Figure A.1, and the last five fly ashes alphabetically are given in Figure A.2. Figures A.3-A.12 show the original fly ash, the 7 d fly ash residue, and the 28 d fly ash residue XRD patterns.

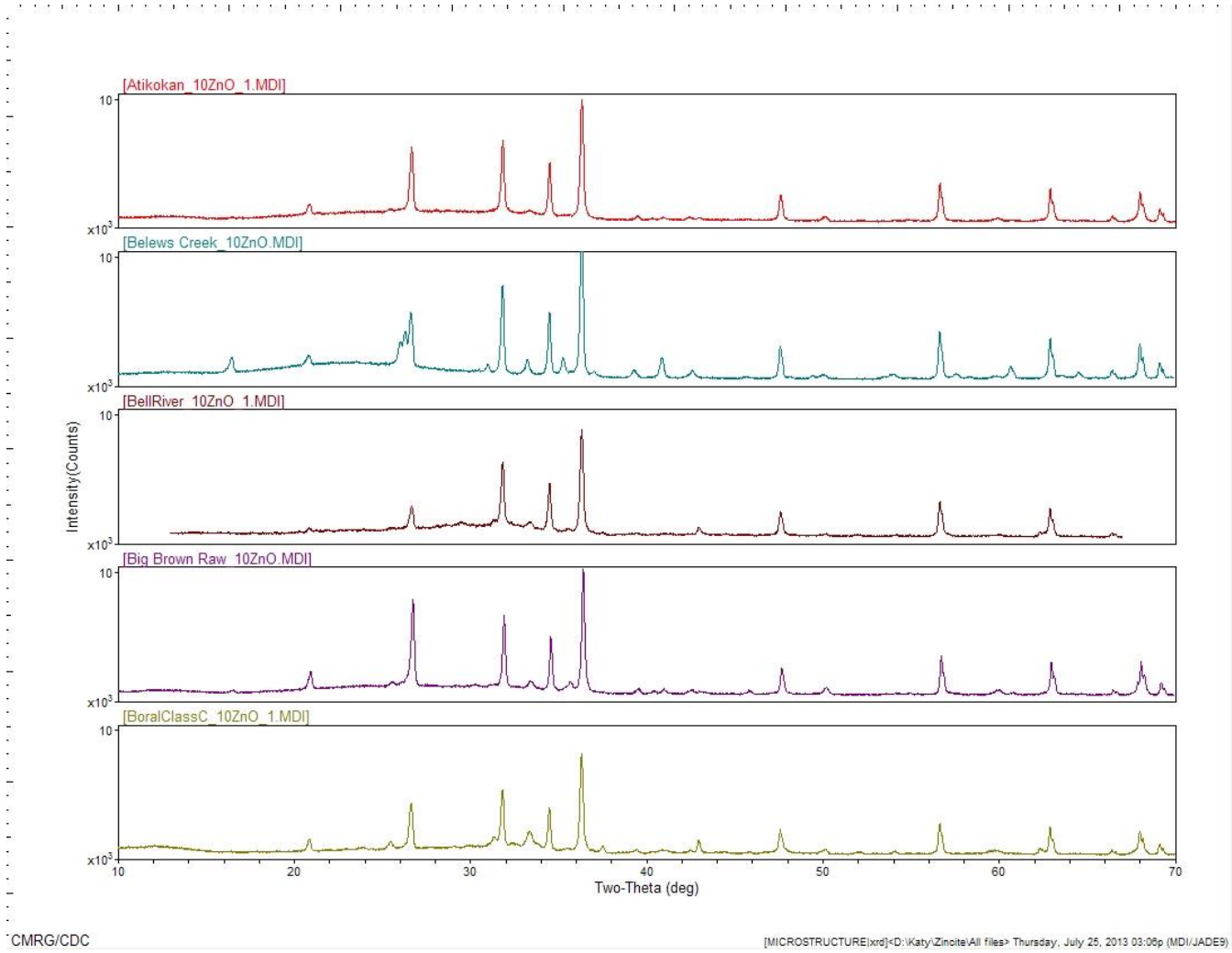

Figure A.1: Atikokan, Belews Creek, Bell River, Big Brown Raw, and Boral Class C fly ash XRD scans

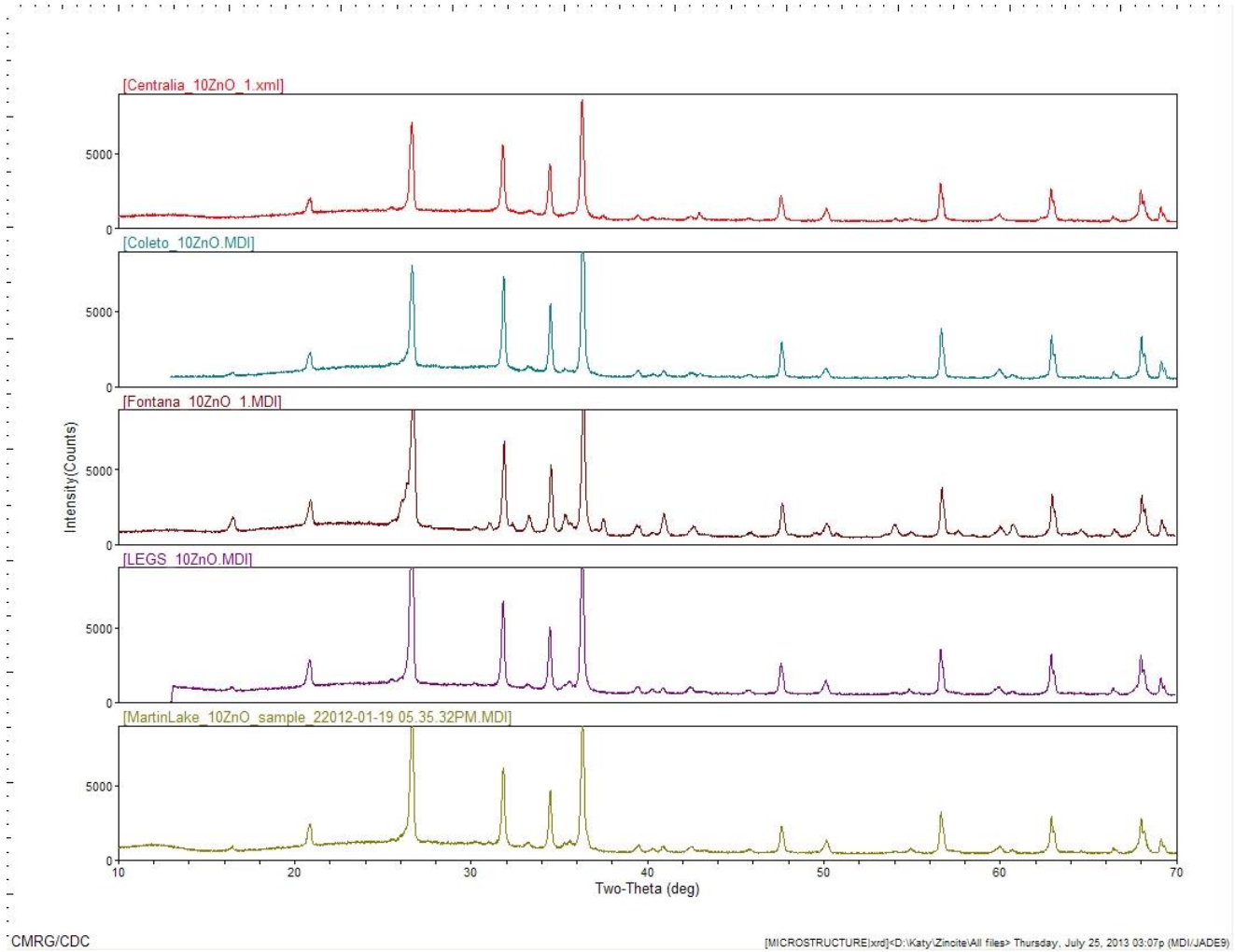

Figure A.2: Centralia, Coleto Creek, Fontana, LEGS, and Martin Lake fly ash XRD scans

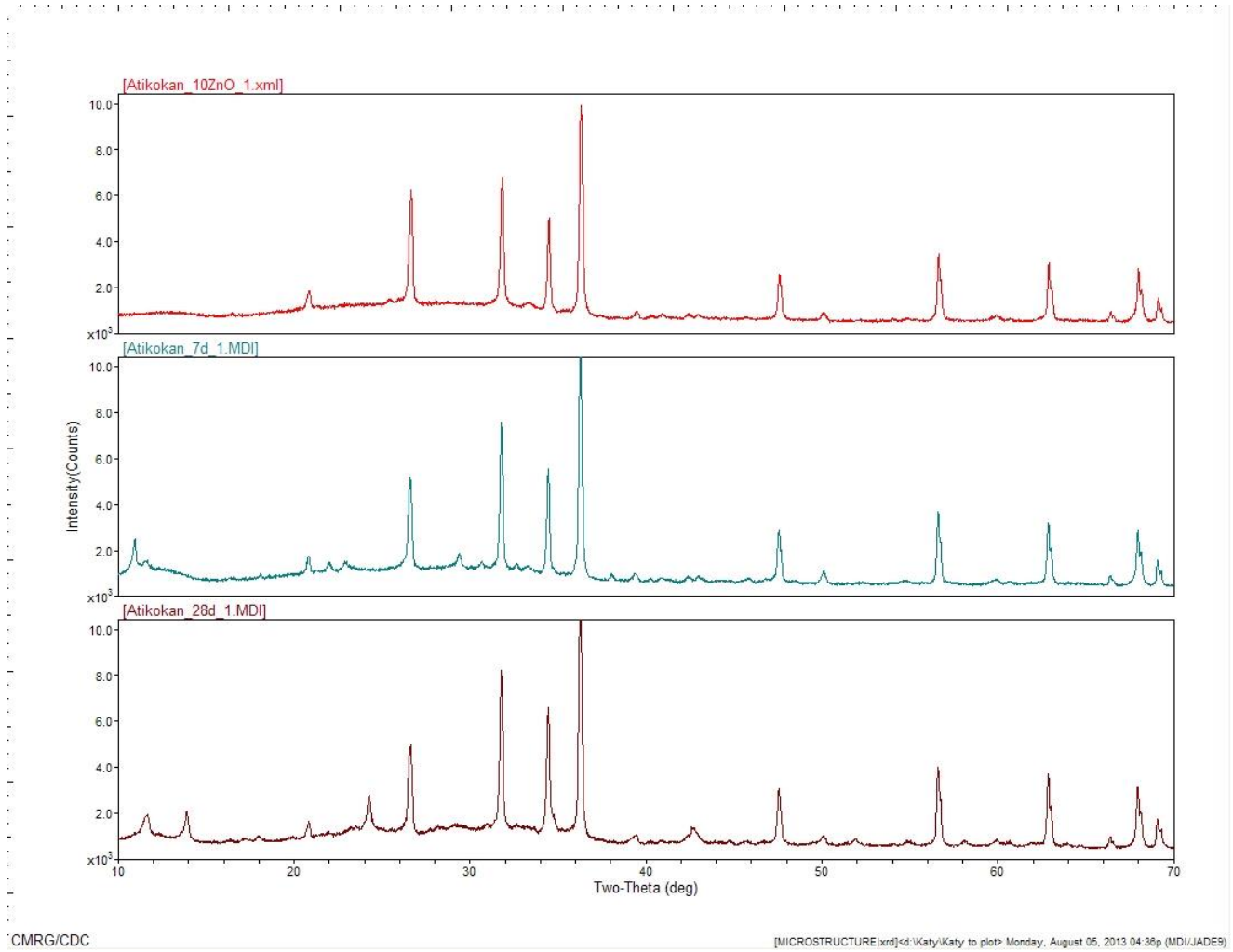

Figure A.3: Atikokan XRD scans of original fly ash (top), 7 d residue (middle), and 28 d residue (bottom)

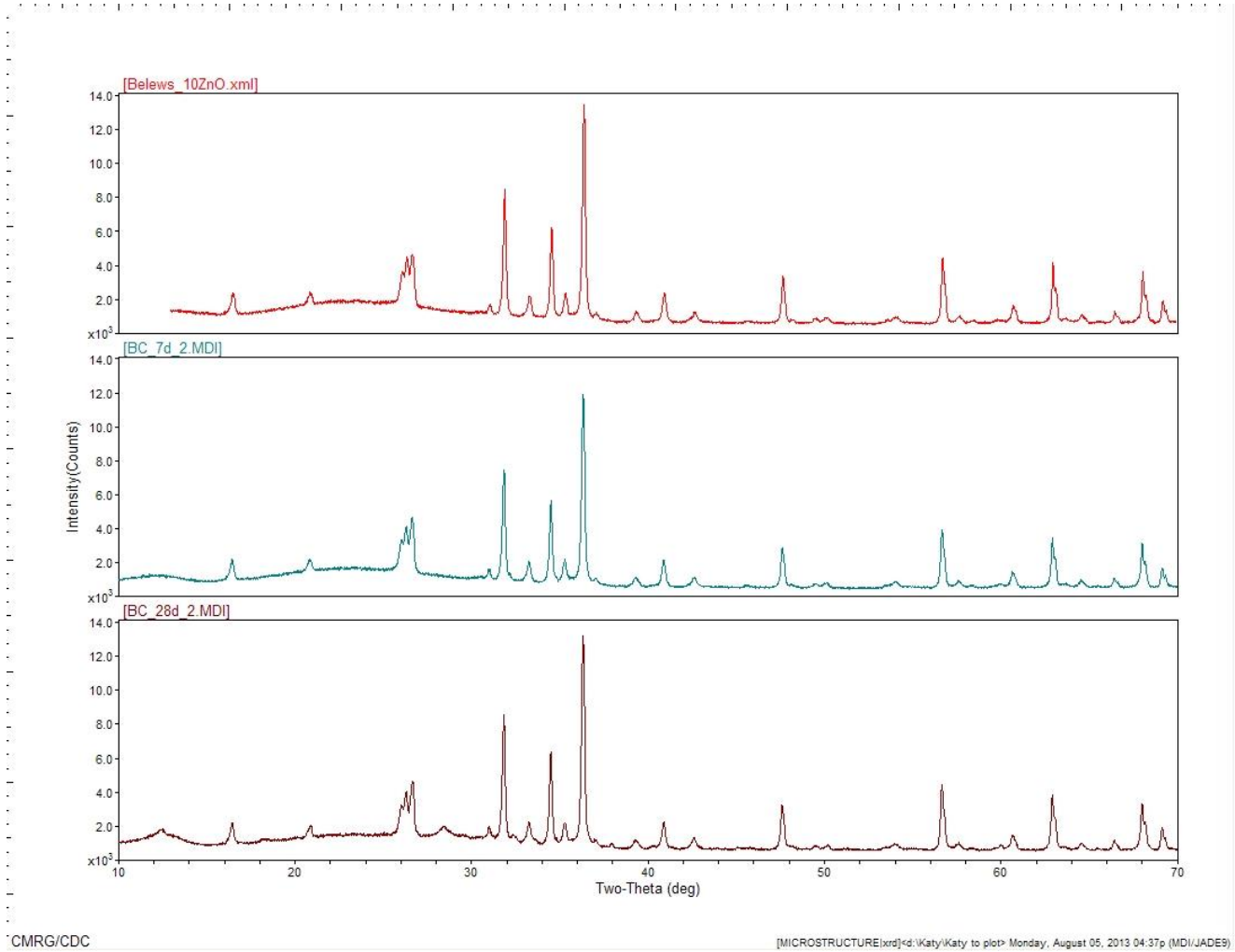

Figure A.4: Belews Creek XRD scans of original fly ash (top), 7 d residue (middle), and 28 d residue (bottom)

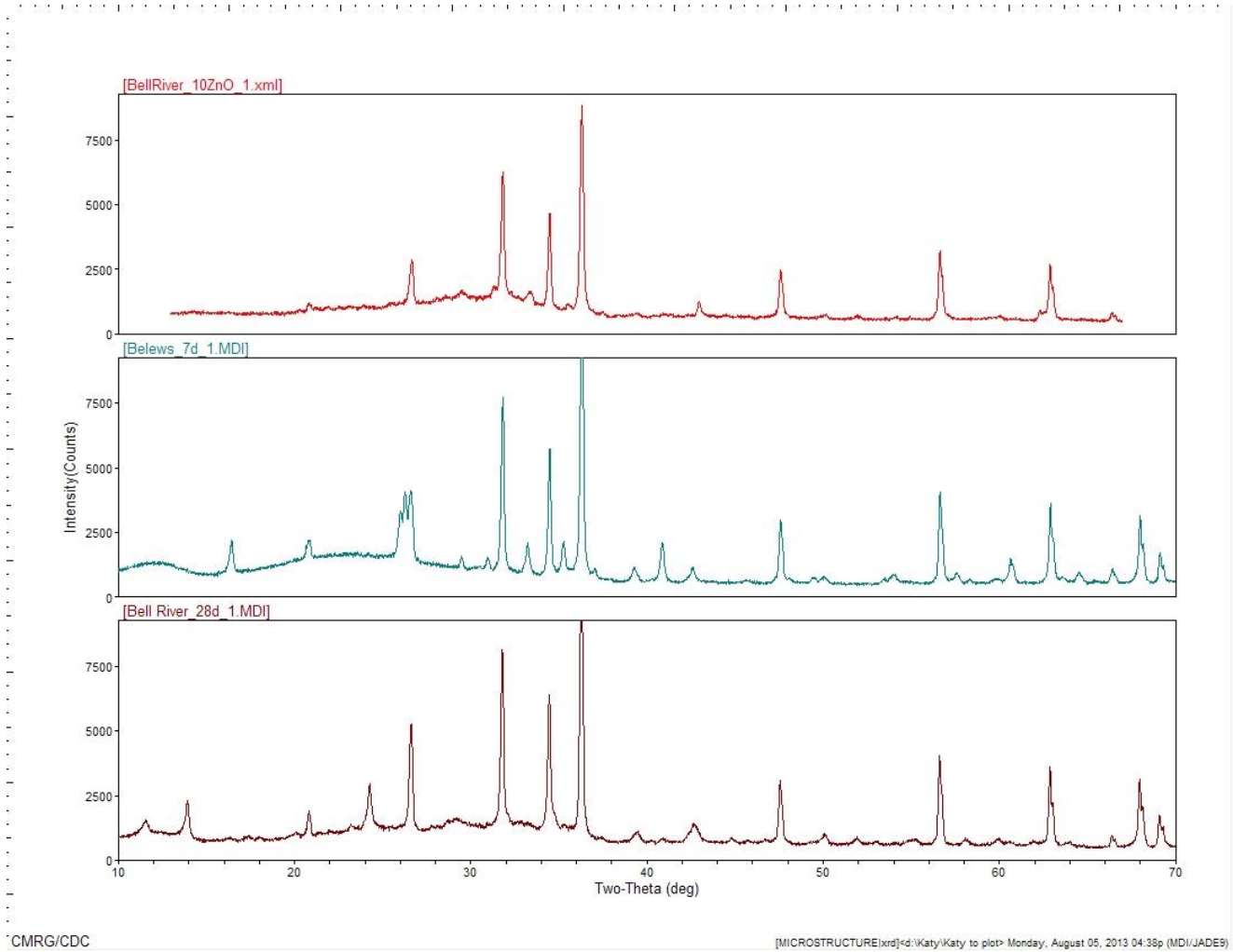

Figure A.5: Bell River XRD scans of original fly ash (top), 7 d residue (middle), and 28 d residue (bottom)

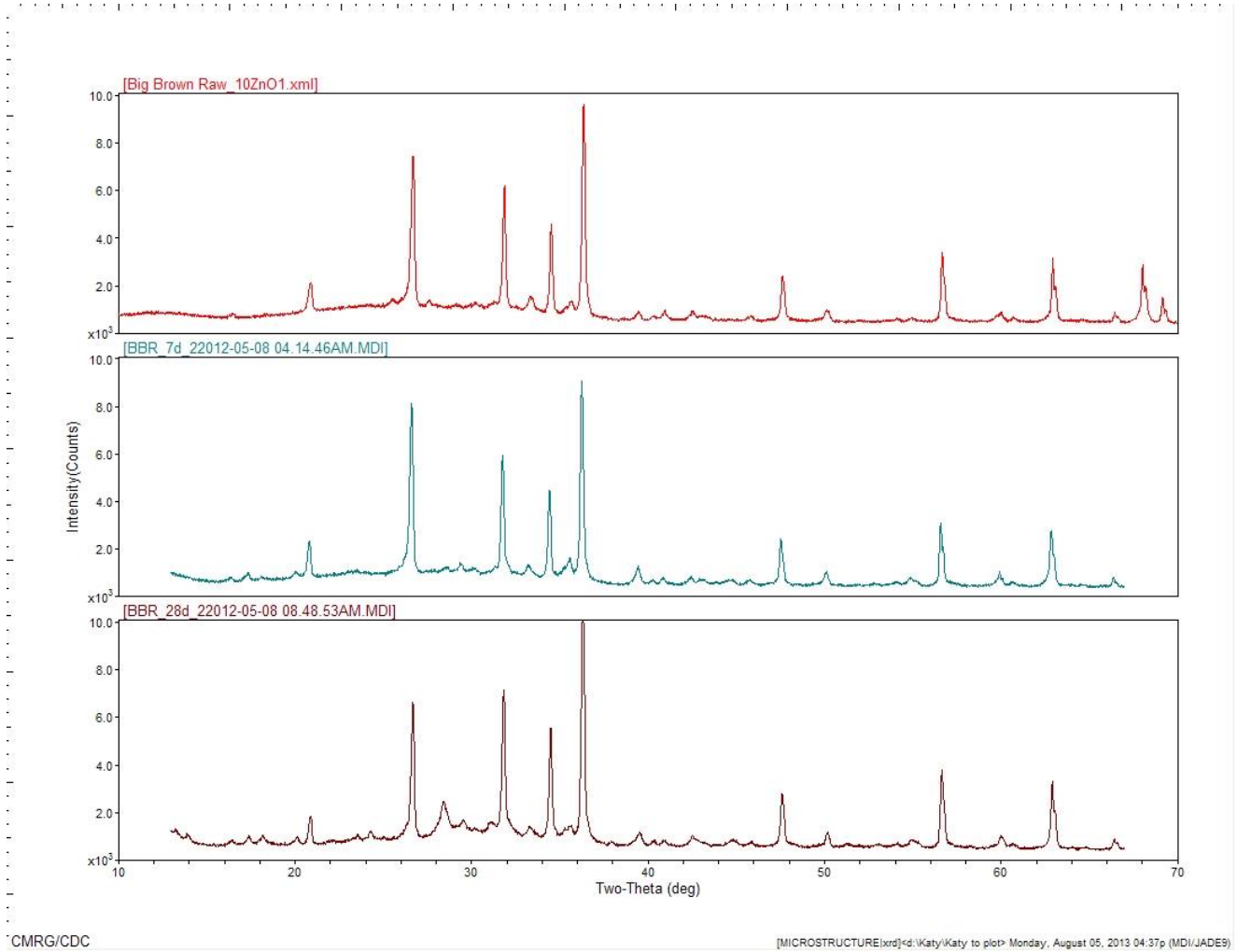

Figure A.6: Big Brown Raw XRD scans of original fly ash (top), 7 d residue (middle), and 28 d residue (bottom)

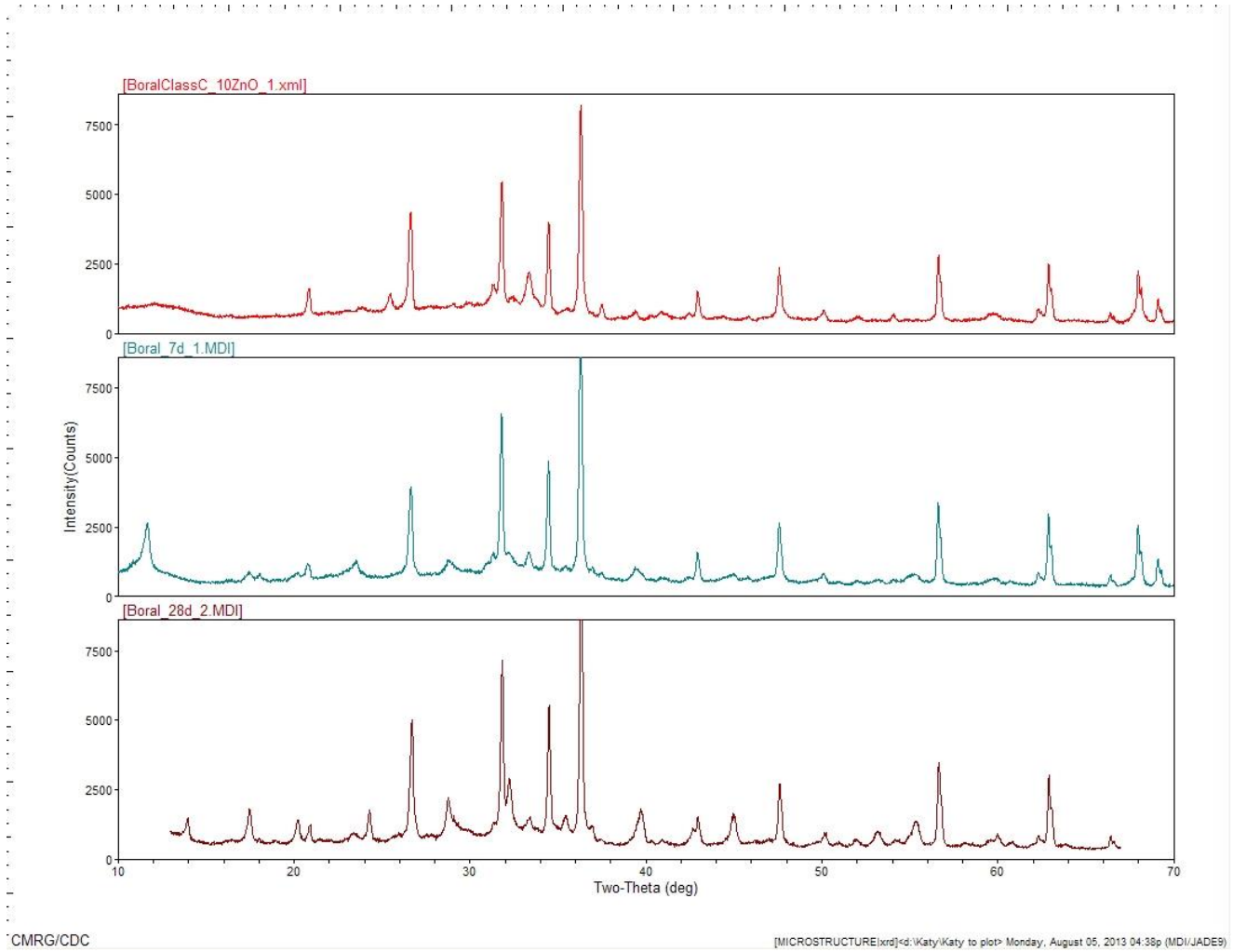

Figure A.7: Boral Class C XRD scans of original fly ash (top), 7 d residue (middle), and 28 d residue (bottom)

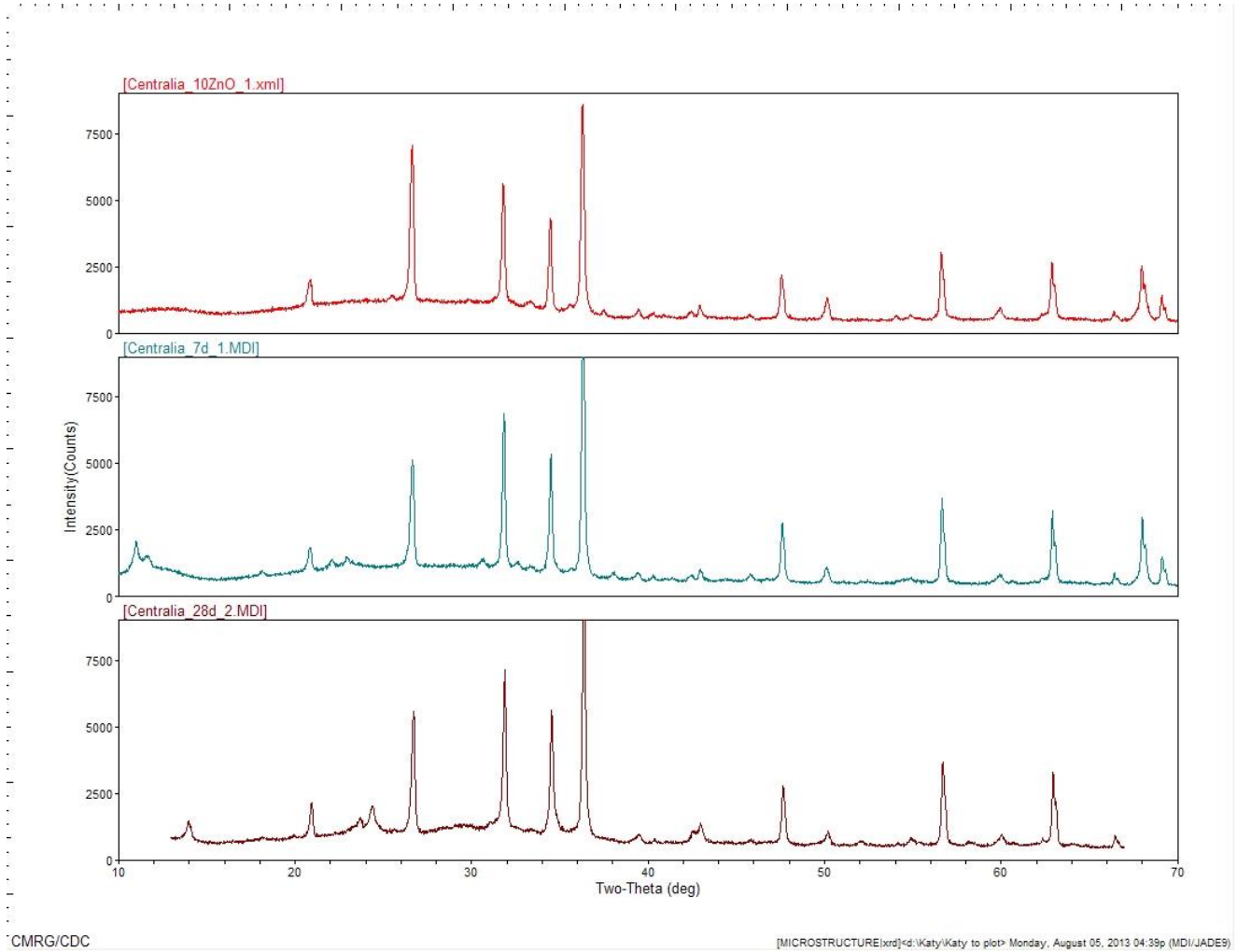

Figure A.8: Centralia XRD scans of original fly ash (top), 7 d residue (middle), and 28 d residue (bottom)

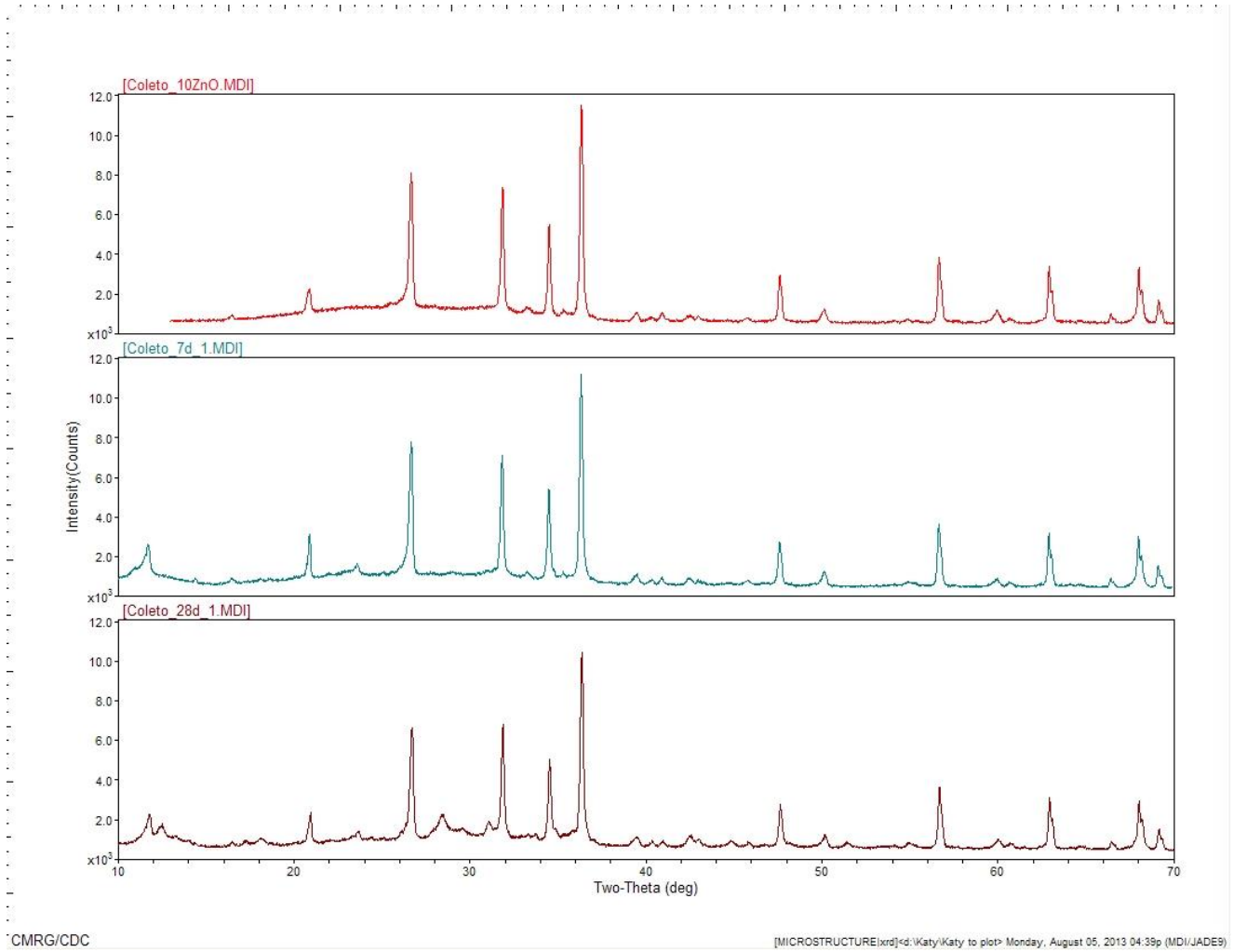

Figure A.9: Coleto Creek XRD scans of original fly ash (top), 7 d residue (middle), and 28 d residue (bottom)

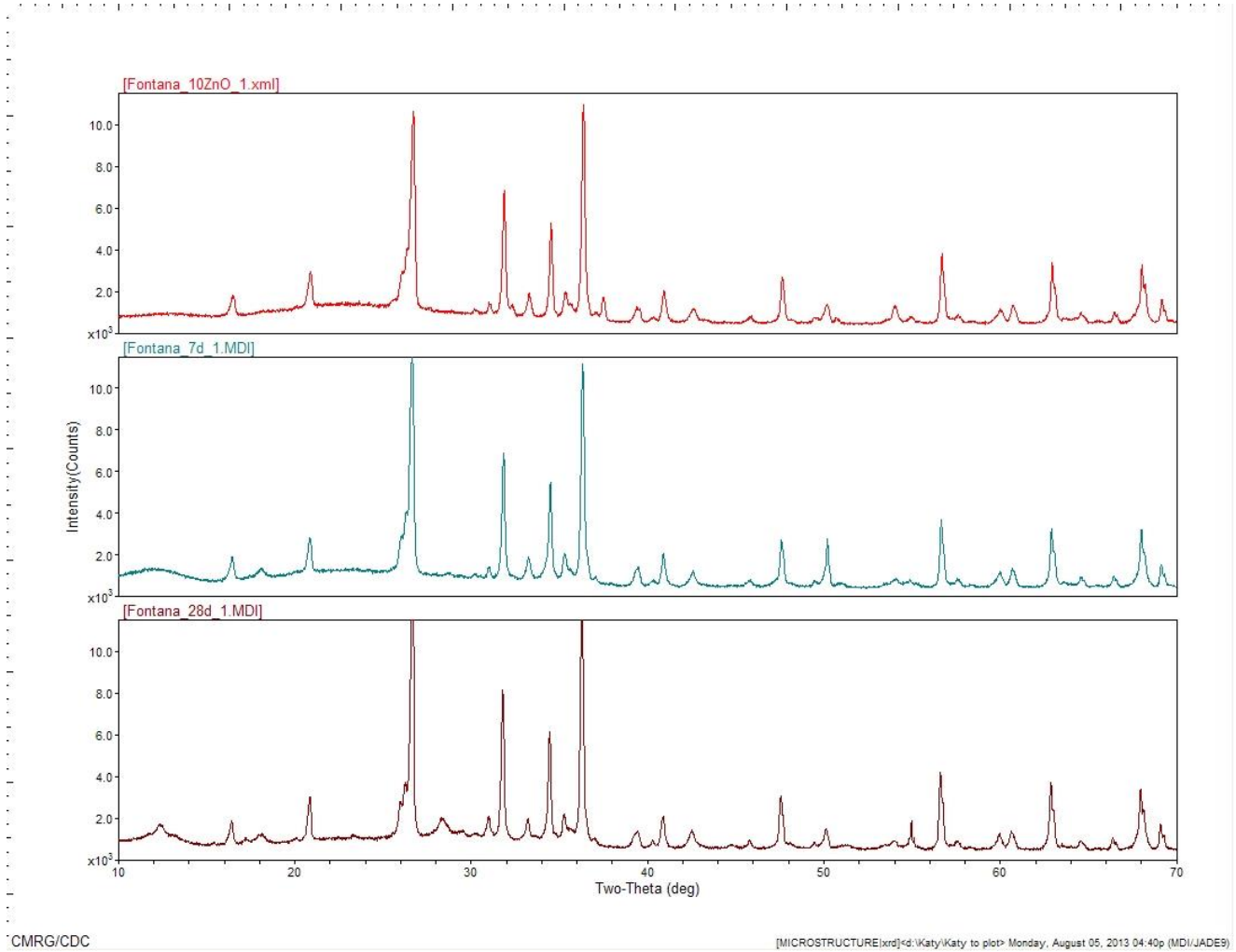

Figure A.10: Fontana XRD scans of original fly ash (top), 7 d residue (middle), and 28 d residue (bottom)

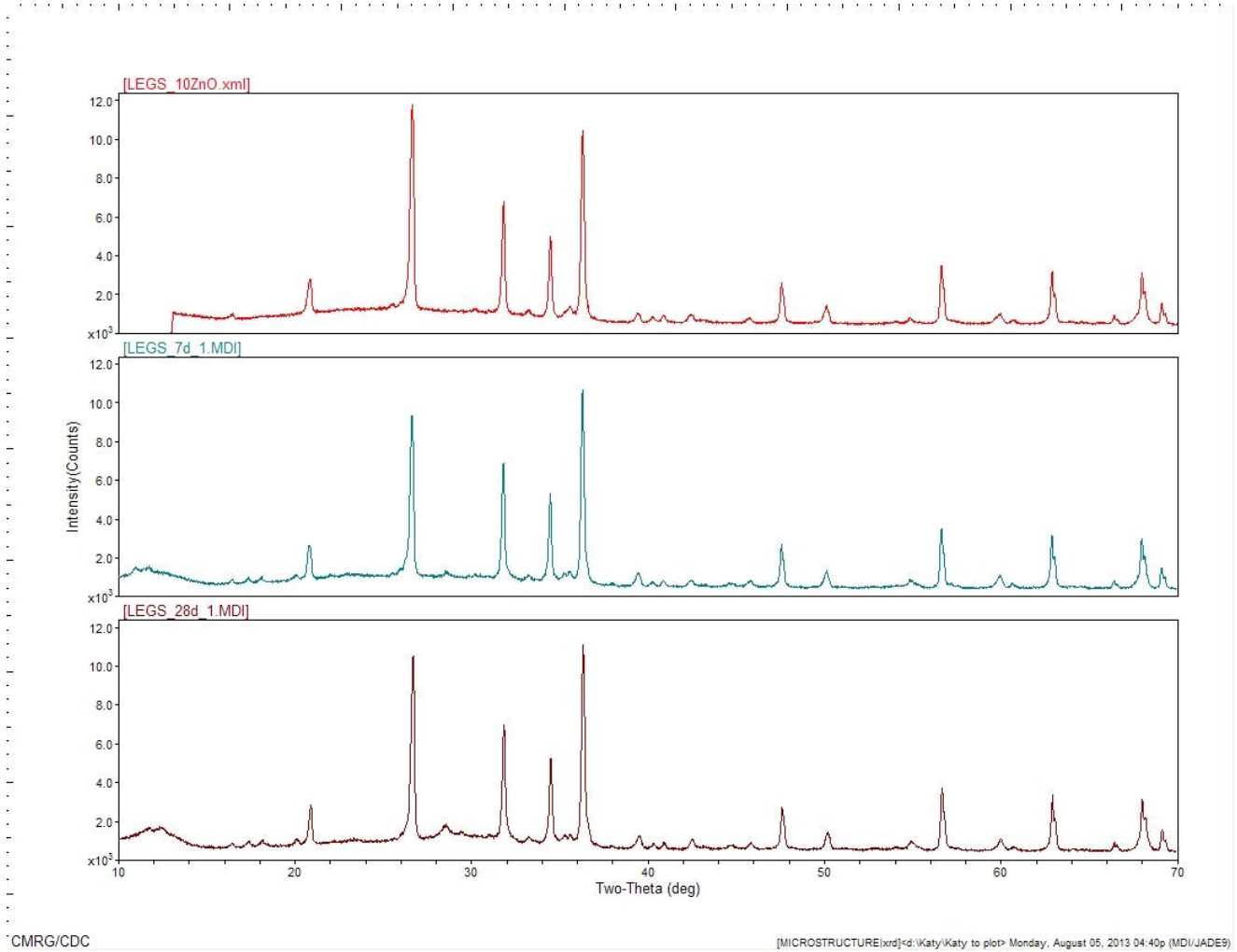

Figure A.11: LEGS XRD scans of original fly ash (top), 7 d residue (middle), and 28 d residue (bottom)

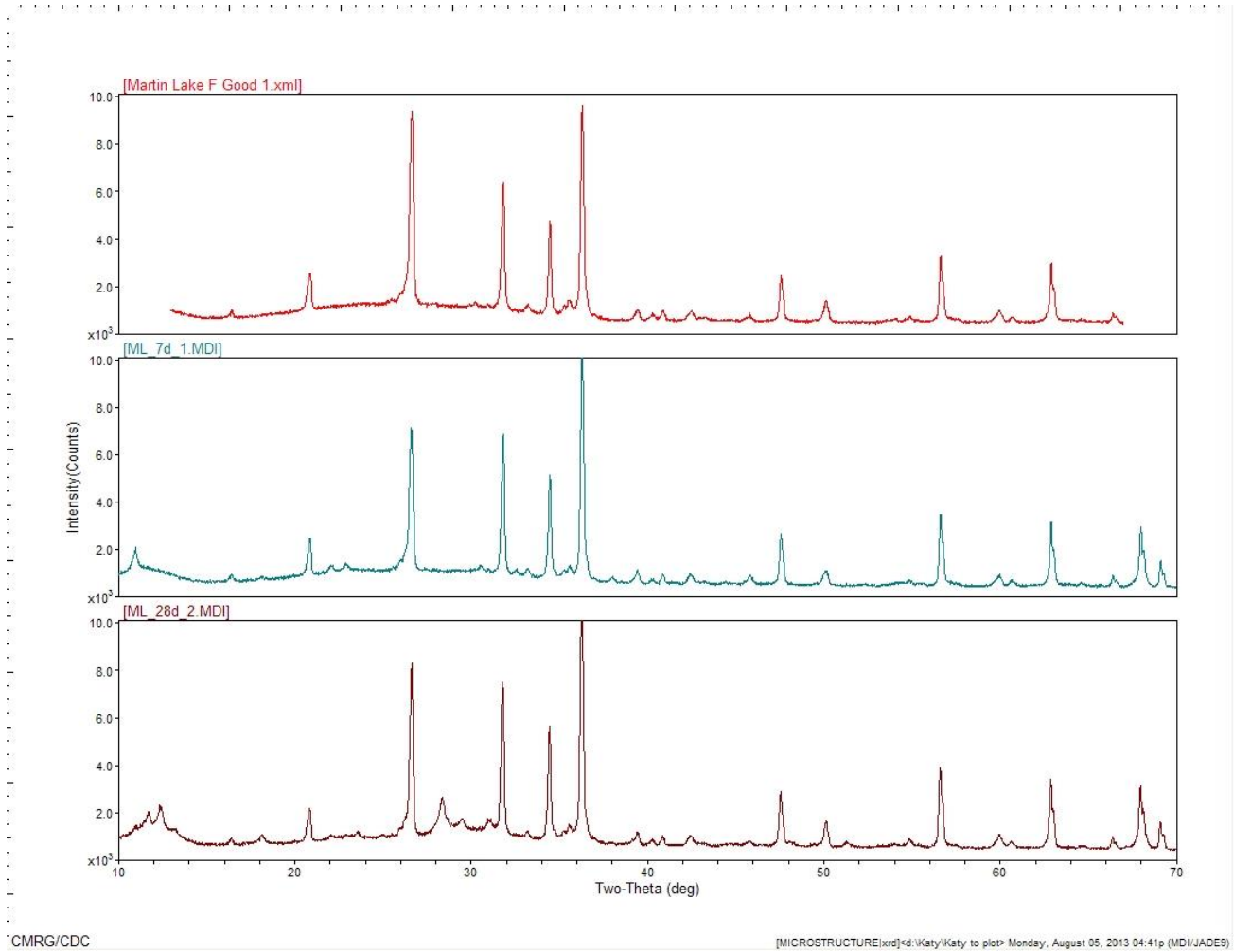

Figure A.12: Martin Lake XRD scans of original fly ash (top), 7 d residue (middle), and 28 d residue (bottom)

Appendix B: SEM Procedures Step-by-Step

The data were presented in the main text of the results (Chapters 4 and 5) using only the phase assignment images to show how the pixels in each image were clustered into phases. A complete example of how these were segmented is given next.

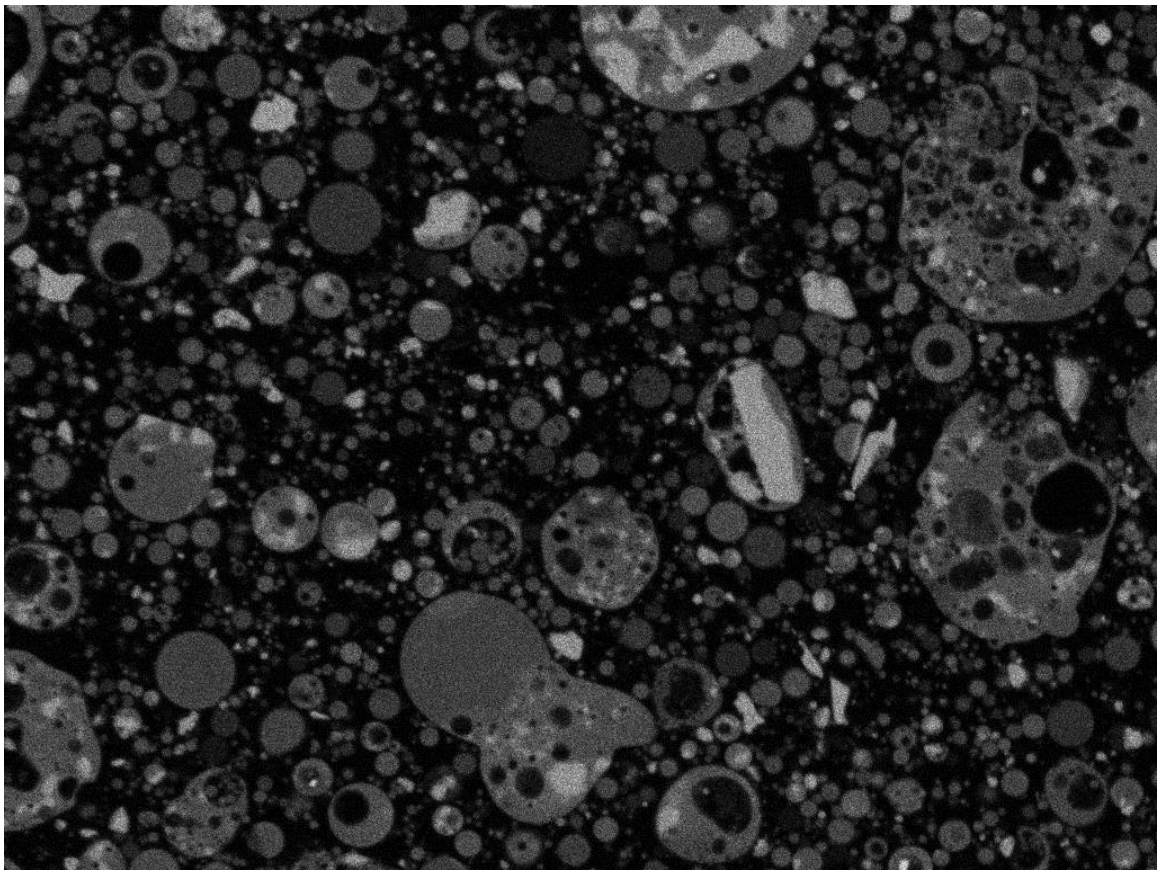

Figure B.1: Silicon map of Martin Lake fly ash, original image, display values were automatically scaled by the computer program

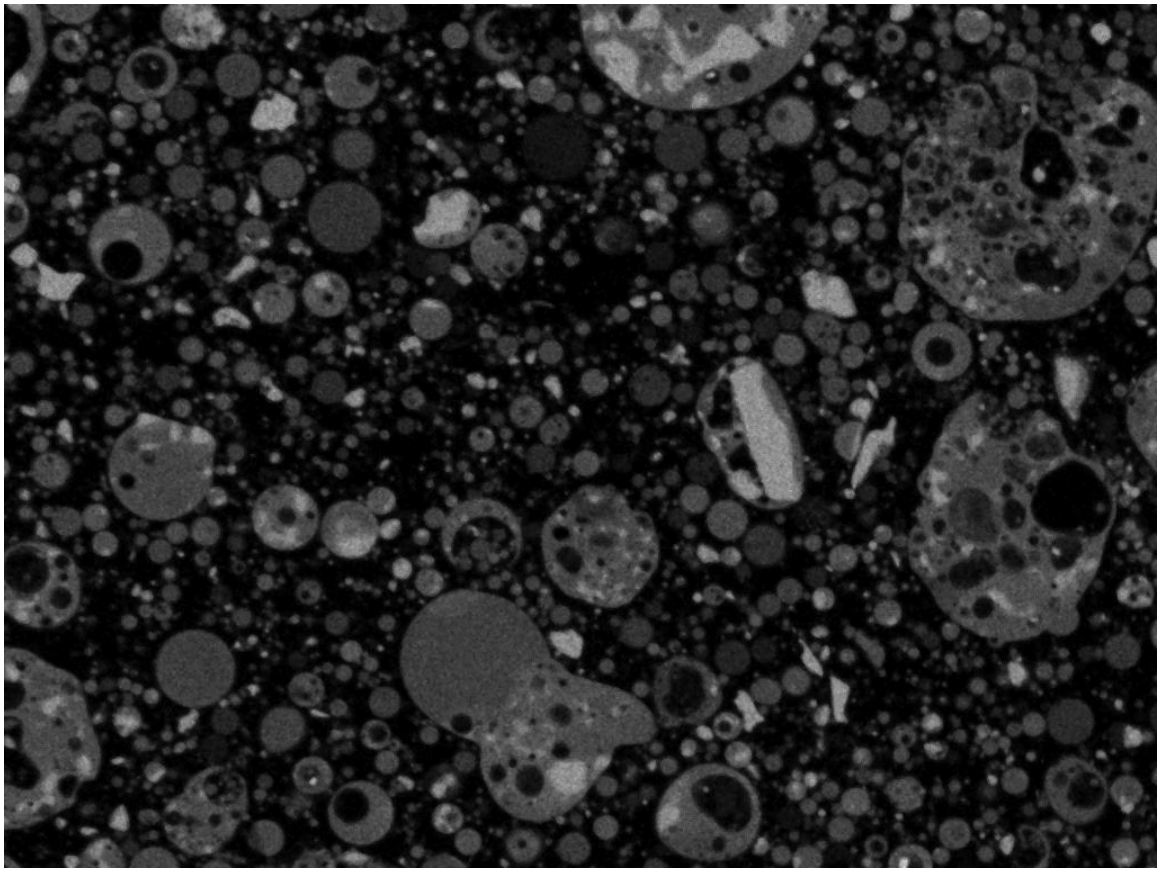

Figure B.2: Silicon map of Martin Lake fly ash after a median radius 1 filter and thresholded to remove noise below the pixel value of 2

The maps for all 7 images were stacked using Multispec. The stack of aluminum (red), calcium (green), and silicon (blue) is shown in Figure B.3. The pixels selected as training classes with aluminum (red), calcium (green), and silicon (blue) displayed are shown in Figure B.4, while the pixels selected as training classes with magnesium (red), sodium (green), and iron (blue) displayed are shown in Figure B.5.

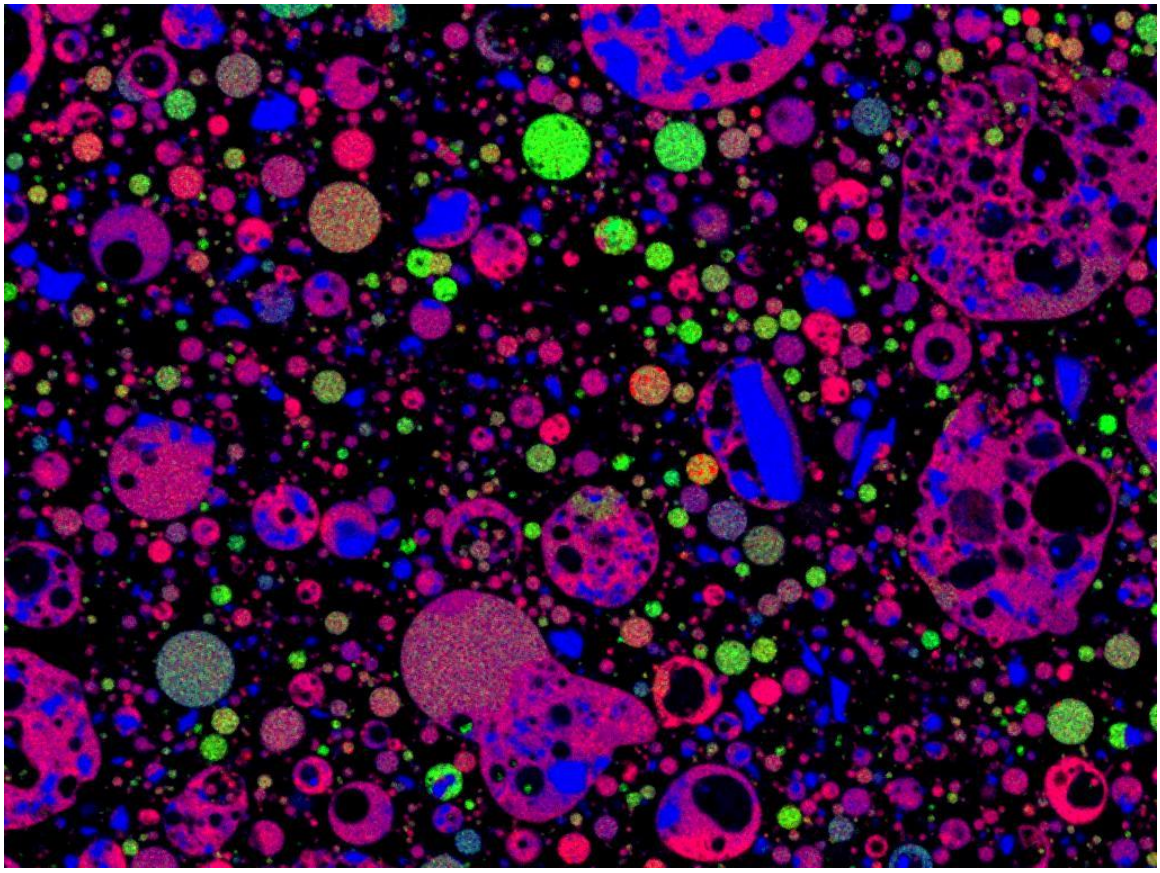

Figure B.3: Stacked RGB image of aluminum (red), calcium (green), silicon (blue) of the Martin Lake fly ash

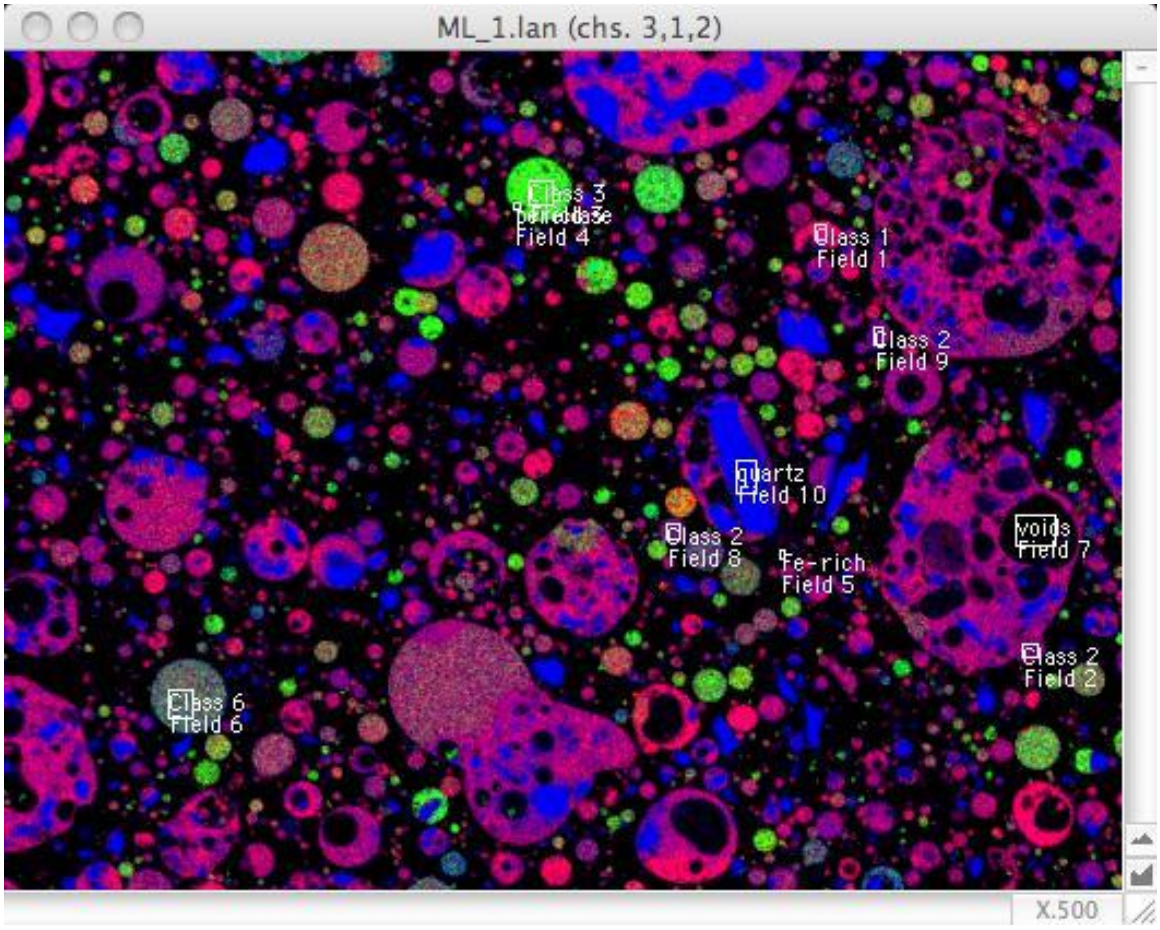

Figure B.4: Training pixel selection with aluminum, calcium, and silicon maps displayed as red, green, and blue

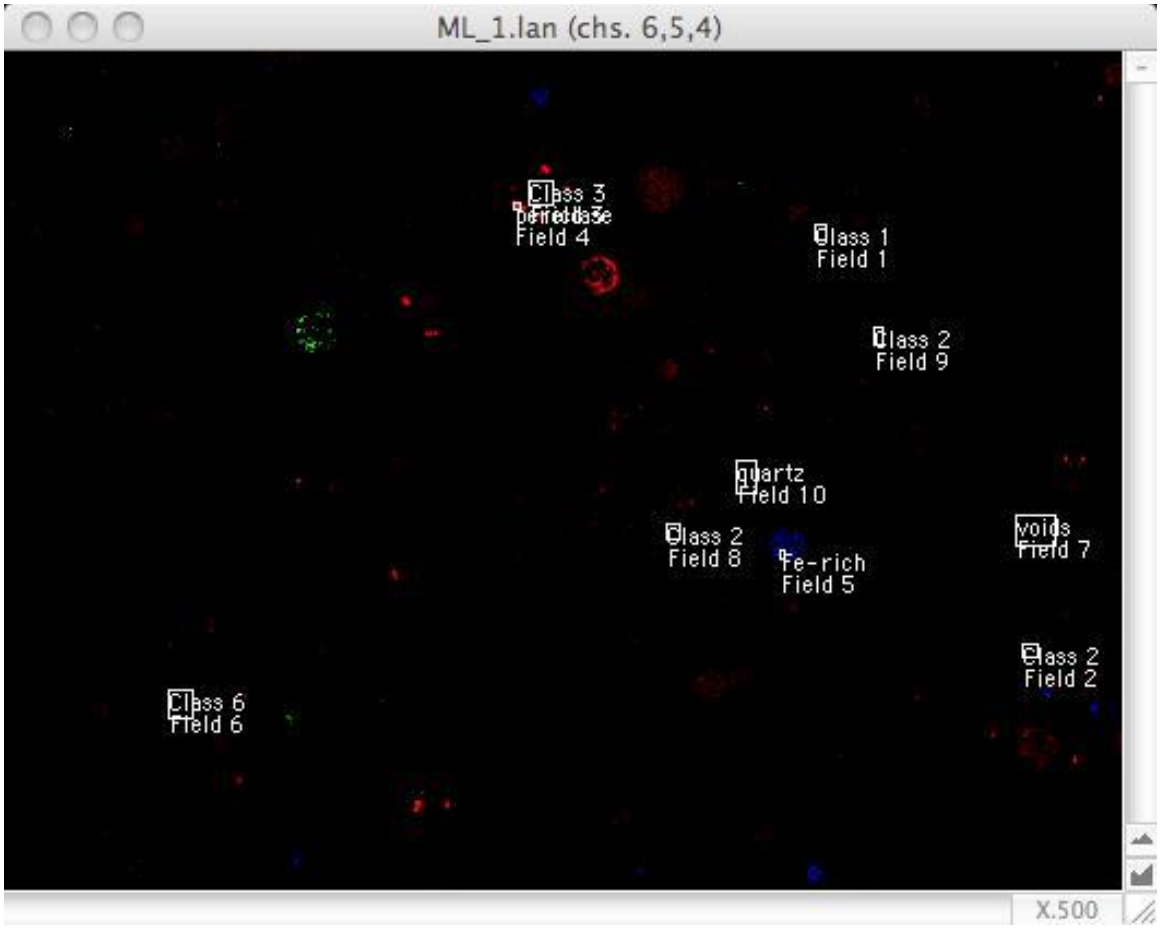

Figure B.5: Training pixel selection with magnesium, sodium, and iron maps displayed as red, green, and blue

The phase assignment image was generated using the Fisher linear likelihood method in Multispec. Each of the selected specifications from the "set classification specification" window are given in parentheses after being described in the following sentences. All channels included in a stack were used for the classification process (Channels: all available), and all of the classes identified were used in the classification (Classify: Class areas: all, training (resubstitution); and Classes: all). The classes were weighted equally (Class weights: equal). The images were written to a Disk file (check box selected). I changed the color scheme after the phase assignment image was

generated as a .gis file. I used the colors designated for each phase for each instance of the phase across all of my data sets (i.e. all ten original fly ashes, the 7 d residues, and the 28 d residues).

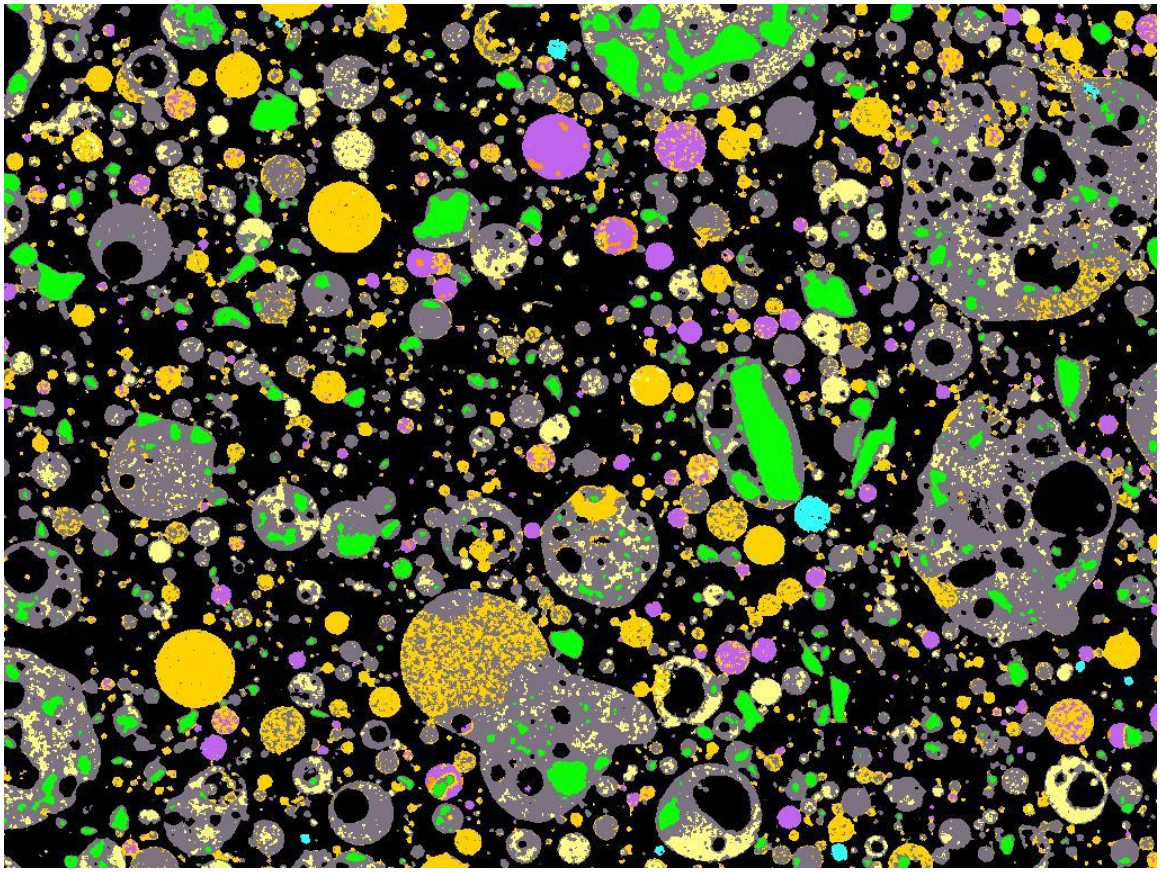

Figure B.6: Phase assignment image for Martin Lake fly ash

The process was used for all SEM images presented in this work. The median filter radius and the threshold value was reported in each section for the specific fly ash.

References

ASTM Standard C109, 2007, " Standard Specification for Coal Fly Ash and Raw or Calcined Natural Pozzolan for Use in Concrete," ASTM International, West Conshohocken, PA, 2005, 10.1520/C0109_C0109M-07, www.astm.org.

ASTM Standard C618, 2012a, " Standard Specification for Coal Fly Ash and Raw or Calcined Natural Pozzolan for Use in Concrete," ASTM International, West Conshohocken, PA, 2005, 10.1520/C0618-12A, www.astm.org.

Aughenbaugh, K., R. Chancey, P. Stutzman, M. Juenger, and D. Fowler. 2013. An Examination of the Reactivity of Fly Ash in Cementitious Pore Solutions. *Materials and Structures* 46, no. 5 (May 1): 869–880.

Bakharev, T. 2005a. Durability of Geopolymer Materials in Sodium and Magnesium Sulfate Solutions. *Cement and Concrete Research* 35, no. 6: 1233–1246.

Bakharev, T. 2005b. Resistance of Geopolymer Materials to Acid Attack. *Cement and Concrete Research* 35, no. 4 (April): 658–670.

Bakharev, T. 2005c. Geopolymeric Materials Prepared Using Class F Fly Ash and Elevated Temperature Curing. *Cement and Concrete Research* 35, no. 6 (June): 1224–1232.

Al Bakri, A., H. Kamarudin, I. Khairul Nizar, M. Bnhussain, Y. Zarina, and A. Rafiza. 2011. Correlation Between Na_2SiO_3/NaOH Ratio and Fly Ash/Alkaline Activator Ratio to the Strength of Geopolymer. *Advanced Materials Research* 341-342 (September): 189–193.

Al Bakri, M., A. Mohd, H. Kamarudin, O. Abdulkareem, C. Ruzaidi, A. Rafiza, and M. Norazian. 2012. Optimization of Alkaline Activator/fly Ash Ratio on the Compressive Strength of Manufacturing Fly Ash-based Geopolymer. *Applied Mechanics and Materials* 110: 734–739.

Barbosa, V., K. MacKenzie, and C. Thaumaturgo. 2000. Synthesis and Characterisation of Materials Based on Inorganic Polymers of Alumina and Silica: Sodium Polysialate Polymers. *International Journal of Inorganic Materials* 2, no. 4 (September): 309–317.

Bentz, D., and S. Remond. 1997. *Incorporation of Fly Ash into a 3-D Cement Hydration Microstructure Model*. Building and Fire Research Laboratory.

Bentz, D., P. Stutzman, C. Haecker, and S. Remond. 1999. SEM/X-ray Imaging of Cement-based Materials. *Proceedings of the 7th Euroseminar on Microscopy Applied to Building Materials Pietersen HS, Larbi JA, Janssen HHA Editors*: 457–466.

Bish, D., and R. Reynolds. 1989. Sample Preparation for X-ray Diffraction. In *Modern Powder Diffraction*, ed. D. Bish and J. Post, 20:73–97. Reviews in Mineralogy. Washington, D.C.: Mineralogical Society of America.

Buchwald, A. 2006. Influence of Geopolymer Composition on Their Structure and Properties. In *Workshop Proceedings Geopolymer Binders: Interdependence of*

Composition, Structure and Properties, ed. A. Buchwald, K. Dombrowski, and M. Weil, 55–70. Bauhaus-University Weimar, Germany: Shaker Verlag.

Buchwald, A., H. Zellmann, and C. Kaps. 2011. Condensation of Aluminosilicate Gels—model System for Geopolymer Binders. *Journal of Non-Crystalline Solids* 357, no. 5 (March 1): 1376–1382.

Bumrongjaroen, W., I. Muller, R. Livingston, and J. Davis. 2011. A Performance-Based Fly Ash Classification System Using Glassy Particle Chemical Compositional Data. In Denver, CO. http://www.flyash.info.

Chancey, R. 2008. Characterization of Crystalline and Amorphous Phases and Respective Reactivities in a Class F Fly Ash. The University of Texas at Austin. http://ezproxy.lib.utexas.edu/login?url=http://search.proquest.com/docview/304474740?accountid=7118.

Chancey, R., P. Stutzman, M. Juenger, and D. Fowler. 2010. Comprehensive Phase Characterization of Crystalline and Amorphous Phases of a Class F Fly Ash. *Cement and Concrete Research* 40, no. 1 (January): 146–156.

Chen, C., W. Gong, W. Lutze, I. Pegg, and J. Zhai. 2011. Kinetics of Fly Ash Leaching in Strongly Alkaline Solutions. *Journal of Materials Science* 46, no. 3 (February 1): 590–597.

Chen-Tan, N., A. van Riessen, C. Ly, and D. Southam. 2009. Determining the Reactivity of a Fly Ash for Production of Geopolymer. *Journal of the American Ceramic Society* 92, no. 4 (April): 881–887.

Chindaprasirt, P., T. Chareerat, and V. Sirivivatnanon. 2007. Workability and Strength of Coarse High Calcium Fly Ash Geopolymer. *Cement and Concrete Composites* 29, no. 3 (March): 224–229.

Chindaprasirt, P., P. De Silva, K. Sagoe-Crentsil, and S. Hanjitsuwan. 2012. Effect of SiO_2 and Al_2O_3on the Setting and Hardening of High Calcium Fly Ash-based Geopolymer Systems. *Journal of Materials Science* 47, no. 12: 4876–4883.

Criado, M., A. Fernández-Jiménez, A. de la Torre, M. Aranda, and A. Palomo. 2007. An XRD Study of the Effect of the SiO_2/Na_2O Ratio on the Alkali Activation of Fly Ash. *Cement and Concrete Research* 37, no. 5: 671–679.

Damtoft, J., J. Lukasik, D. Herfort, D. Sorrentino, and E. Gartner. 2008. Sustainable Development and Climate Change Initiatives. *Cement and Concrete Research* 38, no. 2 (February): 115–127.

Davidovits, J. 1982. Mineral Polymers and Methods of Making Them. http://www.freepatentsonline.com/4349386.html.

Davidovits, J. 1991. Geopolymers: Inorganic Polymeric New Materials. *Symposium on Chemical Thermodynamics, Calorimetry and Thermal Analysis 1989, September 10, 1989 - September 14, 1989* 37, no. 8: 1633–1656.

Van Deventer, J.S.J.V., J.L. Provis, and P. Duxson. 2012. Technical and Commercial Progress in the Adoption of Geopolymer Cement. *Minerals Engineering* 29, no. 0: 89 – 104.

Dhole, R., M. Thomas, K. Folliard, and T. Drimalas. 2013. Characterization of Fly Ashes for Sulfate Resistance. *ACI Materials Journal* 110, no. 2 (March 1): 159–168.

Dombrowski, K., A. Buchwald, and M. Weil. 2007. The Influence of Calcium Content on the Structure and Thermal Performance of Fly Ash Based Geopolymers. *Journal of Materials Science* 42, no. 9 (May 1): 3033–3043.

Duxson, P., A. Fernández-Jiménez, J. Provis, G. Lukey, A. Palomo, and J. Van Deventer. 2007. Geopolymer Technology: The Current State of the Art. *Special Section: Advances in Geopolymer Science and Technology. Guest Editors: Grant C. Lukey, Angel Palomo, John L. Provis, Jannie S. J. van Deventer* 42, no. 9: 2917–2933.

Duxson, P., G. Lukey, F. Separovic, and J. Van Deventer. 2005. Effect of Alkali Cations on Aluminum Incorporation in Geopolymeric Gels. *Industrial and Engineering Chemistry Research* 44, no. 4: 832–839.

Duxson, P., S. Mallicoat, G. Lukey, W. Kriven, and J. van Deventer. 2007. The Effect of Alkali and Si/Al Ratio on the Development of Mechanical Properties of Metakaolin-based Geopolymers. *Colloids and Surfaces A: Physicochemical and Engineering Aspects* 292, no. 1: 8–20.

Duxson, P., and J. Provis. 2008. Designing Precursors for Geopolymer Cements. *Journal of the American Ceramic Society* 91, no. 12: 3864–3869.

Duxson, P., J. Provis, G. Lukey, and J. van Deventer. 2007. The Role of Inorganic Polymer Technology in the Development of 'green Concrete'. *Cement and Concrete Research* 37, no. 12 (December): 1590–1597.

Fernández-Jiménez, A., A. de La Torre, A. Palomo, G. Lopez-Olmo, M. Alonso, and M. Aranda. 2006. Quantitative Determination of Phases in the Alkali Activation of Fly Ash. Part I. Potential Ash Reactivity. *Fuel* 85, no. 5-6: 625–634.

Fernández-Jiménez, A., and A. Palomo. 2003. Characterisation of Fly Ashes. Potential Reactivity as Alkaline Cements. *Fuel* 82, no. 18: 2259–2265.

Fernández-Jiménez, A., and A. Palomo. 2005. Composition and Microstructure of Alkali Activated Fly Ash Binder: Effect of the Activator. *Cement and Concrete Research* 35, no. 10: 1984–1992.

Fernández-Jiménez, A., A. Palomo, and M. Criado. 2005. Microstructure Development of Alkali-activated Fly Ash Cement: a Descriptive Model. *Cement and Concrete Research* 35, no. 6 (June): 1204–1209.

Fernández-Jiménez, A., A. Palomo, and C. Lopez-Hombrados. 2006. Engineering Properties of Alkali-activated Fly Ash Concrete. *ACI Materials Journal* 103, no. 2.

Fernández-Jiménez, A., A. Palomo, I. Sobrados, and J. Sanz. 2006. The Role Played by the Reactive Alumina Content in the Alkaline Activation of Fly Ashes. *Microporous and Mesoporous Materials* 91, no. 1-3: 111–119.

Fernández-Jiménez, A., A. de la Torre, A. Palomo, G. López-Olmo, M. Alonso, and M. Aranda. 2006. Quantitative Determination of Phases in the Alkaline Activation of Fly Ash. Part II: Degree of Reaction. *Fuel* 85, no. 14–15 (October): 1960–1969.

Fletcher, R., K. MacKenzie, C. Nicholson, and S. Shimada. 2005. The Composition Range of Aluminosilicate Geopolymers. *Journal of the European Ceramic Society* 25, no. 9: 1471–1477.

García-Lodeiro, I., A. Palomo, and A. Fernández-Jiménez. 2007. Alkali–aggregate Reaction in Activated Fly Ash Systems. *Cement and Concrete Research* 37, no. 2: 175–183.
Gasteiger, R., W. Frederick, and R. Streisel. 1992. Solubility of Aluminosilicates in Alkaline Solutions and a Thermodynamic Equilibrium Model. *Industrial & Engineering Chemistry Research* 31, no. 4: 1183–1190.
Glukovoski, V. 1979. Alkali-earth binders and concretes produced with them. Kiev, USSR: Visheka Shkola.
Goldstein, J., D. Newbury, D. Joy, C. Lyman, P. Echlin, E. Lifshin, L. Sawyer, and J. Michael. 2003. *Scanning Electron MIcroscopy and X-Ray Microanalysis*. Third Edition. New York: Springer.
Hardjito, D., S. Wallah, D. Sumajouw, and B. Rangan. 2004. On the Development of Fly Ash-based Geopolymer Concrete. *ACI Materials Journal* 101, no. 6: 467 – 472.
Hartigan, J., and M. Wong. 1979. Algorithm AS 136: A K-means Clustering Algorithm. *Journal of the Royal Statistical Society. Series C (Applied Statistics)* 28, no. 1: 100–108.
Heah, C., H. Kamarudin, A. Mustafa Al Bakri, M. Bnhussain, M. Luqman, I. Khairul Nizar, C. Ruzaidi, and Y. Liew. 2012. Study on Solids-to-liquid and Alkaline Activator Ratios on Kaolin-based Geopolymers. *Construction and Building Materials* 35: 912–922.
Hemmings, R., and E. Berry. 1987. On the Glass in Coal Fly Ashes: Recent Advances. *MRS Online Proceedings Library* 113.
Hendricks, C., E. Worrell, L. Price, N. Martin, and L. Ozawa Meida. 1999. Greenhouse Gases from Cement Production. In Utrecht, The Netherlands: ECOFYS.
Jenkins, R. 1989. Experimental Procedures. In *Modern Powder Diffraction*, ed. D. Bish and J. Post, 20:19–43. Reviews in Mineralogy. Washington, D.C.: Mineralogical Society of America.
Joshi, R., G. Natt, R. Day, and D. Tilleman. 1984. Scanning Electron Microscopy and X-Ray Diffraction Analysis of Various Size Fractions of Fly Ash. *MRS Online Proceedings Library* 43.
Juenger, M., F. Winnefeld, J. Provis, and J. Ideker. 2011. Advances in Alternative Cementitious Binders. *Cement and Concrete Research* 41, no. 12 (December): 1232–1243.
Kerrick, D., L. Bminhizer, and J. Villaume. 1973. The Role of Carbon Film Thickness in Electron Microprobe Analysis. *American Mineralogist* 58: 920–925.
Khale, D., and R. Chaudhary. 2007. Mechanism of Geopolymerization and Factors Influencing Its Development: a Review. *Journal of Materials Science* 42, no. 3 (February 1): 729–746.
Kilgour, C., and S. Diamond. 1987. The Internal Structure of a Low-Calcium Fly Ash. *MRS Online Proceedings Library* 113: null–null.
Klein, C., and C. Hurlbut, Jr. 1977. *Manual of Mineralogy*. 20th ed. New York: John Wiley and Sons.

Klug, H., and L. Alexander. 1974. X-ray Diffraction. *Addision-Wilson Publishing Company Inc, USA*: 132.
Kovalchuk, G., A. Fernández-Jiménez, and A. Palomo. 2007. Alkali-activated Fly Ash: Effect of Thermal Curing Conditions on Mechanical and Microstructural Development - Part II. *Fuel* 86, no. 3: 315–322.
Kruse, K. 2012. Characterization of High-Calcium Fly Ash for Evaluating the Sulfate Resistance of Concrete. The University of Texas at Austin.
Lee, S., and J. Stebbins. 1999. The Degree of Aluminum Avoidance in Aluminosilicate Glasses. *American Mineralogist* 84, no. 5-6: 937–945.
Lizcano, M., A. Gonzalez, S. Basu, K. Lozano, and M. Radovic. 2012. Effects of Water Content and Chemical Composition on Structural Properties of Alkaline Activated Metakaolin-Based Geopolymers. *Journal of the American Ceramic Society* 95, no. 7: 2169–2177.
Lloyd, R. 2008. The Durability of Inorganic Polymer Cements. Melbourne, Australia: University of Melbourne.
Loewenstein, W. 1954. The Distribution of Aluminum in the Tetrahedra of Silicates and Aluminates. *American Mineralogist* 39, no. 1-2: 92–96.
Lydon, J. 2005. The Measurement of the Modal Mineralogy of Rocks from SEM Imagery: The Use of Multispec and ImageJ Freeware. *Geological Survey of Canada, Open File* 4941: 37.
Ma, Y., J. Hu, and G. Ye. 2012. The Effect of Activating Solution on the Mechanical Strength, Reaction Rate, Mineralogy, and Microstructure of Alkali-activated Fly Ash. *Journal of Materials Science* 47, no. 11: 4568–4578.
Maniguet, L., F. Robaut, A. Meuris, F. Roussel-Dherbey, and F. Chariot. 2012. X-ray Microanalysis: The State of the Art of SDD Detectors and WDS Systems on Scanning Electron Microscopes (SEM). *IOP Conference Series: Materials Science and Engineering* 32, no. 1 (March 7): 012015.
McCarthy, G. 1987. X-ray Powder Diffraction for Studying the Mineralogy of Fly Ash. In *MRS Proceedings*, 113:75–86.
McCarthy, G., J. Solem, O. Manz, and D. Hassett. 1989. Use of a Database of Chemical, Mineralogical and Physical Properties of North American Fly Ash to Study the Nature of Fly Ashand Its Utilization as a Mineral Admixture in Concrete. In *MRS Proceedings*, 178:3.
Nesse, W. 2000. *Introduction to Mineralogy*. New York: Oxford University Press.
Oh, J., P. Monteiro, S. Jun, S. Choi, and S. Clark. 2010. The Evolution of Strength and Crystalline Phases for Alkali-activated Ground Blast Furnace Slag and Fly Ash-based Geopolymers. *Cement and Concrete Research* 40, no. 2 (February): 189–196.
Palomo, A., S. Alonso, A. Fernández-Jiménez, I. Sobrados, and J. Sanz. 2004. Alkaline Activation of Fly Ashes: NMR Study of the Reaction Products. *Journal of the American Ceramic Society* 87, no. 6: 1141–1145.

Palomo, A., M. Blanco-Varela, M. Granizo, F. Puertas, T. Vazquez, and M. Grutzeck. 1999. Chemical Stability of Cementitious Materials Based on Metakaolin. *Cement and Concrete Research* 29, no. 7 (July): 997–1004.

Palomo, A., M. Grutzeck, and M. Blanco. 1999. Alkali-activated Fly Ashes: A Cement for the Future. *Proceedings of the 1998 Engineering Foundation International Conference on Advances in Cement and Concrete, Jul 5 - Jul 10 1998* 29, no. 8: 1323–1329.

Panagiotopoulou, C., E. Kontori, T. Perraki, and G. Kakali. 2007. Dissolution of Aluminosilicate Minerals and By-products in Alkaline Media. *Journal of Materials Science* 42, no. 9: 2967–2973.

Pietersen, H. 1993. Reactivity of Fly Ash and Slag in Cement. Delft University of Technology, Delft, The Netherlands.

Provis, J., A. Hajimohammadi, C. White, S. Bernal, R. Myers, R. Winarski, V. Rose, T. Proffen, A. Llobet, and J. Deventer. 2013. Nanostructural Characterization of Geopolymers by Advanced Beamline Techniques. *Cement and Concrete Composites* 36, no. 0: 56 – 64.

Purdon, A. 1940. The Action of Alkalis on Blast-furnace Slag. *Journal of the Society of Chemical Industry- Transactions and Communications* 59: 191–202.

Qian, J., and F. Glasser. 1987. Bulk Composition of the Glassy Phase in Some Commercial PFA's. *MRS Online Proceedings Library* 113.

Reed, R. 1989. Instrumentation. In *Modern Powder Diffraction*, ed. D. Bish and J. Post, 20:19–43. Reviews in Mineralogy. Washington, D.C.: Mineralogical Society of America.

Rees, C., J. Provis, G. Lukey, and J. van Deventer. 2007. In Situ ATR-FTIR Study of the Early Stages of Fly Ash Geopolymer Gel Formation. *Langmuir* 23, no. 17: 9076–9082.

Reynolds, Jr., R. 1989. Principles of Powder Diffraction. In *Modern Powder Diffraction*, ed. D.L. Bish and J.E. Post. Vol. 20. Reviews in Mineralogy. Washington, D.C.: Mineralogical Society of America.

Rietveld, H. 1969. A Profile Refinement Method for Nuclear and Magnetic Structures. *Journal of Applied Crystallography* 2, no. 2 (June): 65–71.

Rowles, M., and B. O'Connor. 2003. Chemical Optimisation of the Compressive Strength of Aluminosilicate Geopolymers Synthesised by Sodium Silicate Activation of Metakaolinite. *Journal of Materials Chemistry* 13, no. 5: 1161–1165.

Roy, D., K. Luke, and S. Diamond. 1984. Characterization of Fly Ash and Its Reactions in Concrete. *MRS Online Proceedings Library* 43: null–null.

Ruiz-Santaquiteria, C., J. Skibsted, A. Fernández-Jiménez, and A. Palomo. 2012. Alkaline Solution/binder Ratio as a Determining Factor in the Alkaline Activation of Aluminosilicates. *Cement and Concrete Research* 42, no. 9 (September): 1242–1251.

Sarker, P. 2009. Analysis of Geopolymer Concrete Columns. *Materials and Structures* 42, no. 6: 715–724.

Shelby, J. 2005. *Introduction to Glass Science and Technology*. 2nd ed. Cambridge: Royal Society of Chemistry.

Skorina, T., and I. Tikhomirova. 2012. Alkali Silicate Binders: Effect of SiO_2/Na_2O Ratio and Alkali Metal Ion Type on the Structure and Mechanical Properties. *Journal of Materials Science* 47, no. 12 (June 1): 5050–5059.

Sleight, C. 2013. Global Cement Demand to See +4.9% Growth. *International Construction*. Accessed March 26. http://www.khl.com/magazines/international-construction/detail/item83167/Global-cement-demand-to-see-4,9pc-growth.

Sofi, M., J. Van Deventer, P. Mendis, and G. Lukey. 2007. Engineering Properties of Inorganic Polymer Concretes (IPCs). *Cement and Concrete Research* 37, no. 2: 251–257.

Somna, K., C. Jaturapitakkul, P. Kajitvichyanukul, and P. Chindaprasirt. 2011. NaOH-activated Ground Fly Ash Geopolymer Cured at Ambient Temperature. *Fuel* 90, no. 6 (June): 2118–2124.

Stevenson, R., and T. Huber. 1986. SEM Study of Chemical Variations in Western U.S. Fly Ash. *MRS Online Proceedings Library* 86.

Temuujin, J., A. vanRiessen, and R. Williams. 2009. Influence of Calcium Compounds on the Mechanical Properties of Fly Ash Geopolymer Pastes. *Journal of Hazardous Materials* 167, no. 1–3: 82 – 88.

Temuujin, J., R. Williams, and A. vanRiessen. 2009. Effect of Mechanical Activation of Fly Ash on the Properties of Geopolymer Cured at Ambient Temperature. *Journal of Materials Processing Technology* 209, no. 12–13: 5276 – 5280.

Ward, C., and D. French. 2006. Determination of Glass Content and Estimation of Glass Composition in Fly Ash Using Quantitative X-ray Diffractometry. *Fuel* 85, no. 16 (November): 2268–2277.

Williams, P., J. Biernacki, C. Rawn, L. Walker, and J. Bai. 2005. Microanalytical and Computational Analysis of Class F Fly Ash. *Aci Materials Journal* 102, no. 5 (October): 330–337.

Williams, R., and A. van Riessen. 2010. Determination of the Reactive Component of Fly Ashes for Geopolymer Production Using XRF and XRD. *Fuel* 89, no. 12 (December): 3683–3692.

Worrell, E., L. Price, N. Martin, C. Hendriks, and L. Meida. 2001. Carbon Dioxide Emissions from the Global Cement Industry 1. *Annual Review of Energy and the Environment* 26, no. 1: 303–329.

Xu, H., and J. Van Deventer. 2000. The Geopolymerisation of Alumino-silicate Minerals. *International Journal of Mineral Processing* 59, no. 3 (June): 247–266.

Young, R. 1993. Introduction to the Rietveld Method. In *The Rietveld Method*, 1–38. Oxford University Press.